

Frontier Materials & Technologies

Founded in 2008

№ 3

2024

16+

Quarterly
Scientific Journal

The Founder is
Togliatti State University

Editor-in-Chief

Mikhail M. Krishtal, DSc (Physics and Mathematics), Professor

Deputy Editor-in-Chief

for Metallurgy and Materials Science

Dmitry L. Merson, DSc (Physics and Mathematics), Professor

Deputy Editor-in-Chief

for Mechanical Engineering and Machine Science

Aleksandr P. Shaikin, DSc (Engineering), Professor

Deputy Editor-in-Chief

for Welding and Allied Processes and Technologies

Aleksandr I. Kovtunov, DSc (Engineering), Associate Professor

Editors:

Petr Yu. Bochkarev, DSc (Engineering), Professor

Boris M. Brzhozovskiy, DSc (Engineering), Professor

Aleksandr F. Denisenko, DSc (Engineering), Professor

Yuri Z. Estrin, DSc (Physics and Mathematics), Professor

Sergey S. Gavryushin, DSc (Engineering), Professor

Gregory Gerstein, DSc (Engineering)

Fedor V. Grechnikov, Academician of the Russian Academy of Sciences, DSc (Engineering), Professor

Mikhail I. Karpov, Corresponding Member of the Russian Academy of Sciences, DSc (Engineering), Professor

Aleksandr V. Katsman, PhD (Physics and Mathematics)

Aleksandr A. Kazakov, DSc (Engineering), Professor

Aleksandr V. Kudrya, DSc (Engineering), Professor

Sergey V. Kuzmin, Corresponding Member of the Russian Academy of Sciences, DSc (Engineering), Professor

Aleksey V. Makarov, Corresponding Member of the Russian Academy of Sciences, DSc (Engineering)

Radik R. Mulyukov, Corresponding Member of the Russian Academy of Sciences,

DSc (Physics and Mathematics), Professor

Oleg B. Naimark, DSc (Physics and Mathematics), Professor

Nikolay V. Nosov, DSc (Engineering), Professor

Aleksandr V. Pilinsky, PhD (Engineering), Associate Professor

Aleksey E. Romanov, DSc (Physics and Mathematics), Professor

Vasili V. Rubanik, Corresponding Member of the National Academy of Sciences of Belarus, DSc (Engineering)

Vladimir A. Shishkov, DSc (Engineering)

Tushar Madhukar Sonar, PhD (Engineering)

Rudolf N. Starobinski, DSc (Engineering), Professor

Ramasubbu Sunder, Fellow of the Indian Academy of Sciences, PhD (Engineering)

Vladimir P. Tabakov, DSc (Engineering), Professor

Alexey Yu. Vinogradov, DSc (Engineering), PhD (Physics and Mathematics), Professor

Until December 2021,
the journal was published under
the title
“**Science Vector**
of Togliatti State University”.

Indexed in Scopus.
Included in the List of HAC,
RSCI core, DOAJ,
“White List”.
Available in Crossref,
Google Scholar.

Registered by the Federal
Service for Supervision
of Communications,
Information Technology
and Mass Media
(Registration Certificate
ПИ No. ФС77-83040
dated March 31, 2022).

Subscription index
in the Russian Press catalogue:
13088.

Desktop publishing:

Natalya A. Nikitenko

*Responsible/technical
editor:*

Natalya A. Nikitenko

Mailing Address:

14, Belorusskaya St.,

Togliatti,

Russia, 445020

Phone: **(8482) 44-91-74**

E-mail:

vektornaukitgu@yandex.ru

Website:

<https://vektornaukitech.ru>

Passed for printing
16.09.2024.

Published 30.09.2024.

Format 60×84 1/8.

Digital printing.

Conventional printed sheets 14.4.

Circulation is 30 copies.

Order 3-135-24.

The price is free.

EDITORIAL BOARD INFORMATION

Editor-in-Chief

Mikhail M. Krishtal, Doctor of Sciences (Physics and Mathematics), Professor, Rector (Togliatti State University, Togliatti, Russia).
Scopus AuthorID: [14634063100](#)
ResearcherID: [AAD-7707-2019](#)
ORCID: <https://orcid.org/0000-0001-7189-0002>

Deputy Editor-in-Chief for Metallurgy and Materials Science

Dmitry L. Merson, Doctor of Sciences (Physics and Mathematics), Professor, Director of the Research and Development Institute of Advanced Technologies (Togliatti State University, Togliatti, Russia).
Scopus AuthorID: [6603449333](#)
ResearcherID: [M-7210-2016](#)
ORCID: <https://orcid.org/0000-0001-5006-4115>

Deputy Editor-in-Chief for Mechanical Engineering and Machine Science

Aleksandr P. Shaikin, Doctor of Sciences (Engineering), Professor, Professor of Chair “Energy-Converting Machines and Control Systems” (Togliatti State University, Togliatti, Russia).
Scopus AuthorID: [6602779899](#)
ORCID: <https://orcid.org/0000-0002-9832-4753>

Deputy Editor-in-Chief for Welding and Allied Processes and Technologies

Aleksandr I. Kovtunov, Doctor of Sciences (Engineering), Associate Professor, Professor of Chair “Welding, Pressure Treatment of Materials and Allied Processes” (Togliatti State University, Togliatti, Russia).
Scopus AuthorID: [36761987000](#)
ResearcherID: [B-4545-2016](#)
ORCID: <https://orcid.org/0000-0002-7705-7377>

Editorial board:

Petr Yu. Bochkarev, Doctor of Sciences (Engineering), Professor, Professor of Chair “Mechanical Engineering Technology and Applied Mechanics” (Kamyshin Technological Institute (Branch) of Volgograd State Technical University, Kamyshin, Russia), Professor of Chair “Technical Support of Agro-Industrial Complex” (Saratov State Vavilov Agrarian University, Saratov, Russia).
Scopus AuthorID: [57189893110](#)

Boris M. Brzhozovskiy, Doctor of Sciences (Engineering), Professor, chief researcher of Laboratory of Theory of Mechanisms and Machine Structure (Institute of Machines Science named after A.A. Blagonravov of the Russian Academy of Sciences, Moscow, Russia).
Scopus AuthorID: [55683317200](#)

Alexander F. Denisenko, Doctor of Sciences (Engineering), Professor, Professor of Chair “Technology of Mechanical Engineering, Machines and Tools” (Samara State Technical University, Samara, Russia).

Scopus AuthorID: [36131150100](#)

Yuri Z. Estrin, Doctor of Sciences (Physics and Mathematics), Professor, Professor of Chair of Engineering Materials (Monash University, Melbourne, Australia).

Scopus AuthorID: [7005031984](#)

Sergey S. Gavryushin, Doctor of Sciences (Engineering), Professor, Head of Chair “Computer Systems of Production Automation”, Head of the Theory & Machines Structure Laboratory (Bauman Moscow State Technical University, Moscow, Russia; Mechanical Engineering Research Institute of the Russian Academy of Sciences, Moscow, Russia).

Scopus AuthorID: [6507067486](#)

ResearcherID: [AAT-8610-2020](#)

ORCID: <https://orcid.org/0000-0002-6547-1351>

Gregory Gerstein, Doctor of Sciences (Engineering), Laboratory Head (Leibniz University Hannover, Hanover, Germany).

Scopus AuthorID: [55001912200](#)

Fedor V. Grechnikov, Academician of the Russian Academy of Sciences, Doctor of Sciences (Engineering), Professor, Head of the Chair of Forming Processes (Samara National Research University, Samara, Russia).

Scopus AuthorID: [6506174877](#)

ResearcherID: [P-2319-2016](#)

ORCID: <https://orcid.org/0000-0002-3767-4004>

Mikhail I. Karpov, Corresponding Member of the Russian Academy of Sciences, Doctor of Sciences (Engineering), Professor, Head of the Laboratory of Materials Science (Institute of Solid State Physics of the Russian Academy of Sciences, Chernogolovka, Russia).

Scopus AuthorID: [7004130343](#)

ResearcherID: [Q-9288-2016](#)

Aleksandr V. Katsman, PhD (Physics and Mathematics), Senior Research Associate (Technion – Israel Institute of Technology, Haifa, Israel).

Scopus AuthorID: [7004225554](#)

Aleksandr A. Kazakov, Doctor of Sciences (Engineering), Professor, Professor of Chair “Metallurgy and Casting Technologies”, Head of the Metallurgy Expertise Laboratory (Peter the Great Saint-Petersburg Polytechnic University, St. Petersburg, Russia).

Scopus AuthorID: [56037035400](#)

ResearcherID: [E-6090-2014](#)

ORCID: <https://orcid.org/0000-0001-6511-1228>

Aleksandr V. Kudrya, Doctor of Sciences (Engineering), Professor, Professor of Chair of Physical Metallurgy and Physics of Strength (National University of Science and Technology MISiS, Moscow, Russia).

Scopus AuthorID: [6603628218](#)

Sergey V. Kuzmin, Corresponding Member of the Russian Academy of Sciences, Doctor of Sciences (Engineering), Professor, First Prorector, Professor of Chair “Equipment and Technology of Welding Production” (Volgograd State Technical University, Volgograd, Russia).

Scopus AuthorID: [57217278342](#)

ResearcherID: [I-7424-2012](#)

ORCID: <https://orcid.org/0000-0003-2802-8497>

Aleksey V. Makarov, Corresponding Member of the Russian Academy of Sciences, Doctor of Sciences (Engineering), Chief Research Associate, Head of Chair of Materials Science, Head of the Laboratory of Mechanical Properties (M.N. Mikheev Institute of Metal Physics of Ural Branch of Russian Academy of Sciences, Ekaterinburg, Russia).

Scopus AuthorID: [57195590138](#)

ResearcherID: [D-5663-2016](#)

ORCID: <https://orcid.org/0000-0002-2228-0643>

Radik R. Mulyukov, Corresponding Member of the Russian Academy of Sciences, Doctor of Sciences (Physics and Mathematics), Professor, Director (Institute for Metals Superplasticity Problems of the Russian Academy of Sciences, Ufa, Russia).

Scopus AuthorID: [7003520439](#)

ResearcherID: [B-3800-2016](#)

ORCID: <https://orcid.org/0000-0002-0452-3816>

Oleg B. Naimark, Doctor of Sciences (Physics and Mathematics), Professor, Head of the Laboratory of Physical Foundations of Strength (Institute of Continuous Media Mechanics of Ural Branch of Russian Academy of Sciences, Perm, Russia).

Scopus AuthorID: [6701720806](#)

Nikolay V. Nosov, Doctor of Sciences (Engineering), Professor, Professor of Chair “Technology of Mechanical Engineering, Machines and Tools” (Samara State Technical University, Samara, Russia).

Scopus AuthorID: [6602506825](#)

Aleksandr V. Pilinsky, PhD (Engineering), Associate Professor, MSME (Master of Science in Mechanical Engineering), Los Angeles, USA.

ORCID: <https://orcid.org/0009-0009-8933-195X>

Aleksey E. Romanov, Doctor of Sciences (Physics and Mathematics), Professor, Professor of the Institute of Advanced Data Transfer Systems (ITMO University, St. Petersburg, Russia).

Scopus AuthorID: [7202768874](#)

Vasili V. Rubanik, Corresponding Member of the National Academy of Sciences of Belarus, Doctor of Sciences (Engineering), Head of the Laboratory of Metal Physics (Institute of Technical Acoustics of the National Academy of Sciences of Belarus, Vitebsk, Belarus).

Scopus AuthorID: [57215218253](#)

Vladimir A. Shishkov, Doctor of Sciences (Engineering), Head of the Technical Department (Palladio LLC, Togliatti, Russia).

RSCI AuthorID: [596086](#)

SPIN-code: [9504-4454](#)

Tushar Madhukar Sonar, PhD (Engineering), Senior Research Scientist of Chair “Welding Engineering”

(South Ural State University, Chelyabinsk, Russia).

Scopus AuthorID: [57200800257](#)

ResearcherID: [AAS-6037-2021](#)

ORCID: <https://orcid.org/0000-0002-3997-5337>

Rudolf N. Starobinski, Doctor of Sciences (Engineering), Professor, Scientific Consultant (Silencers. Consulting and Engineering, Hamburg, Germany).

Scopus AuthorID: [6602638504](#)

Ramasubbu Sunder, Fellow of the Indian Academy of Sciences, PhD (Engineering), Director (BISS (P) Ltd, Bangalore, India).

Scopus AuthorID: [7003530245](#)

ResearcherID: [H-6740-2016](#)

ORCID: <https://orcid.org/0000-0001-6143-0723>

Vladimir P. Tabakov, Doctor of Sciences (Engineering), Professor, Head of Chair “Innovative Technologies in Mechanical Engineering” (Ulyanovsk State Technical University, Ulyanovsk, Russia).

Scopus AuthorID: [6701501345](#)

ResearcherID: [E-1832-2017](#)

ORCID: <https://orcid.org/0000-0002-2568-9401>

Alexey Yu. Vinogradov, Doctor of Sciences (Engineering), PhD (Physics and Mathematics), Professor, Professor of Faculty of Mechanical and Industrial Engineering (Norwegian University of Science and Technology, Trondheim, Norway).

Scopus AuthorID: [7402889776](#)

ResearcherID: [A-7175-2009](#)

ORCID: <https://orcid.org/0000-0001-9585-2801>

СВЕДЕНИЯ О ЧЛЕНАХ РЕДКОЛЛЕГИИ

Главный редактор

Кристал Михаил Михайлович, доктор физико-математических наук, профессор, ректор (Тольяттинский государственный университет, Тольятти, Россия).

Scopus AuthorID: [14634063100](#)

ResearcherID: [AAD-7707-2019](#)

ORCID: <https://orcid.org/0000-0001-7189-0002>

Заместитель главного редактора по направлению «Металлургия и материаловедение»

Мерсон Дмитрий Львович, доктор физико-математических наук, профессор, директор Научно-исследовательского института перспективных технологий (Тольяттинский государственный университет, Тольятти, Россия).

Scopus AuthorID: [6603449333](#)

ResearcherID: [M-7210-2016](#)

ORCID: <https://orcid.org/0000-0001-5006-4115>

Заместитель главного редактора по направлению «Машиностроение и машиноведение»

Шайкин Александр Петрович, доктор технических наук, профессор, профессор кафедры «Энергетические машины и системы управления» (Тольяттинский государственный университет, Тольятти, Россия).

Scopus AuthorID: [6602779899](#)

ORCID: <https://orcid.org/0000-0002-9832-4753>

Заместитель главного редактора по направлению «Сварка, родственные процессы и технологии»

Ковтунов Александр Иванович, доктор технических наук, доцент, профессор кафедры «Сварка, обработка материалов давлением и родственные процессы» (Тольяттинский государственный университет, Тольятти, Россия).

Scopus AuthorID: [36761987000](#)

ResearcherID: [B-4545-2016](#)

ORCID: <https://orcid.org/0000-0002-7705-7377>

Редакционная коллегия:

Бочкарев Петр Юрьевич, доктор технических наук, профессор, профессор кафедры «Технология машиностроения и прикладная механика» (Камышинский технологический институт (филиал) Волгоградского государственного технического университета, Камышин, Россия), профессор кафедры «Техническое обеспечение АПК» (Саратовский государственный аграрный университет имени Н.И. Вавилова, Саратов, Россия).

Scopus AuthorID: [57189893110](#)

Бржозовский Борис Максевич, доктор технических наук, профессор главный научный сотрудник лаборатории теории механизмов и структуры машин (Институт машиноведения им. А.А. Благонравова РАН, Москва, Россия).

Scopus AuthorID: [55683317200](#)

Виноградов Алексей Юрьевич, доктор технических наук, кандидат физико-математических наук, профессор факультета механической и промышленной инженерии (Норвежский университет науки и технологии, Тронхейм, Норвегия).

Scopus AuthorID: [7402889776](#)

ResearcherID: [A-7175-2009](#)

ORCID: <https://orcid.org/0000-0001-9585-2801>

Гаврюшин Сергей Сергеевич, доктор технических наук, профессор, заведующий кафедрой «Компьютерные системы автоматизации производства», заведующий лабораторией компьютерных систем автоматизации производства и цифровых технологий (Московский государственный технический университет имени Н.Э. Баумана (национальный исследовательский университет), Москва, Россия; Институт машиноведения им. А.А. Благонравова Российской академии наук, Москва, Россия).

Scopus AuthorID: [6507067486](#)

ResearcherID: [AAT-8610-2020](#)

ORCID: <https://orcid.org/0000-0002-6547-1351>

Герштейн Григорий, доктор технических наук, заведующий лабораторией (Ганноверский университет имени Готфрида Вильгельма Лейбница, Ганновер, Германия).

Scopus AuthorID: [55001912200](#)

Гречников Федор Васильевич, академик РАН, доктор технических наук, профессор, заведующий кафедрой обработки металлов давлением (Самарский национальный исследовательский университет имени академика С.П. Королева, Самара, Россия).

Scopus AuthorID: [6506174877](#)

ResearcherID: [P-2319-2016](#)

ORCID: <https://orcid.org/0000-0002-3767-4004>

Денисенко Александр Федорович, доктор технических наук, профессор, профессор кафедры «Технология машиностроения, станки и инструменты» (Самарский государственный технический университет, Самара, Россия).

Scopus AuthorID: [36131150100](#)

Казаков Александр Анатольевич, доктор технических наук, профессор, профессор кафедры «Металлургические и литейные технологии», руководитель научно-испытательной лаборатории «Металлургическая экспертиза» (Санкт-Петербургский политехнический университет Петра Великого, Санкт-Петербург, Россия).

Scopus AuthorID: [56037035400](#)

ResearcherID: [E-6090-2014](#)

ORCID: <https://orcid.org/0000-0001-6511-1228>

Карнов Михаил Иванович, член-корреспондент РАН, доктор технических наук, профессор, заведующий лабораторией материаловедения (Институт физики твердого тела Российской академии наук, Черноголовка, Россия).

Scopus AuthorID: [7004130343](#)

ResearcherID: [Q-9288-2016](#)

Кацман Александр Владимирович, кандидат физико-математических наук, PhD, старший научный сотрудник (Технион – Израильский технологический институт, Хайфа, Израиль).

Scopus AuthorID: [7004225554](#)

Кудря Александр Викторович, доктор технических наук, профессор, заместитель заведующего кафедрой металловедения и физики прочности (Национальный исследовательский технологический университет «МИСиС», Москва, Россия).

Scopus AuthorID: [6603628218](#)

Кузьмин Сергей Викторович, член-корреспондент РАН, доктор технических наук, профессор, первый проректор, профессор кафедры «Оборудование и технология сварочного производства» (Волгоградский государственный технический университет, Волгоград, Россия).

Scopus AuthorID: [57217278342](#)

ResearcherID: [I-7424-2012](#)

ORCID: <https://orcid.org/0000-0003-2802-8497>

Макаров Алексей Викторович, член-корреспондент РАН, доктор технических наук, главный научный сотрудник, заведующий отделом материаловедения и лабораторией механических свойств (Институт физики металлов имени М.Н. Михеева Уральского отделения Российской академии наук, Екатеринбург, Россия).

Scopus AuthorID: [57195590138](#)

ResearcherID: [D-5663-2016](#)

ORCID: <https://orcid.org/0000-0002-2228-0643>

Мулюков Радик Рафикович, член-корреспондент РАН, доктор физико-математических наук, профессор, директор (Институт проблем сверхпластичности металлов Российской академии наук, Уфа, Россия).

Scopus AuthorID: [7003520439](#)

ResearcherID: [B-3800-2016](#)

ORCID: <https://orcid.org/0000-0002-0452-3816>

Наймарк Олег Борисович, доктор физико-математических наук, профессор, заведующий лабораторией «Физические основы прочности» (Институт механики сплошных сред Уральского отделения Российской академии наук, Пермь, Россия).

Scopus AuthorID: [6701720806](#)

Носов Николай Васильевич, доктор технических наук, профессор, профессор кафедры «Технология машиностроения, станки и инструменты» (Самарский государственный технический университет, Самара, Россия).

Scopus AuthorID: [6602506825](#)

Пилинский Александр Вениаминович, кандидат технических наук, доцент, MSME (Master of Science in Mechanical Engineering), Лос-Анджелес, США.

ORCID: <https://orcid.org/0009-0009-8933-195X>

Романов Алексей Евгеньевич, доктор физико-математических наук, профессор Института перспективных систем передачи данных, руководитель научно-исследовательского центра перспективных функциональных материалов и лазерных коммуникационных систем (Национальный исследовательский университет ИТМО, Санкт-Петербург, Россия).

Scopus AuthorID: [7202768874](#)

Рубаник Василий Васильевич, член-корреспондент Национальной академии наук Беларуси, доктор технических наук, заведующий лабораторией физики металлов (Институт технической акустики Национальной академии наук Беларуси, Витебск, Республика Беларусь).

Scopus AuthorID: [57215218253](#)

Сонар Тушар Мадхукар, кандидат технических наук, старший научный сотрудник кафедры «Оборудование и технология сварочного производства» (Южно-Уральский государственный университет, Челябинск, Россия).

Scopus AuthorID: [57200800257](#)

ResearcherID: [AAS-6037-2021](#)

ORCID: <https://orcid.org/0000-0002-3997-5337>

Старобинский Рудольф Натанович, доктор технических наук, профессор, научный консультант (консалтинг-бюро “Prof. Starobinski. Silencers. Consulting and Engineering”, Гамбург, Германия).

Scopus AuthorID: [6602638504](#)

Сундер Рамасуббу, член Индийской академии наук, кандидат технических наук, директор (“BISS (P) Ltd”, Бангалор, Индия).

Scopus AuthorID: [7003530245](#)

ResearcherID: [H-6740-2016](#)

ORCID: <https://orcid.org/0000-0001-6143-0723>

Табакон Владимир Петрович, доктор технических наук, профессор, заведующий кафедрой «Инновационные технологии в машиностроении» (Ульяновский государственный технический университет, Ульяновск, Россия).

Scopus AuthorID: [6701501345](#)

ResearcherID: [E-1832-2017](#)

ORCID: <https://orcid.org/0000-0002-2568-9401>

Шишков Владимир Александрович, доктор технических наук, начальник технического отдела (ООО «Палладио», Тольятти, Россия).

AuthorID РИНЦ: [596086](#)

SPIN-код: [9504-4454](#)

Эстрин Юрий Захарович, доктор физико-математических наук, профессор, профессор кафедры инженерных материалов (Университет им. Монаша, Мельбурн, Австралия).

Scopus AuthorID: [7005031984](#)

CONTENT

Self-propagating high-temperature synthesis of AlN–TiC powder composition using sodium azide and C₂F₄ fluoroplastic Belova G.S., Titova Yu.V., Maidan D.A., Yakubova A.F.	9
Corrosion-mechanical destruction of bainite structures in oilfield environments Vyboishchik M.A., Gruzkov I.V.	17
The influence of phosphorus microalloying on the structure formation of CuZn₃₂Mn₃Al₂FeNi multicomponent brass Gnusina A.M., Svyatkin A.V.	31
The influence of grain size on hydrogen embrittlement of a multicomponent (FeCrNiMnCo)₉₉N₁ alloy Gurtova D.Yu., Panchenko M.Yu., Melnikov E.V., Astapov D.O., Astafurova E.G.	41
Accuracy of the geometric shape of the hole in the longitudinal section during honing Denisenko A.F., Grishin R.G., Antipova E.D.	53
The influence of 3D printing mode on the chemical composition and structure of 30HGSA steel Kabaldin Yu.G., Anosov M.S., Mordovina Yu.S., Chernigin M.A.	63
Microstructure, crystallographic texture and mechanical properties of the Zn–1%Mg–1%Fe alloy subjected to severe plastic deformation Sitdikov V.D., Khafizova E.D., Polenok M.V.	75
Pulse diffusion welding of female joints Strizhakov E.L., Nescoromniy S.V., Lyudmirsky Yu.G., Mordovtsev N.A.	89
The influence of cutting mode elements on the technological parameters of the process of milling blanks of titanium alloy thin-walled parts Unyanin A.N., Chudnov A.V.	99
Microstructure and strength of a 3D-printed Ti–6Al–4V alloy subjected to high-pressure torsion Usmanov E.I., Savina Ya.N., Valiev R.R.	109
OUR AUTHORS	117

СОДЕРЖАНИЕ

Самораспространяющийся высокотемпературный синтез порошковой композиции AlN–TiC с применением азиды натрия и фторопласта C₂F₄ Белова Г.С., Титова Ю.В., Майдан Д.А., Якубова А.Ф.	9
Коррозионно-механическое разрушение бейнитных структур в нефтепромысловых средах Выбойщик М.А., Грузков И.В.	17
Влияние микролегирования фосфором на структурообразование многокомпонентной латуни ЛМцАЖН Гнусина А.М., Святкин А.В.	31
Влияние размера зерна на закономерности водородного охрупчивания многокомпонентного сплава (FeCrNiMnCo)₉₉N₁ Гуртова Д.Ю., Панченко М.Ю., Мельников Е.В., Астапов Д.О., Астафурова Е.Г.	41
Точность геометрической формы отверстия в продольном сечении при хонинговании Денисенко А.Ф., Гришин Р.Г., Антипова Е.Д.	53
Влияние режима 3D-печати на химический состав и структуру стали 30ХГСА Кабалдин Ю.Г., Аносов М.С., Мордовина Ю.С., Чернигин М.А.	63
Микроструктура, кристаллографическая текстура и механические свойства сплава Zn–1%Mg–1%Fe, подвергнутого интенсивной пластической деформации Ситдииков В.Д., Хафизова Э.Д., Поленок М.В.	75
Импульсная диффузионная сварка охватывающих соединений Стрижаков Е.Л., Нескоромный С.В., Людмирский Ю.Г., Мордовцев Н.А.	89
Влияние элементов режима резания на технологические параметры процесса фрезерования заготовок тонкостенных деталей из титанового сплава Унянин А.Н., Чуднов А.В.	99
Микроструктура и прочность 3D-напечатанного сплава Ti–6Al–4V, подвергнутого кручению под высоким давлением Усманов Э.И., Савина Я.Н., Валиев Р.Р.	109
НАШИ АВТОРЫ.....	117

Self-propagating high-temperature synthesis of AlN–TiC powder composition using sodium azide and C₂F₄ fluoroplastic

© 2024

Galina S. Belova^{*1}, PhD (Engineering),

junior researcher of the Laboratory “Digital Twins of Materials and Technological Procedures of their Processing”

Yulia V. Titova², PhD (Engineering), Associate Professor,

assistant professor of Chair “Materials Science, Powder Metallurgy, Nanomaterials”

Dmitry A. Maidan³, PhD (Engineering), Associate Professor,

assistant professor of Chair “Materials Science, Powder Metallurgy, Nanomaterials”

Alsu F. Yakubova⁴, postgraduate student

Samara State Technical University, Samara (Russia)

*E-mail: galya.belova.94@mail.ru

¹ORCID: <https://orcid.org/0000-0002-6430-9408>

²ORCID: <https://orcid.org/0000-0001-6292-280X>

³ORCID: <https://orcid.org/0000-0002-0195-4506>

⁴ORCID: <https://orcid.org/0000-0002-6081-8264>

Received 26.06.2023

Accepted 13.02.2024

Abstract: Producing powder compositions using conventional processing technology can lead to the formation of large agglomerates and, therefore, makes it difficult to obtain a uniform microstructure. The production of composites by self-propagating high-temperature synthesis can reduce costs and the number of technological stages, as well as lead to obtaining composites that are more homogeneous. Synthesis by the combustion of mixtures of powder reagents of sodium azide (NaN₃), fluoroplastic (C₂F₄), aluminum and titanium with different ratios of reagents in a nitrogen gas atmosphere at a pressure of 4 MPa was used for the production of a highly dispersed powder ceramic AlN–TiC composition. Thermodynamic calculations have confirmed the possibility of synthesis of AlN–TiC compositions of different formulations in combustion mode. The dependences of temperature and combustion rate on the composition of the initial mixtures of reagents were experimentally determined for all stoichiometric reaction equations. The study have shown that the experimentally found dependences of combustion parameters on the ratio of the initial components correspond to the theoretical results of thermodynamic calculations. The formulation of the synthesized composition differs from the theoretical composition by a lower content of target phases and the formation of Al₂O₃, Na₃AlF₆ and TiO₂ side phases. The powder composition consists of aluminum nitride fibers with a diameter of 100–250 nm and ultradisperse particles of predominantly equiaxed and lamellar shapes with a particle size of 200–600 nm. As the combustion temperature increases to produce the largest amount of titanium carbide phase, the particle size increases to the micron level.

Keywords: combustion; self-propagating high-temperature synthesis; ceramic powder; nitride-carbide composition; sodium azide; fluoroplastic (polytetrafluoroethylene); aluminum nitride; titanium carbide.

Acknowledgments: The work was carried out under the financial support of the Russian Science Foundation within the project No. 23-29-00680, <https://rscf.ru/project/23-29-00680/>.

The paper was written on the reports of the participants of the XI International School of Physical Materials Science (SPM-2023), Togliatti, September 11–15, 2023.

For citation: Belova G.S., Titova Yu.V., Maidan D.A., Yakubova A.F. Self-propagating high-temperature synthesis of AlN–TiC powder composition using sodium azide and C₂F₄ fluoroplastic. *Frontier Materials & Technologies*, 2024, no. 3, pp. 9–16. DOI: 10.18323/2782-4039-2024-3-69-1.

INTRODUCTION

Currently, materials with low weight, high strength, corrosion resistance and wear resistance are top requested by the automotive and aerospace industries [1; 2]. Although aluminium alloys satisfy the requirements for light weight (low density), they have low strength and hardness. Aluminium alloys are characterised by excellent formability in addition to high thermal conductivity and good corrosion resistance [3].

Numerous studies on aluminium-based metal-matrix composites (MMCs) have found that Al-based MMCs reinforced with TiC particles, due to their excellent mechanical

and physical properties, are especially attractive for use in the aerospace, automotive, defense and construction industries [4; 5]. In view of the above, TiC is attracting growing interest among researchers due to its high hardness, elastic modulus, low density, relatively high temperature stability, and good wettability with aluminium [5].

The compressive strength of the nanocomposite positively correlates to the content of the reinforcing component. The maximum compressive strength of the highly reinforced nanocomposite is 233 MPa, which is much higher than that of unreinforced aluminium alloy. Nanocomposite containing up to 0.5 wt. % of TiC has a lower relative

density due to the predominance of hardening during processing. Using a finer powder will increase the relative density. The highly hardened nanocomposite exhibited a hardness of 1.18 GPa after sintering at a temperature of 873 K. This value is three times higher than that of the unreinforced microcrystalline sample, and two times higher than that of the unreinforced nanocrystalline sample [6].

When synthesizing the AlN–TiC composition, in addition to the target phases of aluminium nitride (AlN) and titanium carbide (TiC), a certain amount of ternary aluminium carbonitride, including $\text{Al}_5\text{C}_3\text{N}$ and $\text{Al}_6\text{C}_3\text{N}_2$, is formed in the Al–C–N system. These materials are usually produced at a relatively high sintering temperature. In [7], it is indicated that $\text{Al}_5\text{C}_3\text{N}$ is formed only when samples are subjected to hot pressing at ~2073 K.

Compared to other methods for producing ceramic compositions, combustion synthesis, or high-temperature sintering with self-propagation of a combustion wave, is of interest due to obvious advantages, such as short process duration, low energy consumption and high yield of pure products. Combustion synthesis has been used to synthesize many materials [8], including aluminium nitride (AlN) and carbide (TiC).

The possibility of producing a $\text{Ti}_2\text{AlC}_{0.5}\text{N}_{0.5}$ solid solution from powder mixtures consisting of Ti, Al_4C_3 and Al or AlN was studied by self-propagating, high-temperature synthesis (SHS) in gaseous nitrogen. The molar ratio of the three powder reagents was Ti : Al_4C_3 : Al (AlN) = 2 : 1/6 : 1/3. For both types of samples, increasing the nitrogen pressure from 0.45 to 1.82 MPa increases the combustion temperature and thus accelerates the reaction front propagation. Compared to inert AlN, Al particles reacted vigorously with Ti and N_2 during the SHS process, resulting in higher reaction exothermicity for the Al-containing sample than for the AlN-containing sample. The $\text{Ti}_2\text{AlC}_{0.5}\text{N}_{0.5}$ solid solution was the main phase in the final products from Ti– Al_4C_3 –Al powder compacts. However, increasing the nitrogen pressure had a negative effect on the release of $\text{Ti}_2\text{AlC}_{0.5}\text{N}_{0.5}$, since Ti was excessively nitride, and Al reacted with nitrogen. When AlN was used to replace Al, the formation of $\text{Ti}_2\text{AlC}_{0.5}\text{N}_{0.5}$ was deteriorated, due to weak exothermicity and TiAl deficiency. Moreover, Ti(C,N) titanium carbonitride predominated in the products synthesized from Ti– Al_4C_3 –AlN samples at nitrogen pressures of 1.48 and 1.82 MPa. This means that the use of aluminium nitride instead of aluminium is undesirable for producing $\text{Ti}_2\text{AlC}_{0.5}\text{N}_{0.5}$ by synthesis using gaseous nitrogen [9; 10].

The SHS process is attractive, because of its simplicity and economic efficiency; it is one of the promising in situ methods for the direct synthesis of ceramic powders within the desired composition from a mixture of initial cheap reagents. SHS using sodium azide and gasifying halide salts has such distinctive features as relatively low combustion temperatures, the formation of a large amount of intermediate vapour and gaseous reaction products, as well as final condensed and gaseous by-products separating the particles of the target powders,

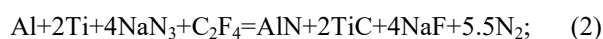
which allows synthesizing highly dispersed ($<1 \mu\text{m}$) AlN–TiC powder composition [11; 12].

Synthesis of both target phases directly in the bulk of a composite powder (in situ) from inexpensive reagents, and not in advance with subsequent mechanical mixing (ex situ) of expensive nanopowders, makes it possible to achieve high homogeneity of the mixture of synthesized inexpensive highly dispersed nitride-carbide compositions.

The purpose of this study is to use a fluoroplastic activating additive (C_2F_4) to produce a highly dispersed composition of AlN–TiC powders with different phase ratios, using the method of azide self-propagating high-temperature synthesis.

METHODS

To synthesize target AlN–TiC compositions with a molar phase ratio from 1:4 to 4:1, the following chemical reaction equations were used:



If we move from the formulation of AlN–TiC compositions expected, according to these stoichiometric equations in moles to the formulation in wt. %, taking into account the molar weights of the phases, the following ratios of the expected theoretical formulation of the synthesized AlN–TiC compositions after removal of the NaF water-soluble by-salt are obtained:

$$(1): \text{AlN}+\text{TiC}=40.6 \% \text{ AlN}+59.4 \% \text{ TiC};$$

$$(2): \text{AlN}+2\text{TiC}=25.5 \% \text{ AlN}+74.5 \% \text{ TiC};$$

$$(3): \text{AlN}+4\text{TiC}=14.6 \% \text{ AlN}+85.4 \% \text{ TiC};$$

$$(4): 2\text{AlN}+\text{TiC}=57.8 \% \text{ AlN}+42.2 \% \text{ TiC};$$

$$(5): 4\text{AlN}+\text{TiC}=73.3 \% \text{ AlN}+26.7 \% \text{ TiC}.$$

To predict the possibility of reactions occurring in the combustion mode by determining thermal effects (enthalpy), adiabatic temperatures and compositions of synthesis products, corresponding thermodynamic calculations were carried out using the Thermo computer program.

In the experimental study, the following raw materials were used: ASD-4 grade aluminium powder (main substance content is ≥ 98.8 wt. %, average particle size is $5 \mu\text{m}$), PTM grade titanium (≥ 99.7 wt. %, $5 \mu\text{m}$), classification "Ch" fluoroplastic powder (≥ 99.1 wt. %, $20 \mu\text{m}$), classification "Ch" sodium azide powder (≥ 98.71 wt. %, $100 \mu\text{m}$). The combustion of a mixture of initial reagents

(charge) with a bulk relative density of 0.4 was carried out in a tracing paper cup with a diameter of 30 mm, and a height of 45 mm wrapped in carbon fabric using a SHS-Az laboratory reactor with a volume of 4.5 l, with two thermocouples at a nitrogen pressure of 4 MPa.

Using thermocouples (thermocouple wire of VR5-20 type, TU 48-1941-73, Moscow Electric Lamp Plant OJSC, Moscow, Russia), combustion temperatures were measured, and combustion rates were calculated. Using a pressure gauge (MP4-U, 1.5 kgf/cm², JSC Manotom, included in the general installation of a constant pressure SHS reactor with a fume hood (armored cabin)), the change in pressure in the reactor during the combustion process was determined.

The resulting synthesis product was weighed and compared with the theoretical yield from reactions (1)–(5). The combustion product was washed with distilled water to remove water-soluble impurities, and the acid-base balance of the washing water was determined, to identify the presence of free sodium in the combustion product, and the completeness of the chemical reaction. Washing consisted of diluting the powders with distilled water in a ratio of 1:10 at room temperature, stirring the resulting suspension, and then filtering the target products in a vacuum funnel for 5–10 min. The pH=7 value indicates the absence of free fluorine/sodium, which indirectly confirms the completeness of the conversion of the starting components into reaction products.

An experimental study of the combustion process was carried out using thermocouple measurements of temperatures and combustion rates. The study of combustion products using scanning electron microscopy and X-ray phase analysis showed that the application of azide self-propagating high-temperature synthesis with the addition of C₂F₄ to the initial charge as a carbon source, allows synthesizing AlN–TiC powder composition of various formulations.

The phase composition of the synthesized combustion products was determined using an ARL X'tra automated X-ray diffractometer (Thermo Scientific). Cu radiation was used with continuous scanning in the 2θ angle range

from 20 to 80° at a speed of 2 degrees/min. The obtained spectra were processed using the WinXRD application package. Quantitative phase analysis was carried out using the full-profile analysis method (Rietveld method) with the help of the PDXL 1.8.1.0 program using the PDF-2009 and COD-2019 crystallographic databases. The essence of the method is to use profile intensities instead of integral ones, which allows extracting the maximum amount of information contained in step-by-step experiments of scanning powder diffraction patterns. The study of the morphology of powder particles was carried out on a Jeol JSM-6390A scanning electron microscope with a JeolJED-2200 attachment.

RESULTS

Thermodynamic analysis of the possibility of forming compositions

Table 1 presents the results of thermodynamic calculations of combustion reactions (1)–(5) using the Thermo program.

From the presented data, it is clear that all reactions have high adiabatic temperatures, sufficient both for the implementation of the SHS process in the combustion mode, and for the formation of the target phases of aluminium nitride and titanium carbide. The reaction enthalpy increases and strongly depends on the ratio of the nitride and carbide phases in the reaction products. The minimum enthalpy value corresponds to equation (1), the maximum reaction enthalpy value is calculated for equation (5). The equilibrium concentrations of reaction products correspond to the right-hand sides of equations (1)–(5), i.e., the target phases of aluminium nitride (AlN) and titanium carbide (TiC).

Experiment results

The results of the experimental determination of the temperature (T_C) and rate (U_C) of combustion of SHS-Az charges for the synthesis of AlN–TiC ceramic nitride-carbide compositions are presented in Table 2.

Table 1. Results of thermodynamic analysis of reactions (1)–(5)
Таблица 1. Результаты термодинамического анализа реакций (1)–(5)

Composition of the initial mixture of powders in reactions	Enthalpy, kJ	Adiabatic temperature, K	Quantity, mole			
			AlN	TiC	NaF	N ₂
2Al+2Ti+4NaN ₃ +C ₂ F ₄	–2139	2768	1.00	4.00	4.00	5.50
Al+2Ti+4NaN ₃ +C ₂ F ₄	–2298	2798	1.00	2.00	4.00	5.50
Al+4Ti+8NaN ₃ +2C ₂ F ₄	–2616	2920	2.00	2.00	4.00	5.00
4Al+2Ti+4NaN ₃ +C ₂ F ₄	–3252	3120	4.00	2.00	4.00	4.00
8Al+2Ti+4NaN ₃ +C ₂ F ₄	–4524	3278	8.00	2.00	4.00	2.00

From the data presented in Table 2, it can be seen that the experimental maximum combustion temperatures correspond to the calculated values of adiabatic temperatures in Table 1, but are slightly lower than the latter due to heat loss in the combustion zone. The minimum values of temperature and rate of combustion are observed in equation (1), which corresponds to the phase ratio AlN : TiC = 1 : 1.

Fig. 1 presents the results of microstructural analysis of the combustion products of the initial mixtures of powders (charges), represented by reaction equations (1)–(5), after water washing from the by-product water-soluble NaF salt. Fig. 1 a shows that the combustion products of the reaction charge (1), consist predominantly of aluminium nitride fibres with a diameter of 100–250 nm, and ultrafine plate-shaped particles of titanium carbide with a size of 200–600 nm. When the aluminium content in the initial mixture is reduced by 2 times (equation 2, Fig. 1 b), the combustion product is represented mainly by plate-shaped titanium carbide particles, with a size of 200–600 nm, and a small amount of aluminium nitride fibres with a diameter of 100–200 nm. When the aluminium content is reduced by half with a simultaneous increase in the titanium content by two times, compared to the initial mixture (equation (3), Fig. 1 c), the combustion products are titanium carbide particles of equiaxial and plate shapes with a size of 200–600 nm. In Fig. 1 d and 1 e, aluminium nitride fibres with diameters of 100–300 and 100–400 nm, respectively, are clearly visible.

The results of qualitative and quantitative X-ray phase analysis of the combustion products of the initial mixtures of powders (charges), represented by reaction equations (1)–(5), after the water washing operation are summarised in Table 3.

The results of X-ray phase analysis (Table 3) show the formation of five phases: target phases of aluminium nitride (AlN) and titanium carbide (TiC), side phases of sodium aluminium hexafluoride (Na_3AlF_6), as well as titanium and aluminium oxides (TiO_2 , Al_2O_3). Thus, the reaction products (1) consist of 32.5 % of AlN, 47.4 % of TiC, 6.5 % of Na_3AlF_6 , 12.8 % of TiO_2 , and 0.8 % of Al_2O_3 . Therefore, the synthesized composition differs from the expected theoretical 40.6 % AlN – 59.4 % TiC composition (1) in the lower content of target phases, while their

ratio is maintained, and the presence of reaction by-products, the total amount of which is 20.1 %.

When the aluminium content is reduced by half compared to the charge (1), the combustion products of the charge (2) also consist of five phases: AlN – 20.6 %, TiC – 61.2 %, TiO_2 – 13.1 %, Al_2O_3 – 0.3 %, and Na_3AlF_6 – 4.8 %. In general, the formulation of the synthesized composition differs from the expected theoretical 25.5 % AlN – 74.5 % TiC composition (2) by an insufficient content of target phases, while their ratio is maintained, and the total amount of reaction by-products is slightly less than for the charge (1) – 18.2 %.

When the aluminium content is reduced by half, with a simultaneous increase in the titanium content by two times compared to the charge (1), the combustion products of the charge (3) contain only three phases: AlN – 14.4 %, TiC – 71.5 %, TiO_2 – 14.5 %, with the largest amount of titanium carbide. This composition differs from the expected 14.6 % AlN – 85.4 % TiC composition (3) by the presence of titanium oxide.

As a result of combustion of the charge (4) with the addition of four moles of aluminium compared to the charge (1) and the same titanium content, four phases are formed: AlN – 53.2 %, TiC – 31.4 %, TiO_2 – 11.6 %, and Al_2O_3 – 3.8 %. The formulation of the synthesized composition differs from the theoretical 57.8 % AlN – 42.2 % TiC composition (4) by the presence of titanium and aluminium oxides in an amount of 15.4 %.

With an increase in aluminium content four times compared to the charge (1), and the same titanium content, the combustion products are phases similar to the charge (4): AlN – 66.4 %, TiC – 15.6 %, TiO_2 – 11.9 %, and Al_2O_3 – 6.1 %. This composition also differs from the theoretical 73.3 % AlN – 26.7 % TiC composition (5) by the presence of by-product titanium and aluminium oxides in an amount of 18 %.

DISCUSSION

The presented experimental results of the synthesis of a composition of highly dispersed AlN–TiC ceramic powders were obtained using fluoroplastic (C_2F_4), with specified

Table 2. Combustion parameters of initial powder mixtures of reactions (1)–(5)
Таблица 2. Параметры горения исходных порошковых смесей реакций (1)–(5)

Composition of the initial mixture of powders in reactions	Combustion temperature, T_C , °C	Combustion rate, U_C , cm/s	Maximum pressure, MPa	pH	Practical yield of combustion products, g
$2\text{Al}+2\text{Ti}+4\text{NaN}_3+\text{C}_2\text{F}_4$	2420	0.72	7.2	8	20.3
$\text{Al}+2\text{Ti}+4\text{NaN}_3+\text{C}_2\text{F}_4$	2520	0.77	7.8	8	17.0
$\text{Al}+4\text{Ti}+8\text{NaN}_3+2\text{C}_2\text{F}_4$	2670	0.81	7.0	8	16.2
$4\text{Al}+2\text{Ti}+4\text{NaN}_3+\text{C}_2\text{F}_4$	2700	0.75	7.3	8	18.3
$8\text{Al}+2\text{Ti}+4\text{NaN}_3+\text{C}_2\text{F}_4$	2940	0.87	6.5	8	20.5

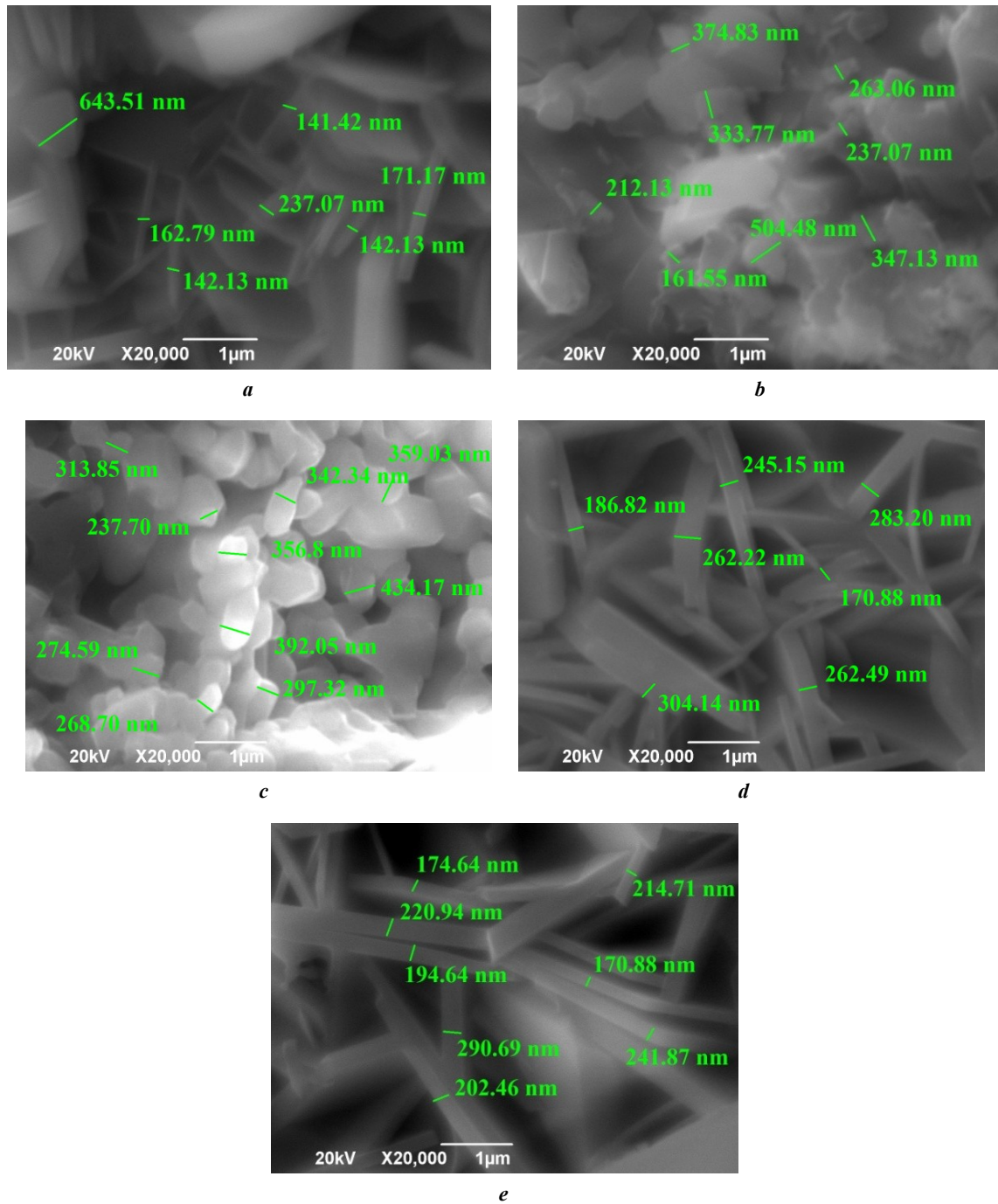


Fig. 1. Morphology of particles of combustion products of the Al–Ti–NaN₃–C₂F₄ system:
a – 2Al+2Ti+4NaN₃+C₂F₄; **b** – Al+2Ti+4NaN₃+C₂F₄; **c** – Al+4Ti+8NaN₃+2C₂F₄;
d – 4Al+2Ti+4NaN₃+C₂F₄; **e** – 8Al+2Ti+4NaN₃+C₂F₄

Рис. 1. Морфология частиц продуктов горения системы Al–Ti–NaN₃–C₂F₄:
a – 2Al+2Ti+4NaN₃+C₂F₄; **b** – Al+2Ti+4NaN₃+C₂F₄; **c** – Al+4Ti+8NaN₃+2C₂F₄;
d – 4Al+2Ti+4NaN₃+C₂F₄; **e** – 8Al+2Ti+4NaN₃+C₂F₄

molar ratios of nitride and carbide phases: 1:1, 1:2, 1:4, 2:1, 4:1. The experimental compositions of synthesis products, upon combustion of the initial powder mixtures of reagents with fluoroplastic, were found according to the stoichiometric equations of azide self-propagating high-temperature synthesis (1)–(5). It is shown that experimental compositions can differ significantly from theoretical phase compositions according to the original stoichiometric equations and the results of thermodynamic calculations. These dif-

ferences are the lower actual content of the target phases of aluminium nitride, and titanium carbide in the composition of all combustion products synthesized experimentally, as well as the presence of side phases of titanium and aluminium oxides, and sodium aluminium hexafluoride (TiO₂, Al₂O₃, Na₃AlF₆), which should not exist according to theoretical calculations. It should be noted that our previous studies showed that aluminium nitride produced by the azide SHS method always contains a sparingly soluble

Table 3. Results of qualitative and quantitative X-ray phase analysis of reactions (1)–(5)
Таблица 3. Результаты качественного и количественного рентгенофазового анализа реакций (1)–(5)

Theoretical composition, %		Ratio AlN:TiC	Experimental composition, %				
AlN	TiC		AlN	TiC	Na ₃ AlF ₆	TiO ₂	Al ₂ O ₃
40.6	59.4	1:1	32.5	47.4	6.5	12.8	0.8
25.5	74.5	1:2	20.6	61.2	4.8	13.1	0.3
14.6	85.4	1:4	14.4	71.5	–	14.5	–
57.8	42.2	2:1	53.2	31.4	–	11.6	3.8
73.3	26.7	4:1	66.4	15.6	–	11.9	6.1

impurity – sodium aluminium hexafluoride [12; 13]. However, in this work, sodium aluminium hexafluoride was formed only during the combustion of charges (1) and (2).

Despite the fact that the reaction products contain significant amounts of side oxide phases, the use of fluoroplastic as a carbon source allowed, increasing the yield of the target carbide, which could not be achieved when using soot (carbon black) in earlier studies [14–17].

Thus, in the case of practical application of the SHS-Az process (azide self-propagating high-temperature synthesis) to obtain a highly dispersed nitride-carbide composition AlN–TiC, it is recommended to use fluoroplastic for synthesis, while further research is required to prevent the formation and/or removal of oxides from the synthesized powder compositions.

CONCLUSIONS

The compositions of the initial mixtures of reagents were substantiated and the corresponding stoichiometric equations for the reactions of azide SHS of AlN–TiC powder compositions, with given molar nitride, and carbide phases were compiled: 1:1, 1:2, 1:4, 2:1, 4:1.

It is shown that in the case of all the reaction equations compiled, thermal effects and adiabatic temperatures are high enough for reactions to occur in the combustion mode, and the formation of target products in full accordance with the stoichiometric equations, and the given molar ratios of the nitride and carbide phases.

Studying the morphology of combustion products showed that in most cases, the use of the azide self-propagating high-temperature synthesis with selected compositions of the initial mixtures of reagents, leads to the production of highly dispersed compositions of powders in the form of fibres with a diameter of 100–250 nm, and particles of equiaxial and plate shapes with a size of 200–600 nm.

It has been found, that the experimental phase composition differs significantly from the theoretical phase composition, by the presence in the compositions of side phases of titanium and aluminium oxides, and in some cases, of sodium aluminium hexafluoride. When the combustion temperature is increased to obtain the largest amount of titanium carbide phase, an enlargement of the particle size to the micron level is observed.

Thus, by burning powder mixtures of sodium azide, fluoroplastic (C₂F₄), aluminium and titanium in a nitrogen atmosphere, it is possible to synthesize a highly dispersed composition of AlN–TiC ceramic powders of various compositions. However, the formulation of the synthesized compositions, along with the target phases, includes side oxides (TiO₂, Al₂O₃) and sodium aluminium hexafluoride (Na₃AlF₆). Further research will be aimed at preventing the formation and/or removal of oxides and sub-fluorides from the synthesized powder compositions.

REFERENCES

- Han Jishuo, Li Yong, Ma Chenhong, Zheng Qingyao, Zhang Xiuhua. Formation mechanism of AlN–SiC solid solution with multiple morphologies in Al–Si–SiC composites under flowing nitrogen at 1300 °C. *Journal of the European Ceramic Society*, 2022, vol. 42, no. 14, pp. 6356–6363. DOI: [10.1016/j.jeurceramsoc.2022.07.011](https://doi.org/10.1016/j.jeurceramsoc.2022.07.011).
- Kultayeva Sh., Kim Young-Wook. Mechanical, thermal, and electrical properties of pressureless sintered SiC–AlN ceramics. *Ceramics International*, 2020, vol. 46, no. 11-B, pp. 19264–19273. DOI: [10.1016/j.ceramint.2020.04.266](https://doi.org/10.1016/j.ceramint.2020.04.266).
- Zhou Zhengrong, Huang Rongjin, Liu Huiming, Zhao Yalin, Miao Zhicong, Wu Zhixiong, Zhao Yanyin, Huang Chuanjun, Li Laifeng. Dielectric AlN/epoxy and SiC/epoxy composites with enhanced thermal and dynamic mechanical properties at low temperatures. *Progress in Natural Science: Materials International*, 2022, vol. 32, no. 3, pp. 304–313. DOI: [10.1016/j.pnsc.2022.03.007](https://doi.org/10.1016/j.pnsc.2022.03.007).
- Wu Xinxin, Deng Chengji, Ding Jun, Zhu Hongxi, Yu Chao. Synthesis of AlN–SiC microrods by the Co-catalysed nitridation of Al₄SiC₄. *Ceramics International*, 2019, vol. 45, no. 2-A, pp. 2680–2683. DOI: [10.1016/j.ceramint.2018.10.164](https://doi.org/10.1016/j.ceramint.2018.10.164).
- Li Zhijian, Guo Ruru, Li Lu, Zheng Ruixiao, Ma Chaoli. Improvement in high-temperature oxidation resistance of SiC nanocrystalline ceramics by doping AlN. *Ceramics International*, 2021, vol. 47, no. 21, pp. 30999–31003. DOI: [10.1016/j.ceramint.2021.07.276](https://doi.org/10.1016/j.ceramint.2021.07.276).
- Jeyasimman D., Sivasankaran S., Sivaprasad K., Narayanasamy R., Kambali R.S. An investigation of

- the synthesis, consolidation and mechanical behaviour of Al 6061 nanocomposites reinforced by TiC via mechanical alloying. *Materials and Design*, 2014, vol. 57, pp. 394–404. DOI: [10.1016/j.matdes.2013.12.067](https://doi.org/10.1016/j.matdes.2013.12.067).
- Qiu C., Metselaar R. Phase relations in the aluminum carbide–aluminum nitride–aluminum oxide system. *Journal of the American Ceramic Society*, 1997, vol. 80, no. 8, pp. 2013–2020. DOI: [10.1111/j.1151-2916.1997.tb03085.x](https://doi.org/10.1111/j.1151-2916.1997.tb03085.x).
 - Abbasi Z., Shariat M.H., Javadpour S. Microwave-assisted combustion synthesis of AlN–SiC composites using a solid source of nitrogen. *Powder Technology*, 2013, vol. 249, pp. 181–185. DOI: [10.1016/j.powtec.2013.08.012](https://doi.org/10.1016/j.powtec.2013.08.012).
 - Xing Guangchao, Deng Chengji, Ding Jun, Zhu Hongxi, Yu Chao. Fabrication and characterisation of AlN–SiC porous composite ceramics by nitridation of Al₄SiC₄. *Ceramics International*, 2020, vol. 46, no. 4, pp. 4959–4967. DOI: [10.1016/j.ceramint.2019.10.234](https://doi.org/10.1016/j.ceramint.2019.10.234).
 - Yeh C.L., Kuo C.W., Wu F.S. Formation of Ti₂AlC_{0.5}N_{0.5} solid solutions by combustion synthesis of Al₄C₃-containing samples in nitrogen. *Journal of Alloys and Compounds*, 2010, vol. 508, no. 2, pp. 324–328. DOI: [10.1016/j.jallcom.2010.08.072](https://doi.org/10.1016/j.jallcom.2010.08.072).
 - Wu Xinxin, Deng Chengji, Ding Jun, Zhu Hongxi, Yu Chao. Synthesis of AlN–SiC microrods by the co-catalysed nitridation of Al₄SiC₄. *Ceramics International*, 2019, vol. 45, no. 2-A, pp. 2680–2683. DOI: [10.1016/j.ceramint.2018.10.164](https://doi.org/10.1016/j.ceramint.2018.10.164).
 - Amosov A.P., Titova Y.V., Maidan D.A., Sholomova A.V. Self-propagating high-temperature synthesis of an aluminum nitride nanopowder from a Na₃AlF₆+3NaN₃+nAl powder mixture. *Russian Journal of Inorganic Chemistry*, 2016, vol. 61, no. 10, pp. 1225–1234. DOI: [10.1134/S0036023616100028](https://doi.org/10.1134/S0036023616100028).
 - Zhang Chitengfei, Cai Yilun, Guo Le, Tu Rong, Zheng Yingqiu, Li Bao-Wen, Zhang Song, Gao Tenghua. Synthesis of transfer-free graphene films on dielectric substrates with controllable thickness via an in-situ co-deposition method for electrochromic devices. *Ceramics International*, 2022, vol. 48, no. 15, pp. 21748–21755. DOI: [10.1016/j.ceramint.2022.04.156](https://doi.org/10.1016/j.ceramint.2022.04.156).
 - Levashov E.A., Rogachev A.S., Yuxhvid V.I. *Perspektivnye materialy i tekhnologii samorasprostranyayushchegosya vysokotemperaturnogo sinteza* [Promissory Materials and Processes of Self-Propagating High-Temperature Synthesis]. Moscow, MISIS Publ., 2011. 377 p.
 - Mamyan S.S. Thermodynamic analysis of SHS processes. *Key Engineering Materials*, 2002, vol. 217, pp. 1–8. DOI: [10.4028/www.scientific.net/KEM.217.1](https://doi.org/10.4028/www.scientific.net/KEM.217.1).
 - Amosov A.P., Belova G.S., Titova Yu.V., Maidan D.A. Synthesis of highly dispersed powder ceramic composition Si₃N₄–SiC by combustion of components in the Si–C–NaN₃–NH₄F system. *Russian Journal of Inorganic Chemistry*, 2022, vol. 67, no. 2, pp. 123–130. DOI: [10.31857/S0044457X22020027](https://doi.org/10.31857/S0044457X22020027).
 - Titova Yu.V., Amosov A.P., Maidan D.A., Belova G.S., Minekhanova A.F. Azide self-propagating high-temperature synthesis of highly dispersed tin-sicceramic nitride-carbide powder composites. *Izvestiya vuzov. Poroshkovaya metallurgiya i funktsionalnye pokrytiya*, 2022, vol. 16, no. 2, pp. 22–37. DOI: [10.17073/1997-308X-2022-2-22-37](https://doi.org/10.17073/1997-308X-2022-2-22-37).
- ### СПИСОК ЛІТЕРАТУРИ
- Han Jishuo, Li Yong, Ma Chenhong, Zheng Qingyao, Zhang Xiuhua. Formation mechanism of AlN–SiC solid solution with multiple morphologies in Al–Si–SiC composites under flowing nitrogen at 1300 °C // *Journal of the European Ceramic Society*. 2022. Vol. 42. № 14. P. 6356–6363. DOI: [10.1016/j.jeurceramsoc.2022.07.011](https://doi.org/10.1016/j.jeurceramsoc.2022.07.011).
 - Kultayeva Sh., Kim Young-Wook. Mechanical, thermal, and electrical properties of pressureless sintered SiC–AlN ceramics // *Ceramics International*. 2020. Vol. 46. № 11-B. P. 19264–19273. DOI: [10.1016/j.ceramint.2020.04.266](https://doi.org/10.1016/j.ceramint.2020.04.266).
 - Zhou Zhengrong, Huang Rongjin, Liu Huiming, Zhao Yalin, Miao Zhicong, Wu Zhixiong, Zhao Wanyin, Huang Chuanjun, Li Laifeng. Dielectric AlN/epoxy and SiC/epoxy composites with enhanced thermal and dynamic mechanical properties at low temperatures // *Progress in Natural Science: Materials International*. 2022. Vol. 32. № 3. P. 304–313. DOI: [10.1016/j.pnsc.2022.03.007](https://doi.org/10.1016/j.pnsc.2022.03.007).
 - Wu Xinxin, Deng Chengji, Ding Jun, Zhu Hongxi, Yu Chao. Synthesis of AlN–SiC microrods by the Co-catalysed nitridation of Al₄SiC₄ // *Ceramics International*. 2019. Vol. 45. № 2-A. P. 2680–2683. DOI: [10.1016/j.ceramint.2018.10.164](https://doi.org/10.1016/j.ceramint.2018.10.164).
 - Li Zhijian, Guo Ruru, Li Lu, Zheng Ruixiao, Ma Chaoli. Improvement in high-temperature oxidation resistance of SiC nanocrystalline ceramics by doping AlN // *Ceramics International*. 2021. Vol. 47. № 21. P. 30999–31003. DOI: [10.1016/j.ceramint.2021.07.276](https://doi.org/10.1016/j.ceramint.2021.07.276).
 - Jeyasimman D., Sivasankaran S., Sivaprasad K., Narayanasamy R., Kambali R.S. An investigation of the synthesis, consolidation and mechanical behaviour of Al 6061 nanocomposites reinforced by TiC via mechanical alloying // *Materials and Design*. 2014. Vol. 57. P. 394–404. DOI: [10.1016/j.matdes.2013.12.067](https://doi.org/10.1016/j.matdes.2013.12.067).
 - Qiu C., Metselaar R. Phase relations in the aluminum carbide–aluminum nitride–aluminum oxide system // *Journal of the American Ceramic Society*. 1997. Vol. 80. № 8. P. 2013–2020. DOI: [10.1111/j.1151-2916.1997.tb03085.x](https://doi.org/10.1111/j.1151-2916.1997.tb03085.x).
 - Abbasi Z., Shariat M.H., Javadpour S. Microwave-assisted combustion synthesis of AlN–SiC composites using a solid source of nitrogen // *Powder Technology*. 2013. Vol. 249. P. 181–185. DOI: [10.1016/j.powtec.2013.08.012](https://doi.org/10.1016/j.powtec.2013.08.012).
 - Xing Guangchao, Deng Chengji, Ding Jun, Zhu Hongxi, Yu Chao. Fabrication and characterisation of AlN–SiC porous composite ceramics by nitridation of Al₄SiC₄ // *Ceramics International*. 2020. Vol. 46. № 4. P. 4959–4967. DOI: [10.1016/j.ceramint.2019.10.234](https://doi.org/10.1016/j.ceramint.2019.10.234).
 - Yeh C.L., Kuo C.W., Wu F.S. Formation of Ti₂AlC_{0.5}N_{0.5} solid solutions by combustion synthesis of Al₄C₃-containing samples in nitrogen // *Journal of Alloys and Compounds*. 2010. Vol. 508. № 2. P. 324–328. DOI: [10.1016/j.jallcom.2010.08.072](https://doi.org/10.1016/j.jallcom.2010.08.072).
 - Wu Xinxin, Deng Chengji, Ding Jun, Zhu Hongxi, Yu Chao. Synthesis of AlN–SiC microrods by the co-catalysed nitridation of Al₄SiC₄ // *Ceramics International*. 2019. Vol. 45. № 2-A. P. 2680–2683. DOI: [10.1016/j.ceramint.2018.10.164](https://doi.org/10.1016/j.ceramint.2018.10.164).
 - Амосов А.П., Титова Ю.В., Майдан Д.А., Шоломова А.В. Самораспространяющийся высокотемпературный синтез нанопорошка нитрида алюминия из смеси порошков Na₃AlF₆+3NaN₃+nAl // *Журнал не-*

- органической химии. 2016. Т. 61. № 10. С. 1282–1291. DOI: [10.7868/S0044457X16100020](https://doi.org/10.7868/S0044457X16100020).
13. Zhang Chitengfei, Cai Yilun, Guo Le, Tu Rong, Zheng Yingqiu, Li Bao-Wen, Zhang Song, Gao Tenghua. Synthesis of transfer-free graphene films on dielectric substrates with controllable thickness via an in-situ co-deposition method for electrochromic devices // *Ceramics International*. 2022. Vol. 48. № 15. P. 21748–21755. DOI: [10.1016/j.ceramint.2022.04.156](https://doi.org/10.1016/j.ceramint.2022.04.156).
14. Леващов Е.А., Рогачев А.С., Юхвид В.И. Перспективные материалы и технологии самораспространяющегося высокотемпературного синтеза. М.: МИСиС, 2011. 377 с.
15. Mamyán S.S. Thermodynamic analysis of SHS processes // *Key Engineering Materials*. 2002. Vol. 217. P. 1–8. DOI: [10.4028/www.scientific.net/KEM.217.1](https://doi.org/10.4028/www.scientific.net/KEM.217.1).
16. Амосов А.П., Белова Г.С., Титова Ю.В., Майдан Д.А. Синтез высокодисперсной порошковой керамической композиции Si₃N₄–SiC при горении компонентов в системе Si–C–NaN₃–NH₄F // *Журнал неорганической химии*. 2022. Т. 67. № 2. С. 139–147. DOI: [10.31857/S0044457X22020027](https://doi.org/10.31857/S0044457X22020027).
17. Титова Ю.В., Амосов А.П., Майдан Д.А., Белова Г.С., Минеханова А.Ф. Азидный СВС высокодисперсных керамических нитридно-карбидных порошковых композиций TiN–SiC // *Известия вузов. Порошковая металлургия и функциональные покрытия*. 2022. Т. 16. № 2. С. 22–37. DOI: [10.17073/1997-308X-2022-2-22-37](https://doi.org/10.17073/1997-308X-2022-2-22-37).

Самораспространяющийся высокотемпературный синтез порошковой композиции AlN–TiC с применением азид натрия и фторопласта C₂F₄

© 2024

Белова Галина Сергеевна^{*1}, кандидат технических наук, младший научный сотрудник лаборатории «Цифровые двойники материалов и технологических процессов их обработки»

Титова Юлия Владимировна², кандидат технических наук, доцент, доцент кафедры «Металловедение, порошковая металлургия, наноматериалы»

Майдан Дмитрий Александрович³, кандидат технических наук, доцент, доцент кафедры «Металловедение, порошковая металлургия, наноматериалы»

Якубова Алсу Фаридовна⁴, аспирант

Самарский государственный технический университет, Самара (Россия)

*E-mail: galya.belova.94@mail.ru

¹ORCID: <https://orcid.org/0000-0002-6430-9408>

²ORCID: <https://orcid.org/0000-0001-6292-280X>

³ORCID: <https://orcid.org/0000-0002-0195-4506>

⁴ORCID: <https://orcid.org/0000-0002-6081-8264>

Поступила в редакцию 26.06.2023

Принята к публикации 13.02.2024

Аннотация: Получение порошковых композиций с помощью обычной технологии обработки может привести к образованию крупных агломератов и, следовательно, осложняет получение однородной микроструктуры. Производство композитов методом самораспространяющегося высокотемпературного синтеза может снизить затраты и количество технологических стадий, а также привести к получению более однородных композитов. Для получения высокодисперсной порошковой керамической композиции AlN–TiC применен синтез методом горения смесей порошковых реагентов азид натрия (NaN₃), фторопласта (C₂F₄), алюминия и титана при разном соотношении реагентов в атмосфере газообразного азота при давлении 4 МПа. Термодинамические расчеты подтвердили возможность синтеза композиции AlN–TiC разного состава в режиме горения. Экспериментально определены зависимости температуры и скорости горения от состава исходных смесей реагентов по всем стехиометрическим уравнениям реакций. Показано, что экспериментально найденные зависимости параметров горения от соотношения исходных компонентов соответствуют теоретическим результатам термодинамических расчетов. Состав синтезированной композиции отличается от теоретического состава меньшим содержанием целевых фаз и образованием побочных фаз Al₂O₃, Na₃AlF₆ и TiO₂. Порошковая композиция представляет собой волокна нитрида алюминия диаметром 100–250 нм и ультрадисперсные частицы преимущественно равноосной и пластинчатой форм с размером частиц 200–600 нм. При увеличении температуры горения для получения наибольшего количества фазы карбида титана наблюдается укрупнение размера частиц до микронного уровня.

Ключевые слова: горение; самораспространяющийся высокотемпературный синтез; керамический порошок; нитридно-карбидная композиция; азид натрия; фторопласт (политетрафторэтилен); нитрид алюминия; карбид титана.

Благодарности: Работа выполнена при финансовой поддержке Российского научного фонда в рамках проекта № 23-29-00680, <https://rscf.ru/project/23-29-00680/>.

Статья подготовлена по материалам докладов участников XI Международной школы «Физическое материаловедение» (ШФМ-2023), Тольятти, 11–15 сентября 2023 года.

Для цитирования: Белова Г.С., Титова Ю.В., Майдан Д.А., Якубова А.Ф. Самораспространяющийся высокотемпературный синтез порошковой композиции AlN–TiC с применением азид натрия и фторопласта C₂F₄ // *Frontier Materials & Technologies*. 2024. № 3. С. 9–16. DOI: [10.18323/2782-4039-2024-3-69-1](https://doi.org/10.18323/2782-4039-2024-3-69-1).

Corrosion-mechanical destruction of bainite structures in oilfield environments

© 2024

Mikhail A. Vyboishchik^{1,3}, Doctor of Sciences (Physics and Mathematics), Professor, professor of Chair “Welding, Pressure Treatment of Materials and Allied Processes”

Igor V. Gruzkov^{*1,2,4}, postgraduate student,

Head of the Laboratory of Optical and Electron Microscopy

¹Togliatti State University, Togliatti (Russia)

²IT-Service Limited Liability Company, Samara (Russia)

*E-mail: gruzkov@its-samara.com,
gigabon7@mail.ru

³ORCID: <https://orcid.org/0000-0003-2797-5396>

⁴ORCID: <https://orcid.org/0009-0007-9580-9935>

Received 12.12.2023

Accepted 15.08.2024

Abstract: The main direction in solving the problem of increasing the reliability of field equipment, is the creation of new steels with higher resistance to corrosion-mechanical destruction. Currently, to produce oil and gas pipeline systems, low-carbon, low-alloy steels are used, in which lath carbide-free bainite is formed when quenched in water. Such a structure provides a combination of high strength and resistance to brittle fracture. However, issues of increasing corrosion resistance are still open. The purpose of this work is to identify the structural condition of low-carbon, low-alloy, pipe steels, providing a combination of high mechanical properties with increased corrosion resistance in oilfield environments. The studies were carried out on the latest generation 08KhFA, 08KhFMA and 05KhGB steels, most popular when manufacturing oil and gas pipelines. Samples for the study were cut from the pipes and quenched from the austenite region in water, which formed the structure of lath carbide-free bainite. The quenched samples were tempered at temperatures of 200, 300, 400, 500, 600, and 700 °C. To identify the relationship between the morphology of bainite structures and their properties, the samples after quenching and tempering at each temperature, were subjected to metallographic analysis, X-ray diffraction analysis, mechanical tests, and corrosion resistance tests. The work shows the sequence of structure transformation, temperature ranges of phase and structural transformations, changes in mechanical properties, and corrosion resistance that occur during tempering of lath carbide-free low-carbon bainite. It is shown that tempering of lath carbide-free bainite (08KhFA, 08KhMFA and 05KhGB steels) does not affect the rate of carbon dioxide corrosion. It has been found that medium tempering forms the structural condition of carbide-free low-carbon lath bainite providing a combination of high mechanical properties and high corrosion resistance in oil field environments. For each of the steels under study, the authors give recommended heat treatment modes.

Keywords: corrosion-mechanical destruction; destruction of bainite structures; oilfield environment; pipe steels; structural condition.

For citation: Vyboishchik M.A., Gruzkov I.V. Corrosion-mechanical destruction of bainite structures in oilfield environments. *Frontier Materials & Technologies*, 2024, no. 3, pp. 17–29. DOI: 10.18323/2782-4039-2024-3-69-2.

INTRODUCTION

The constant increase in the aggressiveness of oilfield environments, and the intensity of oil production (injection of water and carbon dioxide into the formation) [1], leads to a sharp increase in the rate of corrosion-mechanical destruction of oilfield equipment. A significant improvement of the mechanical properties and corrosion resistance of the pipe steels used is required. High alloying, significantly increases the cost of steel, and in some cases, reduces the strength properties. Other approaches ensuring high resistance to corrosion-mechanical destruction are required. Currently, low-carbon low-alloy steels with a bainite structure after quenching in water are used for the production of oil and gas pipeline systems (pipes and pipeline fittings). Bainite structures having a unique combination of high strength and ductility provide high resistance to mechanical destruction of pipe steels [2–4]. The formation of the bainite structure, and the relationship of their structural condition with mechanical properties are described in sufficient detail [5–7]. The most complete classification of bainite

structures is given in [8]. Bainite structures of low-carbon low-alloy steels are singled out as a separate group and considered in works [5; 9]. The preferred structure providing the highest plastic properties of these steels is lath carbide-free bainite, in which residual (untransformed) austenite is located at the boundaries of the laths, that causes high resistance to brittle fracture [6; 10; 11].

At the same time, it should be noted that, despite a large number of studies of bainitic steels, the issues of changes in the structure and properties of bainite structures, with an increase in tempering temperature, have not been sufficiently studied, and the relationship between the morphology of bainites and their corrosion resistance has barely been considered. Such information is necessary for a practical solution to the issue of increasing the reliability of pipe steels.

The purpose of this work is to find the structural condition of low-carbon low-alloy pipe steels, providing a combination of high mechanical properties with increased corrosion resistance in oilfield environments.

METHODS

08KhFA, 08KhMFA and 05KhGB steels were selected for the study. Their elemental composition (Table 1) and thermokinetic diagrams of the supercooled austenite decomposition (Fig. 1) are given according to the data of the manufacturer. In 08KhMFA steel, compared to 08KhFA steel, the carbon content is reduced from 0.09 to 0.05 % and

0.2 % of Mo is introduced. 05KhGB steel is additionally alloyed with niobium, and due to the favorable Mn/Si ratio, has higher weldability.

All samples were water-quenched (20 °C) from the austenitic region (08KhFA and 08KhMFA steels – from a temperature of 930 °C, 05KhGB steel – from 920 °C), and then tempered at 200, 300, 400, 500, 600, and 700 °C.

*Table 1. Chemical composition of steels under study
Таблица 1. Химический состав исследуемых сталей*

Steel grade	Weight fraction of elements, %											
	C	Si	Mn	Cr	Ni	Cu	Nb	V	Mo	Al	S	P
08KhFA	0.09	0.20	0.44	0.52	0.12	0.11	0.020	0.088	0.003	0.034	0.002	0.011
08KhMFA	0.05	0.39	0.39	0.70	0.10	0.17	0.011	0.061	0.190	0.057	0.004	0.003
05KhGB	0.05	0.22	0.71	0.61	0.08	0.18	0.029	0.003	0.010	0.013	0.001	0.006

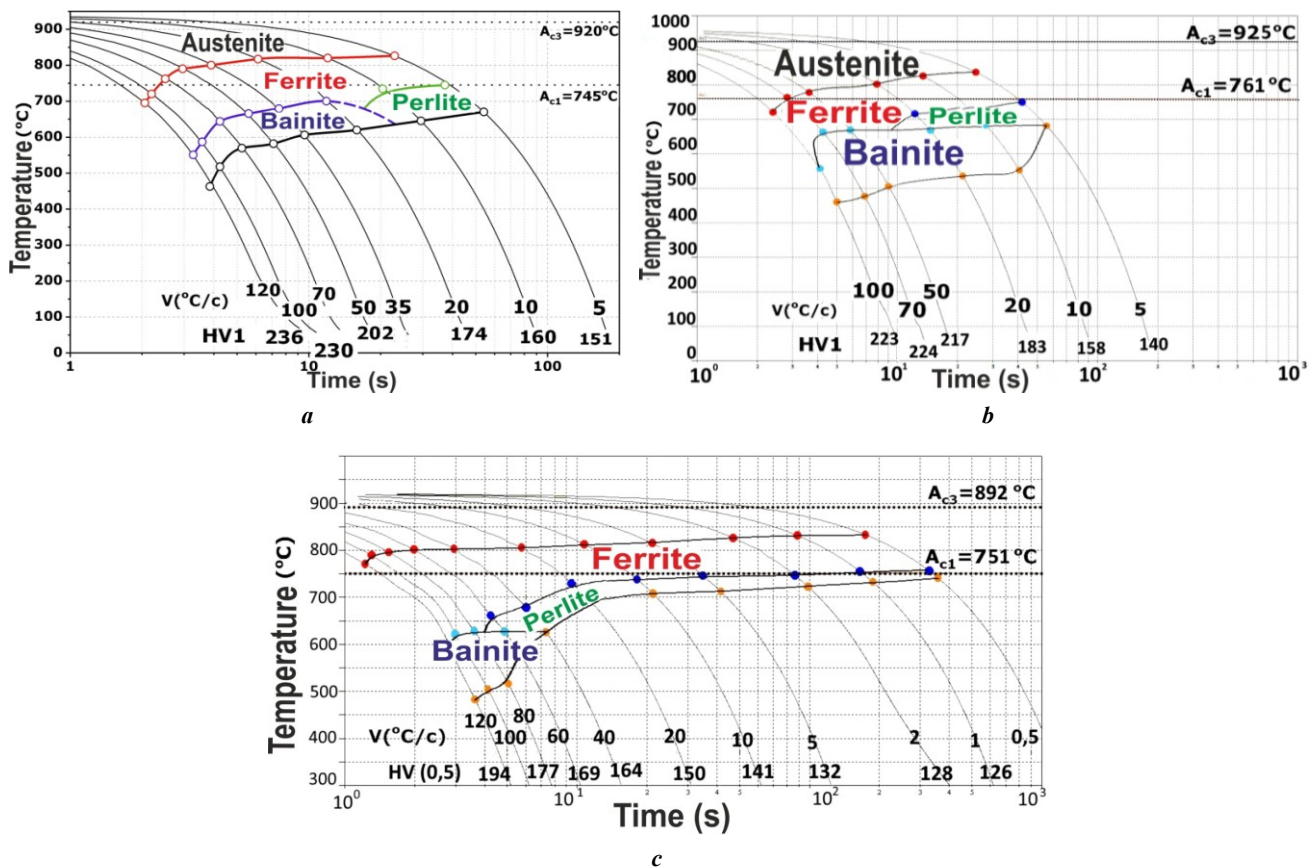


*Fig. 1. Thermokinetic diagrams of decomposition of supercooled austenite of steels under study:
a – 08KhFA steel; b – 08KhMFA steel; c – 05KhGB steel.*

The diagrams are based on the data from Vyksa metallurgical plant

*Рис. 1. ТермокINETические диаграммы распада переохлажденного аустенита исследуемых сталей:
а – сталь 08ХФА; б – сталь 08ХМФА; в – сталь 05ХГБ.*

Диаграммы приведены по данным Выксунского металлургического завода

Quenching from the austenitic region provides a large amount of bainite component in the steel structure, and water is the most technologically advanced medium. For each tempering temperature, the structural condition was studied and mechanical and corrosion properties due to this structure were determined.

To conduct the studies, longitudinal strips measuring 120×20×7 mm were cut from Ø146×7 mm pipes produced using conventional factory technology. The strips were subjected to heat treatment, and then samples were made from them. To ensure identical and relatively homogeneous structural condition, all samples were subjected to normalisation (08KhFA and 08KhMFA steels at a temperature of 940 °C, 05KhGB steel at 930 °C, holding time – 30 min), with cooling in still air. This ensured similar grain sizes and identical ferrite-pearlite structure, with lamellar cementite in pearlite in the samples before heat treatment.

The research and testing methods are presented in the form of groups according to their purpose.

Metallographic analysis included light microscopy (GX51 microscope, Olympus, Japan), SEM electron scanning microscopy (XL-30 microscope, Philips, Netherlands), EBSD technique (identifying intergranular disorientation angles), TEM transmission electron microscopy (EMV-100L microscope, Russia), and diffraction analysis.

Quantitative assessment of structural components was carried out using Thixomet Pro software.

X-ray diffraction analysis for volumetric determination of phase composition and stress state (3rd type residual stresses and dislocation density), was performed using a Shimadzu Maxima XRD-7000S diffractometer, Japan (Cu-K α radiation, tube power is 1.6 kW) in the angle range of 40–100°. Crystalline phases were identified using the Shimadzu PDF2 database. Full-profile analysis of diffraction patterns was performed using the LeBel and Rietveld methods in the Jana2006 program.

Hardness tests (GOST 9013), uniaxial tensile tests (GOST 1497), and impact toughness tests (GOST 9454) were performed to determine mechanical properties.

To determine resistance to corrosion destruction, hydrogen cracking tests (NACE TM0284 standard), sulfide stress corrosion cracking tests (NACE TM0177 standard), carbon dioxide corrosion resistance tests (technique developed by IT-Service LLC, 400-hour exposure in an aggressive environment with 3.5 % of chlorides at 65 °C, and a CO₂ pressure of 0.1 MPa, which allowed creating corrosion products on the sample surface similar to those that form in real conditions during many months of operation in carbon dioxide oilfield environments), were carried out.

RESULTS

Phase transformations during cooling

Thermokinetic diagrams of austenite decomposition in 08KhFA, 08KhMFA and 05KhGB steels (Fig. 1), and panoramic images of changes in the structure of these steels along the length of the sample during end quenching (Fig. 2), provide an idea of the effect of the cooling rate on the formation of the structure of steels. The studied steels acquire a bainite structure after water quenching. 08KhMFA

steel has a wider range of cooling rates that form bainite structures (Fig. 1). Continuous hardenability for all steels is ensured to a depth of 10 mm.

The studied steels have one type of bainite structure and a similar nature of its change upon heating therefore, the ongoing processes of structure transformation and property changes (Fig. 3–5), are shown using the example of one steel – 08KhMFA steel with higher corrosion resistance.

Structural condition after quenching

After water quenching, a structure consisting of lath carbide-free bainite with thin layers of residual austenite, and a small proportion of excess ferrite localised along the boundaries of the former austenite grain, is formed in the steels under study (Fig. 3).

The amount of excess ferrite is insignificant – from 3 to 10 %, the largest amount is in 05KhGB steel. Ferrite is located mainly along the boundaries of the former austenite grain. Bainite consists of laths of bainitic ferrite, along the boundaries of which there are thin layers of residual austenite. Ordered sequence of bainite laths and layers of residual austenite predominates. The width of the laths for the steels under study varies from 200 to 800 nm.

Wider laths (average width is \approx 600 nm), are observed in sections of 08KhMFA steel. The amount of residual austenite is 0.5–1.5 %. X-ray diffraction analysis reveals only its traces. Microdiffraction analysis of transmission electron microscopy images identified the γ -phase (Fig. 3 c). With a small amount, residual austenite in the form of thin layers (\approx 40 nm) located along the boundaries of bainitic ferrite laths determines the mechanical properties (high ductility) of carbide-free bainites in low-carbon steels.

Thus, 08KhFA, 08KhMFA, 05KhGB steels after quenching, have a structure of lath carbide-free bainite with close parameters of the structural condition.

The evolution of the structural condition with an increase in the tempering temperature is shown in Fig. 4, 5. During tempering, as the temperature increases to Ac₁, a successive transition of carbide-free lath bainite, with excess ferrite along the grain boundaries into a mixture of ferrite with globular carbide particles occurs (Fig. 4, 5). The fine grain obtained during quenching (numbers 9–11 according to GOST 5639) in the tempering temperature range of up to 700 °C remains virtually unchanged. A further increase in the tempering temperature (730 °C) for 08KhFA steel leads to the development of secondary recrystallisation processes and a sharp grain growth. With an increase in the tempering temperature, a constant increase in the intergranular disorientation angles, and accordingly, an increase in the proportion of high-angle boundaries is observed in the studied steels, which causes an increase in plasticity. It is characteristic that the high dislocation density after quenching $(3–5)\times 10^{14} \text{ m}^{-2}$ remains virtually unchanged, up to a tempering temperature of 600 °C (Table 2). The 3rd type residual stresses decrease continuously with increasing tempering temperature, especially intensively from 400 °C (Table 2).

The results of mechanical tests, impact bending tests, as well as the assessment of the 3rd type residual stresses and dislocation density are given in Table 2.

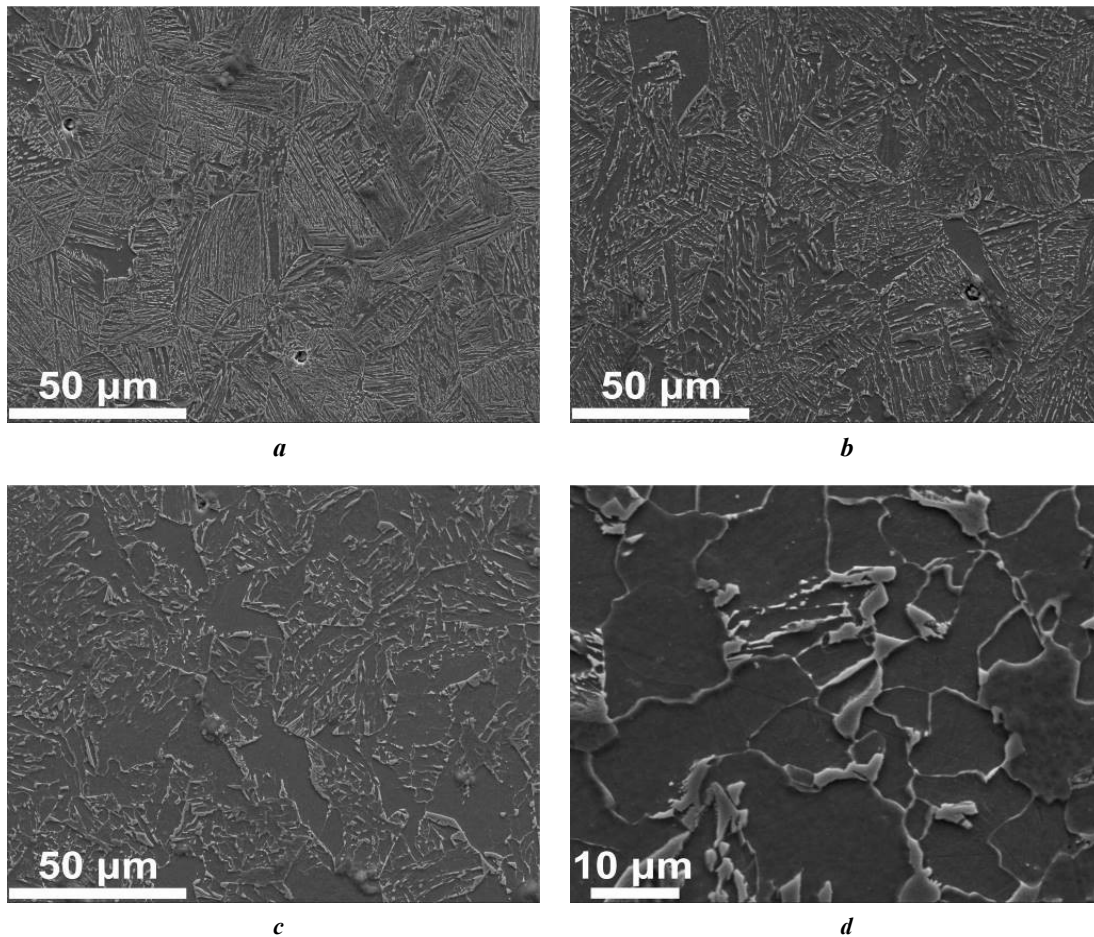


Fig. 2. Change in the structure of 08KhMFA steel during end quenching: **a** – distance from the sample end is $h=2$ mm, hardness is 298 HV; **b** – $h=7$ mm, 235 HV; **c** – $h=12$ mm, 205 HV; **d** – $h=17$ mm, 176 HV

Рис. 2. Изменение структуры стали 08ХМФА при торцевой закалке: **a** – расстояние от торца образца $h=2$ мм, твердость 298 HV; **b** – $h=7$ мм, 235 HV; **c** – $h=12$ мм, 205 HV; **d** – $h=17$ мм, 176 HV

The change in resistance to corrosion destruction in oil-field environments with increasing tempering temperature is given in Table 3 and shown in Fig. 6, 7.

DISCUSSION

Changes in structure and properties with increasing tempering temperature

Structure

After tempering at 200 °C, the residual austenite disappears. This is also observed in 08KhFA [12] and 05KhGB [13] steels. The temperature stability of the residual austenite or complex (austenite-martensite phase) is considered in [14; 15], the effect of V and Nb microadditives is considered in [16; 17], where it is indicated that with a particle size of 0.5–3 μm, the austenite decomposition occurs in the temperature range of 300–400 °C [14; 15]. In the lath bainite of the steels under study, untransformed austenite is in the form of thin layers (≈ 40 nm), and its decomposition can be expected at lower temperatures. Estimated calculations show that after 30 min of holding at a temperature of 200 °C, the distance of diffusion of carbon atoms from

austenite is more than an order of magnitude greater than the width of the interlayers and fully ensures the residual austenite decomposition [12]. The type of austenite transformation (martensite, bainite or α -ferrite) remains debatable.

Further transformation of the structure is associated with the formation and growth of carbides, the development of polygonisation and recrystallisation processes. The change in the structural condition of lath carbide-free bainite, with an increase in the tempering temperature occurs in the following sequence:

- at 200 °C, untransformed austenite disappears;
- when tempering at 300 °C, the first needle-shaped iron carbide precipitates appear;
- in the temperature range of 400–500 °C, carbide particles appear throughout at the boundaries of the laths, they coalesce and spheroidise, and chains of carbide inclusions appear at the boundaries of bainitic laths (Fig. 5 b and 5 c). 3rd type residual stresses decrease sharply (Table 2), which indicates the transition of carbon from the crystal lattice to a bound state in the form of carbides. Polygonisation processes develop: a decrease in low-angle boundaries and an increase in high-angle ones, while the dislocation density remains virtually unchanged;

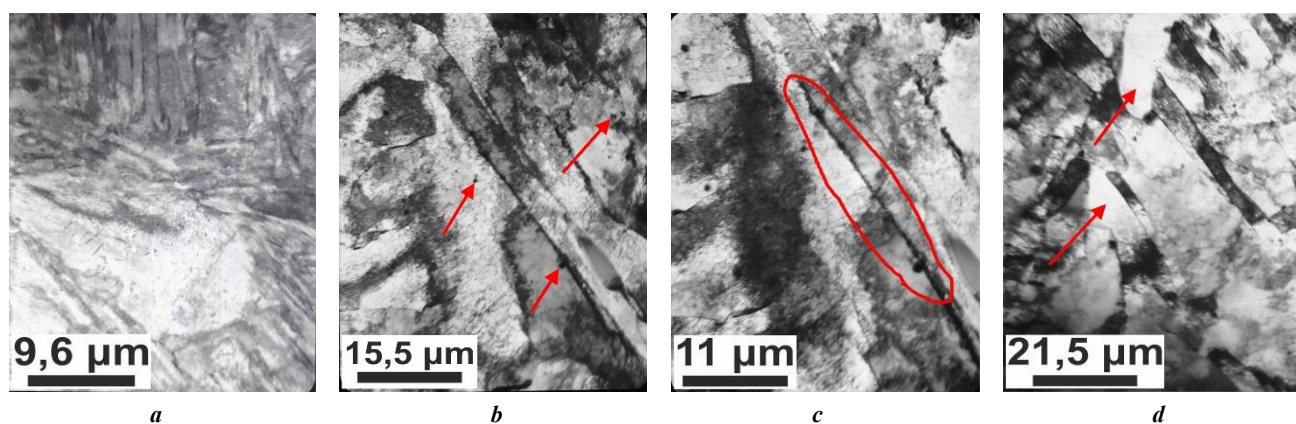


Fig. 5. Change in the structure of 08KhMFA steel with the growth in the tempering temperature (TEM):

a – tempering at 300 °C; **b** – tempering at 400 °C (arrows indicate globular carbides);
c – tempering at 500 °C (carbide chains are encircled); **d** – tempering at 600 °C (arrows indicate recrystallisation nuclei)

Рис. 5. Изменение структуры стали 08ХМФА с ростом температуры отпуска (ПЭМ):

a – отпуск при 300 °C; **b** – отпуск при 400 °C (стрелками показаны глобулярные карбиды);
c – отпуск при 500 °C (обведены цепочки карбидов); **d** – отпуск при 600 °C (стрелками показаны зародыши рекристаллизации)

– from a tempering temperature of 600 °C (Fig. 5 d), the main factor determining the change in structure and properties is the intensity of recrystallisation processes. Carbide reactions of cementite replacement by special carbides are possible;

– tempering at a temperature above 700 °C can cause secondary recrystallisation and a sharp grain growth (08KhFA steel).

Mechanical properties

Usually, in pipe production technologies, bainite structures are subjected to high tempering by analogy with martensite structures. For pipes made of low-carbon low-alloy steels, this is 600–750 °C, when partial recrystallisation significantly reduces strength [18]. There is some information on the effect of lower tempering temperatures on the properties and morphology of bainite [19; 20], but no general picture of changes in mechanical properties during tempering has been found in the literature.

The authors studied changes in the structure, mechanical properties, and corrosion resistance over the entire tempering temperature range (20–730 °C), which is 50 °C below the A_{c1} line, for 08KhFA, 08KhMFA, and 05KhGB steels.

An increase in temperature to 730 °C for 08KhFA steel led to a sharp increase in grain size. The steels under study after quenching and subsequent tempering to a temperature of 600 °C are characterised by a combination of high strength and plastic properties (Table 2), which for most heat treatment modes is higher than the requirements of K52 strength group. Characterising the thermal stability of mechanical properties, one can note that the strength properties (σ_{UTS} and $\sigma_{0.2}$) remain virtually unchanged upon tempering to a temperature of 400 °C. Apparently, this is associated with the appearance of precipitates of dispersed cementite particles. The plasticity characteristics (δ and KCV-50) after quenching are quite high and increase with a growth of the tempering temperature (Table 2). A sharp softening appears from a tempering temperature of 600 °C,

which is caused by an increase in the intensity of recrystallisation processes. On the whole, the general nature of the change in mechanical properties for the three steels under study is identical.

Corrosion resistance

Steels in aggressive oilfield environments are subjected to the following types of corrosion destruction: hydrogen cracking (HC), sulfide stress corrosion cracking (SSCC), carbon dioxide and bacterial corrosion [21; 22]. The studied low-carbon chromium-containing steels ($\approx 0.6\%$ of Cr) are relatively resistant to biocorrosion [22]. Modification with rare earth metals (REM) significantly increases their resistance to bacterial attack. The main problem is to ensure resistance to carbon dioxide corrosion.

The obtained values of HC, SSCC and carbon dioxide corrosion rate (Table 3) indicate, that the studied steels have increased corrosion resistance in oilfield environments, compared to traditionally used 20, 20F, 17G1, 09G2S pipe steels.

An interesting and unexpected result is that tempering of low-carbon steels with a lath carbide-free bainite structure, has virtually no effect on the intensity of carbon dioxide corrosion. With an increase in tempering temperature to 700 °C, the structural condition changes from lath carbide-free bainite to a ferrite-carbide mixture and the carbon dioxide corrosion rate remains constant. This phenomenon is characteristic of all the steels under study (Table 3, Fig. 6). The correctness of the obtained corrosion rate values is also confirmed by the proximity and similarity of the curves for changing the Fe^{+2} concentration in the corrosion environment during testing (Fig. 7). These curves also characterise the kinetics of corrosion processes, and the influence of corrosion products on the intensity of corrosion destruction. For the steels under study, the nature of the change in the corrosion rate depending on the test time is similar (Fig. 6).

According to existing concepts, the rate of carbon dioxide corrosion of steels is determined by the formation

Table 2. Dependence of mechanical properties, residual stresses and dislocation density of 08KhFA, 08KhMFA, 05KhGB steels on the temperature of tempering
Таблица 2. Зависимость механических свойств, остаточных напряжений и плотности дислокаций сталей 08ХФА, 08ХМФА, 05ХГБ от температуры отпуска

Steel grade	Heat treatment mode		σ_{UTS} , MPa	$\sigma_{0.2}$, MPa	δ , %	KCV-50, J/cm ² (shear area fraction)	3 rd type residual stresses, MPa	Dislocation density, $\rho \times 10^{14}$, m ⁻²
	Quenching	Tempering						
08KhFA	930 °C	–	830	740	22.0	230 (100 %)	300	5.1
		200 °C	820	710	19.0	240 (100 %)	225	4.4
		300 °C	810	730	17.5	240 (100 %)	220	4.1
		400 °C	785	690	18.0	252 (100 %)	140	5.1
		500 °C	710	645	18.5	260 (100 %)	91	4.7
		600 °C	680	605	22.0	260 (100 %)	71	5.2
		700 °C	615	535	25.0	–	64	2.8
08KhMFA	930 °C	–	775	700	19.5	180 (80 %)	190	4.0
		200 °C	780	650	19.0	215 (100 %)	200	4.7
		300 °C	785	660	18.0	200 (100 %)	180	4.5
		400 °C	760	650	19.5	215 (100 %)	120	4.2
		500 °C	710	635	20.0	235 (100 %)	–	–
		600 °C	685	605	21.5	250 (100 %)	86	3.4
		700 °C	590	520	23.5	270 (100 %)	63	3.6
05KhGB	920 °C	–	605	490	29.0	290 (100 %)	570	5.4
		200 °C	–	–	–	–	–	–
		300 °C	590	500	29.0	315 (100 %)	460	4.9
		400 °C	560	470	27.0	330 (100 %)	215	4.7
		500 °C	530	430	28.0	314 (100 %)	90	4.5
		600 °C	510	420	27.0	325 (100 %)	45	4.0
		700 °C	–	–	–	–	–	–
Strength group K52			510–630	≥353	≥20	≥58,8	–	–

Table 3. Dependence of corrosion properties of 08KhFA, 08KhMFA, 05KhGB steels on the temperature of tempering
Таблица 3. Зависимость коррозионных свойств сталей 08ХФА, 08ХМФА, 05ХГБ от температуры отпуска

Steel grade	Heat treatment mode		Hydrogen cracking		Sulfide stress corrosion cracking		Carbon dioxide corrosion rate, mm/year
	Quenching	Tempering	CLR, %	CTR, %	% of σ_t	K_{ISSC} , MPa/m ^{1/2}	
08KhFA	930 °C	–	0	0	75	–	2.30
		200 °C				–	1.83
		300 °C				30.6	2.24
		400 °C				31.0	1.79
		500 °C				56.9	1.65
		600 °C				58.4	1.75
		700 °C				61.8	1.94
08KhMFA	930 °C	–	0	0	75	–	1.20
		200 °C					1.25
		300 °C					1.30
		400 °C					1.60
		500 °C					1.69
		600 °C					1.41
		700 °C					1.40
05KhGB	920 °C	–	0	0	70	–	2.07
		200 °C	–	–	–		–
		300 °C	0	0	70		2.07
		400 °C					1.93
		500 °C					1.93
		600 °C					1.40
		700 °C	–	–	–		–

Note. CLR is crack length ratio; CTR is crack thickness ratio; K_{ISSC} is critical stress intensity factor at the crack tip.

Примечание. CLR – коэффициент длины трещин; CTR – коэффициент толщины трещин;

K_{ISSC} – критический коэффициент интенсивности напряжений в вершине трещины.

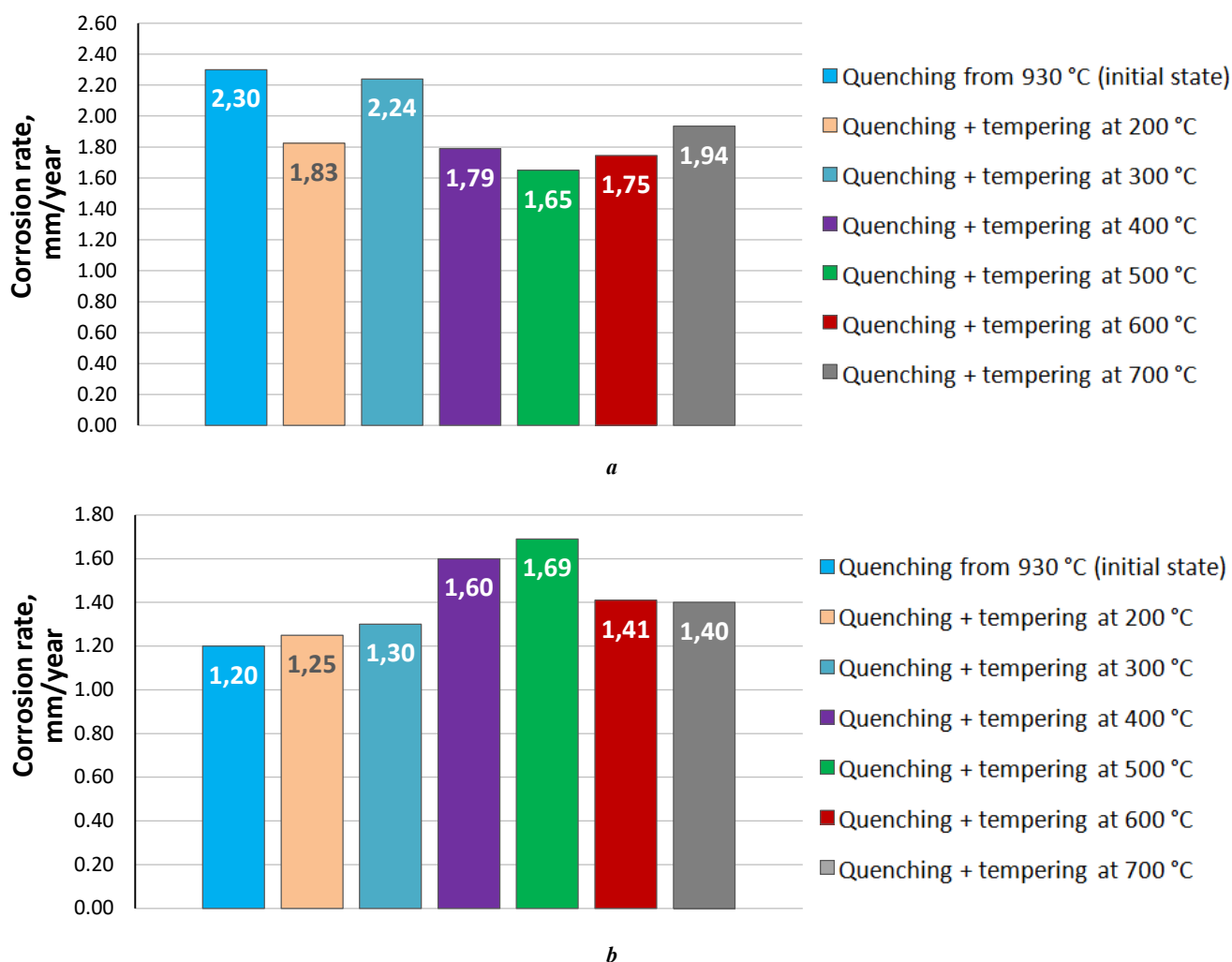


Fig. 6. Carbon dioxide corrosion of 08KhFA and 08KhMFA steels.

Dependence of corrosion rate on the temperature of tempering: **a** – 08KhFA steel; **b** – 08KhMFA steel

Рис. 6. Углекислотная коррозия сталей 08ХФА и 08ХМФА.

Зависимость скорости коррозии от температуры отпуска: **a** – сталь 08ХФА; **b** – сталь 08ХМФА

of a layer of corrosion products on the surface. Chromium and molybdenum are concentrated in corrosion products, and form amorphous $\text{Cr}(\text{OH})_3$ and $\text{Mo}(\text{OH})_3$ phases [21; 23], determining the protective properties of corrosion products. Only Cr and Mo contained in the solid solution participate in the formation of the protective properties of corrosion products. In a bound state in the form of carbides, they are inert and are excluded from the process. In the studied low-carbon steels, in the tempering temperature range of up to 600 °C, the formation of special carbides with the participation of Mo and Cr practically does not occur, and their concentration in the solid solution does not change. This, apparently, determines the absence of the effect of tempering on corrosion resistance. A slightly lower rate of carbon dioxide corrosion of 08KhMFA, steel compared to 08KhFA and 05KhGB steels (Table 3), is associated with the additional contribution of Mo to the protective properties of the corrosion products.

According to existing estimates, the studied steels have increased resistance to HC and SSCC under all heat treatment modes (Table 3). In SSCC tests, 08KhFA and

08KhMFA steels at a load of $0.75 \sigma_r$ and 05KhGB steel at a load of $0.7 \sigma_r$ withstood without destruction 720 h. However, the presence of high residual stresses after quenching and the anisotropy of the quenched structures determine the need for more stringent conditions for testing samples for SSCC resistance after quenching, and low-temperature tempering. It is proposed to conduct tests for SSCC at stresses of 0.8 or 0.85 of $\sigma_{0.2}$ determined in mechanical tensile tests for this group of samples.

The obtained data indicating that the resistance to carbon dioxide corrosion of steels, with a lath carbide-free bainite structure, does not change with increasing tempering temperature, allow choosing heat treatment modes more reasonably. In the production of pipes from low-carbon low-alloy steels with a bainite structure after water quenching, instead of traditional heat treatment (single or double quenching + high tempering), quenching from the austenitic region in water + medium tempering can be used, which provides a combination of higher strength properties with high corrosion resistance in aggressive oilfield environments. Medium tempering in steels with a lath carbide-free bainite structure, allows maintaining high strength properties,

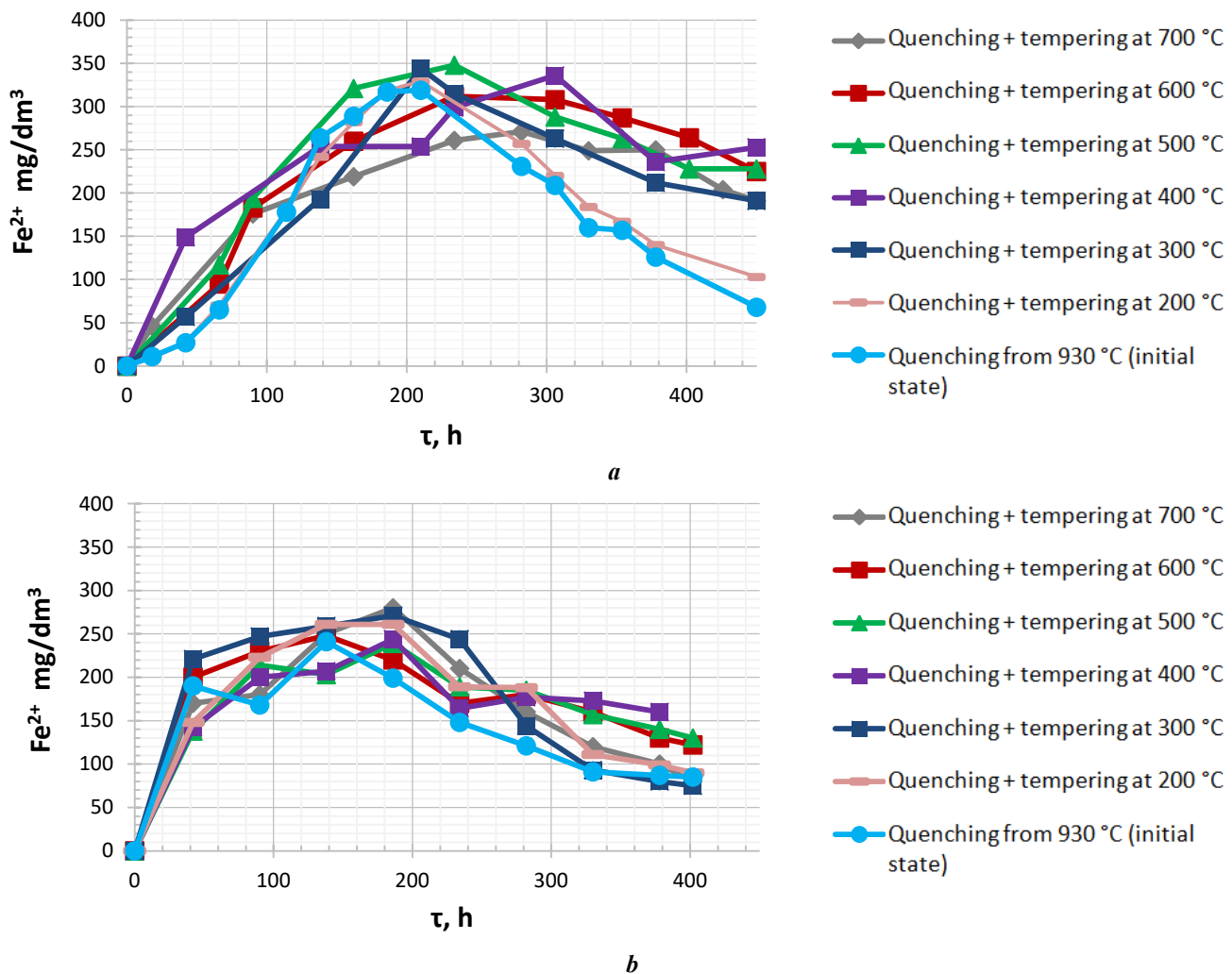


Fig. 7. Dependence of the Fe^{+2} concentration in the model environment on the test time: **a** – 08KhFA steel; **b** – 08KhMFA steel
 Рис. 7. Зависимость концентрации Fe^{+2} в модельной среде от времени испытаний: **a** – сталь 08ХФА; **b** – сталь 08ХМФА

relieves the most dangerous residual stresses, and ensures the carbide phase formation. Tempering can be excluded or limited to low-temperature tempering for pipes operating in environments with a low H_2S content, or if the steel used withstands the more stringent SSCC tests proposed above. In the proposed heat treatment technology (without high tempering), microalloying of steel with V and Nb is advisable, when the precipitation of carbonitride particles of these elements occurs at the stage of formation of bainite structures.

CONCLUSIONS

1. The general structure type and mechanical properties of lath carbide-free bainite of low-carbon steels in the tempering temperature range up to 500 °C change insignificantly.
2. Tempering of lath carbide-free low-carbon bainite (08KhFA, 08KhMFA and 05KhGB steels), has little effect on its resistance to carbon dioxide corrosion.
3. Quenching and medium tempering in low-carbon low-alloy steels with bainitic hardenability, form a structural condition that ensures a combination of high mechanical properties, and high corrosion resistance in oilfield environments.

REFERENCES

1. Khromykh L.N., Litvin A.T., Nikitin A.V. Application of carbon dioxide in enhanced oil recovery. *Vestnik Evraziyskoy nauki*, 2018, vol. 10, no. 5, pp. 82–91. EDN: [VREXBN](https://doi.org/10.1134/S0031918X20040171).
2. Efron L.I. *Metalovedenie v "bolshoy" metallurgii. Trubnye stali* [Metal science as part of "big" metallurgy. Pipe steel]. Moscow, Metallurgizdat Publ., 2012. 696 p.
3. Ioffe A.V. Assimilation of bainite structures in the production of pipe steels. *Perspektivnye materialy*. Tolyatti, TGU Publ., 2017. Vol. 6, pp. 153–196.
4. Yakovleva I.L., Tereshchenko N.A., Urtsev N.V. Observation of the martensitic-austenitic component in the structure of low-carbon low-alloy pipe steel. *Physics of Metals and Metallography*, 2020, vol. 121, no. 4, pp. 352–358. DOI: [10.1134/S0031918X20040171](https://doi.org/10.1134/S0031918X20040171).
5. Rudskoy A.I. *Nauchnye osnovy upravleniya strukturoy i svoystvami staley v protsessakh termomekhanicheskoy obrabotki* [Scientific basis of controlling the structure and properties of steels in the heat treatment processes]. Moscow, RAN Publ., 2019. 276 p.
6. Maisuradze M.V., Ryzhkov M.A., Antakov E.V., Popov N.A., Proskuryakov P.A. Special features of trans-

- formations of supercooled austenite in modern structural steels. *Metal Science and Heat Treatment*, 2020, vol. 62, no. 7-8, pp. 448–456. DOI: [10.1007/s11041-020-00583-4](https://doi.org/10.1007/s11041-020-00583-4).
7. Mandal M., Poole W.J., Militzer M., Collons L. Temperature Dependence of Mechanical Properties for Advanced Line Pipe Steels With Bainitic Microstructures. *Metallurgical and Materials Transaction A*, 2023, vol. 54, pp. 3086–3100. DOI: [10.1007/s11661-023-07072-2](https://doi.org/10.1007/s11661-023-07072-2).
 8. Zajac S., Morris P., Komenda J. *Quantitative structure-property relationships for complex bainitic microstructures: final report*. Luxembourg, Office for Official Publications of the European Communities Publ., 2005. 161 p.
 9. Ohmori Y., Ohtani H., Kunitake T. The Bainite in Low Carbon Low Alloy High Strength Steels. *Transactions of the Iron and Steel Institute of Japan*, 1971, vol. 11, no. 4, pp. 250–259. DOI: [10.2355/isijinternational1966.11.250](https://doi.org/10.2355/isijinternational1966.11.250).
 10. Kaletin A.Y., Kaletina Y.V. The role of retained austenite in the structure of carbide-free bainite of construction steels. *Physics of Metals and Metallography*, 2018, vol. 119, no. 9, pp. 893–898. DOI: [10.1134/S0031918X18090053](https://doi.org/10.1134/S0031918X18090053).
 11. Kolbasnikov N.G., Zaitsev A.M., Adigamov R.R., Sakharov M.S., Matveev M.A. Role of Martensite-Austenite Component of Bainitic Structure in Formation of Properties of Pipe Steel. 3. Effect of Martensitic Transformation of Austenite in the MA-Component of Bainite on the Ductility of Steel. *Metal Science and Heat Treatment*, 2023, vol. 64, no. 9-10, pp. 547–553. DOI: [10.1007/s11041-023-00849-7](https://doi.org/10.1007/s11041-023-00849-7).
 12. Vyboishchik M.A., Gruzkov I.V., Chistopoltseva E.A., Tetyueva T.V. Formation of structure and properties of low-carbon bainite in steel 08KHFA. *Metal Science and Heat Treatment*, 2023, vol. 65, no. 7-8, pp. 400–409. DOI: [10.1007/s11041-023-00947-6](https://doi.org/10.1007/s11041-023-00947-6).
 13. Vyboishchik M.A., Fedotova A.V., Chistopoltseva E.A., Kudashov D.V., Gruzkov I.V. Changes in structure and properties of low-carbon steel with structure of lath-type carbide-free bainite during tempering. *Deformatsiya i razrushenie materialov*, 2023, no. 8, pp. 31–39. DOI: [10.31044/1814-4632-2023-8-31-39](https://doi.org/10.31044/1814-4632-2023-8-31-39).
 14. Kolbasnikov N.G., Sakharov M.S., Kuzin S.A., Teteryatnikov V.S. Stability of untransformed austenite in M/A phase of bainitic structure of low-carbon steel. *Metal Science and Heat Treatment*, 2021, vol. 63, no. 1-2, pp. 63–69. DOI: [10.1007/s11041-021-00648-y](https://doi.org/10.1007/s11041-021-00648-y).
 15. Kolbasnikov N.G., Kuzin S.A., Teteryatnikov V.S., Adigamov R.R., Sakharov M.S., Matveev M.A. Role of bainitic structure martensitic-austenitic component in pipe steel property formation. 2. Austenite deformation and thermal stability. *Metal Science and Heat Treatment*, 2022, vol. 64, no. 3-4, pp. 137–145. DOI: [10.1007/s11041-022-00774-1](https://doi.org/10.1007/s11041-022-00774-1).
 16. Matrosov Yu.I. Mechanism of the influence of microadditions of niobium on microstructure and properties of thick-sheet low-alloy pipe steel. *Metal Science and Heat Treatment*, 2022, vol. 64, no. 1-2, pp. 87–94. DOI: [10.1007/s11041-022-00766-1](https://doi.org/10.1007/s11041-022-00766-1).
 17. Matrosov Yu.I. Comparison of the Effect of Microadditions of Niobium, Titanium and Vanadium on Formation of Microstructure of Low-Carbon Low-Alloy Steels. *Metal Science and Heat Treatment*, 2023, vol. 65, no. 3-4, pp. 152–158. DOI: [10.1007/s11041-023-00907-0](https://doi.org/10.1007/s11041-023-00907-0).
 18. Tetyueva T.V., Ioffe A.V., Denisova T.V., Trifonova E.A. special features of formation of structure in low-alloy steel 08KHMFBCHA upon quenching and tempering. *Metal Science and Heat Treatment*, 2013, vol. 54, no. 9-10, pp. 524–529. DOI: [10.1007/s11041-013-9542-7](https://doi.org/10.1007/s11041-013-9542-7).
 19. Zavalishchin A.N., Rumyantsev M.I., Kozhevnikova E.V. Effect of quenching and tempering on the structure and properties of hot-rolled pipe steels of strength categories K60 and K65. *Metal Science and Heat Treatment*, 2023, vol. 65, no. 1-2, pp. 12–17. DOI: [10.1007/s11041-023-00884-4](https://doi.org/10.1007/s11041-023-00884-4).
 20. Efron L.I., Stepanov P.P., Smetanin K.S., Vorkachev K.G., Kantor M.M., Bozhenov V.A. Questioning the effect of bainite morphology on the impact viscosity of low-carbon steels. *Steel in Translation*, 2021, vol. 51, no. 9, pp. 670–676. DOI: [10.3103/S0967091221090035](https://doi.org/10.3103/S0967091221090035).
 21. Vyboishchik M.A., Ioffe A.V. Scientific basis of development and the methodology of creation of steels for the production of oilfield casing and tubular goods with the increased strength and corrosion resistance. *Frontier materials and technologies*, 2019, no. 1, pp. 13–21. DOI: [10.18323/2073-5073-2019-1-13-20](https://doi.org/10.18323/2073-5073-2019-1-13-20).
 22. Li Y.Y., Wang Z.Z., Zhu G.Y., Zhang Q.H., Hou B.S., Lei Y., Wang X., Zhang G.A. Developing a water chemistry model in the CO₂-mixed salts – H₂O system to predict the corrosion of carbon steel in supercritical CO₂-containing formation water. *Corrosion Science*, 2021, vol. 192, article number 109806. DOI: [10.1016/j.corsci.2021.109806](https://doi.org/10.1016/j.corsci.2021.109806).
 23. Keiichi K., Yoon-Shoi C., Srdjan N. Effect of Small Amount of Cr and Mo on Aqueous CO₂ Corrosions of Low-Alloyed Steel and Formation of Protective FeCO₃ in Near-Saturation Conditions. *Corrosion*, 2022, vol. 79, no. 1, pp. 97–110. DOI: <https://doi.org/10.5006/4100>.

СПИСОК ЛИТЕРАТУРЫ

1. Хромых Л.Н., Литвин А.Т., Никитин А.В. Применение углекислого газа в процессе повышения нефтеотдачи пластов // Вестник Евразийской науки. 2018. Т. 10. № 5. С. 82–91. EDN: [VRFXBN](https://doi.org/10.26907/2542-0419.2018.5.82-91).
2. Эфрон Л.И. *Металловедение в «большой» металлургии. Трубные стали*. М.: Металлургиздат, 2012. 696 с.
3. Иоффе А.В. Освоение бейнитных структур в производстве трубных сталей // Перспективные материалы. Т. 6. Тольятти: ТГУ, 2017. С. 153–196.
4. Яковлева И.Л., Терещенко Н.А., Урцев Н.В. Наблюдение мартенситно-аустенитной составляющей в структуре низкоуглеродистой низколегированной трубной стали // Физика металлов и металлостроение. 2020. Т. 121. № 4. С. 396–402. DOI: [10.31857/S0015323020040178](https://doi.org/10.31857/S0015323020040178).

5. Рудской А.И. Научные основы управления структурой и свойствами сталей в процессах термомеханической обработки. М.: РАН, 2019. 276 с.
6. Майсурадзе М.В., Рыжков М.А., Антаков Е.В., Попов Н.А., Проскуряков П.А. Особенности превращений переохлажденного аустенита в современных конструкционных сталях // *Металловедение и термическая обработка металлов*. 2020. № 7. С. 29–38. EDN: [AEAGTO](#).
7. Mandal M., Poole W.J., Militzer M., Collons L. Temperature Dependence of Mechanical Properties for Advanced Line Pipe Steels With Bainitic Microstructures // *Metallurgical and Materials Transaction A*. 2023. Vol. 54. P. 3086–3100. DOI: [10.1007/s11661-023-07072-2](#).
8. Zajac S., Morris P., Komenda J. Quantitative structure-property relationships for complex bainitic microstructures: final report. Luxembourg: Office for Official Publications of the European Communities, 2005. 161 p.
9. Ohmori Y., Ohtani H., Kunitake T. The Bainite in Low Carbon Low Alloy High Strength Steels // *Transactions of the Iron and Steel Institute of Japan*. 1971. Vol. 11. № 4. P. 250–259. DOI: [10.2355/isijinternational1966.11.250](#).
10. Калетин А.Ю., Калетина Ю.В. Роль остаточного аустенита в структуре бескарбидного бейнитного конструкционных сталей // *Физика металлов и металловедение*. 2018. Т. 119. № 9. С. 946–952. DOI: [10.1134/S001532301809005X](#).
11. Колбасников Н.Г., Зайцев А.М., Адигамов Р.Р., Сахаров М.С., Матвеев М.А. О роли мартенситно-аустенитной составляющей бейнитной структуры в формировании свойств трубной стали. 3. Влияние мартенситного превращения аустенита в МА-составляющей бейнита на пластичность стали // *Металловедение и термическая обработка металлов*. 2022. № 10. С. 12–19. DOI: [10.30906/mitom.2022.10.12-19](#).
12. Выбойщик М.А., Грузков И.В., Чистопольцева Е.А., Тетюева Т.В. Формирование структуры и свойств низкоуглеродистого бейнита в стали 08ХФА // *Металловедение и термическая обработка металлов*. 2023. № 7. С. 8–16. DOI: [10.30906/mitom.2023.7.8-16](#).
13. Выбойщик М.А., Федотова А.В., Чистопольцева Е.А., Кудашов Д.В., Грузков И.В. Изменение структуры и свойств низкоуглеродистой стали со структурой речного бескарбидного бейнита в процессе отпуска // *Деформация и разрушение материалов*. 2023. № 8. С. 31–39. DOI: [10.31044/1814-4632-2023-8-31-39](#).
14. Колбасников Н.Г., Сахаров М.С., Кузин С.А., Тетерятников В.С. О стабильности непревращенного аустенита в М/А – фазе бейнитной структуры низкоуглеродистой стали // *Металловедение и термическая обработка металлов*. 2021. № 2. С. 3–10. EDN: [BPZXXG](#).
15. Колбасников Н.Г., Кузин С.А., Тетерятников В.С., Адигамов Р.Р., Сахаров М.С., Матвеев М.А. О роли мартенситно-аустенитной составляющей бейнитной структуры в формировании свойств трубной стали. 2. Деформационная и термическая стабильность аустенита // *Металловедение и термическая обработка металлов*. 2022. № 3. С. 3–12. DOI: [10.30906/mitom.2022.3.3-12](#).
16. Матросов Ю.И. Механизм влияния микродобавок ниобия на микроструктуру и свойства толстолистовых низколегированных трубных сталей // *Металловедение и термическая обработка металлов*. 2022. № 2. С. 18–26. DOI: [10.30906/mitom.2022.2.18-26](#).
17. Матросов Ю.И. Сопоставление влияния микродобавок Nb, Ti, V на процессы формирования микроструктуры низкоуглеродистой низколегированной стали. // *Металловедение и термическая обработка металлов*. 2023. № 3. С. 25–31. DOI: [10.30906/mitom.2023.3.25-31](#).
18. Тетюева Т.В., Иоффе А.В., Денисова Т.В., Трифонова Е.А. Особенности формирования структуры в низкоуглеродистой стали 08ХМФБЧА при закалке и отпуске // *Металловедение и термическая обработка металлов*. 2012. № 10. С. 34–38. EDN: [PHHLAT](#).
19. Завалицин А.Н., Румянцев М.И., Кожевникова Е.В. Влияние закалки и отпуска на структуру и свойства горячекатаного проката из сталей трубного сортамента категорий прочности К60 и К65 // *Металловедение и термическая обработка металлов*. 2023. № 1. С. 13–18. DOI: [10.30906/mitom.2023.1.13-18](#).
20. Эфрон Л.И., Степанов П.П., Воркачев К.Г., Кантор М.М., Боженков В.А., Сметанин К.С. К вопросу о влиянии морфологии бейнита на ударную вязкость низкоуглеродистых сталей // *Сталь*. 2021. № 9. С. 45–50. EDN: [XYMRAF](#).
21. Выбойщик М.А., Иоффе А.В. Научные основы разработки и методология создания сталей для производства нефтепромысловых труб, повышенной прочности и коррозионной стойкости // *Вектор науки Тольяттинского государственного университета*. 2019. № 1. С. 13–21. DOI: [10.18323/2073-5073-2019-1-13-20](#).
22. Li Y.Y., Wang Z.Z., Zhu G.Y., Zhang Q.H., Hou B.S., Lei Y., Wang X., Zhang G.A. Developing a water chemistry model in the CO₂-mixed salts – H₂O system to predict the corrosion of carbon steel in supercritical CO₂-containing formation water // *Corrosion Science*. 2021. Vol. 192. Article number 109806. DOI: [10.1016/j.corsci.2021.109806](#).
23. Keiichi K., Yoon-Shoi C., Srdjan N. Effect of Small Amount of Cr and Mo on Aqueous CO₂ Corrosions of Low-Alloyed Steel and Formation of Protective FeCO₃ in Near-Saturation Conditions // *Corrosion*. 2022. Vol. 79. № 1. P. 97–110. DOI: <https://doi.org/10.5006/4100>.

Коррозионно-механическое разрушение бейнитных структур в нефтепромысловых средах

© 2024

Выбойщик Михаил Александрович^{1,3}, доктор физико-математических наук, профессор, профессор кафедры «Сварка, обработка материалов давлением и родственные процессы»

Грузков Игорь Викторович^{*1,2,4}, аспирант,

заведующий лабораторией оптической и электронной микроскопии

¹Тольяттинский государственный университет, Тольятти (Россия)

²ООО «ИТ-Сервис», Самара (Россия)

*E-mail: gruzkov@its-samara.com,
gigabon7@mail.ru

³ORCID: <https://orcid.org/0000-0003-2797-5396>

⁴ORCID: <https://orcid.org/0009-0007-9580-9935>

Поступила в редакцию 12.12.2023

Принята к публикации 15.08.2024

Аннотация: Основным направлением в решении проблемы повышения надежности промышленного оборудования является создание новых сталей с более высоким сопротивлением коррозионно-механическому разрушению. В настоящее время для изготовления нефтегазопроводных систем используются низкоуглеродистые низколегированные стали, в которых при закалке в воду образуется речный бескарбидный бейнит. Такая структура дает сочетание высокой прочности и сопротивления хрупкому разрушению. Однако вопросы повышения коррозионной стойкости остаются нерешенными. Цель работы – установить структурное состояние низкоуглеродистых низколегированных трубных сталей, обеспечивающее сочетание высоких механических свойств с повышенной коррозионной стойкостью в нефтепромысловых средах. Исследования проводились на сталях последнего поколения 08ХФА, 08ХФМА и 05ХГБ, наиболее распространенных при изготовлении нефтегазопроводных труб. Образцы для исследования вырезались из труб и закачивались из аустенитной области в воду, что формировало структуру речного бескарбидного бейнита. Закаленные образцы подвергались отпуску при температурах 200, 300, 400, 500, 600 и 700 °С. Для установления связи между морфологией бейнитных структур и их свойствами образцы после закалки и отпуска с каждой температуры подвергались металлографическому анализу, рентгеноструктурному анализу, механическим испытаниям, испытаниям на стойкость к коррозии. В работе показаны последовательность трансформации структуры, температурные интервалы фазовых и структурных превращений, изменения механических свойств и коррозионной стойкости, происходящие при отпуске речного бескарбидного низкоуглеродистого бейнита. Показано, что отпуск речного бескарбидного бейнита (стали 08ХФА, 08ХМФА и 05ХГБ) не влияет на скорость углекислотной коррозии. Установлено, что средний отпуск формирует структурное состояние бескарбидного низкоуглеродистого речного бейнита, обеспечивающее сочетание высоких механических свойств и высокой коррозионной стойкости в нефтепромысловых средах. Для каждой из исследуемых сталей приводятся рекомендуемые режимы термообработки.

Ключевые слова: коррозионно-механическое разрушение; разрушение бейнитных структур; нефтепромысловая среда; трубные стали; структурное состояние.

Для цитирования: Выбойщик М.А., Грузков И.В. Коррозионно-механическое разрушение бейнитных структур в нефтепромысловых средах // Frontier Materials & Technologies. 2024. № 3. С. 17–29. DOI: 10.18323/2782-4039-2024-3-69-2.

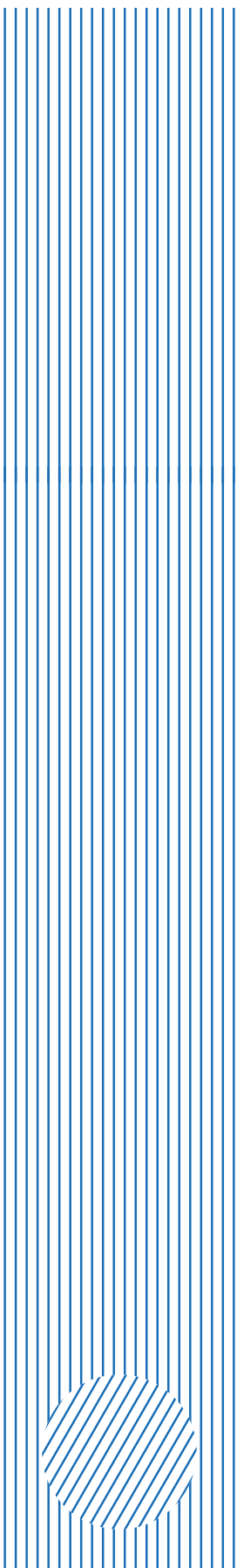
Togliatti State University is a participant in the Priority-2030 program of strategic academic leadership, a flagship university in the Samara region, a center for innovative and technological development of the region.

Togliatti State University was created in 2001 by merging Togliatti Polytechnic Institute (founded in 1951 as a branch of Kuibyshev Industrial Institute) and Togliatti branch of Samara State Pedagogical University (founded in 1987).

Togliatti State University today

- More than 22,000 students of all modes of study.
- Ten institutes implementing more than 170 higher education programs for 25 integrated groups of training areas, advanced technologies research institute, Zhiguli Valley Institute of Additional Education, military training center.
- 38 resource centers with up-to-date facilities and equipment created since 2011.
- Accreditation in eight systems for standard testing, research, and engineering.
- Main areas: advanced digital, intelligent manufacturing technologies, robotic systems, advanced materials and design methods, environmentally friendly and resource-saving energy engineering, personalized medicine, countering industrial threats.

University main achievements

- Ongoing project and professional practical activity was introduced for 100 % of full-time undergraduate/specialist students.
 - Four mega-grants were implemented according to the Resolutions of the Government of the Russian Federation dated April 9, 2010 No. 219 and No. 220 – three laboratories in the field of physical materials science and nanotechnology (with the invitation of leading scientists), as well as an innovation technology center were created. The latter was transformed into a university innovation technopark.
 - A member of the extraterritorial scientific and educational center “Engineering of the Future”.
 - An initiator of the formation of eight consortiums, which brought together 69 organizations, including 36 universities, six scientific partners, among which there are three organizations of the Russian Academy of Sciences.
 - A twice winner of the RF Government award in the field of quality (2009, 2019).
 - An Online Higher Education System promoted under the Rosdistant brand was created. The project is the winner of the Project Olympus competition of the Analytical Center under the Government of the Russian Federation in the Project Management in the System of Higher Education and Science nomination (2019).
- 

The influence of phosphorus microalloying on the structure formation of CuZn₃₂Mn₃Al₂FeNi multicomponent brass

© 2024

Anastasiya M. Gnusina*¹, postgraduate student
of Chair “Nanotechnologies, Materials Science and Mechanics”

Aleksey V. Svyatkin², PhD (Engineering),

assistant professor of Chair “Nanotechnologies, Materials Science and Mechanics”

Togliatti State University, Togliatti (Russia)

*E-mail: anastasiya.gnusina@vaz.ru,
myripru@gmail.com

¹ORCID: <https://orcid.org/0000-0002-8600-7566>

²ORCID: <https://orcid.org/0000-0002-8121-9084>

Received 26.06.2023

Accepted 19.07.2024

Abstract: Phosphorus in brass can have both a positive effect, such as improving mechanical properties, increasing corrosion resistance and machinability, and a negative effect, such as adversely affecting weldability and causing cracking. The study of the role of phosphorus in the processes of brass structure formation is of practical relevance, since it helps optimise the properties of the material, reduce the risk of defects, improve treatment processes and control properties and quality. The work covers the study of the role of phosphorus in brass, the need to control its content during production by limiting the share of secondary use. The study revealed the possibility of a positive effect of modifying copper alloys with phosphorus in order to improve performance properties, as well as the prospects of using phosphorus as a safe replacement for lead in brass. The authors assessed the content and distribution of phosphorus impurity at a concentration of 0.005 % in a brass sample of the CuZn₃₂Mn₃Al₂FeNi grade, studied the nature of its interaction with other components of the alloy and the changes occurring at different temperatures of heat treatment. It has been found that phosphorus actively participates in diffusion processes and forms phosphides in both defective and defect-free blanks. When heated to the hot deformation temperature range, phosphorus redistribution occurs, phosphide locally dissolves, and metastable inclusions form. Due to differences in the concentration of elements in areas adjacent to the phosphide, the brass structure changes leading to the formation of areas different from the matrix β -phase. Manganese phosphide in brass can improve its mechanical properties and cutting ability, but an excess of this compound can lead to problems with strength, crack resistance, and moulding.

Keywords: duplex and multicomponent brasses; phosphorus distribution analysis; silicides; phosphorus; compounds with phosphorus; shape and size of inclusions; effect of heating on microstructure; phosphorus redistribution; manganese phosphide; diffusion processes; metastable inclusions.

Acknowledgments: The paper was written on the reports of the participants of the XI International School of Physical Materials Science (SPM-2023), Togliatti, September 11–15, 2023.

For citation: Gnusina A.M., Svyatkin A.V. The influence of phosphorus microalloying on the structure formation of CuZn₃₂Mn₃Al₂FeNi multicomponent brass. *Frontier Materials & Technologies*, 2024, no. 3, pp. 31–40. DOI: 10.18323/2782-4039-2024-3-69-3.

INTRODUCTION

Multicomponent brasses have many promising functional properties, due to which they remain essential materials in the automotive industry and other industries. Despite the long history of research into this engineering material, not all the relationships between structure and properties during technological processing have been fully studied up to date.

There are technological difficulties in the production of semi-finished products and the manufacture of products made of brass caused by its tendency to crack within certain temperature ranges [1]. The state diagrams of multicomponent systems presented in the form of isothermal sections focus on the main components, while not taking into account the redistribution of elements that form reinforcing inclusions – silicides, which are also often complex compounds [2]. Depending on the chemical composition, processing and production conditions, intermetallic compounds in brasses acquire different forms. For example, the pre-

sence of manganous phosphides leads to the formation of columnar or lamellar inclusions, and silicon forms intermetallic compounds with manganese that undergo complex shape changes during the nucleation and growth [3]. Depending on the element for alloying brass, one or another shape of inclusions will predominate in the alloy, but intermetallics that differ in geometry from the predominant one will also occur. Moreover, the shape of intermetallic compounds can be modified as a result of mechanical and thermal treatment [4]. Today, metallurgical enterprises use as a source material both pure ores and components, and recycled materials, obtained during their own production. Even if slag is processed, only manual selection of coarse-grained beads of copper, brass, bronze and alloying element is usually carried out, or screening by size is used with subsequent return of the metal part to the metallurgical process. Phosphorus gets into the alloy as a result of secondary use.

Phosphorus and its compounds may be present in brass as an impurity, but its content should usually be small, no more than 0.25–0.3 % by weight. This is associated with the fact that a high phosphorus content can negatively affect the properties of brass. In particular, a high phosphorus content can lead to the following problems:

1) the electrical conductivity of the material decreases: the presence of only 0.04 % of phosphorus reduces the conductivity of pure copper to 80 % (compared to 100 % for copper without phosphorus) [5];

2) brass becomes more brittle and prone to cracking under bending or fracture [1];

3) the presence of phosphorus can lead to undesirable hardening of brass, which can reduce its ability to deform without destruction [6].

Because of these negative effects, high phosphorus content in brass is limited in production.

On the other hand, phosphorus is actively used in the smelting of copper and copper-based alloys. Phosphorus deoxidised copper exhibits higher plastic properties than pure copper, which is explained by the influence of residual phosphorus [5]. Phosphorus is introduced into alloyed brass to reduce the growth rate of the Cu_5Zn_8 compound (γ -phase): the phase is formed more uniformly throughout the volume, which helps improving the mechanical properties of brasses and increasing corrosion resistance [7–9]. In the literature, there are data on the industrial modification of copper alloys with phosphorus [10; 11]; however, the technology used today poses a significant danger to the environment. Theoretically, other methods of modifying brass with phosphorus are also possible, but to perform this operation, the structures of crystal lattice of copper phosphide and silicides must be identical, according to the principles of structural and dimensional correspondence [12].

There are sources that demonstrate the use of phosphorus to replace lead [1]. Adding lead to brass alloys improves the tightness and cutting machinability of the material [13]. However, due to the health hazards associated with lead, stricter regulations on lead content in brass products have been introduced. Frequent use of lead-covered brass in plumbing fixtures could result in toxic lead particles being released into drinking water. An alternative is the more environmentally friendly lead-free brass, which does not contain toxic lead impurities that could leach into drinking water. Moreover, brasses with phosphorus have significantly higher corrosion resistance compared to leaded brass [14].

From the analysis of literary sources, it follows that information on the phosphorus distribution in multicomponent brass is incomplete, and there is no data on the behavior of phosphorus and its compounds, when heated in the hot deformation temperature range. One can assume that the phosphorus redistribution may negatively affect the technological properties of brass.

The aim of this work is to determine the role of phosphorus in the processes of structure formation of multicomponent CuZn32Mn3Al2FeNi brass.

METHODS

The object of study in this work is brass of the CuZn32Mn3Al2FeNi grade (hereinafter referred to as CuZn32Mn3Al2FeNi), in which the matrix is the β -phase, and the reinforcing component is silicide inclusions in the form of a dispersed phase. The role of phosphorus microadditives in structure formation was the subject of the study.

The main methodological approach was a comparative analysis of brass samples in the initial state (a pipe pressed at a temperature of 780 °C with stress-relieving annealing at 500 °C, 1 h), and samples after heating simulating a typical [15] technological process – heating for stamping at 780 °C for 12 min.

Primary studies were conducted by the method of structural analysis of samples in the initial state using an Olympus-GX51 optical microscope (Japan), equipped with a SIAMS 800 microstructure analyser (Russia). The surface was etched to reveal the alloy microstructure. A 1:1 solution of glacial acetic and nitric acid was used as an etchant. The chemical composition was determined using an OBLF QSG 750-II optical emission spectrometer (Germany). A Wilkers microhardness tester mod. 536 from Karl Frank (USA), with a load of HV30, was used to measure hardness using the Vickers method in accordance with GOST R ISO 6507-1. The hardness values were obtained as the arithmetic mean of five repeated measurements of the sample.

Further studies were conducted using a Zeiss scanning electron microscope (Germany) with Bruker software. Additionally, a comparative analysis of changes in the chemical composition of silicides and phosphosilicides upon heating was performed. 350 silicides were analysed after heating to temperatures of 700, 750, 800, and 830 °C.

The paper presents micrographs, obtained using the mapping function, which provide a concept of the chemical composition distribution over the volume of the rod-shaped inclusion in the state after heating. To increase conductivity, gold treatment was performed on a single-target magnetron sputtering device SBC900 (China), using a gold-platinum target in a ratio of 70:30.

X-ray spectral analysis was performed on an EVO18 scanning electron microscope with an EDX detector from Bruker (Germany). The chemical composition of the solid solution and intermetallic compounds of various shapes was determined, the data were processed and summarised in a table.

RESULTS

Table 1 presents the results of chemical analysis of the CuZn32Mn3Al2FeNi alloy. Fig. 1 shows the microstructure of the as-delivered (original) etched samples. The hardness value of the original sample was 184–189 HV. The microstructure consists mainly of grains of β -phase and rounded intermetallic compounds 0.5–4 μm in size (Fig. 2, 3). Rod-shaped inclusions (Fig. 3) up to 30 \times 4 μm in size were detected, single rod-shaped inclusions can reach 70 μm in length. Secondary crystals were identified on the rod-shaped

inclusions (Fig. 4). The formation and growth of secondary crystals is caused by a higher level of stress in the inclusion compared to the matrix solution. The hardness of the samples after heating changed insignificantly, within 1–2 HV, which does not exceed the measurement error.

As a result of X-ray spectral analysis, the chemical composition of the phases was determined (Tables 2, 3). Phosphorus was identified in rod-shaped compounds (up to 25 %), and in smaller quantities in individual rounded silicides (up to 3 % of the inclusion weight). Phosphorus was not detected in the solid solution, or at the grain boundaries.

Thus, phosphorus in the multicomponent CuZn32Mn3Al2FeNi alloy is bound completely into compounds. The elemental composition of the rods corresponds to a compound of the (Mn,Fe)₂P type with a Si admixture. In finely dispersed rounded silicides, phosphorus apparently replaces silicon in Me₃Si compounds. The maximum phosphorus concentration is identified in the central part of the inclusion.

The electron microscopic image with colour indication of chemical elements (Fig. 4) shows a rod-shaped intermetallic compound, which is a manganese-iron phosphosilicide with secondary crystals of manganese silicide. Secondary crystals on the rod consist mainly of iron (Fig. 4 a) and silicon (Fig. 4 b). The intermetallic compound is highlighted in green due to the high content of manganese and phosphorus. The inclusion is a compound of manganese and iron with phosphorus and silicon. The

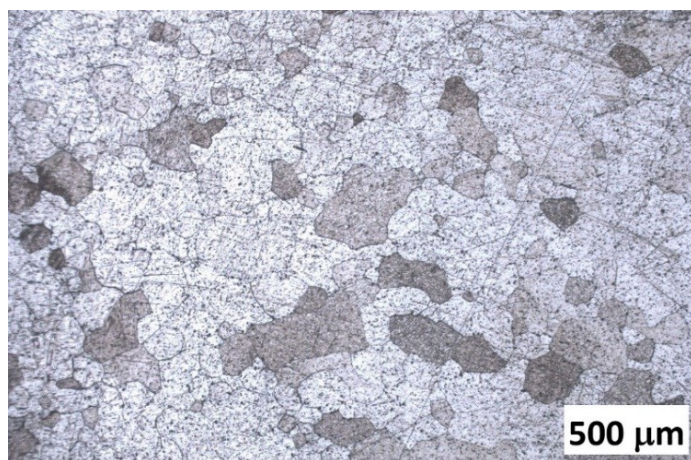
linear scanning method showed that phosphorus interacts mainly with manganese (Fig. 5), their concentration lines completely coincide. The growth of secondary crystals occurs due to iron and silicon.

After heating to hot deformation temperatures, the phosphides are transformed (Fig. 6), due to partial dissolution of the inclusions. In this case, regular-shaped precipitates with an increased phosphorus concentration are identified in the matrix solution (Fig. 7). Probably, such formations take place in areas adjacent to silicides. Linear scanning of these sections showed that after heating to 780 °C, a redistribution of aluminium and phosphorus occurs: the maximum aluminium and phosphorus concentrations coincide, and are shifted relative to the maximum of silicon by 1...2 µm. Thus, phosphorus, along with aluminium, contributes to dispersion strengthening in the CuZn32Mn3Al2FeNi brass. Due to the low phosphorus concentration in the samples, the degree of strengthening was not studied.

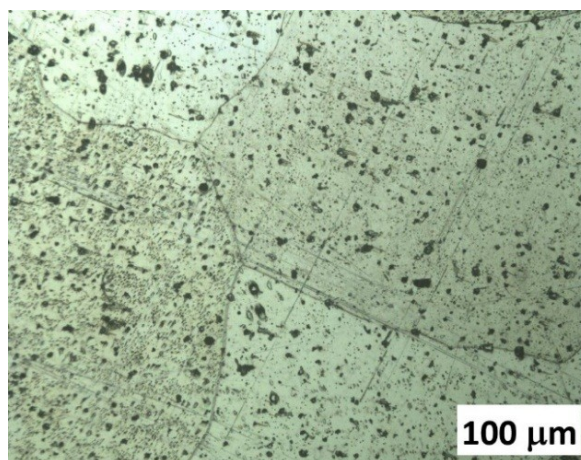
Fig. 6 shows a phosphosilicide after heating at 780 °C. Local dissolution of the intermetallic compound is detected. Moreover, a darkened area and structure distortion around the inclusion are revealed. Differences in the concentration of elements lead to areas with different chemical compositions in the areas adjacent to the phosphide (Table 4). Table 4 shows that when heated in the hot deformation range, the main elements are redistributed with the components passing into the solid solution of the matrix.

Table 1. Chemical composition of the CuZn32Mn3Al2FeNi brass alloy
Таблица 1. Химический состав сплава ЛМцАЖН 59-3,5-2,3-0,5-0,3

Concentration of elements, wt. %										
Cu	Mn	Al	Fe	Ni	Zn	Si	Pb	Cr	Sn	P
53.660	3.403	2.438	0.575	0.520	39.220	0.033	0.116	0.004	0.012	0.005



a



b

Fig. 1. Microstructure of the CuZn32Mn3Al2FeNi alloy at magnification of: *a* – 100 times; *b* – 200 times
Рис. 1. Микроструктура сплава ЛМцАЖН 59-3,5-2,3-0,5-0,3 при увеличении: *a* – в 100 раз; *b* – в 200 раз

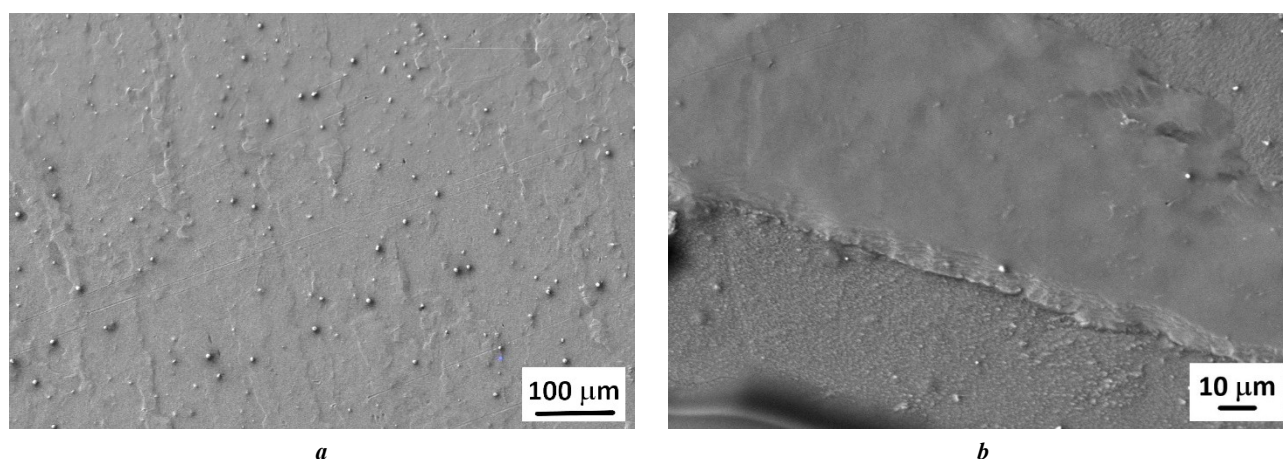


Fig. 2. Electron micrograph of the structure of the CuZn32Mn3Al2FeNi alloy at magnification of:
a – 400 times; *b* – 1640 times

Рис. 2. Электронно-микроскопический снимок структуры сплава ЛМцАЖН 59-3,5-2,3-0,5-0,3 при увеличении: *a* – в 400 раз; *b* – в 1640 раз

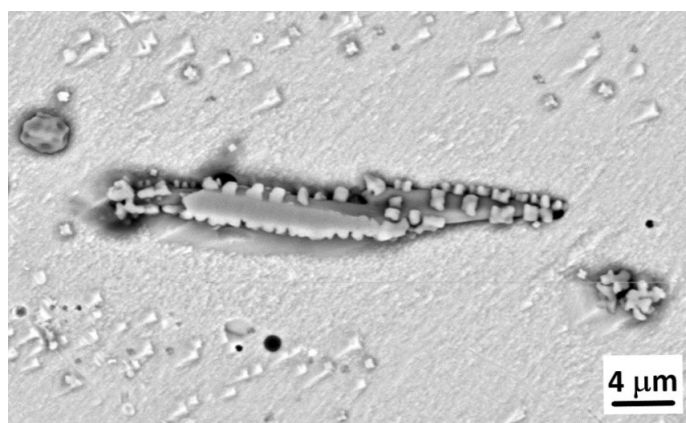


Fig. 3. Electron micrograph of a rod-shaped inclusion with secondary crystal precipitations

Рис. 3. Электронно-микроскопический снимок стержневидного включения с выделением вторичных кристаллов

Table 2. Chemical composition of the solid solution (β -phase)
Таблица 2. Химический состав твердого раствора (β -фазы)

Concentration of elements, wt. %					
Cu	Mn	Al	Fe	Ni	Zn
57.293	3.521	2.301	0.910	0.524	35.461

Comparison of the influence of heating temperature on the chemical composition of silicides and phosphosilicides showed that in the hot deformation range of 700...830 °C typical for industrial production, phosphosilicides remain more thermally stable, while silicides have a pronounced Mn/Si ratio maximum at 750 °C and a minimum – at 800 °C (Fig. 8).

DISCUSSION

Currently, the influence of phosphorus on the properties of multicomponent brasses is poorly reflected in domestic and foreign literature. The increased applicability of brasses with phosphorus is associated with the growing attention in the “global West” countries to environmental aspects [1; 14].

Table 3. Chemical composition of intermetallic inclusions
Таблица 3. Химический состав интерметаллидных включений

Type	Concentration of elements, wt. %						
	Al	Mn	Fe	Cr	Ni	Si	P
Rod-shaped inclusion (Mn,Fe) ₂ P	3.22	32.58	31.57	2.72	1.17	4.47	24.27
Plate (Mn,Fe) ₂ P	1.18	32.09	46.31	2.94	0.41	4.48	12.59
Round silicide	8.43	13.53	57.40	1.58	1.42	17.64	–
Round silicide with phosphorus	5.24	17.46	62.24	1.57	–	10.54	2.94

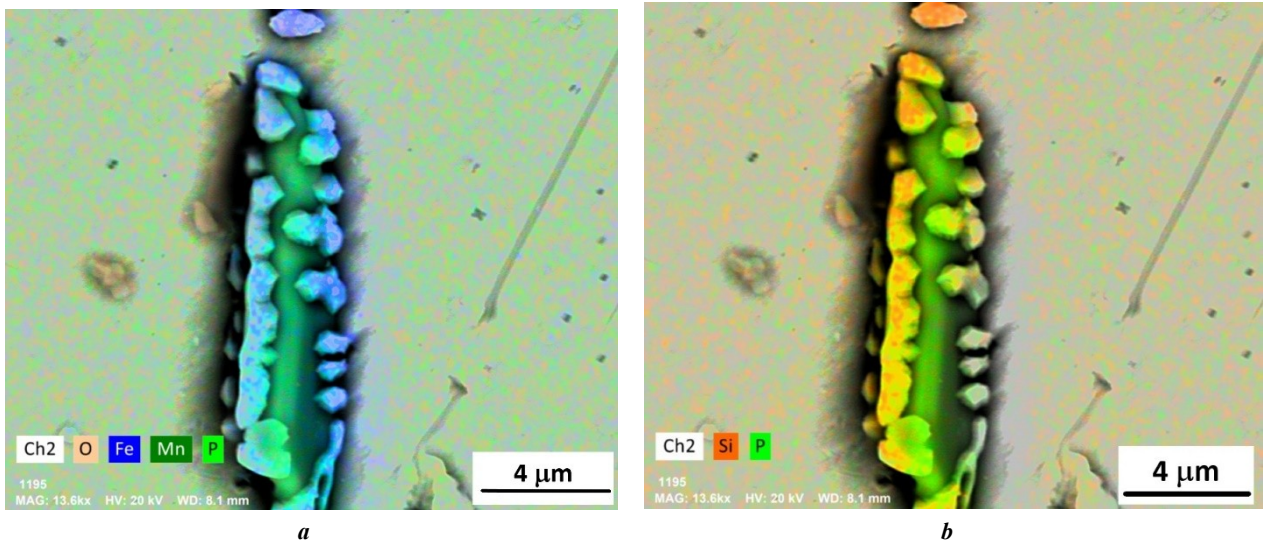


Fig. 4. Electron micrograph of an inclusion with color highlighting of chemical elements:
a – oxygen, iron, manganese and phosphorus; **b** – silicon and phosphorus

Рис. 4. Электронно-микроскопический снимок включения с цветовым выделением химических элементов:
a – кислорода, железа, марганца и фосфора; **b** – кремния и фосфора

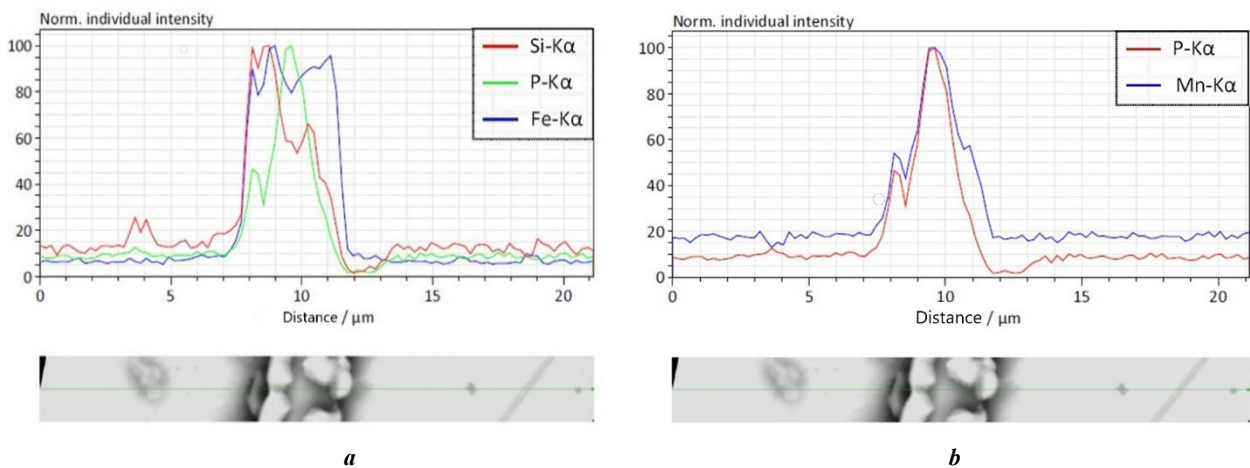
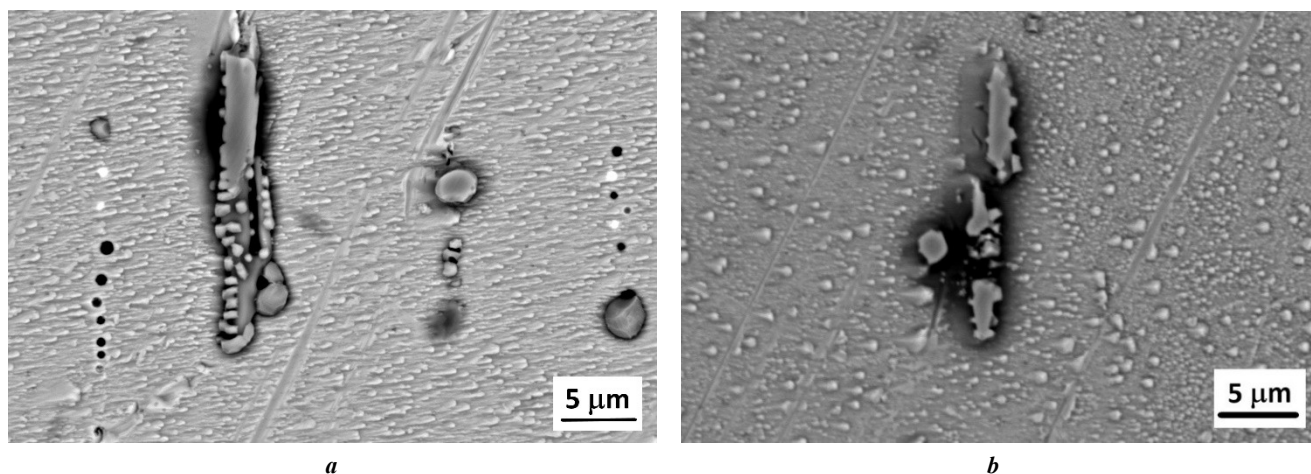


Fig. 5. Linear scanning of solid solution and silicide for chemical element content:
a – silicon, phosphorus and iron; **b** – phosphorus and manganese

Рис. 5. Линейное сканирование твердого раствора и силицида на содержание химических элементов:
a – кремния, фосфора и железа; **b** – фосфора и марганца



a

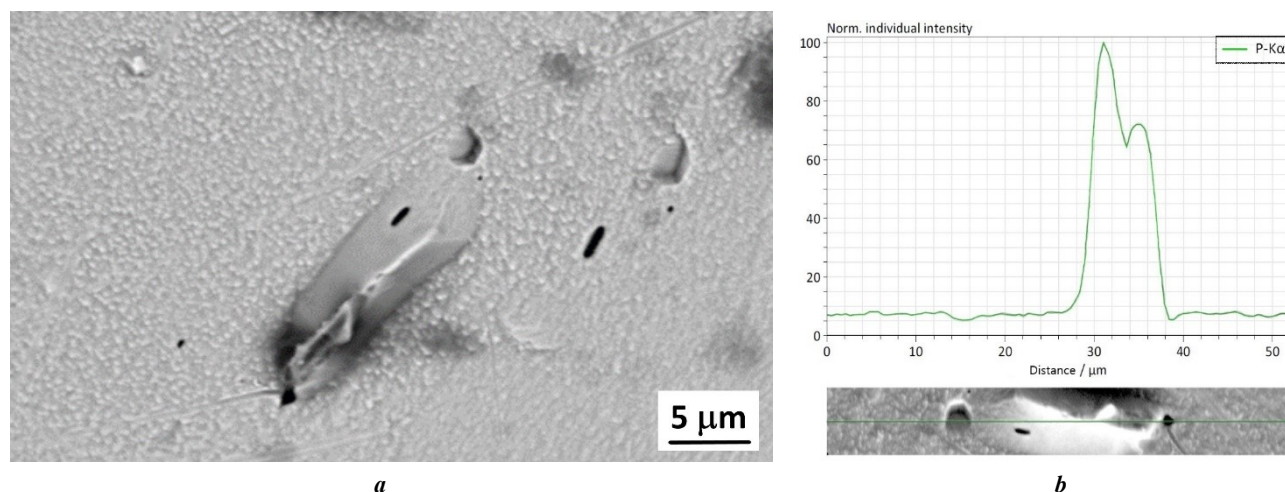
b

Fig. 6. Electron micrograph of an intermetallic inclusion:

a – initial state (after pressing and annealing); *b* – stamped sample after heating at 780 °C

Рис. 6. Электронно-микроскопический снимок интерметаллидного включения:

a – исходное состояние (после прессования и отжига); *b* – отштампованный образец после нагрева при 780 °C



a

b

Fig. 7. Metastable precipitation with increased phosphorus concentration:

a – electron micrograph; *b* – linear scanning

Рис. 7. Метастабильное выделение с повышенной концентрацией фосфора:

a – электронно-микроскопический снимок; *b* – линейное сканирование

Table 4. Local chemical composition of the solid solution after heating at 780 °C

Таблица 4. Локальный химический состав твердого раствора после нагрева при 780 °C

Location	Concentration of elements, wt. %								
	Al	Si	Mn	Cu	Zn	Fe	Ni	P	Cr
The area adjacent to the phosphide	1.38	1.11	10.54	43.80	27.78	9.70	0.63	4.80	0.73
Solid solution, β-phase	2.47	0.18	3.34	57.72	35.41	0.32	0.47	–	–

The effect of phosphorus on creep and embrittlement of grain boundaries of copper alloys was studied [16–18]. It was shown that phosphorus segregations cannot be the cause of embrittlement and can increase the ductility of polycrystalline copper [17; 18].

Phosphorus in multicomponent brasses actively participates in diffusion processes and forms large rod-shaped phosphosilicides together with manganese, iron and silicon. This work shows that the sizes of such inclusions are many times greater than the sizes of silicides. The formation of iron–manganese phosphosilicides was also noted in [19]. The fact of inclusion growth can be explained by the higher temperature of the formation of manganese phosphides compared to silicides. The authors investigated similar rod-shaped inclusions of the $Me_2(Si,P)$ type before heating for stamping and after heating [19]. It was found that the chemical composition of inclusions of blanks prone to cracking changes upon heating, and inclusions of blanks without cracking are thermally stable. Thus, an increase in the thermal stability of inclusions in the hot deformation range, contributes to an increase in crack resistance.

The ability of iron and phosphorus to form Fe_3P and Fe_2P compounds in two-phase brass is also shown in [10]. It was also considered there, that for copper and iron crystals with a Fe content of more than about 0.3 % by weight, partial decomposition can occur upon quenching from high temperatures, depending on the quenching temperature and cooling rate; lower phosphorus concentrations have not been studied. The authors of [10] note that contamination with iron and phosphorus greatly affects the behaviour of brass semi-finished products during production, since recrystallisation of the metal is difficult, especially in the combined presence of both elements. It is also indicated that α -brass and iron can exist in the form of equilibrium phases. In [20], it was found that such inclusions are γ -Fe. Moreover, depending on the heating temperature and duration, the α -brass matrix contains different amounts of iron. It is shown that suitable heat treatment can increase the amount of these deposits, and that heat treatment, at a temperature of 650 °C is optimal for obtaining the greatest amount of γ -Fe. However, the behaviour of iron in β -brass in the presence of silicon and phosphorus has not been studied. However, based on the results of [10; 19; 21], the presence of silicon and phosphorus inevitably binds iron into silicides and phosphides. Enlargement of inclusions, on the one hand, can promote their chipping during mechanical processing, on the other hand, it can increase wear resistance. The authors note congruent behaviour of manganese and phosphorus concentration lines during scanning of phosphosilicides and phosphorus, and aluminium during scanning of metastable inclusions. To understand how an increase in phosphorus concentration will affect the structure formation of multicomponent brasses, it will be necessary to conduct additional studies, with an increased phosphorus concentration. For this purpose, it is necessary to create a set of experimental brass samples with phosphorus in different concentrations.

The influence of phosphorus on hardness is difficult to estimate due to its low concentration, since other factors that can affect hardness are also active after heating. However, one can assume that an increase in the concentration

of phosphorus, not bound in manganese phosphosilicides, will lead to an increase in hardness and an acceleration of the ageing process due to the formation of additional crystallisation centres.

When heated to the temperature of hot deformation of the material, the phosphidosilicide partially dissolves, and the components of the intermetallic compound pass into the matrix, but the change in the chemical composition of phosphosilicides is not as intense as that of silicides. The process is studied in more detail in [21]. It is noted that in the range of hot deformation of multicomponent brasses, phosphosilicides are more thermally stable.

Since the studies were conducted on samples with a low phosphorus concentration, at the microalloying level, it is difficult to trace the effect of the obtained patterns of phosphorus behaviour in brass. It is advisable to study the effect at different concentrations. Additional studies are required, since it is necessary to estimate the solubility of intermetallic compounds with phosphorus in multicomponent brasses.

CONCLUSIONS

It has been found that a significant portion of phosphorus in the multicomponent CuZn32Mn3Al2FeNi brass in low concentration (up to 0.005 % wt.) is bound in manganese phosphosilicides.

When combined with manganese and iron, phosphorus forms rod-shaped inclusions. When scanning, the concentration lines of manganese and phosphorus coincide. Secondary crystals in these compounds consist mainly of iron and silicon.

When heated to the hot deformation temperature, phosphorus is redistributed, the intermetallic compound dissolves, and metastable inclusions are formed, while phosphorus is redistributed together with aluminium.

Phosphosilicides in the range of hot deformation of brasses are more thermally stable than silicides.

REFERENCES

1. Stavroulakis P., Toulfatzis A.I., Pantazopoulos G.A., Paipetis A.S. Machinable Leaded and Eco-Friendly Brass Alloys for High Performance Manufacturing Processes: A Critical Review. *Metals*, 2022, vol. 12, no. 2, article number 246. DOI: [10.3390/met12020246](https://doi.org/10.3390/met12020246).
2. Wang Jiong, Xua Honghui, Shang Shunli, Zhang Lijun, Du Yong, Zhang Wenqing, Liu Shuhong, Wang Peisheng, Liu Zi-Kui. Experimental investigation and thermodynamic modeling of the Cu–Si–Zn system with the refined description for the Cu–Zn system. *Calphad*, 2011, vol. 35, no. 35, pp. 191–203. DOI: [10.1016/j.calphad.2011.02.001](https://doi.org/10.1016/j.calphad.2011.02.001).
3. Bie Lifu, Chen Xiaohong, Liu Ping, Zhang Tao, Xu Xiangliu. Morphology Evolution of Mn_5Si_3 Phase and Effect of Mn content on Wear Resistance of Special Brass. *Metals and Materials International*, 2019, vol. 26, pp. 431–443. DOI: [10.1007/s12540-019-00243-0](https://doi.org/10.1007/s12540-019-00243-0).
4. Porter D.A., Easterling K.E., Sherif M.Y. *Phase transformations in metals and alloys*. London, Taylor & Francis Group Publ., 2009. 538 p.

5. Chen Nannan, Wang Hongliang, Veeresh P. et al. Achieving brittle-intermetallic-free and high-conductivity aluminum/copper joints using nickel-phosphorus coatings. *Materials & Design*, 2021, vol. 199, article number 109435. DOI: [10.1016/j.matdes.2020.109435](https://doi.org/10.1016/j.matdes.2020.109435).
6. Gholami M.D., Hashemi R., Davoodi B. Investigation of microstructure evolution on the fracture toughness behaviour of Brass/Low Carbon Steel/Brass clad sheets fabricated by Cold Roll Bonding process. *Journal of Materials Research and Technology*, 2023, vol. 25, pp. 2570–2588. DOI: [10.1016/j.jmrt.2023.06.103](https://doi.org/10.1016/j.jmrt.2023.06.103).
7. Galai M., Benqlilou H., Ebntouhami M., Nassali H., Belhaj T., Berrami Kh., Mansouri I., Ouaki B. Effect of phosphorus content of α brass on its corrosion resistance in aggression soil: experimental and characterization studies. *Euro-Mediterranean Journal for Environmental Integration*, 2021, vol. 6, article number 41. DOI: [10.1007/s41207-021-00244-9](https://doi.org/10.1007/s41207-021-00244-9).
8. Alistratov V.N., Chigarev V.V., Ilenko V.V. Development of a powder tape composition intended for surfacing bronze operating under electrical erosion wear conditions. *Vestnik Priazovskogo gosudarstvennogo tekhnicheskogo universiteta. Seriya: Tekhnicheskije nauki*, 2003, no. 13, pp. 1–4.
9. Kozaderov O.A., Taranov D.M., Krivoshlykov A.N., Borodkina S.V. Kinetics of Phase Transformations during Selective Dissolution of Cu₅Zn₈. *Condensed Matter and Interphases*, 2020, vol. 22, no. 3, pp. 344–352. DOI: [10.17308/kcmf.2020.22/2965](https://doi.org/10.17308/kcmf.2020.22/2965).
10. Dürschnabel W. Eisen und Phosphor in CuZn₃₆: I. Die Löslichkeit von Eisen und Phosphor in CuZn₃₆. *International Journal of Materials Research*, 1968, vol. 59, no. 12, pp. 887–894. DOI: [10.1515/ijmr-1968-591201](https://doi.org/10.1515/ijmr-1968-591201).
11. Shechepochkina Yu.A. *Latun* [Brass], patent RF no. 2625853, 2017. 3 p.
12. Stetsenko V.Yu. On modifying of hypereutectic silumins. *Lite i metallurgiya*, 2008, no. 1, pp. 151–154. EDN: [WAMPTB](https://www.edn.ru/wamptb/).
13. Adineh M., Doostmohammadi H., Raiszadeh R. Effect of Si and Al on the Microstructure, Mechanical Properties and Machinability of 65Cu–35Zn Brass. *Iranian Journal of Materials Science & Engineering*, 2019, vol. 16, no. 2, pp. 21–32. DOI: [10.22068/IJMSE.16.2.21](https://doi.org/10.22068/IJMSE.16.2.21).
14. Huang Hui-zhen, Lu De, Shuai Ge-wang, Wei Xiu-qin. Effects of Phosphorus Addition on the Corrosion Resistance of Sn–0.7Cu Lead-Free Solder Alloy. *Transactions of the Indian Institute of Metals*, 2016, vol. 69, pp. 1537–1543. DOI: [10.1007/s12666-015-0727-1](https://doi.org/10.1007/s12666-015-0727-1).
15. Svyatkin A.V. The influence of heating temperature for forging on the cracking tendency of a Cu-Mn-Al-Fe-Ni 59-3.5-2.5-0.5-0.4 workpiece. *Science Vector of Togliatti State University*, 2018, no. 3, pp. 48–56. DOI: [10.18323/2073-5073-2018-3-48-56](https://doi.org/10.18323/2073-5073-2018-3-48-56).
16. Sandström R. *The role of phosphorus for mechanical properties in copper: technical reports*. Stralsäkerhetsmyndigheten, 2014. 23 p.
17. Yunguo Li, Korzhavyi P.A., Sandström R., Lilja C. Impurity effects on the grain boundary cohesion in copper. *Physical Review Materials*, 2017, vol. 1, no. 7, article number 070602(R). DOI: [10.1103/PhysRevMaterials.1.070602](https://doi.org/10.1103/PhysRevMaterials.1.070602).
18. Sandström R., Lousada C. The role of binding energies for phosphorus and sulphur at grain boundaries in copper. *Journal of Nuclear Materials*, 2020, vol. 544, article number 152682. DOI: [10.1016/j.jnucmat.2020.152682](https://doi.org/10.1016/j.jnucmat.2020.152682).
19. Svyatkin A.V., Vyboyschik M.A., Gnusina A.M. Effect of metastable compounds on susceptibility to cracking of multicomponent brasses. *Deformatsiya i razrushenie materialov*, 2024, no. 4, pp. 32–40. EDN: [OGLZJL](https://www.edn.ru/oglzjl/).
20. Kamali-M S., Häggström L., Ericsson T., Wappling R. Metallurgical behavior of iron in brass studied using Mössbauer spectroscopy. *Hyperfine Interact*, 2006, vol. 168, pp. 995–999. DOI: [10.1007/s10751-006-9386-2](https://doi.org/10.1007/s10751-006-9386-2).
21. Svyatkin A.V., Gnusina A.M., Gryzunova N.N. On the effect of heating of two-phase alloyed brasses on morphological peculiarities of intermetallic inclusions. *Physics of Metals and Metallography*, 2024, vol. 125, no. 6, pp. 594–602.

СПИСОК ЛИТЕРАТУРЫ

1. Stavroulakis P., Toulfatzis A.I., Pantazopoulos G.A., Paipetis A.S. Machinable Leaded and Eco-Friendly Brass Alloys for High Performance Manufacturing Processes: A Critical Review // *Metals*. 2022. Vol. 12. № 2. Article number 246. DOI: [10.3390/met12020246](https://doi.org/10.3390/met12020246).
2. Wang Jiong, Xua Honghui, Shang Shunli, Zhang Lijun, Du Yong, Zhang Wenqing, Liu Shuhong, Wang Peisheng, Liu Zi-Kui. Experimental investigation and thermodynamic modeling of the Cu–Si–Zn system with the refined description for the Cu–Zn system // *Calphad*. 2011. Vol. 35. № 35. P. 191–203. DOI: [10.1016/j.calphad.2011.02.001](https://doi.org/10.1016/j.calphad.2011.02.001).
3. Bie Lifu, Chen Xiaohong, Liu Ping, Zhang Tao, Xu Xiangliu. Morphology Evolution of Mn₅Si₃ Phase and Effect of Mn content on Wear Resistance of Special Brass // *Metals and Materials International*. 2019. Vol. 26. P. 431–443. DOI: [10.1007/s12540-019-00243-0](https://doi.org/10.1007/s12540-019-00243-0).
4. Porter D.A., Easterling K.E., Sherif M.Y. *Phase transformations in metals and alloys*. London: Taylor & Francis Group, 2009. 538 p.
5. Chen Nannan, Wang Hongliang, Veeresh P. et al. Achieving brittle-intermetallic-free and high-conductivity aluminum/copper joints using nickel-phosphorus coatings // *Materials & Design*. 2021. Vol. 199. Article number 109435. DOI: [10.1016/j.matdes.2020.109435](https://doi.org/10.1016/j.matdes.2020.109435).
6. Gholami M.D., Hashemi R., Davoodi B. Investigation of microstructure evolution on the fracture toughness behaviour of Brass/Low Carbon Steel/Brass clad sheets fabricated by Cold Roll Bonding process // *Journal of Materials Research and Technology*. 2023. Vol. 25. P. 2570–2588. DOI: [10.1016/j.jmrt.2023.06.103](https://doi.org/10.1016/j.jmrt.2023.06.103).
7. Galai M., Benqlilou H., Ebntouhami M., Nassali H., Belhaj T., Berrami Kh., Mansouri I., Ouaki B. Effect of phosphorus content of α brass on its corrosion resistance in aggression soil: experimental and characterization studies // *Euro-Mediterranean Journal for Environmental Integration*. 2021. Vol. 6. Article number 41. DOI: [10.1007/s41207-021-00244-9](https://doi.org/10.1007/s41207-021-00244-9).

8. Алистратов В.Н., Чигарев В.В., Ильенко В.В. Разработка состава порошковой ленты, предназначенной для наплавки бронзы, работающей в условиях электроэрозионного износа // Вестник Приазовского государственного технического университета. Серия: Технические науки. 2003. № 13. С. 1–4.
9. Козадеров О.А., Таранов Д.М., Кривошлыков А.Н., Бородин С.В. Кинетика фазовых превращений при селективном растворении интерметаллида Cu_5Zn_8 // Конденсированные среды и межфазные границы. 2020. Т. 22. № 3. С. 344–352. DOI: [10.17308/kcmf.2020.22/2965](https://doi.org/10.17308/kcmf.2020.22/2965).
10. Dürrschnabel W. Eisen und Phosphor in CuZn_{36} : I. Die Löslichkeit von Eisen und Phosphor in CuZn_{36} // International Journal of Materials Research. 1968. Vol. 59. № 12. P. 887–894. DOI: [10.1515/ijmr-1968-591201](https://doi.org/10.1515/ijmr-1968-591201).
11. Щепочкина Ю.А. Латунь: патент РФ № 2625853, 2017. 3 с.
12. Стеценко В.Ю. О модифицировании заэвтектических сулмунинов // Литье и металлургия. 2008. № 1. С. 151–154. EDN: [WAMPTB](https://doi.org/10.1515/ijmr-1968-591201).
13. Adineh M., Doostmohammadi H., Raiszadeh R. Effect of Si and Al on the Microstructure, Mechanical Properties and Machinability of 65Cu–35Zn Brass // Iranian Journal of Materials Science & Engineering. 2019. Vol. 16. № 2. P. 21–32. DOI: [10.22068/IJMSE.16.2.21](https://doi.org/10.22068/IJMSE.16.2.21).
14. Huang Hui-zhen, Lu De, Shuai Ge-wang, Wei Xiu-qin. Effects of Phosphorus Addition on the Corrosion Resistance of Sn–0.7Cu Lead-Free Solder Alloy // Transactions of the Indian Institute of Metals. 2016. Vol. 69. P. 1537–1543. DOI: [10.1007/s12666-015-0727-1](https://doi.org/10.1007/s12666-015-0727-1).
15. Святкин А.В. Влияние температуры нагрева под штамповку на склонность к растрескиванию заготовок из ЛМцАЖН 59-3,5-2,5-0,4-0,2 // Вектор науки Тольяттинского государственного университета. 2018. № 3. С. 48–56. DOI: [10.18323/2073-5073-2018-3-48-56](https://doi.org/10.18323/2073-5073-2018-3-48-56).
16. Sandström R. The role of phosphorus for mechanical properties in copper: technical reports. Stralsäkerhetsmyndigheten, 2014. 23 p.
17. Yunguo Li, Korzhavyi P.A., Sandström R., Lilja C. Impurity effects on the grain boundary cohesion in copper // Physical Review Materials. 2017. Vol. 1. № 7. Article number 070602(R). DOI: [10.1103/PhysRevMaterials.1.070602](https://doi.org/10.1103/PhysRevMaterials.1.070602).
18. Sandström R., Lousada C. The role of binding energies for phosphorus and sulphur at grain boundaries in copper // Journal of Nuclear Materials. 2020. Vol. 544. Article number 152682. DOI: [10.1016/j.jnucmat.2020.152682](https://doi.org/10.1016/j.jnucmat.2020.152682).
19. Святкин А.В., Выбойщик М.А., Гнусина А.М. Влияние метастабильных соединений на склонность к растрескиванию многокомпонентных латуней // Деформация и разрушение материалов. 2024. № 4. С. 32–40. EDN: [OGLZJL](https://doi.org/10.1515/ijmr-1968-591201).
20. Kamali-M S., Häggström L., Ericsson T., Wappling R. Metallurgical behavior of iron in brass studied using Mössbauer spectroscopy // Hyperfine Interact. 2006. Vol. 168. P. 995–999. DOI: [10.1007/s10751-006-9386-2](https://doi.org/10.1007/s10751-006-9386-2).
21. Svyatkin A.V., Gnusina A.M., Gryzunova N.N. On the effect of heating of two-phase alloyed brasses on morphological peculiarities of intermetallic inclusions // Physics of Metals and Metallography. 2024. Vol. 125. № 6. P. 594–602.

Влияние микролегирования фосфором на структурообразование многокомпонентной латуни ЛМцАЖН

© 2024

Гнусина Анастасия Михайловна^{*1}, аспирант

кафедры «Нанотехнологии, материаловедение и механика»

*Святкин Алексей Владимирович*², кандидат технических наук,

доцент кафедры «Нанотехнологии, материаловедение и механика»

*Тольяттинский государственный университет, Тольятти (Россия)**E-mail: anastasiya.gnusina@vaz.ru,
myripru@gmail.com¹ORCID: <https://orcid.org/0000-0002-8600-7566>²ORCID: <https://orcid.org/0000-0002-8121-9084>

Поступила в редакцию 26.06.2023

Принята к публикации 19.07.2024

Аннотация: Фосфор в латуни может оказывать как положительное влияние – улучшать механические свойства, повышать коррозионную стойкость и обрабатываемость, так и отрицательное – негативно сказываться на свариваемости и приводить к растрескиванию. Исследование роли фосфора в процессах структурообразования латуни имеет практическую актуальность, поскольку способствует оптимизации свойств материала, снижению возможности появления дефектов, улучшению процессов обработки и контролю свойств и качества. Работа посвящена исследованию роли фосфора в латуни, необходимости контроля его содержания при производстве путем ограничения доли вторичного использования. Выявлена возможность положительного влияния модификации медных сплавов фосфором с целью улучшения эксплуатационных свойств, а также перспектива использования фосфора в качестве безопасной замены свинца в латуни. Проведена оценка содержания и распределения примеси фосфора в концентрации 0,005 % в латунном образце марки ЛМцАЖН 59-3,5-2,3-0,5-0,3, изучены характер его взаимодействия с другими компонентами сплава и изменения, происходящие при различных температурах термической обработки. Установлено, что фосфор активно участвует в диффузионных процессах и образует фосфиды как в дефектных, так и в бездефектных заготовках. При нагреве в области температур горячей деформации происходит

перераспределение фосфора, локальное растворение фосфида и образование метастабильных включений. Из-за различий в концентрации элементов в областях, прилегающих к фосфиду, происходит изменение структуры латуни, что приводит к образованию участков, отличных от матричной β -фазы. Фосфид марганца в латуни может улучшить ее механические свойства и обрабатываемость резанием, но избыток этого соединения может привести к проблемам с прочностью, трещиностойкостью и формованием.

Ключевые слова: двойные и многокомпонентные латуни; анализ распределения фосфора; силициды; фосфор; соединения с фосфором; форма и размеры включений; влияние нагрева на микроструктуру; перераспределение фосфора; марганцевый фосфид; диффузионные процессы; метастабильные включения.

Благодарности: Статья подготовлена по материалам докладов участников XI Международной школы «Физическое материаловедение» (ШФМ-2023), Тольятти, 11–15 сентября 2023 года.

Для цитирования: Гнусина А.М., Святкин А.В. Влияние микролегирования фосфором на структурообразование многокомпонентной латуни ЛМцАЖН // Frontier Materials & Technologies. 2024. № 3. С. 31–40. DOI: 10.18323/2782-4039-2024-3-69-3.

The influence of grain size on hydrogen embrittlement of a multicomponent (FeCrNiMnCo)₉₉N₁ alloy

© 2024

Darya Yu. Gurtova^{*1}, student

Marina Yu. Panchenko^{2,3}, junior researcher

of Laboratory of Physics of Hierarchic Structures in Metals and Alloys

Evgeny V. Melnikov^{2,4}, junior researcher

of Laboratory of Physics of Hierarchic Structures in Metals and Alloys

Denis O. Astapov^{1,5}, student

Elena G. Astafurova^{2,6}, Doctor of Sciences (Physics and Mathematics),

Head of Laboratory of Physics of Hierarchic Structures in Metals and Alloys

¹Tomsk State University, Tomsk (Russia)

²Institute of Strength Physics and Materials Science of Siberian Branch of RAS, Tomsk (Russia)

*E-mail: dasha_gurtova@mail.ru

³ORCID: <https://orcid.org/0000-0003-0236-2227>

⁴ORCID: <https://orcid.org/0000-0001-8238-6055>

⁵ORCID: <https://orcid.org/0000-0002-1277-4180>

⁶ORCID: <https://orcid.org/0000-0002-1995-4205>

Received 26.06.2023

Accepted 05.02.2024

Abstract: The problem of hydrogen embrittlement remains relevant in many areas, so the FeCrNiMnCo alloy (Cantor alloy) generates increased interest among researchers as one of the materials least exposed to the negative effect of hydrogen. Nevertheless, the issue of the influence of microstructure parameters on hydrogen embrittlement of the Cantor alloy and multicomponent alloys of the FeCrNiMnCo system in general remains understudied. This work studies the influence of grain size on the susceptibility of a nitrogen-doped high-entropy Cantor alloy to hydrogen embrittlement. For this purpose, states with different grain sizes (43 ± 21 , 120 ± 57 , and 221 ± 97 μm) were formed in the (FeCrNiMnCo)₉₉N₁ alloy, using thermomechanical treatments. It is experimentally found that grain refinement leads to an increase in the strength properties of the alloy under study and promotes an increase in the resistance to the hydrogen embrittlement: in samples with the smallest grain size, the hydrogen-induced decrease in ductility is less than in samples with the largest one. A decrease in grain size causes as well a decrease in the length of the brittle zone detected on the fracture surfaces of samples after tension. This is caused by a decrease in hydrogen diffusion during the hydrogen-charging process and a decrease in the transport of hydrogen atoms with mobile dislocations during plastic deformation due to a decrease in grain size.

Keywords: hydrogen embrittlement; multicomponent alloys; high-entropy alloys; Cantor alloy; (FeCrNiMnCo)₉₉N₁; hydrogen-induced brittle zone; grain boundaries; fracture; mechanical properties.

Acknowledgements: The research was supported by the grant of the Russian Science Foundation No. 20-19-00261, <https://rscf.ru/project/20-19-00261/>.

The research was carried out on the equipment of the “Nanotech” Core Facility Centre of the Institute of Strength Physics and Materials Science of Siberian Branch of RAS (ISPMS SB RAS).

The authors thank S.V. Astafurov, PhD (Physics and Mathematics), and K.A. Reunova for their help in conducting experimental research.

The paper was written on the reports of the participants of the XI International School of Physical Materials Science (SPM-2023), Togliatti, September 11–15, 2023.

For citation: Gurtova D. Yu., Panchenko M. Yu., Melnikov E. V., Astapov D. O., Astafurova E. G. The influence of grain size on hydrogen embrittlement of a multicomponent (FeCrNiMnCo)₉₉N₁ alloy. *Frontier Materials & Technologies*, 2024, no. 3, pp. 41–51. DOI: 10.18323/2782-4039-2024-3-69-4.

INTRODUCTION

It is known that hydrogen has a negative effect on metals and alloys, leading to a deterioration in their properties and a reduction in service life. The issue of the need to create new structural materials resistant to the negative effects of hydrogen, and to find methods for reducing the tendency to hydrogen embrittlement for existing materials is acute today in many industries, including nuclear energy, the oil and gas industry, and promising and rapidly developing hydrogen energy indus-

try. Currently, structural elements used in hydrogen-containing working environments are made of stable austenitic steels as well-proven materials, that are least prone to hydrogen embrittlement among steels of various classes. However, the high-entropy FeCrNiMnCo alloy named after its discoverer B. Cantor demonstrates greater resistance to the hydrogen embrittlement effects than the above-mentioned austenitic steels under the same hydrogen-charging conditions [1; 2]. Besides, Cantor alloy has unique mechanical and physical

properties: resistance to radiation damage and corrosion, wear resistance, a combination of high ductility and strength, due to which it can be used even in extreme conditions [3; 4]. However, the alloy has a relatively low yield strength [5]. One of the most effective methods to solve this problem is considered to be doping the alloy with interstitial atoms, in particular nitrogen, to increase the strength properties of the material without significant loss of ductility [6; 7].

In addition, it has been found that alloying materials also affects their susceptibility to hydrogen embrittlement. Thus, in [8] it was found that alloying the CoCrFeNi alloy with aluminum helps to increase resistance to the hydrogen embrittlement effects, as well as an increase in strength and ductility. In the work [9], covering the study of the hydrogen embrittlement in the Cantor alloy, it is shown that adding of 0.5 at. % carbon increases the alloy susceptibility to the hydrogen negative effects. At the same time, works [10; 11] found that alloying with carbon, on the contrary, can increase the resistance of the Cantor alloy and alloys based on it to hydrogen-induced degradation of mechanical characteristics. The ambiguity of the results obtained, when studying the influence of interstitial atoms on hydrogen embrittlement of the Cantor alloy, necessitates further development of this scientific problem.

It is known that the diffusion of hydrogen is a critical parameter affecting the hydrogen embrittlement of alloys [12]. A significant aspect affecting the hydrogen diffusion is the sites of its capture (so-called traps), which usually include interstices, dislocations, grain boundaries and inter-phase boundaries, cracks, particles, etc. [13–15]. Increasing the number of traps, for example, grain boundaries, by grain refinement makes it possible to reduce the hydrogen negative impact on metals and alloys. In works [16; 17], it was found that reducing the grain size in the Cantor alloy reduces the specific concentration of hydrogen at the grain boundaries, while suppressing brittle cracking and increasing the alloy's resistance to hydrogen embrittlement. Based on this, studying the influence of grain size on hydrogen embrittlement in a multicomponent Cantor alloy doped with nitrogen atoms is of interest.

The purpose of this study is to identify the patterns of hydrogen embrittlement of the $(\text{FeCrNiMnCo})_{99}\text{N}_1$ high-entropy alloy with different grain sizes.

METHODS

A multicomponent high-entropy alloy based on Cantor alloy (HEA-N) was chosen as the object of study. Cast billets were obtained by induction melting of Cr, Ni, Fe, Co powders with the manganese nitride addition. The composition specified during melting corresponded to the stoichiometric ratio of $(\text{FeCrNiMnCo})_{99}\text{N}_1$ (19.8Fe–19.8Cr–19.8Ni–19.8Mn–19.8Co–1N, at. %).

The cast billets were subjected to heat treatment, which consisted of annealing at a temperature of 1200 °C for 2 h followed by quenching in water. After this, the billets were rolled to 80 % reduction. To obtain states with different grain sizes, the rolled bars were soaked at different temperatures, and quenched in water:

to obtain the smallest grain size (S_HEA-N) – at a temperature of 1000 °C for 1 h; medium (M_HEA-N) – at a temperature of 1100 °C for 1 h; coarse grains (C_HEA-N) – at a temperature of 1200 °C for 2 h. After all thermomechanical treatments, the samples had the chemical composition: 19.9Fe–20.1Cr–20.0Ni–19.9Mn–19.3Co–0.8N, at. %. The elemental composition of the samples (Co, Cr, Ni, Mn, and Fe) was analyzed using a LEO EVO 50 scanning electron microscope (Zeiss, Germany), with a device for energy-dispersive spectroscopy. Nitrogen concentration was determined using a LECO ONH spectrometer (LECO, USA).

Dumbbell-shaped tensile samples of $12 \times 2.6 \times 1.4 \text{ mm}^3$ in gauge section, were cut from the resulting blanks on an electric spark machine.

Electrochemical hydrogen-charging of the samples was carried out at room temperature in a 3 % aqueous NaCl solution containing 3 g/L of NH_4SCN as a recombination poison. The charging duration was 50 h at a current density of 10 mA/cm².

The intensity of hydrogen desorption from the surface of the samples was analyzed by thermal desorption spectroscopy (TDS). The samples were studied in the temperature range of 25–800 °C (heating rate is 4 °C/min), using a vacuum chamber with the simultaneous collection of thermal desorption spectra by an RGA100 quadrupole mass spectrometer (Stanford Research Systems, USA). The hydrogen concentration profile over the depth of the samples was obtained using a GD-Profilier 2 glow discharge optical emission spectrometer (Horiba, France).

The microstructure of the samples was studied using an Apreo 2 S scanning electron microscope (FEG SEM), equipped with a Velocity Super system for analyzing the structure and texture of crystalline materials, by the electron backscattered diffraction (EBSD) method. The average grain size was determined by the interseption method using electron microscopic photographs (without taking into account twin boundaries).

Uniaxial tension tests of the samples were carried out with the initial strain rates of $5 \times 10^{-4} \text{ s}^{-1}$ and $1 \times 10^{-2} \text{ s}^{-1}$ on an electromechanical machine LFM-125 (Walter+Bai AG, Switzerland), at room temperature. Mechanical tests were also carried out at a strain rate of $1 \times 10^{-2} \text{ s}^{-1}$ at low temperature (–196 °C) on an electromechanical machine Instron 1185 (Instron, USA). At least 5 samples were used to validate each condition.

RESULTS

After thermomechanical treatments according to the selected modes, three types of samples with different grain sizes were formed. All states have a single-phase (γ -fcc) structure. According to the images obtained by the EBSD method, all the studied samples are characterized by a disordered polycrystalline structure; no predominant grain orientation is observed. Moreover, the structure contains a large number of annealing twins, which may indicate a rather low energy of stacking faults in the alloy under study (Fig. 1). The average grain size of all samples received is presented in Table 1.

For all the studied samples, the TDS curves (Fig. 2) show one low-temperature peak with a maximum intensity at about 145 °C, which characterizes the desorption of diffusible hydrogen trapped in the crystal lattice or weak reversible traps: interstices, dislocations, vacancies, grain boundaries. In this case, changes in grain size have little effect on the position and intensity of the TDS peak.

According to the stress–strain diagrams (Fig. 3), grain refinement leads to an increase in the yield strength and ultimate tensile strength of the HEA-N alloy, and a slight decrease in its ductility.

The influence of hydrogen-charging of samples with different grain sizes on their mechanical characteristics, such as yield strength $\sigma_{0.2}$, ultimate tensile strength σ_{UTS} , elongation to failure δ , and hydrogen embrittlement index I_H is shown in Table 2. The I_H value characterizing the reduction in ductility caused by hydrogen, was defined as

$$I_H = \frac{\delta_0 - \delta_H}{\delta_0} \times 100\%,$$

where δ_0 and δ_H are the total elongation to failure of the samples before and after hydrogen-charging, respectively.

Electrochemical hydrogen-charging does not contribute to the occurrence of noticeable effects of solid solution strengthening by hydrogen atoms, consequently, without causing a significant change in the value of the yield strength $\sigma_{0.2}$. Hydrogen-charging leads as well to a decrease in tensile strength σ_{UTS} , and the smallest decrease is observed in S_HEA-N samples with a minimum grain size.

The hydrogen embrittlement index I_H has a maximum value in C_HEA-N samples with the largest grain size, and a significant decrease in the I_H value is observed with decreasing grain size. In S_HEA-N samples with the smallest grain size ($d=43\pm 21 \mu\text{m}$), the value of $I_H \approx 0$: a hydrogen-induced decrease in plasticity under these charging conditions, is not observed in such samples. Thus, grain structure refinement helps to increase the resistance of the studied HEA-N alloy to the hydrogen embrittlement effects.

Hydrogen-charging of samples leads to the formation of a brittle surface layer, which undergoes intense cracking during deformation (Fig. 4). The fracture behavior of the side surfaces of hydrogen-charged samples is predominantly intergranular, but single transgranular cracks are also observed in M_HEA-N and C_HEA-N samples (Fig. 4 a–c). Despite the brittle fracture behavior, a large number of slip lines are observed on the side surfaces.

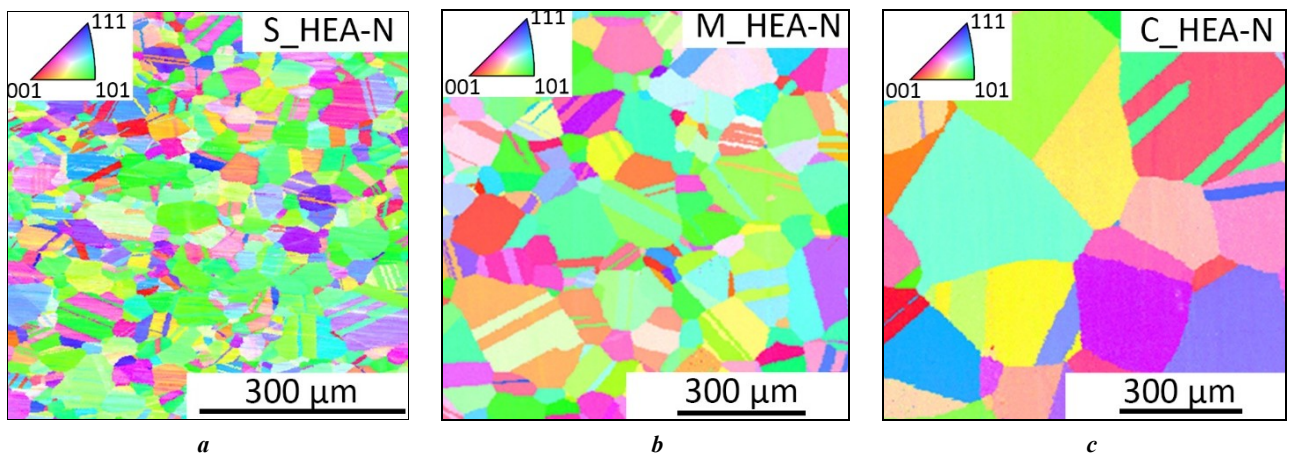


Fig. 1. EBSD image of the microstructure of samples: **a** – with the smallest grain size (S_HEA-N); **b** – with the medium grain size (M_HEA-N); **c** – with the largest grain size (C_HEA-N)

Рис. 1. ДОЭ-изображения микроструктуры образцов: **a** – с меньшим размером зерна (S_HEA-N); **b** – со средним размером зерна (M_HEA-N); **c** – с самым крупным размером зерна (C_HEA-N)

Table 1. The average size of austenitic grains in the alloy under study depending on the treatment mode
Таблица 1. Средний размер аустенитных зерен в исследуемом сплаве в зависимости от режима обработки

HEA-N	Treatment mode		
	1000 °C, 1 h	1100 °C, 1 h	1200 °C, 2 h
Average grain size d , μm	43±21	120±57	221±97
Designation	S_HEA-N	M_HEA-N	C_HEA-N
Phase composition	γ -phase		

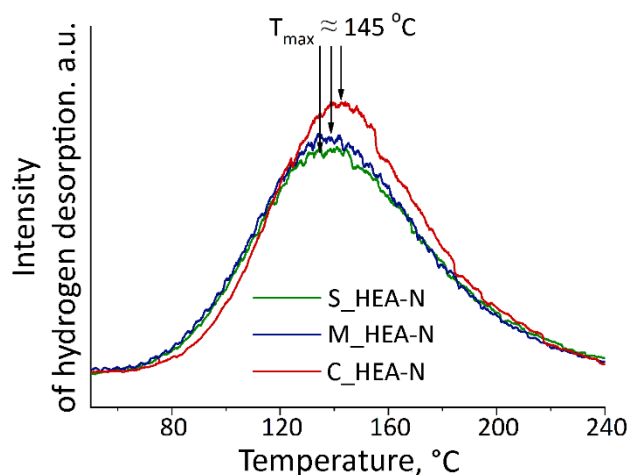


Fig. 2. TDS spectra of hydrogen desorption for the $(FeCrMnCoNi)_{99}N_1$ alloy samples with different grain sizes
Рис. 2. ТДС-спектры десорбции водорода для образцов сплава $(FeCrMnCoNi)_{99}N_1$ с разным размером зерна

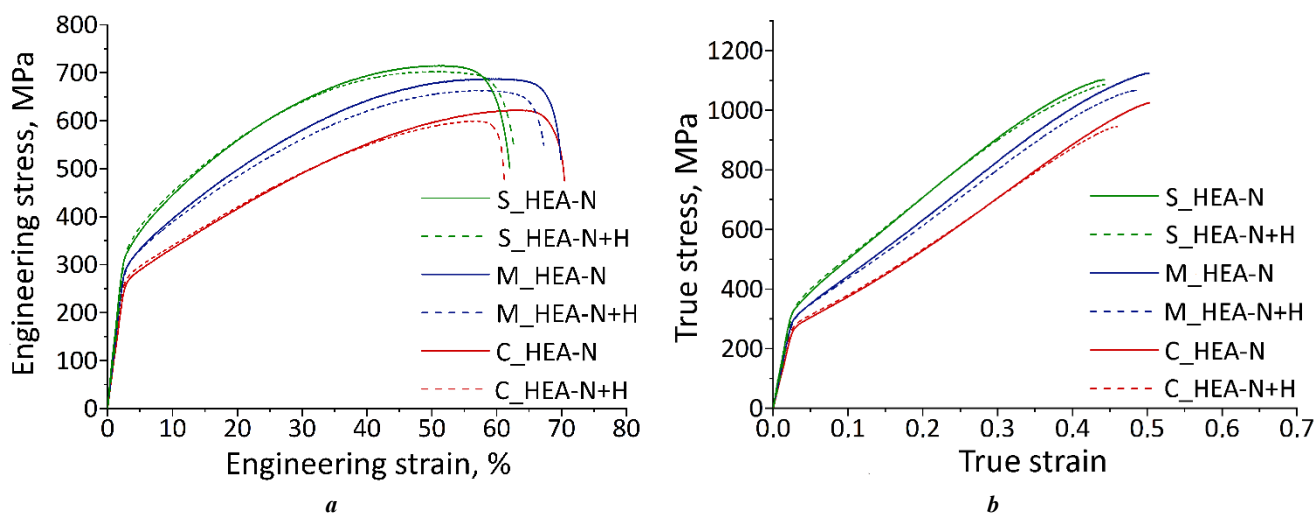


Fig. 3. Strain-stress diagrams of the samples with the smallest (S_{HEA-N}), medium (M_{HEA-N}) and the largest (C_{HEA-N}) grain size before and after hydrogen-charging (+H):
a – engineering coordinates; **b** – true coordinates

Рис. 3. Диаграммы растяжения образцов с малым (S_{HEA-N}), средним (M_{HEA-N}) и крупным (C_{HEA-N}) размером зерна до и после наводороживания (+H):
a – инженерные координаты; **b** – истинные координаты

Table 2. The influence of hydrogen-charging (+H) on the mechanical properties of a HEA-N alloy with different grain sizes
Таблица 2. Влияние насыщения водородом (+H) на механические свойства сплава ВЭС-N с разным размером зерна

Material	$\sigma_{0.2}$, MPa (± 5 MPa)	σ_{UTS} , MPa (± 10 MPa)	δ , % (± 2 %)	I_H , %
S_HEA-N	310	715	58	0
S_HEA-N+H	312	703	58	
M HEA-N	282	688	65	6
M_HEA-N+H	285	663	61	
C_HEA-N	252	622	66	14
C HEA-N+H	260	600	57	

According to SEM analysis of the fracture surfaces, the central part of the samples after hydrogen-charging fractures in a ductile transgranular regime with the formation of a dimple fracture (Fig. 4 d–f). The fracture mechanism and the length of the brittle zone in the fracture depend on the grain size of hydrogen-charged samples. The fracture behavior of the brittle zone in coarse-grained C_HEA-N samples is mixed – both transgranular and intergranular facets are observed. Reducing the grain size helps to reduce the proportion of transgranular cracks in the M_HEA-N samples and almost completely suppresses the transgranular fracture in the S_HEA-N samples.

The length of the hydrogen-induced brittle zone D after mechanical tensile tests at room temperature, does not correspond to the initial thickness of the hydrogen-assisted layer, formed immediately after electrochemical hydrogen-charging (D_0), since during plastic deformation hydrogen atoms are redistributed on mobile dislocations (ΔD_d) and due to diffusion under stress (ΔD_s).

The brittle zone in the fracture of hydrogen-charged samples is characterized by the greatest length in all samples subjected to deformation in mode I. Changing the ten-

sile mode for all samples leads to a reduction in the brittle zone length to a minimum (mode III), due to the suppression of hydrogen transport during deformation (Table 3). The same patterns can be observed for all modes of mechanical tests: the maximum length of the hydrogen-induced brittle zone is characteristic of coarse-grained C_HEA-N samples, and grain refinement leads to its reduction (Table 3).

Fig. 5 shows the hydrogen distribution profile in the structure of coarse-grained C_HEA-N samples. Comparison of data in Fig. 5 with the results given in Table 3, showed that in the case when the diffusion and dislocation transport of hydrogen is suppressed (mode III), the brittle zone length has values close to the thickness of the hydrogen-induced surface layer.

DISCUSSION

The results of the analysis of thermal desorption curves of the high-entropy alloy under study differ from those obtained in works studying hydrogen embrittlement in traditional materials with one basic component. For the cases of

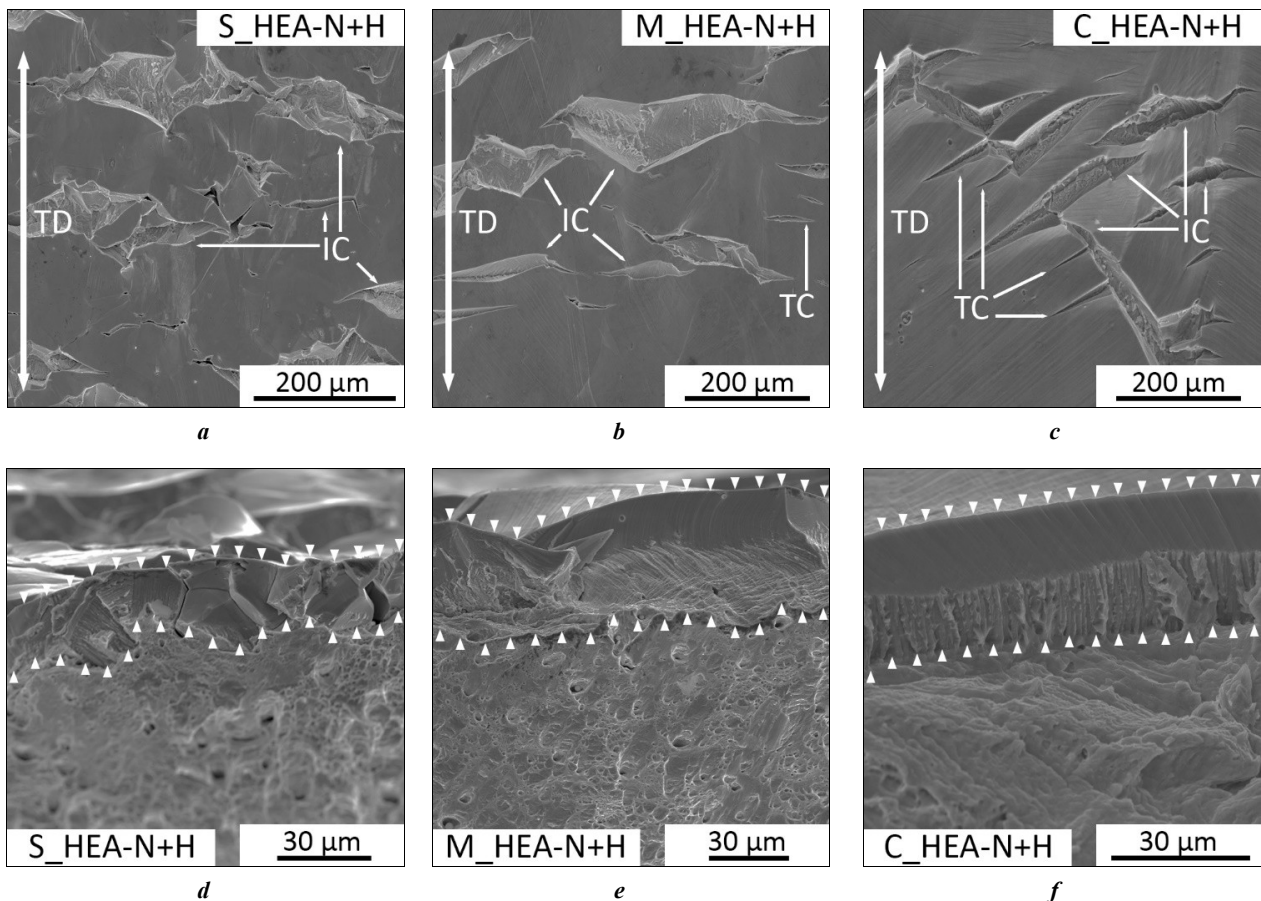


Fig. 4. SEM images of hydrogen-charged (+H) samples with the smallest (S_HEA-N), medium (M_HEA-N) and the largest (C_HEA-N) grain size after failure:

a, b, c – side surface; d, e, f – fracture surface

(TD – tension direction, IC – intergranular cracks, TC – transgranular cracks)

Рис. 4. СЭМ-изображения насыщенных водородом (+H) образцов с малым (S_HEA-N), средним (M_HEA-N) и крупным (C_HEA-N) размером зерна после растяжения:

a, b, c – боковая поверхность; d, e, f – поверхность разрушения

(TD – направление растяжения, IC – интеркристаллитные трещины, TC – транскристаллитные трещины)

Table 3. Modes of mechanical tensile tests of hydrogen-charged samples of the HEA-N alloy with the smallest (*S*_HEA-N), medium (*M*_HEA-N) and the largest (*C*_HEA-N) grain size and their influence on the length of a brittle zone in a fracture

Таблица 3. Режимы механических испытаний на растяжение насыщенных водородом образцов сплава ВЭС-N с малым (*S*_HEA-N), средним (*M*_HEA-N) и крупным (*C*_HEA-N) размером зерна и их влияние на длину хрупкой зоны в изломе

Deformation parameters and characteristics of brittle zone		Mode		
		I	II	III
Strain rate, c^{-1}		5×10^{-4}	1×10^{-2}	1×10^{-2}
Testing temperature, K		293	293	77
Hydrogen transport on dislocations		active	significantly suppressed	suppressed
Hydrogen transport due to the stress-assisted diffusion		active	active	suppressed
Brittle zone length <i>D</i> , μm	<i>S</i> _HEA-N	25 \pm 5	20 \pm 6	12 \pm 3
	<i>M</i> _HEA-N	33 \pm 7	25 \pm 8	13 \pm 5
	<i>C</i> _HEA-N	35 \pm 12	27 \pm 8	18 \pm 7

austenitic [18], ferritic [19] and martensitic [20] steels, it has been shown that a decrease in grain size leads to an increase in the content of diffusible hydrogen in the samples (in the crystal lattice or weak reversible traps). In this case, the hydrogen-charging modes of all the above materials were the same.

In [18], the smallest grain size presented was 0.58 μm , the maximum was 19 μm , while the hydrogen concentration in coarse-grained samples was 3.3 wppm (weight parts per million), which is more than two times less than in ultrafine-grained samples (7.1 wppm). For the HEA-N alloy, the decrease in grain size by ≈ 2 times for *M*_HEA-N samples ($d=120 \pm 57 \mu\text{m}$) and by ≈ 5 times for *S*_HEA-N samples ($d=43 \pm 21 \mu\text{m}$) relative to samples with the largest grain size *C*_HEA-N ($d=221 \pm 97 \mu\text{m}$) does not lead to significant differences in the thermal desorption curves: the intensity and position of the TDS peaks do not undergo significant changes. This is consistent with the data of [16],

where similar results were obtained for the equiatomic high-entropy Cantor alloy without interstitial atoms and with grain sizes from 1.5 to 22 μm , which was saturated with hydrogen from a gas atmosphere. In [16], the author concludes that in steels of different classes, grain boundaries play a significant role in the hydrogen trapping, while in the multicomponent Cantor alloy, hydrogen atoms are trapped mainly by the crystal lattice interstices.

A noticeable increase in resistance to the hydrogen embrittlement effects expressed in a decrease in the values of the hydrogen embrittlement index I_H , is observed in HEA-N samples with a small grain size. Typically, a decrease in the susceptibility to hydrogen embrittlement during grain refinement is associated with the fact that when a large number of grain boundaries are formed, the amount of absorbed hydrogen in the grains [1] and its content per unit of boundary area decreases, which reduces the stress concentration at the grain boundaries.

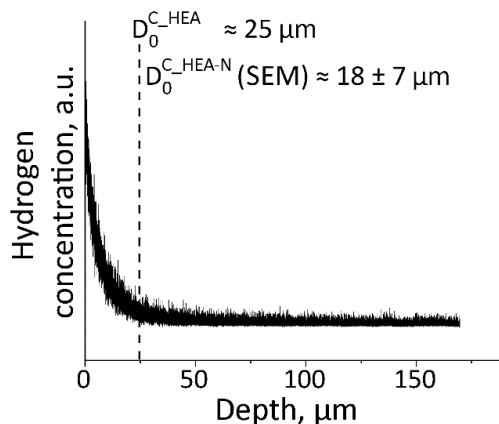


Fig. 5. Hydrogen concentration profile for the samples with the largest grain size (*C*_HEA-N)
Рис. 5. Концентрационный профиль водорода для образцов с крупным размером зерна (*C*_HEA-N)

By analyzing the data obtained experimentally, as a result of mechanical tests for uniaxial tension in various modes (Table 3), the length of the brittle zone in the fracture immediately after hydrogen-charging was assessed, as well as the contributions to the hydrogen transfer by dislocation transport and due to diffusion under stress during the deformation process. However, numerous factors influencing the brittle zone formation in the process of plastic deformation do not allow obtaining exact quantitative values for each of the contributions; therefore, this assessment method makes it possible only to qualitatively establish the patterns of the grain size influence on the hydrogen behavior in the material.

As stated earlier, the suppression of both contributions to hydrogen redistribution at cryogenic test temperatures and high strain rates makes the length of the hydrogen-induced brittle zone formed after mode III (D_{III}) of deformation closest to the length of the brittle zone immediately after electrochemical charging (without deformation) D_0 .

The length of the brittle zone in samples deformed in mode II significantly exceeds the values characteristic of samples deformed in mode III (Table 3). For low degrees of plastic deformation, when the dislocation range is limited primarily by grain boundaries and dislocation transport of hydrogen can be realized over long distances, dislocation densities of the order of 10^{12} $1/m^2$ are typical. With such a dislocation density and strain rate of $SR=10^{-2}$ $1/s$, the rate of dislocation movement is $v=4\times 10^{-5}$ m/s ($SR=\rho bv$, $b=2.55$ Å – dislocation Burgers vector). In that case, the time during which a dislocation moves one interatomic distance $a=3.6$ Å is $\tau=9\times 10^{-6}$ s, and the movement of hydrogen on the cores of mobile dislocations requires that the diffusion coefficient be $D=7\times 10^{-15}$ m^2/s ($D=a^2/2\tau$ [21]). This value is significantly greater than that characteristic of hydrogen diffusion in the crystal lattice of gamma iron at room temperature ($D=1\times 10^{-16}$ m^2/s [22]). Thus, at a strain rate of $SR=10^{-2}$ $1/s$ (mode II) dislocation transport is significantly suppressed, and the brittle zone length increases relative to the values characteristic of deformation in mode III mainly due to hydrogen lattice diffusion under stress (ΔD_s).

Assuming that the length of the brittle zone in the fracture of hydrogen-charged samples subjected to deformation mode I is determined by the additive contributions of different hydrogen transfer mechanisms ($D_I\approx D_0+\Delta D_d+\Delta D_s$), one can find the joint contribution from transport on dislocations (ΔD_d) and from stresses (ΔD_s) as follows $D_I-D_{III}=\Delta D_d+\Delta D_s$. The contribution of hydrogen transfer by diffusion under stress can be roughly estimated as $\Delta D_s=D_I-D_{II}$. Further, it is possible to estimate to a first approximation the contribution of dislocation transport ΔD_d to the brittle zone length. Fig. 6 presents the results of estimates of the D_0 , ΔD_d and ΔD_s contributions to the length of the hydrogen-induced brittle zone in the alloy under study, depending on the grain size.

The greatest length of the brittle zone immediately after hydrogen-charging D_0 is observed in coarse-grained C_HEA-N samples. The D_0 value decreases with decreasing grain size (Fig. 6). Since the D_0 value is determined solely by the hydrogen distribution during charging, it depends only on the diffusion of hydrogen atoms in the mate-

rial during hydrogen-charging. The effective hydrogen diffusion coefficient in samples can be estimated using the formula [21]

$$x \approx \sqrt{2D_{eff}t}, \quad (1)$$

where x is the characteristic diffusion path; D_{eff} is an effective diffusion coefficient; t is the hydrogen-charging duration.

The D_0 length can be taken as the characteristic diffusion path x , since analysis of the profile of hydrogen concentration distribution along the depth of coarse-grained C_HEA-N samples shows the consistency of the results between the experimentally obtained hydrogen distribution along the depth immediately after charging and the length of the brittle zone in the fracture $D_{III}\approx D_0$ estimated by SEM-images of the fracture surface of C_HEA-N samples (Fig. 5, 6).

An assessment of the effective diffusion coefficient (1) of hydrogen in samples of the studied HEA-N alloy shows that a decrease in grain size contributes to a decrease in D_{eff} :

$$D_{eff}^{C_HEA-N} \approx 9\times 10^{-16} \text{ m}^2/\text{s}, \quad D_{eff}^{M_HEA-N} \approx 5\times 10^{-16} \text{ m}^2/\text{s} \text{ and}$$

$$D_{eff}^{S_HEA-N} \approx 4\times 10^{-16} \text{ m}^2/\text{s}. \text{ The obtained } D_{eff} \text{ values are of}$$

the same order; however, the minimum value is characteristic of samples with the smallest grain size. Thus, a decrease in grain size or, in other words, an increase in the density of grain boundaries (including an increase in the number of annealing twins) leads to the suppression of hydrogen diffusion deep into the samples. Despite the existence of dual opinions about the influence of grain boundaries and twins on the hydrogen behavior in the material [21; 23; 24], they can act both as traps for hydrogen atoms and as preferential paths for their diffusion. In this work, in samples of the HEA-N alloy within the given conditions of hydrogen charging, they rather play the role of capture sites, although the second option should not be completely excluded.

The grain size of the studied HEA-N samples affects both the hydrogen distribution during charging, and the hydrogen diffusion, during plastic deformation (Fig. 6). Changes in the grain size of the studied samples have a weak effect on the hydrogen diffusion under stress during plastic deformation (Fig. 6). At the same time, the hydrogen transfer by mobile dislocations, directly depends on the grain size. The contribution of dislocation transport decreases with decreasing grain size and reaches a minimum value in the S_HEA-N samples. They are two times smaller than in the coarse-crystalline C_HEA-N samples, which is associated with a decrease in the free path of dislocations during plastic deformation.

CONCLUSIONS

Using various types of thermomechanical treatment, a series of states with different grain sizes was formed in the (FeCrNiMnCo)₉₉N₁ alloy: 43±21 (S_HEA-N), 120±57 (M_HEA-N), and 221±97 μm (C_HEA-N).

Grain refinement helps to increase the strength properties of the alloy under study and reduce the elongation to

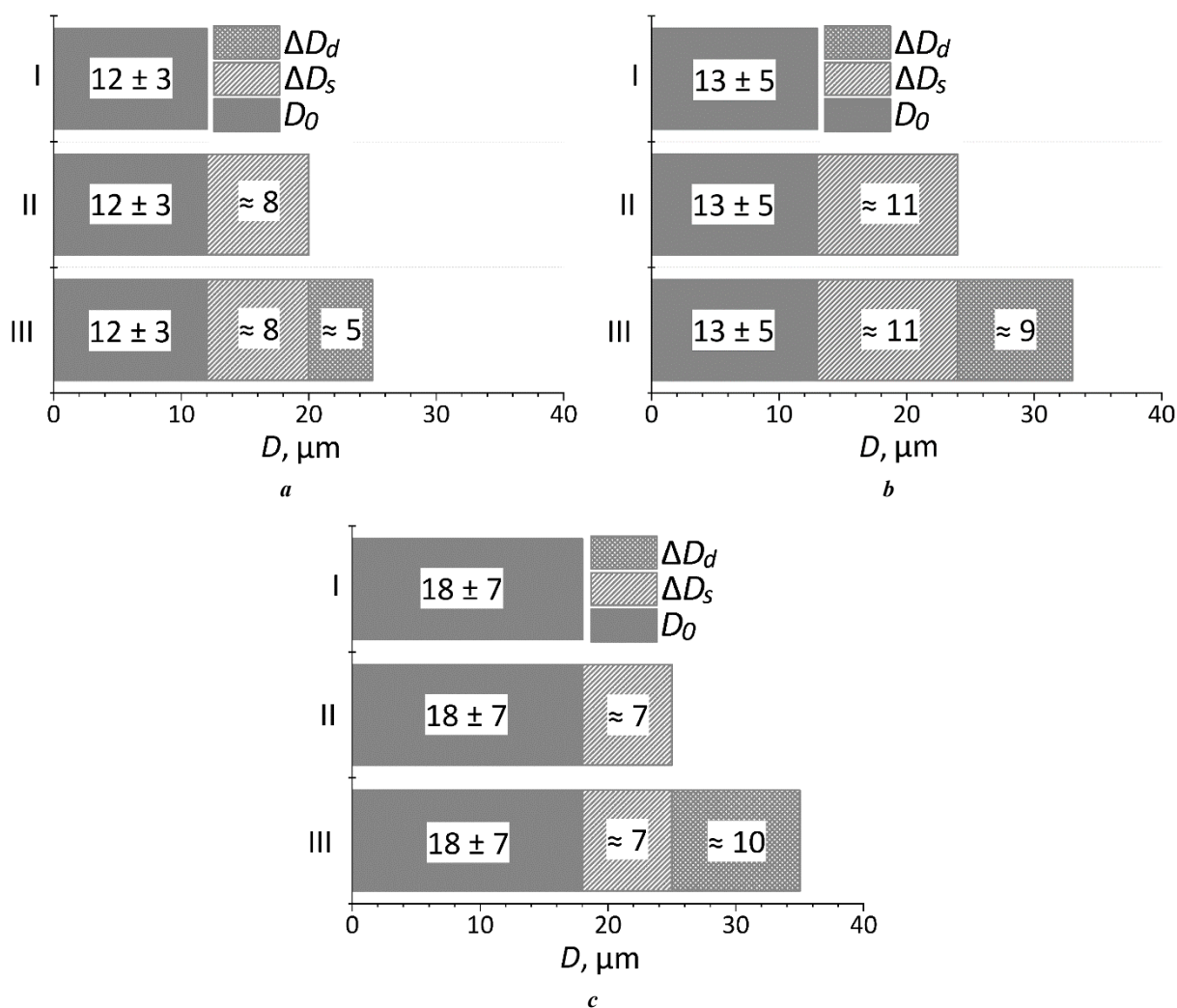


Fig. 6. The influence of a mechanical testing mode on the length of a brittle hydrogen-induced zone and evaluation of the main contributions from diffusion and dislocation hydrogen transport during plastic deformation of samples with the smallest (S_{HEA-N}) (a), medium (M_{HEA-N}) (b), and the largest (C_{HEA-N}) (c) grain size

Рис. 6. Влияние режима механических испытаний на длину хрупкой водородно-индуцируемой зоны и оценка основных вкладов от диффузионного и дислокационного транспорта водорода при пластической деформации образцов с малым (S_{HEA-N}) (a), средним (M_{HEA-N}) (b) и крупным (C_{HEA-N}) (c) размером зерна

failure, the values of which in all cases remain high ($\delta_{S_{HEA-N}}=58\%$, $\delta_{M_{HEA-N}}=65\%$, $\delta_{C_{HEA-N}}=66\%$).

Hydrogen charging of samples of the alloy under study has little effect on the yield strength, however, leads to a decrease in the ultimate tensile strength and elongation to failure. The formed hydrogen-induced surface zone in samples with the largest grain size, is fractured in a brittle way; cracks are observed both along the body of the grains, and along their boundaries on the side surfaces of the destroyed hydrogen-charged samples. An increase in the number of grain boundaries due to grain refinement is accompanied by a change in the nature of the fracture of the surface brittle hydrogen-assisted zone to a predominantly intergranular one.

It has been experimentally found that a decrease in grain size helps to increase the resistance of the $(FeCrNiMnCo)_{99}N_1$ alloy to the negative effects of hydrogen. This is manifested by a decrease in the hydrogen embrittlement index, as well as in a decrease in the length of the hydrogen-induced brittle

zone detected on the fracture surfaces. This is caused by a decrease in the effective coefficient of hydrogen diffusion in the material, as well as a decrease in the free path of dislocations transferring hydrogen deep into the material during plastic deformation.

REFERENCES

- Feng Zheng, Li Xinfeng, Song Xiaolong, Gu Tang, Zhang Yong. Hydrogen Embrittlement of CoCrFeMnNi High-Entropy Alloy Compared with 304 and IN718 Alloys. *Metals*, 2022, vol. 12, no. 6, article number 998. DOI: [10.3390/met12060998](https://doi.org/10.3390/met12060998).
- Zhao Yakai, Lee Dong-Hyun, Seok Moo-Young, Lee Jung-A, Phaniraj M.P., Suh Jin-Yoo, Ha Heon-Young, Kim Ju-Young, Ramamurty U., Jang Jae-il. Resistance of CoCrFeMnNi high-entropy alloy to gaseous hydrogen embrittlement. *Scripta Materialia*, 2017, vol. 135, pp. 54–58. DOI: [10.1016/j.scriptamat.2017.03.029](https://doi.org/10.1016/j.scriptamat.2017.03.029).

3. Cantor B., Chang I.T.H., Knight P., Vincent A.J.B. Microstructural development in equiatomic multi-component alloys. *Materials Science and Engineering: A*, 2004, vol. 375-377, pp. 213–218. DOI: [10.1016/j.msea.2003.10.257](https://doi.org/10.1016/j.msea.2003.10.257).
4. Cantor B. Multicomponent high-entropy Cantor alloys. *Progress in Materials Science*, 2021, vol. 120, article number 100754. DOI: [10.1016/j.pmatsci.2020.100754](https://doi.org/10.1016/j.pmatsci.2020.100754).
5. Bertsch K.M., Nygren K.E., Wang S., Bei H., Nagao A. Hydrogen-enhanced compatibility constraint for intergranular failure in FCC FeNiCoCrMn high-entropy alloy. *Corrosion Science*, 2021, vol. 184, article number 109407. DOI: [10.1016/j.corsci.2021.109407](https://doi.org/10.1016/j.corsci.2021.109407).
6. Traversier M., Mestre-Rinn P., Peillon N., Rigal E., Boulmat X., Tancret F., Dhers J., Fraczkiwicz A. Nitrogen-induced hardening in an austenitic CrFeMnNi high-entropy alloy (HEA). *Materials Science and Engineering: A*, 2021, vol. 804, article number 140725. DOI: [10.1016/j.msea.2020.140725](https://doi.org/10.1016/j.msea.2020.140725).
7. Klimova M., Shaysultanov D., Semenyuk A., Zherebtsov S., Salishchev G., Stepanov N. Effect of nitrogen on mechanical properties of CoCrFeMnNi high entropy alloy at room and cryogenic temperatures. *Journal of Alloys and Compounds*, 2020, vol. 849, article number 156633. DOI: [10.1016/j.jallcom.2020.156633](https://doi.org/10.1016/j.jallcom.2020.156633).
8. Zhang Shidong, Liu Min, Luo Yun, Wang Lianbo, Wang Zemin, Wang Zhanyong, Li Fangjie, Shen Qin, Wang Xiaowei. Immunity of Al_{0.25}CoCrFeNi high-entropy alloy to hydrogen embrittlement. *Materials Science and Engineering: A*, 2021, vol. 821, article number 141590. DOI: [10.1016/j.msea.2021.141590](https://doi.org/10.1016/j.msea.2021.141590).
9. Luo Hong, Li Zhiming, Lu Wenjun, Ponge D., Raabe D. Hydrogen embrittlement of an interstitial equimolar high-entropy alloy. *Corrosion Science*, 2018, vol. 136, pp. 403–408. DOI: [10.1016/j.corsci.2018.03.040](https://doi.org/10.1016/j.corsci.2018.03.040).
10. Wu Z., Parish C.M., Bei H. Nano-twin mediated plasticity in carbon-containing FeNiCoCrMn high entropy alloys // *Journal of Alloys and Compounds*. 2015. Vol. 647. P. 815–822. DOI: [10.1016/j.jallcom.2015.05.224](https://doi.org/10.1016/j.jallcom.2015.05.224).
11. Wang Zhangwei, Baker I. Interstitial strengthening of a f.c.c. FeNiMnAlCr high entropy alloy. *Materials Letters*, 2016, vol. 180, pp. 153–156. DOI: [10.1016/j.matlet.2016.05.122](https://doi.org/10.1016/j.matlet.2016.05.122).
12. Li Xinfeng, Yin Jing, Zhang Jin, Wang Yanfei, Song Xiaolong, Zhang Yong, Ren Xuechong. Hydrogen embrittlement and failure mechanisms of multi-principal element alloys: A review. *Journal of Materials Science & Technology*, 2022, vol. 122, pp. 20–32. DOI: [10.1016/j.jmst.2022.01.008](https://doi.org/10.1016/j.jmst.2022.01.008).
13. Bhadeshia H.K.D.H. Prevention of hydrogen embrittlement in steels. *ISIJ international*, 2016, vol. 56, no. 1, pp. 24–36. DOI: [10.2355/isijinternational.ISIJNT-2015-430](https://doi.org/10.2355/isijinternational.ISIJNT-2015-430).
14. Lynch S. Hydrogen embrittlement phenomena and mechanisms. *Corrosion reviews*, 2012, vol. 30, no. 3-4, pp. 105–123. DOI: [10.1515/corrrev-2012-0502](https://doi.org/10.1515/corrrev-2012-0502).
15. Panchenko M.Yu., Nifontov A.S., Astafurova E.G. Microstructural effect on hydrogen embrittlement of high nitrogen chromium-manganese steel. *Physical mesomechanics*, 2022, vol. 25, no. 5, pp. 453–465. DOI: [10.55652/1683-805X_2022_25_3_84](https://doi.org/10.55652/1683-805X_2022_25_3_84).
16. Koyama M., Ichii K., Tsuzaki K., Grain refinement effect on hydrogen embrittlement resistance of an equiatomic CoCrFeMnNi high-entropy alloy. *International Journal of Hydrogen Energy*, 2019, vol. 44, no. 31, pp. 17163–17167. DOI: [10.1016/j.ijhydene.2019.04.280](https://doi.org/10.1016/j.ijhydene.2019.04.280).
17. Fu Z.H., Yang B.J., Chen M., Gou G.Q., Chen H. Effect of recrystallization annealing treatment on the hydrogen embrittlement behavior of equimolar CoCrFeMnNi high entropy alloy. *International Journal of Hydrogen Energy*, 2021, vol. 46, no. 9, pp. 6970–6978. DOI: [10.1016/j.ijhydene.2020.11.154](https://doi.org/10.1016/j.ijhydene.2020.11.154).
18. Bai Y., Momotani Y., Chen M.C., Shibata A., Tsuji N. Effect of grain refinement on hydrogen embrittlement behaviors of high-Mn TWIP steel. *Materials Science and Engineering: A*, 2016, vol. 651, pp. 935–944. DOI: [10.1016/j.msea.2015.11.017](https://doi.org/10.1016/j.msea.2015.11.017).
19. Park C., Kang N., Liu S. Effect of grain size on the resistance to hydrogen embrittlement of API 2W grade 60 steels using in situ slow-strain-rate testing. *Corrosion Science*, 2017, vol. 128, pp. 33–41. DOI: [10.1016/j.corsci.2017.08.032](https://doi.org/10.1016/j.corsci.2017.08.032).
20. Fuchigami H., Minami H., Nagumo M. Effect of grain size on the susceptibility of martensitic steel to hydrogen-related failure. *Phil Mag Lett*, 2006, vol. 86, pp. 21–29.
21. Li J., Hallil A., Metsue A., Oudriss A., Bouhattate J., Feaugas X. Antagonist effects of grain boundaries between the trapping process and the fast diffusion path in nickel bicrystals. *Scientific Reports*, 2021, vol. 11, article number 15533. DOI: [10.1038/s41598-021-94107-6](https://doi.org/10.1038/s41598-021-94107-6).
22. Owczarek E., Zakroczymski T. Hydrogen transport in a duplex stainless steel. *Acta Materialia*, 2000, vol. 48, no. 12, pp. 3059–3070. DOI: [10.1016/S1359-6454\(00\)00122-1](https://doi.org/10.1016/S1359-6454(00)00122-1).
23. Du Y.A., Ismer L., Rogal J., Hickel T., Neugebauer J., Drautz R. First-principles study on the interaction of H interstitials with grain boundaries in α - and γ -Fe. *Physical Review B*, 2011, vol. 84, article number 144121. DOI: [10.1103/PhysRevB.84.144121](https://doi.org/10.1103/PhysRevB.84.144121).
24. Oudriss A., Creus J., Bouhattate J., Savall C., Peraudeau B., Feaugas X. The diffusion and trapping of hydrogen along the grain boundaries in polycrystalline nickel. *Scripta Materialia*, 2012, vol. 66, no. 1, pp. 37–40. DOI: [10.1016/j.scriptamat.2011.09.036](https://doi.org/10.1016/j.scriptamat.2011.09.036).

СПИСОК ЛИТЕРАТУРЫ

1. Feng Zheng, Li Xinfeng, Song Xiaolong, Gu Tang, Zhang Yong. Hydrogen Embrittlement of CoCrFeMnNi High-Entropy Alloy Compared with 304 and IN718 Alloys // *Metals*. 2022. Vol. 12. № 6. Article number 998. DOI: [10.3390/met12060998](https://doi.org/10.3390/met12060998).
2. Zhao Yakai, Lee Dong-Hyun, Seok Moo-Young, Lee Jung-A, Phaniraj M.P., Suh Jin-Yoo, Ha Heon-Young, Kim Ju-Young, Ramamurty U., Jang Jae-il. Resistance of CoCrFeMnNi high-entropy alloy to gaseous hydrogen embrittlement // *Scripta Materialia*. 2017. Vol. 135. P. 54–58. DOI: [10.1016/j.scriptamat.2017.03.029](https://doi.org/10.1016/j.scriptamat.2017.03.029).
3. Cantor B., Chang I.T.H., Knight P., Vincent A.J.B. Microstructural development in equiatomic multi-component alloys // *Materials Science and Engineering: A*. 2004. Vol. 375-377. P. 213–218. DOI: [10.1016/j.msea.2003.10.257](https://doi.org/10.1016/j.msea.2003.10.257).

4. Cantor B. Multicomponent high-entropy Cantor alloys // *Progress in Materials Science*. 2021. Vol. 120. Article number 100754. DOI: [10.1016/j.pmatsci.2020.100754](https://doi.org/10.1016/j.pmatsci.2020.100754).
5. Bertsch K.M., Nygren K.E., Wang S., Bei H., Nagao A. Hydrogen-enhanced compatibility constraint for intergranular failure in FCC FeNiCoCrMn high-entropy alloy // *Corrosion Science*. 2021. Vol. 184. Article number 109407. DOI: [10.1016/j.corsci.2021.109407](https://doi.org/10.1016/j.corsci.2021.109407).
6. Traversier M., Mestre-Rinn P., Peillon N., Rigal E., Boulnat X., Tancret F., Dhers J., Fraczkiewicz A. Nitrogen-induced hardening in an austenitic CrFeMnNi high-entropy alloy (HEA) // *Materials Science and Engineering: A*. 2021. Vol. 804. Article number 140725. DOI: [10.1016/j.msea.2020.140725](https://doi.org/10.1016/j.msea.2020.140725).
7. Klimova M., Shaysultanov D., Semenyuk A., Zhreb-tsov S., Salishchev G., Stepanov N. Effect of nitrogen on mechanical properties of CoCrFeMnNi high entropy alloy at room and cryogenic temperatures // *Journal of Alloys and Compounds*. 2020. Vol. 849. Article number 156633. DOI: [10.1016/j.jallcom.2020.156633](https://doi.org/10.1016/j.jallcom.2020.156633).
8. Zhang Shidong, Liu Min, Luo Yun, Wang Lianbo, Wang Zemin, Wang Zhanyong, Li Fangjie, Shen Qin, Wang Xiaowei. Immunity of Al_{0.25}CoCrFeNi high-entropy alloy to hydrogen embrittlement // *Materials Science and Engineering: A*. 2021. Vol. 821. Article number 141590. DOI: [10.1016/j.msea.2021.141590](https://doi.org/10.1016/j.msea.2021.141590).
9. Luo Hong, Li Zhiming, Lu Wenjun, Ponge D., Raabe D. Hydrogen embrittlement of an interstitial equimolar high-entropy alloy // *Corrosion Science*. 2018. Vol. 136. P. 403–408. DOI: [10.1016/j.corsci.2018.03.040](https://doi.org/10.1016/j.corsci.2018.03.040).
10. Wu Z., Parish C.M., Bei H. Nano-twin mediated plasticity in carbon-containing FeNiCoCrMn high entropy alloys // *Journal of Alloys and Compounds*. 2015. Vol. 647. P. 815–822. DOI: [10.1016/j.jallcom.2015.05.224](https://doi.org/10.1016/j.jallcom.2015.05.224).
11. Wang Zhangwei, Baker I. Interstitial strengthening of a f.c.c. FeNiMnAlCr high entropy alloy // *Materials Letters*. 2016. Vol. 180. P. 153–156. DOI: [10.1016/j.matlet.2016.05.122](https://doi.org/10.1016/j.matlet.2016.05.122).
12. Li Xinfeng, Yin Jing, Zhang Jin, Wang Yanfei, Song Xiaolong, Zhang Yong, Ren Xuechong. Hydrogen embrittlement and failure mechanisms of multi-principal element alloys: A review // *Journal of Materials Science & Technology*. 2022. Vol. 122. P. 20–32. DOI: [10.1016/j.jmst.2022.01.008](https://doi.org/10.1016/j.jmst.2022.01.008).
13. Bhadeshia H.K.D.H. Prevention of hydrogen embrittlement in steels // *ISIJ international*. 2016. Vol. 56. № 1. P. 24–36. DOI: [10.2355/isijinternational.ISIJINT-2015-430](https://doi.org/10.2355/isijinternational.ISIJINT-2015-430).
14. Lynch S. Hydrogen embrittlement phenomena and mechanisms // *Corrosion reviews*. 2012. Vol. 30. № 3-4. P. 105–123. DOI: [10.1515/correv-2012-0502](https://doi.org/10.1515/correv-2012-0502).
15. Панченко М.Ю., Астафурова Е.Г., Нифонтов А.С. Влияние микроструктуры на особенности водородного охрупчивания высокоазотистой хромомарганцевой стали // *Физическая мезомеханика*. 2022. Т. 25. № 3. С. 84–97. DOI: [10.55652/1683-805X_2022_25_3_84](https://doi.org/10.55652/1683-805X_2022_25_3_84).
16. Koyama M., Ichii K., Tsuzaki K., Grain refinement effect on hydrogen embrittlement resistance of an equiatomic CoCrFeMnNi high-entropy alloy // *International Journal of Hydrogen Energy*. 2019. Vol. 44. № 31. P. 17163–17167. DOI: [10.1016/j.ijhydene.2019.04.280](https://doi.org/10.1016/j.ijhydene.2019.04.280).
17. Fu Z.H., Yang B.J., Chen M., Gou G.Q., Chen H. Effect of recrystallization annealing treatment on the hydrogen embrittlement behavior of equimolar CoCrFeMnNi high entropy alloy // *International Journal of Hydrogen Energy*. 2021. Vol. 46. № 9. P. 6970–6978. DOI: [10.1016/j.ijhydene.2020.11.154](https://doi.org/10.1016/j.ijhydene.2020.11.154).
18. Bai Y., Momotani Y., Chen M.C., Shibata A., Tsuji N. Effect of grain refinement on hydrogen embrittlement behaviors of high-Mn TWIP steel // *Materials Science and Engineering: A*. 2016. Vol. 651. P. 935–944. DOI: [10.1016/j.msea.2015.11.017](https://doi.org/10.1016/j.msea.2015.11.017).
19. Park C., Kang N., Liu S. Effect of grain size on the resistance to hydrogen embrittlement of API 2W grade 60 steels using in situ slow-strain-rate testing // *Corrosion Science*. 2017. Vol. 128. P. 33–41. DOI: [10.1016/j.corsci.2017.08.032](https://doi.org/10.1016/j.corsci.2017.08.032).
20. Fuchigami H., Minami H., Nagumo M. Effect of grain size on the susceptibility of martensitic steel to hydrogen-related failure // *Philosophical Magazine Letters*. 2006. Vol. 86. P. 21–29. DOI: [10.1080/09500830500482316](https://doi.org/10.1080/09500830500482316).
21. Li J., Hallil A., Metsue A., Oudriss A., Bouhattate J., Feaugas X. Antagonist effects of grain boundaries between the trapping process and the fast diffusion path in nickel bicrystals // *Scientific Reports*. 2021. Vol. 11. Article number 15533. DOI: [10.1038/s41598-021-94107-6](https://doi.org/10.1038/s41598-021-94107-6).
22. Owczarek E., Zakroczymski T. Hydrogen transport in a duplex stainless steel // *Acta Materialia*. 2000. Vol. 48. № 12. P. 3059–3070. DOI: [10.1016/S1359-6454\(00\)00122-1](https://doi.org/10.1016/S1359-6454(00)00122-1).
23. Du Y.A., Ismer L., Rogal J., Hickel T., Neugebauer J., Drautz R. First-principles study on the interaction of H interstitials with grain boundaries in α - and γ -Fe // *Physical Review B*. 2011. Vol. 84. Article number 144121. DOI: [10.1103/PhysRevB.84.144121](https://doi.org/10.1103/PhysRevB.84.144121).
24. Oudriss A., Creus J., Bouhattate J., Savall C., Peraudeau B., Feaugas X. The diffusion and trapping of hydrogen along the grain boundaries in polycrystalline nickel // *Scripta Materialia*. 2012. Vol. 66. № 1. P. 37–40. DOI: [10.1016/j.scriptamat.2011.09.036](https://doi.org/10.1016/j.scriptamat.2011.09.036).

Влияние размера зерна на закономерности водородного охрупчивания многокомпонентного сплава $(\text{FeCrNiMnCo})_{99}\text{N}_1$

© 2024

Гуртова Дарья Юрьевна*¹, студент

Панченко Марина Юрьевна^{2,3}, младший научный сотрудник
лаборатории физики иерархических структур в металлах и сплавах

Мельников Евгений Васильевич^{2,4}, младший научный сотрудник
лаборатории физики иерархических структур в металлах и сплавах

Астапов Денис Олегович^{1,5}, студент

Астафурова Елена Геннадьевна^{2,6}, доктор физико-математических наук,
заведующий лабораторией физики иерархических структур в металлах и сплавах

¹Томский государственный университет, Томск (Россия)

²Институт физики прочности и материаловедения Сибирского отделения РАН, Томск (Россия)

*E-mail: dasha_gurtova@mail.ru

³ORCID: <https://orcid.org/0000-0003-0236-2227>

⁴ORCID: <https://orcid.org/0000-0001-8238-6055>

⁵ORCID: <https://orcid.org/0000-0002-1277-4180>

⁶ORCID: <https://orcid.org/0000-0002-1995-4205>

Поступила в редакцию 26.06.2023

Принята к публикации 05.02.2024

Аннотация: Проблема водородного охрупчивания остается актуальной во многих сферах, поэтому повышенный интерес среди исследователей вызывает сплав FeCrNiMnCo (сплав Кантора) как один из наименее подверженных негативному воздействию водорода материалов. Тем не менее малоизученным остается вопрос о влиянии параметров микроструктуры на закономерности водородного охрупчивания сплава Кантора и многокомпонентных сплавов системы FeCrNiMnCo в целом. В работе изучено влияние размера зерна на склонность высокоэнтропийного сплава Кантора, легированного азотом, к водородной хрупкости. Для этого с помощью термомеханических обработок в сплаве $(\text{FeCrNiMnCo})_{99}\text{N}_1$ были сформированы состояния с разным размером зерен (43 ± 21 , 120 ± 57 и 221 ± 97 мкм). Экспериментально установлено, что измельчение зерна приводит к увеличению прочностных свойств исследуемого сплава и способствует повышению устойчивости к эффектам водородной хрупкости: в образцах с наименьшим из представленных размером зерна водородно-индуцируемое снижение пластичности меньше, чем в образцах с наибольшим размером зерна. Уменьшение размера зерна вызывает также снижение длины хрупкой зоны, выявляемой на поверхностях разрушения образцов после растяжения. Это вызвано снижением диффузии водорода в процессе насыщения и уменьшением транспорта атомов водорода с подвижными дислокациями в процессе пластической деформации за счет уменьшения размера зерна.

Ключевые слова: водородное охрупчивание; многокомпонентные сплавы; высокоэнтропийные сплавы; сплав Кантора; $(\text{FeCrNiMnCo})_{99}\text{N}_1$; водородная хрупкость; водородно-индуцируемая хрупкая зона; границы зерен; разрушение; механические свойства.

Благодарности: Исследование выполнено за счет гранта Российского научного фонда № 20-19-00261, <https://rscf.ru/project/20-19-00261/>.

Исследования выполнены на оборудовании ЦКП «Нанотех» ИФПМ СО РАН.

Авторы благодарны кандидату физико-математических наук С.В. Астафурову и К.А. Реуновой за помощь в проведении экспериментальных исследований.

Статья подготовлена по материалам докладов участников XI Международной школы «Физическое материаловедение» (ШФМ-2023), Тольятти, 11–15 сентября 2023 года.

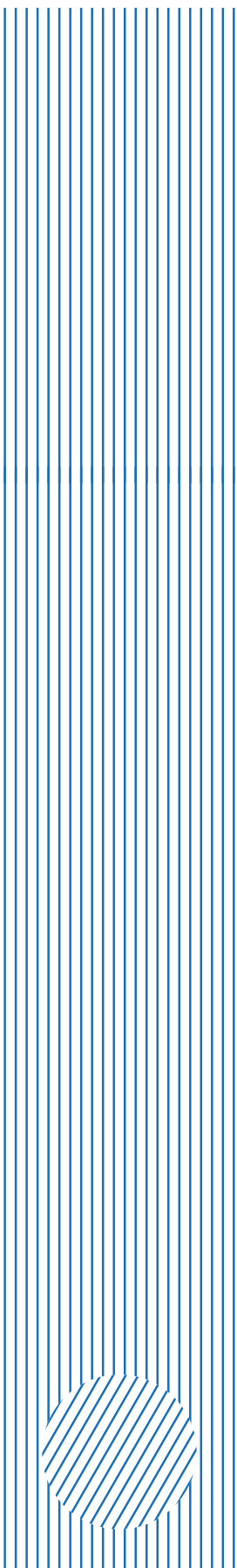
Для цитирования: Гуртова Д.Ю., Панченко М.Ю., Мельников Е.В., Астапов Д.О., Астафурова Е.Г. Влияние размера зерна на закономерности водородного охрупчивания многокомпонентного сплава $(\text{FeCrNiMnCo})_{99}\text{N}_1$ // Frontier Materials & Technologies. 2024. № 3. С. 41–51. DOI: 10.18323/2782-4039-2024-3-69-4.

The Research and Development Institute of Advanced Technologies is a structural division of Togliatti State University.

The Research and Development Institute of Advanced Technologies today

- More than 60 employees, including seven Doctors of Sciences and fourteen PhDs.
- Three centers, four departments, nineteen laboratories equipped with the up-to-date testing and research facilities for amount over 500 million roubles.
- Accreditation in three systems for testing and research, including in the ILAC international system (laboratory accreditation authority – Association of Analytical Centers “Analitika”, a full member and participant of the ILAC and APLAC mutual recognition agreements).
- Basic areas: fundamental research in the field of physical materials science (the development of the promising materials design, the issues of strength, plasticity, corrosion resistance, fatigue strength, stress corrosion cracking, improving the surface functional properties) and chemistry (methods for synthesis of molecules with the properties of selective fluorescent probes); applied research and inventions in the field of non-destructive control, micro-arc oxidation, manufacturing of cast products, etc.; services for testing and research of various materials, metallographic evaluations, environmental analyses, chemical monitoring of the environment.

Main achievements of the Research and Development Institute of Advanced Technologies

- Three mega-grants were implemented according to the Resolution of the Government of the Russian Federation dated April 9, 2010 No. 220; five projects within the Federal Targeted Programme for Research and Development in Priority Areas of Development of the Russian Scientific and Technological Complex for 2014–2020, including three international ones; in 2023, nine projects of the Russian Science Foundation and two state assignments are being implemented; under the auspices of the extraterritorial scientific and educational center “Engineering of the Future”, a youth Laboratory for the design of magnesium alloys was created.
 - Annually:
 - the number of papers is more than 35, half of them are in specialized journals of the Q1 and Q2 levels;
 - more than 1,500 test reports and conclusions at the request of enterprises, arbitration courts, and the prosecutor’s office
 - An initiator and organizer of 11 Physical Materials Science international schools with the participation of leading scientists-material engineers and metal physicists, the lectures of which became the basis for publishing nine volumes of the Advanced Materials textbook
 - International cooperation with the universities of Kumamoto (Japan), Seoul (South Korea), Prague (Czech Republic), and Freiberg (Germany), academic cooperation with IMP UB RAS (Yekaterinburg), IMSP RAS (Ufa), ISPMS SB RAS (Tomsk) and others; technical cooperation with more than 150 organizations in the real sector of the economy.
- 

Accuracy of the geometric shape of the hole in the longitudinal section during honing

© 2024

Aleksandr F. Denisenko^{*1}, Doctor of Sciences (Engineering), Professor,
professor of Chair “Mechanical Engineering Technology, Machines and Tools”

Roman G. Grishin², PhD (Engineering), Associate Professor,
assistant professor of Chair “Mechanical Engineering Technology, Machines and Tools”

Evgeniya D. Antipova³, postgraduate student
of Chair “Mechanical Engineering Technology, Machines and Tools”

Samara State Technical University, Samara (Russia)

*E-mail: tmsi@samgtu.ru,
sammortor@yandex.ru

¹ORCID: <https://orcid.org/0000-0001-6393-2831>

²ORCID: <https://orcid.org/0000-0003-4511-9147>

³ORCID: <https://orcid.org/0000-0002-1759-7080>

Received 29.02.2024

Accepted 16.07.2024

Abstract: The wide application of honing as a finishing treatment of internal cylindrical surfaces for cylinder-piston systems, used in some structures, is caused by high accuracy measured in tenths of a micrometer, and high productivity of the process. The most important indicator of reliable operation of cylinder-piston systems are high requirements for the geometric accuracy of holes. Due to the lack of sufficient theoretical justification for the selection of honing parameters ensuring the accuracy of the geometric shape of the hole in the longitudinal section, the authors proposed a model for the formation of errors in the geometric shape of the hole. The model is built on the kinematic characteristics of the process including the ratio of the honing stone dimensions, the length of the hole, the stroke of the honing head, the ratio of the speeds of translational and rotational movements, and the force action in the processing zone, which changed due to the presence of an overrun of the honing stone. To obtain analytical dependencies ensuring the minimisation of form deviations, the conditions for stock removal for the points of the machined surface were considered, the value of which was taken proportional to the path of movement, and the pressure value. For this purpose, graphs of the distribution functions of displacements and pressure changes were constructed depending on the coordinate of the point location on the generating line of the hole being machined. Using the obtained analytical dependencies, the potential occurrence of a shape error in the form of a saddle shape was found, the dominant factor influencing the value of which is the value of the honing stone overrun. At the same time, it was identified that the ratio of the speeds of translational and rotational movements has an insignificant effect on the violation of the form in the longitudinal section.

Keywords: honing; geometric accuracy of holes; kinematic characteristics of honing; value of overrun; displacement distribution function.

For citation: Denisenko A.F., Grishin R.G., Antipova E.D. Accuracy of the geometric shape of the hole in the longitudinal section during honing. *Frontier Materials & Technologies*, 2024, no. 3, pp. 53–62. DOI: 10.18323/2782-4039-2024-3-69-5.

INTRODUCTION

Honing has been on the rise in recent years due to the need to improve the tribological performance of cylinder-piston systems used in materials-handling machines, hydraulic jacks, engine components, and robotics. In process engineering, abrasive machining methods have always been an important area of research in terms of development and modelling, as they determine the surface quality characteristics of the blank. Honing is an abrasive machining process most often used in roughing, semi-finishing and finishing of cylindrical bores to produce parts with high surface quality and minimal geometric errors [1–3]. A special feature of honing is the transverse scratches made on the surface by two tool strokes. These transverse scratches give the surface special performance characteristics in terms of oil retention and circulation. Therefore, honing is usually used to ensure that the surface of elements that are in contact with others during relative motion, such as in

the piston-cylinder system, meets the requirements for geometric and dimensional accuracy and texture [4–6]. One of the key tasks that must be solved in the honing process is to ensure a characteristic surface texture consisting of a network of oil scratches that form cross-hatching, as well as the required values of the roughness profile parameters [1; 2; 7].

During the use of honing processes, many studies have been carried out on both traditional and non-traditional honing. For example, in [8] positive results are noted for the processing with variable kinematic parameters, and it is indicated that honing performed with variable kinematic parameters affects the value of the resulting roughness profile parameters, which is an additional incentive, influencing the further development of CNC machines used for honing.

According to the data given in [9; 10], the honing process is characterised by three overlapping motions of the honing tool: rotation around the tool axis, linear

reciprocating motion, and feed motion of the honing stone in the radial direction. The main parameters determining the honing kinematics are: axial linear speed of the honing head during reciprocating motion V_A , m/min, and peripheral speed of the honing head V_P , m/min:

$$V_A = 2l_X n_A; V_P = 0.001\pi Dn, \quad (1)$$

where l_X is the stroke length of the honing head during reciprocating motion, m;

n_A is the stroke rate of the honing head during reciprocating motion, 1/min;

n is the rotational frequency of the honing head, rpm;

D is the diameter of the hole being honed, mm.

The specified speeds determine the cutting speed V and the honing angle α :

$$V = \sqrt{V_A^2 + V_P^2}; \operatorname{tg}\alpha = V_P/V_A. \quad (2)$$

The radial motion of the honing stone can be controlled either by feed or by force. In feed-controlled honing, the honing stone is fed outward in certain stages, and at certain intervals using various mechanisms, for example, a mandrel with conical elements. In force-controlled honing, the height of the feed steps depends on the difference between the required and measured process forces, which leads to different process forces during the honing process [9]. When processing is carried out with a constant honing force, the quality of honed holes can be improved [11].

One of the main goals of the honing process is to reduce the deviation of the shape of honed holes. In [12], based on a comparison of the deviations in the hole shape that can be obtained with certain types of processing, it was concluded that the honing process significantly improves the cylindricity of the processed hole compared to other production methods. The authors of [13] noted that the cylindricity of the cylinder hole is determined primarily by six groups of factors, such as the machine and fixture rigidity, the honing head design, the location of the honing stones, the properties of the material being processed, the honing process parameters and the pre-created initial cylindricity of the honed hole, during previously performed processing.

The work [14] considered the effect of the honing stone speed on obtaining holes with minimal geometric errors. However, the author limits himself to studying the hole accuracy only in the cross-section, without considering its effect on the accuracy in the longitudinal direction. The author of [15] described the effect of changing the reciprocating speed and rotation speed on improving the ovality, and noted that with constant overrun, a decrease in ovality was observed with an increase in the reciprocating speed. Maximum ovality was observed at a higher reciprocating speed, and at a relatively lower rotation speed. At a higher rotation speed of the honing head, ovality decreases for all values of the reciprocating speed [15]. In [16], the effect of axial acceleration of the honing head on cylindrical deviation

was confirmed. It was found that with an acceleration of $<1 g$ and with an acceleration of $>2 g$, greater deviations in cylindricity of the honed hole were obtained than when processing with an acceleration of $1.5 g$ (g is the gravitational value of acceleration).

As follows from the above review, the production of honed holes, with minimal deviations of cylindrical shape, has been studied in sufficient detail in published works. At the same time, as for ensuring the shape of the hole in the longitudinal section, in the few published works, for example [17–19], there are recommendations for the selection of honing parameters, in particular the overrun value, which do not contain sufficient theoretical justifications, and are built only based on some experimental data, the value of which essentially depends on the specific honing conditions.

An analysis of works covering the honing process allowed identifying the main parameters affecting the accuracy of the hole geometric shape: the dimensions of the honing stones, the ratio of the speeds of the rotational and reciprocating motions of the honing head and the rational choice of pressure in the zone of a contact of the stones with the part.

In work [19], it is noted that to obtain the correct geometric shape of the processed hole, the stones must recede out of the hole for a certain length, called the overrun. However, it is emphasised that with an incorrectly selected symmetrical overrun in the hole, a saddle shape or barrel shape can be obtained. It is concluded that if one considers the redistribution of contact radial forces to be the dominant cause, then at any overrun values, an error in the shape in the longitudinal section in the form of a saddle must inevitably form, which increases as the overrun values increase. In this case, the author considers the overrun value l' to be optimal, determined by the relationship

$$l' = (0.33 \dots 0.25)l = \operatorname{opt}, \quad (3)$$

where the length of the stone l is determined by the expressions

$$l = (1.2 \dots 0.8)L \text{ and } l = 1.5\pi D \operatorname{tg}\alpha / z, \quad (4)$$

where L and D are the length and diameter of the honed hole, respectively;

z is the number of stones:

$$z = (0.25 \dots 0.35) \frac{\pi D}{b}, \quad (5)$$

where α is the angle of elevation of the trajectory of the cutting tools;

b is the width of the stone.

The range of changes in overrun values specified in [19] fits the values proposed in [18; 20], but without clear justification for their selection.

The purpose of this study is to develop recommendations based on modelling of real honing cycles that will help end users when setting up the machining process.

METHODS

The formation of geometric shape errors during honing can be carried out only on a cutting model, that takes into account local contacts between the blank, and the abrasive tool changing due to the impact of kinematic and force factors.

To obtain analytical dependencies that ensure the minimisation of shape deviations, it is necessary to consider the conditions for metal removal, during rotational and reciprocating motion of the honing head. This problem can be solved by assuming that the amount of metal removal U is proportional to the amount of movement of individual points of the stone relative to the selected point of the machined surface S and the value of pressure p :

$$U = kpS, \tag{6}$$

where k is the coefficient of specific material removal under given honing conditions.

To determine the shape of the machined hole in the longitudinal direction, we denote the metal removal at point x along the length of the hole by $U(x)$ (Fig. 1). The pressure in the contact zone of the stones with the part can depend both on the position of the stones relative to the part, i. e. be a function of the x coordinate on the machined surface (Fig. 1), and on the position of the considered point on the stone contact line, i. e. be a function of the x^* coordinate in the moving coordinates system associated with the honing head:

$$p = p(x, x^*).$$

In further calculations, we will assume that the pressure $p=p(x, x^*)$ does not depend on the x^* coordinate, but only on the x coordinate on the machined surface, i. e. $p=p(x)$.

The direction of the rotational speed V_p does not change during the machining cycle, and the direction of the translational speed V_A changes at the end of each stroke of the head. In extreme positions, the translational motion velocity decreases to zero, and then increases from zero to V_A in the opposite direction, resulting in a delay in the stroke for some time.

This nature of the head movements leads to an inequality in the path of movement of individual points of the cutting surface of the stones, relative to the machined surface. To take into account what share of the total friction path falls on particular areas of the part surface, and the working surface of the stones, the authors of [20] proposed to introduce a function of the distribution of displacements $\alpha(x)$ in the longitudinal direction, and a function of the distribution of displacements $\beta(x)$ resulting from the head rotation.

Fig. 2, 3 show the distribution functions for two possible conditions of symmetrical honing (under the same conditions for processing the ends of the hole). For the case shown in Fig. 2, when the overrun value $l'=0$, the stroke length of the head is determined as

$$l_x = L - l.$$

For the extreme sections, the length of which is equal to l , the ordinates of the curve of the longitudinal displacement distribution change according to a linear law, and the ordinates for the middle section of length $(L-2l)$ remain constant, and are determined from the normalisation requirement, according to which the area bounded by the distribution curve and the abscissa axis is equal to one:

$$\alpha_{\max}l + \alpha_{\max}(L-2l) = 1; \tag{7}$$

$$\alpha_{\max} = 1/(L-l). \tag{8}$$

For the displacement distribution curve at relative rotation $\beta(x)$, the constancy of the ordinates for each section is characteristic, although their values differ from each other. This difference is determined by the nature of the change in the velocity of the longitudinal displacement of the head at the end of the longitudinal stroke, and the time spent on changing the direction of the head movement. The duration of the stroke delay depends on the inertia of the control system.

Fig. 3 shows a case for which the relation is observed:

$$L-l < l_x < L+l.$$

RESULTS

During head displacement, part of the stone comes out of the hole in both directions, and only part of the cutting surface of the stones passes over the extreme points of the part forming the hole. The longitudinal displacement curve for the extreme sections is a trapezoid. The middle section of length (l_x-l) is characterised by constant ordinates, the values of which are determined from the normalisation requirement:

$$(L+2l'-2l)\alpha_{\max} + 2\frac{\alpha_{\max} + \alpha(0)}{2}(l-l') = 1, \tag{9}$$

where $\alpha(0) = \alpha_{\max}l'/l$.

Hence

$$\alpha_{\max} = \frac{l}{Ll - (l-l')^2}. \tag{10}$$

The equation of the $\alpha(x)$ straight line for the section $0 \leq x \leq l-l'$:

$$\alpha(x) = \frac{(x+l')}{Ll - (l-l')^2}. \tag{11}$$

Therefore, the magnitude of the relative displacement of particular points of the stone for a point of the machined surface with coordinate x can be determined in the longitudinal direction as

$$S_A = V_A\alpha(x)\tau,$$

and in the direction of the head rotation as

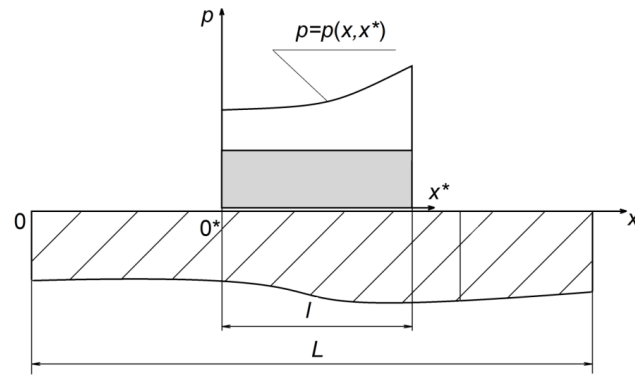


Fig. 1. Computational scheme for determining metal removal during honing
Рис. 1. Расчетная схема для определения съема металла при хонинговании

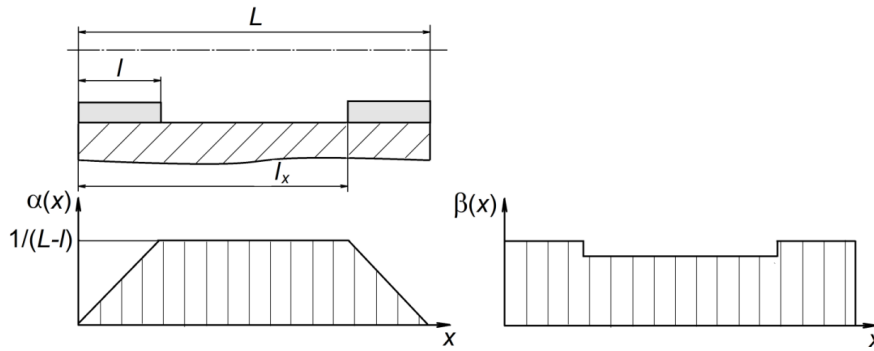


Fig. 2. Distribution curves of displacements $\alpha(x)$ and $\beta(x)$ during honing without overrun ($l'=0$)
Рис. 2. Кривые распределения перемещений $\alpha(x)$ и $\beta(x)$ при хонинговании при отсутствии перебега ($l'=0$)

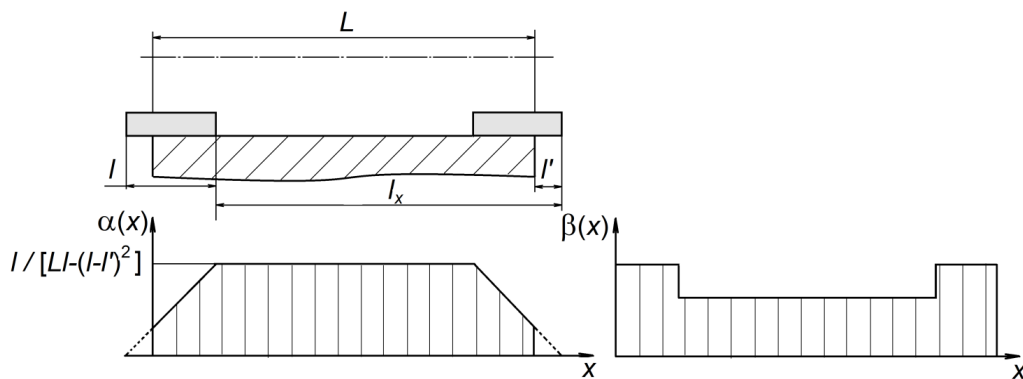


Fig. 3. Distribution curves of displacements $\alpha(x)$ and $\beta(x)$ during honing in the presence of overrun ($l' \neq 0$)
Рис. 3. Кривые распределения перемещений $\alpha(x)$ и $\beta(x)$ при хонинговании при наличии перебега ($l' \neq 0$)

$$S_p = V_p \beta(x) \tau,$$

where τ is the honing duration.

To find the function $U(x)$ that determines the metal removal in the hole section with coordinate x , it is necessary to take into account the pressure of the honing stone $p=p(x)$ on this section of the hole:

$$U(x) = U_A(x) + U_P(x) = k_A S_A p(x) + k_P S_P p(x), \quad (12)$$

where $U_A(x)$, $U_P(x)$ are the metal removal at the point with coordinate x due to the stone movement in the longitudinal direction and in the direction of rotation of the honing head, respectively;

k_A , k_P are coefficients of specific material removal under the given honing conditions caused only by the translational or rotational movement of the honing head, respectively.

Let us consider in more detail the case of honing in the presence of overrun ($l' \neq 0$) (Fig. 3), if the pressure diagram within the length of the contact of the stone with the part is a rectangle, i. e. there is a uniform pressure distribution in the contact zone. Taking into account the symmetrical nature of the processing (the overruns at the ends of the hole are the same), we will consider only one side of the hole (Fig. 4) for the case when $2l < L$. The graph $p=p(x)$ displayed in Fig. 4 shows a gradual decrease in pressure due to an increase in the contact area of the stone with the part. Therefore, three areas can be distinguished along the x coordinate, differing in processing conditions: 1) $0 \leq x \leq l-l'$; 2) $l-l' < x < l$; 3) $l < x < L-l$.

Consequently, within sections 1 and 3, the pressure $p=p(x)$ does not change and is:

$$\text{– for section 1: } p(x) = p_1 = \frac{P_y}{(l-l')b};$$

$$\text{– for section 3: } p(x) = p_3 = \frac{P_y}{lb}.$$

Then for section 2

$$p(x) = p_2 = \frac{P_y}{l(l-l')b} (2l - l' - x),$$

where P_y is the force of pressing the stone to the processed surface;

b is the stone width.

Thus, in accordance with formula (12), assuming that $k_A = k_P = k$, we obtain:

$$U_1(x) = U_{1A}(x) + U_{1P}(x) = k\tau [V_A \alpha_1(x) + V_P \beta(x)] p_1; \quad (13)$$

$$U_2(x) = U_{2A}(x) + U_{2P}(x) = k\tau [V_A \alpha_2(x) + V_P \beta(x)] p_2; \quad (14)$$

$$U_3(x) = U_{3A}(x) + U_{3P}(x) = k\tau [V_A \alpha_3(x) + V_P \beta(x)] p_3, \quad (15)$$

where, taking into account the absence of delays in the extreme positions $\beta(x) = 1/L$.

If we assume that $V_A = \xi V_P$, then for comparison of stock removal by sections, the obtained dependencies (13)–(15) can be presented in the following way:

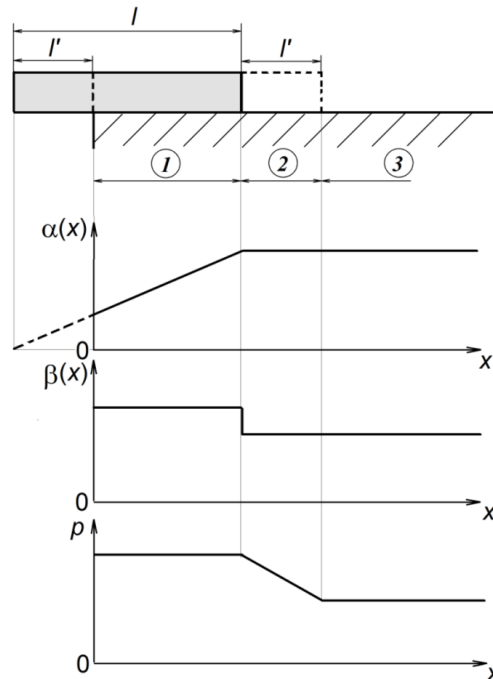


Fig. 4. Distribution functions of displacements $\alpha(x)$, $\beta(x)$ and pressures $p(x)$

Рис. 4. Функции распределения перемещений $\alpha(x)$, $\beta(x)$ и давлений $p(x)$

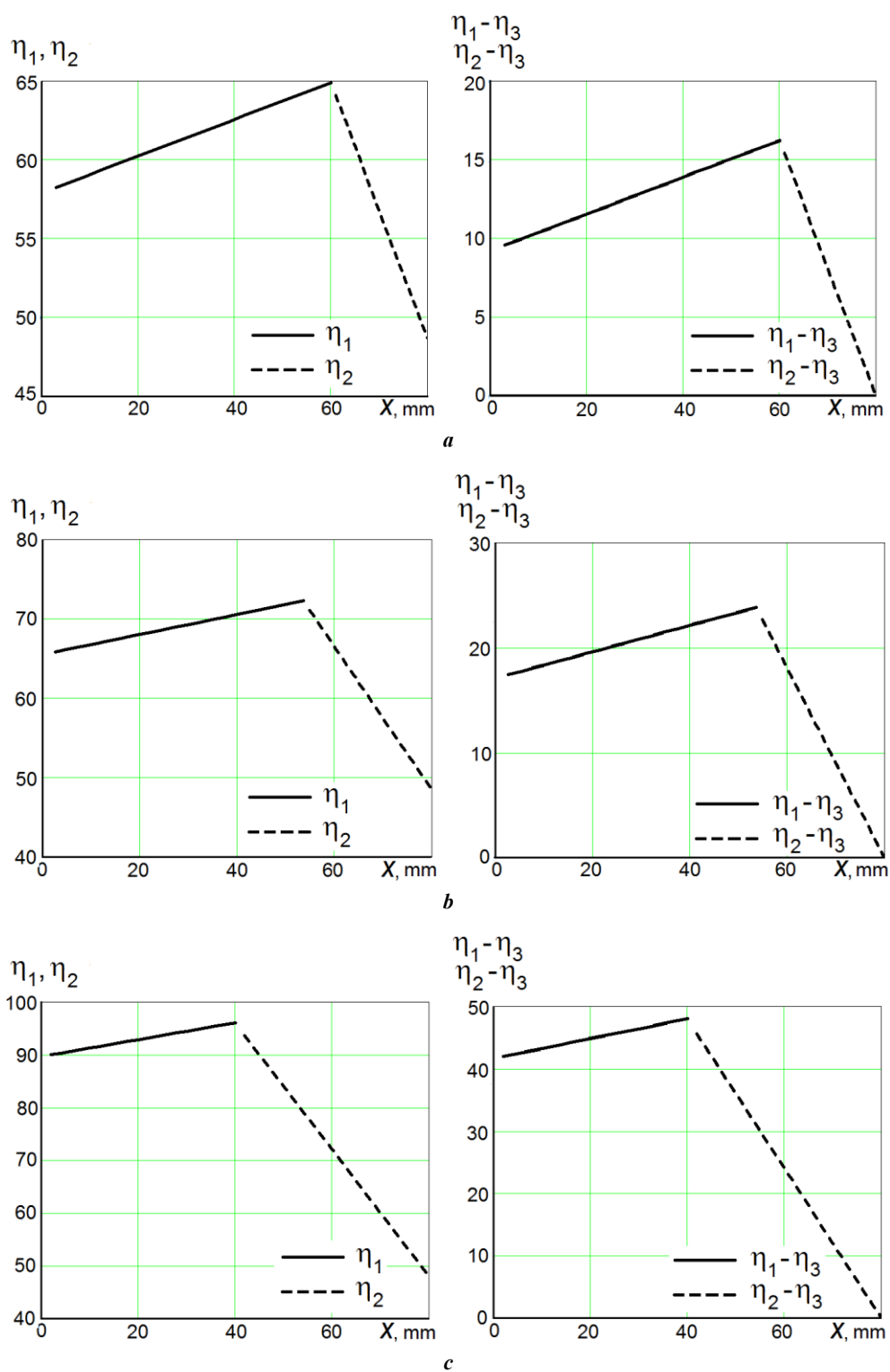


Fig. 5. Values of η_1, η_2, η_3 for $L=300$ mm; $l=80$ mm and $\zeta=1/7$: **a** – $\varepsilon=0.25$; **b** – $\varepsilon=0.33$; **c** – $\varepsilon=0.5$
Рис. 5. Значения η_1, η_2, η_3 для $L=300$ мм; $l=80$ мм и $\zeta=1/7$: **a** – $\varepsilon=0,25$; **b** – $\varepsilon=0,33$; **c** – $\varepsilon=0,5$

$$\eta_1 = \frac{U_1(x)b}{k\tau V_p P_y} = \left[\xi \alpha_1(x) + \frac{1}{L} \right] \frac{1}{(l-l')} = \left[\xi \frac{(x+l')}{Ll - (l-l')^2} + \frac{1}{L} \right] \frac{1}{(l-l')} ; \quad (16)$$

$$\eta_2 = \frac{U_2(x)b}{k\tau V_p P_y} = \left[\xi \alpha_2(x) + \frac{1}{L} \right] \frac{1}{l(l-l')} (2l-l'-x) = \left[\xi \frac{l}{Ll - (l-l')^2} + \frac{1}{L} \right] \frac{1}{l(l-l')} (2l-l'-x) ; \quad (17)$$

$$\eta_3 = \frac{U_3(x)b}{k\tau V_p P_y} = \left[\xi \alpha_3(x) + \frac{1}{L} \right] \frac{1}{l} = \left[\xi \frac{l}{Ll - (l-l')^2} + \frac{1}{L} \right] \frac{1}{l} . \quad (18)$$

Fig. 5 shows the values of η_1 , η_2 , $(\eta_1-\eta_3)$ and $(\eta_2-\eta_3)$ for sections 1 and 2 at different values of overrun, where $\varepsilon=l'/l$.

The graph in Fig. 6 shows the influence of the overrun value on the maximum values of $(\eta_1-\eta_3)$ when changing the length of the stone (80; 100; 120 mm).

DISCUSSION

From the graphs in Fig. 5 and 6, it follows that the maximum values $(\eta_1-\eta_3)$ located on the boundary of sections 1 and 2, and determining the maximum deviations from the straightness of the generating line of the machined hole will increase non-linearly as the overhang increases. The obtained result coincides with the conclusions of work [19] that in the presence of overrun, a shape error in the longitudinal section in the form of a saddle is inevitably formed, which increases as the overrun value increases.

The influence of the overrun value on the maximum values $(\eta_1-\eta_3)$ with a change in the length of the stone

shown in Fig. 6, indicates that the processing accuracy will increase with an increase in the length of the stone.

The developed model allows estimating the effect of the ratio of translational and rotational speeds, i. e. the coefficient ξ ($V_A = \xi V_p$). Fig. 7 shows the dependence $\max(\eta_1-\eta_3) = f(\xi)$ for $L=300$ mm, $l=100$ mm and $l'=0.3l$ indicating that the maximum deviation of the hole generating line from straightness depends linearly on the coefficient ξ . However, when comparing the results shown in Fig. 6 and 7, one can note that the influence of pressure due to a change in overrun is much more significant than the choice of the ratio of the translational and rotational speeds of the stone.

Taking into account specific honing conditions (k , τ , V_p , P_y , and b parameters) allows finding the $U_1(x)$, $U_2(x)$, $U_3(x)$ values using dependencies (12)...(18) and determining the linear dimensions of the deviations of the hole generating line. The obtained analytical dependencies allow estimating the accuracy of the hole geometric shape in the longitudinal section, during honing both with symmetrical and asymmetrical processing, when the overruns at the ends of the hole are not the same. This circumstance is especially relevant when honing blind holes.

CONCLUSIONS

Based on the developed honing model, taking into account the influence of the kinematic factor, dependencies are obtained that allow estimating the errors in the geometric shape of the hole in the longitudinal section. It is shown that the dominant factor is the presence of overrun. It is found that due to the presence of overrun, the machined surface has a tendency to saddle-shaped appearance. To improve the accuracy of the geometric shape of the hole in the longitudinal section during honing, well-founded recommendations can be used to increase the length of the honing stone and ensure constant pressure in the contact zone of the hone, and the machined surface during tool overrun.

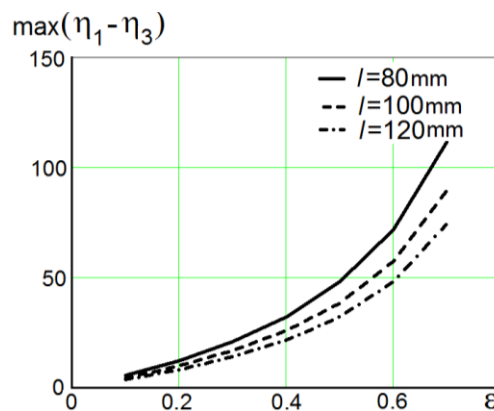


Fig. 6. The influence of the overrun value on the maximum values of $\eta_1-\eta_3$ when changing the length of the stone for $L=300$ mm and $\xi=1/7$

Рис. 6. Влияние величины перебега на максимальные значения $\eta_1-\eta_3$ при изменении длины бруска для $L=300$ мм и $\xi=1/7$

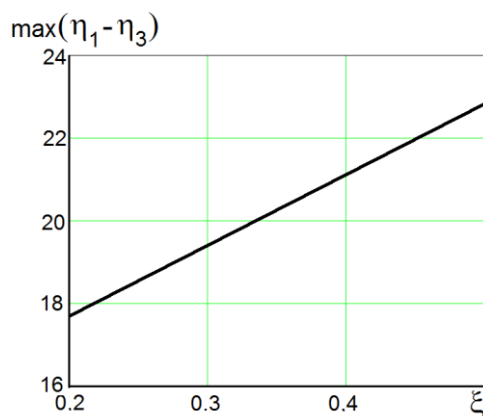


Fig. 7. Dependence of maximum $\eta_1 - \eta_3$ values on the ζ coefficient for $L=300$ mm; $l=100$ mm and $\varepsilon=0.3$
 Рус. 7. Зависимость максимальных значений $\eta_1 - \eta_3$ от коэффициента ζ для $L=300$ мм; $l=100$ мм и $\varepsilon=0,3$

REFERENCES

1. Sender P., Buj-Corral I. Influence of Honing Parameters on the Quality of the Machined Parts and Innovations in Honing Processes. *Metals*, 2023, vol. 13, no. 1, article number 140. DOI: [10.3390/met13010140](https://doi.org/10.3390/met13010140).
2. Buj-Corral I., Vivancos-Calvet J., Coba-Salcedo M. Modelling of surface finish and material removal rate in rough honing. *Precision Engineering*, 2014, vol. 38, no. 1, pp. 100–108. DOI: [10.1016/j.precisioneng.2013.07.009](https://doi.org/10.1016/j.precisioneng.2013.07.009).
3. Barakaev N.R., Isamov R.N., Rakhmonov S.K. ugli. Improvement of quality of internal cylindrical surfaces. *European Scholar Journal*, 2021, vol. 2, no. 6, pp. 60–63.
4. Pawlus P., Reizer R., Wieczorowski M. Analysis of surface texture of plateau-honed cylinder liner – A review. *Precision Engineering*, 2021, vol. 72, pp. 807–822. DOI: [10.1016/j.precisioneng.2021.08.001](https://doi.org/10.1016/j.precisioneng.2021.08.001).
5. Zhang Xueping, Zhou Zaoyang, Yao Zhenqiang, Xi Lifeng. Analytically Predicating the Multi-Dimensional Accuracy of the Honed Engine Cylinder Bore. *Journal of Tribology*, 2020, vol. 142, no. 9, article number 091201. DOI: [10.1115/1.4046677](https://doi.org/10.1115/1.4046677).
6. Yang Changyong, Su Hao, Gao Shaowu, Fu Yucan, Ding Wenfeng, Xu Jiuhoa. Surface quality and geometric accuracy control of fuel nozzle single-pass honing. *The International Journal of Advanced Manufacturing Technology*, 2021, vol. 114, pp. 3325–3336. DOI: [10.1007/s00170-021-07103-5](https://doi.org/10.1007/s00170-021-07103-5).
7. Bobrovskiy I.N. The characterization parameters of the texture after honing. *Bulletin of the South Ural State University. Series "Mechanical engineering industry"*, 2017, vol. 17, no. 3, pp. 26–35. DOI: [10.14529/engin170303](https://doi.org/10.14529/engin170303).
8. Hoffmeister H.-W., Grosse T., Gerdes A. Investigation of the Influence of Different Process Setting Parameters on the Surface Formation at Honing of Thermally Sprayed Layers. *Procedia CIRP*, 2012, vol. 1, pp. 371–376. DOI: [10.1016/j.procir.2012.04.066](https://doi.org/10.1016/j.procir.2012.04.066).
9. Schmitt C., Bahre D. An Approach to the Calculation of Process Forces During the Precision Honing of Small Bores. *Procedia CIRP*, 2013, vol. 7, pp. 282–287. DOI: [10.1016/j.procir.2013.05.048](https://doi.org/10.1016/j.procir.2013.05.048).
10. Barylski A., Sender P. The Proposition of an Automated Honing Cell with Advanced Monitoring. *Machines*, 2020, vol. 8, no. 4, article number 70. DOI: [10.3390/machines8040070](https://doi.org/10.3390/machines8040070).
11. Schmitt C., Bahre D. Analysis of the Process Dynamics for the Precision Honing of Bores. *Procedia CIRP*, 2014, vol. 17, pp. 692–697. DOI: [10.1016/j.procir.2014.01.055](https://doi.org/10.1016/j.procir.2014.01.055).
12. Akkurt A. Comparison of Roller Burnishing Method with Other Hole Surface Finishing Processes Applied on AISI 304 Austenitic Stainless Steel. *Journal of Materials Engineering and Performance*, 2010, vol. 20, pp. 960–968. DOI: [10.1007/s11665-010-9718-x](https://doi.org/10.1007/s11665-010-9718-x).
13. Pawlus P., Cieslak T., Mathia T. The study of cylinder liner plateau honing process. *Journal of Materials Processing Technology*, 2009, vol. 209, no. 20, pp. 6078–6086. DOI: [10.1016/j.jmatprotec.2009.04.025](https://doi.org/10.1016/j.jmatprotec.2009.04.025).
14. Sabri L., El Mansori M. Process variability in honing of cylinder liner with vitrified bonded diamond tools. *Surface and Coatings Technology*, 2009, vol. 204, no. 6-7, pp. 1046–1050. DOI: [10.1016/j.surfcoat.2009.05.013](https://doi.org/10.1016/j.surfcoat.2009.05.013).
15. Kapoor J. Parametric Investigations into Bore Honing through Response Surface Methodology. *Materials Science Forum*, 2014, vol. 808, pp. 11–18. DOI: [10.4028/www.scientific.net/MSF.808.11](https://doi.org/10.4028/www.scientific.net/MSF.808.11).
16. El Mansori M., Goedel B., Sabri L. Performance impact of honing dynamics on surface finish of precoated cylinder bores. *Surface and Coatings Technology*, 2013, vol. 215, pp. 334–339. DOI: [10.1016/j.surfcoat.2012.09.062](https://doi.org/10.1016/j.surfcoat.2012.09.062).
17. Babichev A.P., Polyanchikov Yu.N., Slavin A.V., Shumyacher V.M., Polyanchikova M.Yu., Gusakova L.V. *Khoningovanie* [Honing]. Volgograd, VolgGASU Publ., 2013. 246 p.
18. Kremen Z.I., Stratievskiy I.Kh. *Khoningovanie i superfinishirovanie detaley* [Honing and superfinishing of parts]. Leningrad, Mashinostroenie Publ., 1988. 137 p.
19. Buyukli I.M., Kolesnik V.M. Improving accuracy of holes honing. *Trudy Odesskogo politekhnicheskogo universiteta*, 2015, no. 1, pp. 34–43. EDN: [TSNFFJ](https://doi.org/10.26907/2542-0419.2015.1.34-43).
20. Naerman M.S., Popov S.A. *Pretzionnaya obrabotka detaley almaznymi i abrazivnymi bruskami* [Precision machining of parts with diamond and abrasive stones]. Moscow, Mashinostroenie Publ., 1971. 224 p.

СПИСОК ЛИТЕРАТУРЫ

1. Sender P., Buj-Corral I. Influence of Honing Parameters on the Quality of the Machined Parts and Innovations in Honing Processes // *Metals*. 2023. Vol. 13. № 1. Article number 140. DOI: [10.3390/met13010140](https://doi.org/10.3390/met13010140).
2. Buj-Corral I., Vivancos-Calvet J., Coba-Salcedo M. Modelling of surface finish and material removal rate in rough honing // *Precision Engineering*. 2014. Vol. 38. № 1. P. 100–108. DOI: [10.1016/j.precisioneng.2013.07.009](https://doi.org/10.1016/j.precisioneng.2013.07.009).
3. Barakaev N.R., Isamov R.N., Rakhmonov S.K. ugli. Improvement of quality of internal cylindrical surfaces // *European Scholar Journal*. 2021. Vol. 2. № 6. P. 60–63.
4. Pawlus P., Reizer R., Wieczorowski M. Analysis of surface texture of plateau-honed cylinder liner – A review // *Precision Engineering*. 2021. Vol. 72. P. 807–822. DOI: [10.1016/j.precisioneng.2021.08.001](https://doi.org/10.1016/j.precisioneng.2021.08.001).
5. Zhang Xueping, Zhou Zaoyang, Yao Zhenqiang, Xi Lifeng. Analytically Predicating the Multi-Dimensional Accuracy of the Honed Engine Cylinder Bore // *Journal of Tribology*. 2020. Vol. 142. № 9. Article number 091201. DOI: [10.1115/1.4046677](https://doi.org/10.1115/1.4046677).
6. Yang Changyong, Su Hao, Gao Shaowu, Fu Yucan, Ding Wenfeng, Xu Jihua. Surface quality and geometric accuracy control of fuel nozzle single-pass honing // *The International Journal of Advanced Manufacturing Technology*. 2021. Vol. 114. P. 3325–3336. DOI: [10.1007/s00170-021-07103-5](https://doi.org/10.1007/s00170-021-07103-5).
7. Бобровский И.Н. Параметры характеризации текстуры после хонингования // *Вестник Южно-Уральского государственного университета. Серия: Машиностроение*. 2017. Т. 17. № 3. С. 26–35. DOI: [10.14529/engin170303](https://doi.org/10.14529/engin170303).
8. Hoffmeister H.-W., Grosse T., Gerdes A. Investigation of the Influence of Different Process Setting Parameters on the Surface Formation at Honing of Thermally Sprayed Layers // *Procedia CIRP*. 2012. Vol. 1. P. 371–376. DOI: [10.1016/j.procir.2012.04.066](https://doi.org/10.1016/j.procir.2012.04.066).
9. Schmitt C., Bahre D. An Approach to the Calculation of Process Forces During the Precision Honing of Small Bores // *Procedia CIRP*. 2013. Vol. 7. P. 282–287. DOI: [10.1016/j.procir.2013.05.048](https://doi.org/10.1016/j.procir.2013.05.048).
10. Barylski A., Sender P. The Proposition of an Automated Honing Cell with Advanced Monitoring // *Machines*. 2020. Vol. 8. № 4. Article number 70. DOI: [10.3390/machines8040070](https://doi.org/10.3390/machines8040070).
11. Schmitt C., Bahre D. Analysis of the Process Dynamics for the Precision Honing of Bores // *Procedia CIRP*. 2014. Vol. 17. P. 692–697. DOI: [10.1016/j.procir.2014.01.055](https://doi.org/10.1016/j.procir.2014.01.055).
12. Akkurt A. Comparison of Roller Burnishing Method with Other Hole Surface Finishing Processes Applied on AISI 304 Austenitic Stainless Steel // *Journal of Materials Engineering and Performance*. 2010. Vol. 20. P. 960–968. DOI: [10.1007/s11665-010-9718-x](https://doi.org/10.1007/s11665-010-9718-x).
13. Pawlus P., Cieslak T., Mathia T. The study of cylinder liner plateau honing process // *Journal of Materials Processing Technology*. 2009. Vol. 209. № 20. P. 6078–6086. DOI: [10.1016/j.jmatprotec.2009.04.025](https://doi.org/10.1016/j.jmatprotec.2009.04.025).
14. Sabri L., El Mansori M. Process variability in honing of cylinder liner with vitrified bonded diamond tools // *Surface and Coatings Technology*. 2009. Vol. 204. № 6-7. P. 1046–1050. DOI: [10.1016/j.surfcoat.2009.05.013](https://doi.org/10.1016/j.surfcoat.2009.05.013).
15. Kapoor J. Parametric Investigations into Bore Honing through Response Surface Methodology // *Materials Science Forum*. 2014. Vol. 808. P. 11–18. DOI: [10.4028/www.scientific.net/MSF.808.11](https://doi.org/10.4028/www.scientific.net/MSF.808.11).
16. El Mansori M., Goeldel B., Sabri L. Performance impact of honing dynamics on surface finish of precoated cylinder bores // *Surface and Coatings Technology*. 2013. Vol. 215. P. 334–339. DOI: [10.1016/j.surfcoat.2012.09.062](https://doi.org/10.1016/j.surfcoat.2012.09.062).
17. Бабичев А.П., Полянчиков Ю.Н., Славин А.В., Шумячер В.М., Полянчикова М.Ю., Гусакова Л.В. Хонингование. Волгоград: ВолгГАСУ, 2013. 246 с.
18. Кремень З.И., Стратиевский И.Х. Хонингование и суперфиниширование деталей. Л.: Машиностроение, 1988. 137 с.
19. Буюкли И.М., Колесник В.М. Повышение точности хонингования отверстий // *Труды Одесского политехнического университета*. 2015. № 1. С. 34–43. EDN: [TSNFFJ](https://doi.org/10.26907/2542-0419.2015.1.34-43).
20. Наерман М.С., Попов С.А. Прецизионная обработка деталей алмазными и абразивными брусками. М.: Машиностроение, 1971. 224 с.

Точность геометрической формы отверстия в продольном сечении при хонинговании

© 2024

Денисенко Александр Федорович^{*1}, доктор технических наук, профессор, профессор кафедры «Технология машиностроения, станки и инструменты»

*Гришин Роман Георгиевич*², кандидат технических наук, доцент, доцент кафедры «Технология машиностроения, станки и инструменты»

*Антипова Евгения Дмитриевна*³, аспирант кафедры «Технология машиностроения, станки и инструменты» Самарский государственный технический университет, Самара (Россия)

*E-mail: tmsi@samgtu.ru,
sammortor@yandex.ru

¹ORCID: <https://orcid.org/0000-0001-6393-2831>

²ORCID: <https://orcid.org/0000-0003-4511-9147>

³ORCID: <https://orcid.org/0000-0002-1759-7080>

Поступила в редакцию 29.02.2024

Принята к публикации 16.07.2024

Аннотация: Широкое применение хонингования в качестве финишной обработки внутренних цилиндрических поверхностей для цилиндропоршневых систем, используемых в ряде конструкций, обусловлено высокой точностью, измеряемой десятками долями микрометра, и высокой производительностью процесса. Важнейшим показателем надежной работы цилиндропоршневых систем являются высокие требования к геометрической точности отверстий. В связи с отсутствием достаточных теоретических обоснований выбора параметров хонингования, обеспечивающих точность геометрической формы отверстия в продольном сечении, была предложена модель образования погрешностей геометрической формы отверстия, построенная на учете кинематических характеристик процесса, включающих соотношение размеров хонинговального бруска, длины отверстия, хода хонинговальной головки, соотношения скоростей поступательного и вращательного движений и силового воздействия в зоне обработки, которое изменялось за счет наличия перебега хонинговального бруска. Для получения аналитических зависимостей, обеспечивающих минимизацию отклонений формы, были рассмотрены условия съема припуска для точек обрабатываемой поверхности, величина которого принималась пропорциональной пути перемещения и величине давления. С этой целью были построены графики функций распределения перемещений и изменения давлений в зависимости от координаты расположения точки на образующей обрабатываемого отверстия. В результате использования полученных аналитических зависимостей установлено потенциальное появление погрешности формы в виде седлообразности, доминирующим фактором влияния на значение которой является величина перебега хонинговального бруска. Вместе с тем показано, что соотношение скоростей поступательного и вращательного движений несущественно влияет на нарушение формы в продольном сечении.

Ключевые слова: хонингование; геометрическая точность отверстий; кинематические характеристики хонингования; величина перебега; функция распределения перемещений.

Для цитирования: Денисенко А.Ф., Гришин Р.Г., Антипова Е.Д. Точность геометрической формы отверстия в продольном сечении при хонинговании // Frontier Materials & Technologies. 2024. № 3. С. 53–62. DOI: 10.18323/2782-4039-2024-3-69-5.

The influence of 3D printing mode on the chemical composition and structure of 30HGSA steel

© 2024

Yury G. Kabaldin, Doctor of Sciences (Engineering), Professor,
professor of Chair “Technology and Equipment of Mechanical Engineering”

Maksim S. Anosov*, PhD (Engineering), Associate Professor,
assistant professor of Chair “Technology and Equipment of Mechanical Engineering”

Yuliya S. Mordovina, postgraduate student,
educational process engineer of the Institute of Retraining of Specialists

Mikhail A. Chernigin, postgraduate student,
engineer of Chair “Technology and Equipment of Mechanical Engineering”

R.E. Alekseev Nizhny Novgorod State Technical University, Nizhny Novgorod (Russia)

*E-mail: anosov.ms@nntu.ru,
anosov-maksim@list.ru

Received 31.07.2023

Accepted 18.12.2023

Abstract: The authors carried out the study of the influence of 3D printing modes on the structure and chemical composition of 30HGSA steel (chromansil) samples produced by the method of additive electric arc surfacing. To study the influence of the electric arc surfacing mode on the chemical composition of the steel under study, an optical emission analysis of the samples was carried out. The influence of the surfacing mode on the resulting structure was assessed over the entire height of the deposited walls at magnifications of $\times 50$, $\times 100$, $\times 200$ and $\times 500$. Optical emission analysis identified a change in the material chemical composition associated with the loss of chemical elements. It was found that the degree of loss of C, Cr and Si increases almost linearly and is directly proportional to the surfacing heat input (Q , J/mm). The exact influence of an increase in the surfacing heat input on the Mn content was not found, but a relationship between the degree of its loss and the voltage (U , V) during surfacing of samples was identified. Microstructural studies of all samples did not reveal a large number of systemically formed structural defects characteristic of cast and welded products (pores, shrinkage cavities, etc.), which confirms the high quality of the metal in goods produced by electric arc surfacing. Analysis of micrographs taken in different areas of the samples allowed determining that the metal microstructure does not undergo significant changes under different surfacing modes; the main tendencies in changes in the structure along the height of the sample are preserved. All samples demonstrated the formation of a highly dispersed structure, regardless of the 3D printing parameters. The most favorable metal structure, suitable for subsequent use in the production of goods using additive manufacturing, was recognized as the structure of the sample deposited using mode No. 5 ($I=160$ A, $U=24$ V, $Q=921.6$ J/mm). This mode can be used for further study of the problems of additive electric arc surfacing of 30HGSA steel.

Keywords: 30HGSA steel; additive electric arc surfacing; optical emission analysis; metallographic study; additive manufacturing.

Acknowledgements: The study was supported by the grant of the Russian Science Foundation No. 22-79-00095 “Development of scientific and technological foundations for the structure formation of structural materials obtained by additive electric arc growth for the formation of mechanical properties under fatigue using artificial intelligence approaches”, <https://www.rscf.ru/project/22-79-00095/>.

For citation: Kabaldin Yu.G., Anosov M.S., Mordovina Yu.S., Chernigin M.A. The influence of 3D printing mode on the chemical composition and structure of 30HGSA steel. *Frontier Materials & Technologies*, 2024, no. 3, pp. 63–73. DOI: 10.18323/2782-4039-2024-3-69-6.

INTRODUCTION

The intensive development of 3D printing (additive manufacturing) technologies, leads to the necessity of a thorough study of the mechanical properties, structure and chemical composition of metals produced by this method. Today, the main methods of 3D metal printing are layer-by-layer powder melting (Selective Laser Melting, SLM), laser powder surfacing (Laser Engineered Net Shape, LENS / Direct Metal Deposition, DMD) and electric arc surfacing (Wire and Arc Additive Manufacturing, WAAM) [1]. The most technologically produc-

tive, and simplest is the method of 3D printing by WAAM, used in this work [2; 3].

The advantages of additive methods include, the ability to automate fully the process of producing goods; a significant reduction in material consumption when manufacturing products from expensive materials, such as titanium and nickel alloys; the possibility of small-scale production of goods, which is unprofitable when using traditional production methods [4–6].

Despite the noted advantages of additive manufacturing methods, the application of these technologies faces

a number of difficulties due to the complexity of selecting printing modes, and thermal cycle parameters. Depending on the selected 3D printing mode, it is possible to obtain different mechanical properties of the material.

SLM is a technology for manufacturing complex products by laser melting of metal powder, using mathematical CAD models. SLM is considered a high-energy process. At the point where the powder melts, the energy density is higher compared to other electric arc processes (for example, welding), but lower than with laser irradiation [7]. One of the problems of SLM-produced parts is the relatively high surface roughness, which reduces fatigue resistance by increasing the stress concentration on the sample surface [8].

Laser powder surfacing (LENS/DMD) is an additive technology for growing a part by fusing a powder material layer onto a substrate. The laser beam creates a welding pool, into which the metal in powder form is injected, where it melts and solidifies to form a metallic bond to the substrate. Typically, this process uses a single-mode continuous wave solid-state fiber laser, operating at a wavelength of 1075 nm. During the process, metal powder from the feed system is automatically fed to the substrate, which is lowered to a height equal to the deposited layer thickness. However, it is noted that the laser surfacing method does not have the reproducibility of the chemical composition, and mechanical properties of the final products [9; 10], which is a serious shortcoming.

WAAM is a relatively new technology emerged in the 1990s. It consists of fusing conventional welding wire widely available commercially onto a substrate, which results in the finished part formation. Compared to conventional manufacturing, WAAM allows reducing production time by 40–60 % and post-processing time by 15–20 %, depending on part size. Thus, aircraft landing gear stiffeners using this technology are manufactured with raw material savings of approximately 78 % compared to conventional production [11]. Metals with good weldability can potentially be used for the WAAM process, and so far, researchers have successfully produced objects from the alloys based on Ti [11], Al [12], steel [13], and Ni [14] using this method.

Stainless low carbon steels (austenitic, martensitic and duplex) are the most preferred candidates for WAAM surfacing due to their combination of mechanical properties, high corrosion resistance and weldability. However, this cannot be said about medium-carbon steels widely used in mechanical engineering, aircraft manufacturing and other fields. Therefore, the study of the behavior of medium-carbon steels during the WAAM

process with the prospect of using the developments in industry is of interest.

During the process of surfacing layers, the metal is in a liquid state and is then subjected to multiple heating cycles to temperatures above critical, which leads to a possible change in the chemical composition of the starting material. As a result of non-equilibrium crystallization and repeated heating of the metal, the microstructure of the resulting material differs significantly from the structure of the material obtained from rolled products [15–17].

Foreign research is increasingly considering additive technologies, including WAAM. At the same time, in Russia, these methods are studied locally and are not so widespread. However, it is the use of additive technologies that can reduce the cost of single and small-scale production of goods from widely used structural materials, such as 30HGSA steel. The development of these technologies will contribute to the development of Russian science and import substitution.

The purpose of this research is to study the influence of additive electric arc surfacing modes on the chemical composition and microstructure of 30HGSA steel.

METHODS

The research material was 30HGSA structural steel (GOST 4543-2016 "Rolled Products Made of Alloy Structural Steel. Technical Specifications"). Table 1 presents the grade chemical composition of the deposited 30HGSA steel.

Samples for studying the chemical composition and microstructure of the deposited metal were prepared on a specialized stand for additive electric arc surfacing [18]. Nine blanks in the form of walls (Fig. 1) were produced using various printing modes. The width of the deposited walls was 1 surfacing bead, the height of the walls was formed by depositing 10 layers. A drop of metal was transferred by short circuits.

The surfacing mode was specified by the following parameters: current (I , A), voltage (U , V), arc gap (z , mm), wire feed speed (V , mm/s), and shielding gas consumption. In this case, the arc gap, wire feed speed and shielding gas consumption were constant for all experiments, and amounted to 11 mm and 200 mm/min, respectively (determined by preliminary tests) [19; 20].

Based on the 3D printing modes, the heat input (Q) of the process (electrical energy consumed per length unit of the seam) was determined as one of the complex informative parameters, in accordance with GOST R ISO 857-1-2009, taking into account the energy loss coefficient of 0.8:

Table 1. Chemical composition of the 30HGSA steel (GOST 4543-2016)
Таблица 1. Химический состав стали 30ХГСА (ГОСТ 4543-2016)

Element	C	Si	Mn	Cr	S	P
Content, %	0.28–0.34	0.90–1.20	0.80–1.10	0.80–1.10	<0.025	<0.025

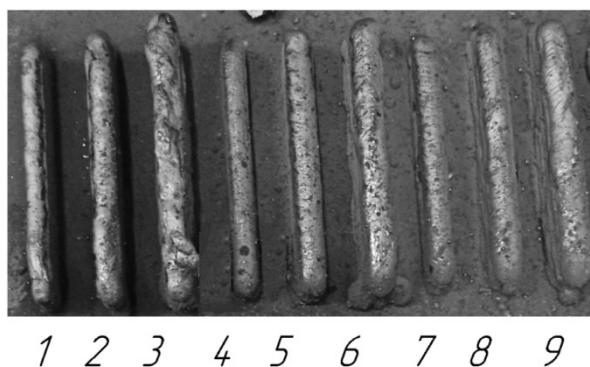


Fig. 1. General view of the deposited walls
Рис. 1. Общий вид наплавленных стенок

$$Q = \frac{0,8 I U}{V}$$

Table 2 shows the surfacing modes for each welded blank, and the values of the heat input of the surfacing process.

Samples were cut from a wall deposited using the WAAM method across the direction of deposition to study changes in the structure and hardness along the height of the grown metal.

The material chemical composition was determined by emission spectral analysis on a Foundry-Master stationary optical emission analyzer – a high-precision laboratory multi-matrix analyzer with a sensitivity range for most elements of 0.001 % (according to some data, up to 0.0001 %).

The metal microstructure was studied on microsections using an Altami MET 1C optical microscope at magnifications of $\times 50$, $\times 100$, $\times 200$, and $\times 500$. Sample preparation was carried out according to standard technique (mechanical grinding with sandpaper of different grain sizes and polishing using various pastes). Etching was carried out with a 4 % aqueous solution of nitric acid [21].

RESULTS

During the study of the chemical composition of the samples, data reflected in the diagram (Fig. 2) were obtained. The original wire was sample No. 0 shown in Fig. 2. The content of other chemical elements acting as

impurities is constant in all studied samples, so these elements are not shown in Fig. 2.

During the study of the microstructure of the samples, practically no technological defects were identified. Large single defects were found only on samples manufactured using modes No. 3 and 7 (Fig. 3).

To compare the quality of different surfacing modes, the microstructure was studied in different regions along the height of the deposited wall of the samples (Fig. 4).

The main microstructural changes are presented in Fig 5–7, and correspond to samples melted using modes No. 1, 5 and 9, respectively, since they allow assessing the main changes in the height of the deposited metal most completely.

In sample No. 1, the wall microstructure near the substrate consists of tempered bainite (Fig. 5 a). In the center of the sample, the bainite structure is generally preserved, but the appearance of other structural components (troostite) is visible. At the top of the sample, the microstructure changes, and consists predominantly of troostosorbite (Fig. 5 c), while the columnarity of the grains caused by the temperature gradient during cooling of the deposited bead is partially retained. Clearly defined ferrite grains are observed. One should note that the last deposited layers of sample No. 1 are characterized by a rather high degree of grain size nonhomogeneity.

The microstructure of sample No. 5 near the substrate is also represented by tempered bainite (Fig. 6 a). In this sample, the tendency for a uniform transition from the bainite structure to the troostosorbite structure

Table 2. Deposition modes for each blank produced by the WAAM method
Таблица 2. Режимы наплавки для каждой заготовки, полученной методом WAAM

Blank No.	1	2	3	4	5	6	7	8	9
<i>I, A</i>	120	160	200	120	160	200	120	160	200
<i>U, B</i>	18	18	18	24	24	24	27	27	27
<i>Q, J/mm</i>	518.4	691.2	864.0	691.2	921.6	1,152.0	777.6	1,036.8	1,296.0

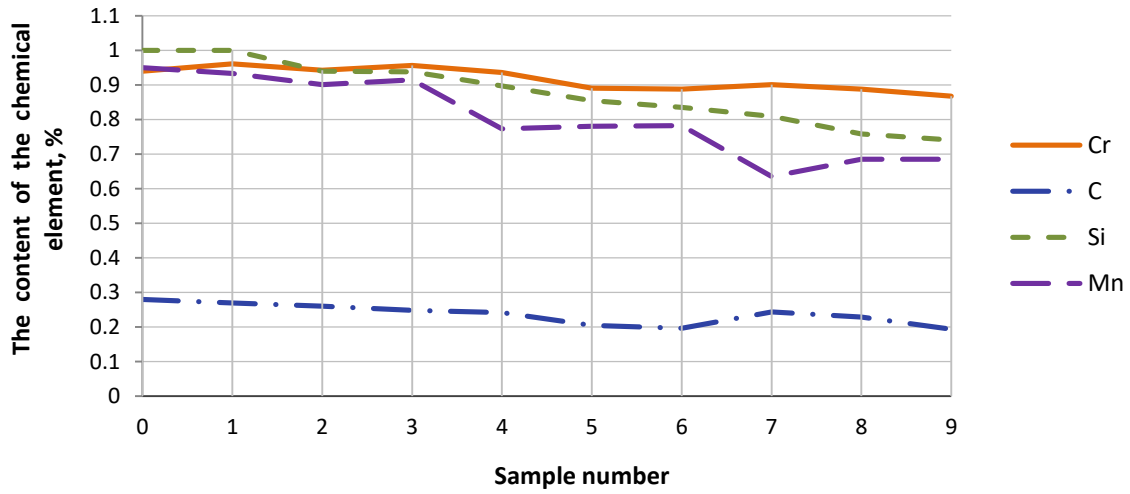


Fig. 2. Change in the content of alloying elements depending on the deposition mode
Рис. 2. Изменение содержания легирующих элементов в зависимости от режима наплавки

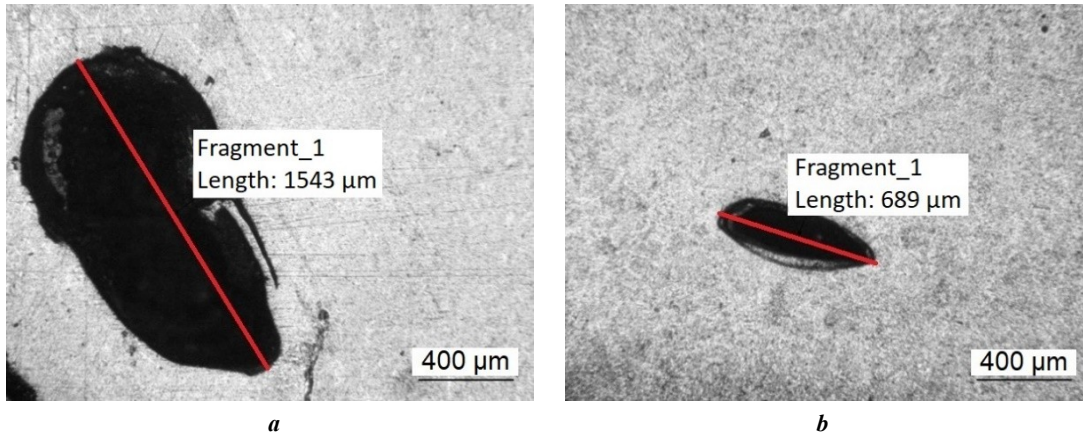


Fig. 3. Defects identified in the structure of samples, $\times 50$:
a – sample No. 3; **b** – sample No. 7
Рис. 3. Дефекты, выявленные в структуре образцов, $\times 50$:
a – образец № 3; **b** – образец № 7

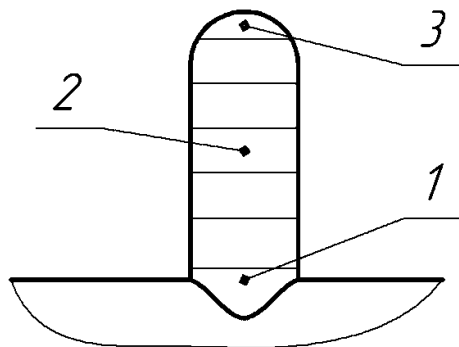


Fig. 4. Location of characteristic zones for studying the microstructure of the sample:
1 – base; **2** – center; **3** – top
Рис. 4. Расположение характерных зон для исследования микроструктуры образца:
1 – основание; **2** – центр; **3** – вершина

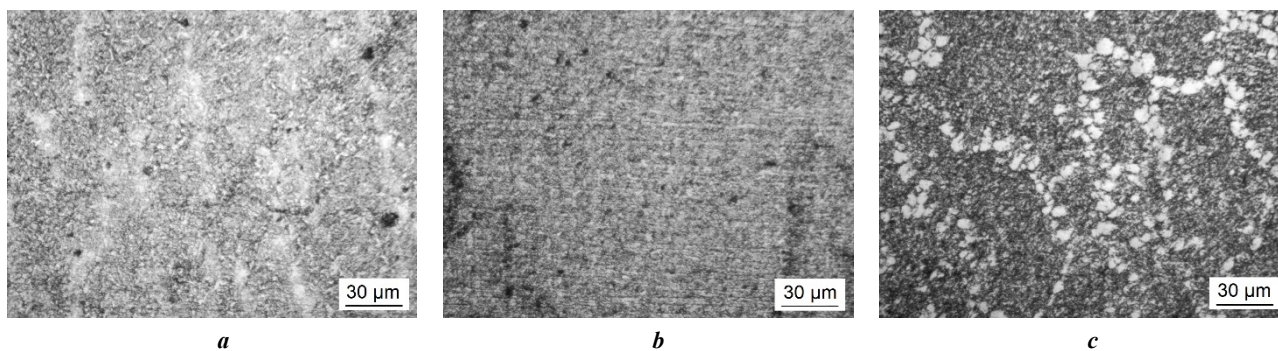


Fig. 5. Microstructure of the deposited wall (30HGSA steel, sample No. 1, $Q=518.4$ J/mm) ($\times 500$):
a – near the substrate; **b** – in the center of the sample; **c** – at the top of the sample

Рис. 5. Микроструктура наплавленной стенки (сталь 30ХГСА, образец № 1, $Q=518,4$ Дж/мм) ($\times 500$):
a – вблизи подложки; **b** – в центре образца; **c** – в вершине образца

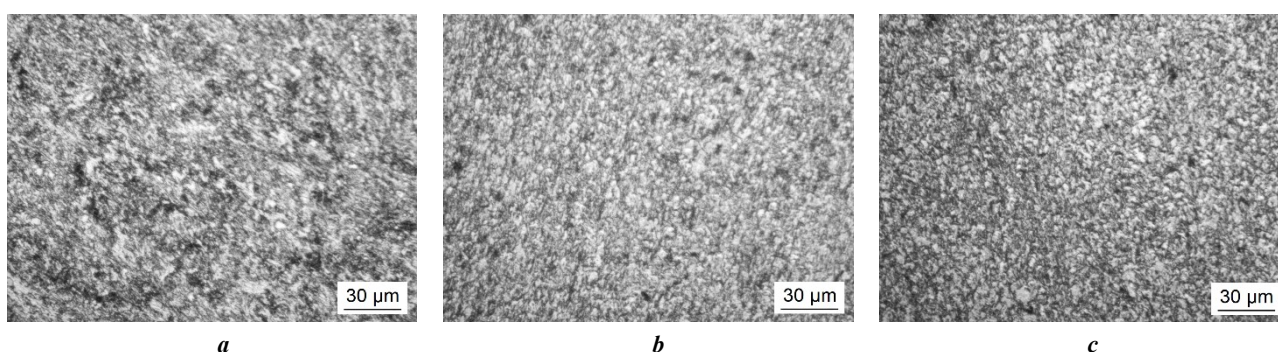


Fig. 6. Microstructure of the deposited wall (30HGSA steel, sample No. 5, $Q=921.6$ J/mm) ($\times 500$):
a – near the substrate; **b** – in the center of the sample; **c** – at the top of the sample

Рис. 6. Микроструктура наплавленной стенки (сталь 30ХГСА, образец № 5, $Q=921,6$ Дж/мм) ($\times 500$):
a – вблизи подложки; **b** – в центре образца; **c** – в вершине образца

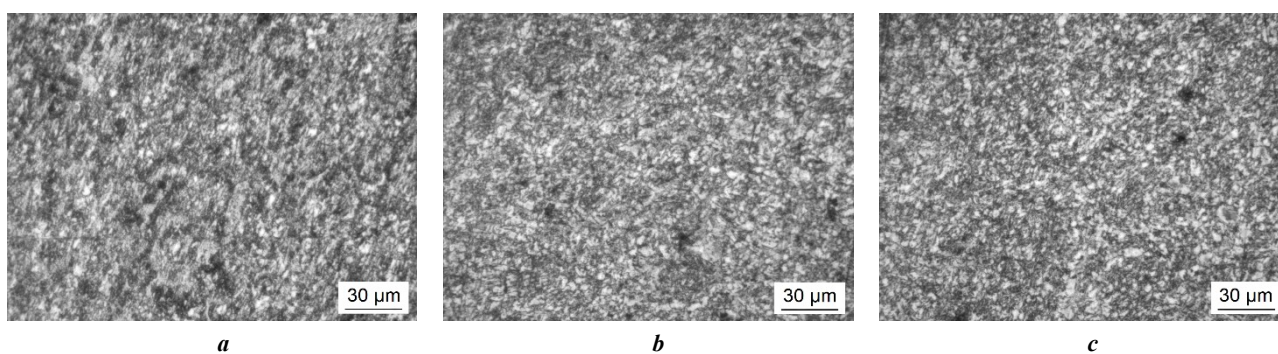


Fig. 7. Microstructure of the deposited wall (30HGSA steel, sample No. 9, $Q=1296$ J/mm) ($\times 500$):
a – near the substrate; **b** – in the center of the sample; **c** – at the top of the sample

Рис. 7. Микроструктура наплавленной стенки (сталь 30ХГСА, образец № 9, $Q=1296$ Дж/мм) ($\times 500$):
a – вблизи подложки; **b** – в центре образца; **c** – в вершине образца

remains, but the structure change proceeds more smoothly. The microstructure of all areas does not reveal grain size nonhomogeneity, and grain columnarity in the last surfacing beads.

The microstructure of sample No. 9 near the surfacing, mainly consists of tempered bainite (Fig. 7 a). One should note that with this surfacing mode, inclusions of other

structural components (troostosorbite), are visible in the main bainite structure. This sample also retains the tendency of a gradual transition from the bainite structure to the troostosorbite structure, but it is represented by larger grains. In general, the microstructure of the sample deposited using mode No. 9 is coarser than the structure of the other samples.

In samples No. 1–3, an area with a sharp change in the structure relating to the last 2–3 layers of surfacing was identified (Fig. 8).

The study of micrographs of different samples did not reveal a large number of structural defects characteristic of cast and welded products (pores, shrinkage cavities, etc.). One should note that a highly dispersed structure was obtained for all surfacing modes.

DISCUSSION

Based on the results of spectral analysis, the authors found that when manufacturing products using 3D metal printing technology, there is a decrease in the content of carbon and main alloying elements, such as Si, Mn and Cr. This phenomenon actively manifests itself during welding and casting of metals, and is associated with the material liquid state. Technologically, the process of 3D metal printing is similar to welding; therefore, a change in the content of chemical elements is a loss of metal.

It was found that the C, Si and Cr content decreases almost linearly. One can note that when increasing the heat input of the surfacing process, the proportion of loss increases. The influence of the heat input of surfacing on the Mn content is not so clear. It was found that the loss of Mn is the same for samples deposited with the same voltage. The decrease in Mn content occurs in steps and corresponds to a voltage increase during surfacing.

Microstructural analysis revealed virtually no defects characteristic of cast or welded products (pores, shrinkage cavities, etc.) [22]. Large single defects (shrinkage cavities) were detected only in samples manufactured according to modes No. 3 and 7 (Fig. 3). The above defects were not detected in samples made using other surfacing modes.

When studying other sections of samples No. 3 and 7, defects were not re-identified, which may indicate the non-

systemic nature of the formation of shrinkage cavities in the samples. One can conclude that the occurrence of cavities is not related to the surfacing mode, and is caused by a single violation of the surfacing technology.

Summarizing the microstructural analysis data, one can identify zoning in the deposited material depending on the order of the deposited layer, with the zones smoothly transitioning from one to another (except for samples No. 1–3). Thus, near the substrate, the structure is represented by tempered bainite. The occurrence of this structure is caused by a rather high cooling temperature after surfacing, and the supply of sufficient heat energy during surfacing of subsequent layers. The microstructure of the middle deposited layers of 30HGSA steel, in addition to bainite, contained troostite, which can be explained by the slower cooling of this area, during which the S-curve nose was affected (Fig. 5 b). The energy supplied after surfacing is also sufficient for tempering processes to occur. According to mode No. 5, the most homogeneous microstructure is formed, which should ensure isotropy of properties.

In the last deposited layers, troostosorbite is detected, but in sample No. 1, grain size nonhomogeneity with a sharp zone transition is observed (Fig. 8), which may be associated with the shorter time when the metal of these areas is at temperatures close to critical; sample No. 9 has coarse grains with columnar crystals. These shortcomings lead to a decrease in strength properties, and unsatisfactory results during subsequent heat treatment.

Unlike samples No. 1 and 9, these defects were not found in the upper layers of sample No. 5. Consequently, even without heat treatment, this structure is more efficient, and further heat treatment according to the correct mode will only improve the properties of the deposited 30HGSA metal.

The described differences in the microstructure of the samples are explained by the heat input during

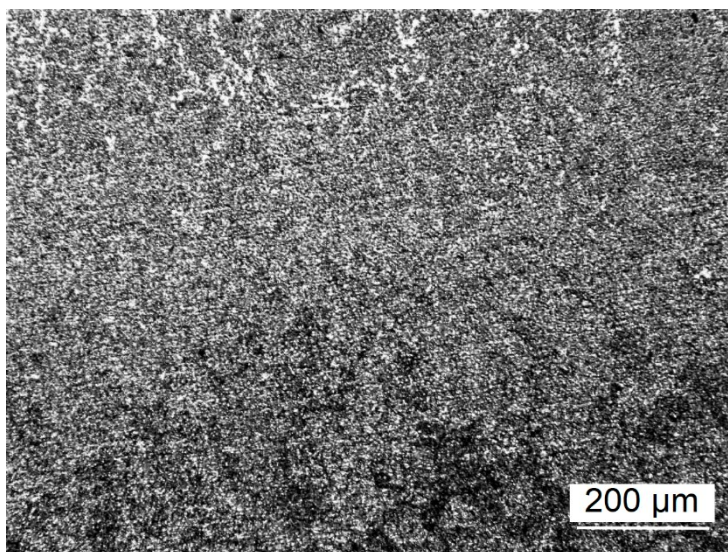


*Fig. 8. Example of an area with a sharp change in the structure, $\times 100$
Рис. 8. Пример области с резким изменением структуры, $\times 100$*

surfacing, and the cooling rate. Due to the relatively small heat input (compared to other modes), sample No. 1 has a lower cooling rate, which facilitates the phase transformation of steel, through the diffusion mechanism. Therefore, troostite and ferrite grains appear in the microstructure (Fig. 5 c).

For sample No. 5, the amount of heat input during the surfacing process is optimal, so the temperature gradient between the metal and the environment is sufficient, so that after surfacing, the 30HGSA steel cools at the rate necessary for the formation of highly dispersed bainite. A similar bainitic structure in the 30HGSA steel is formed during the fabrication of welds [23].

The heat input of surfacing for sample No. 9 promotes the bainite formation; however, a large amount of heat input provokes grain growth, which makes the structure of the upper layers coarser.

Pores of various sizes were observed in the deposited samples (Fig. 3), and this fact raises the question of the permissible porosity level. The same question arose in [24] in relation to SLM technology, which is related to WAAM technology. As the authors note, controlling the energy density in limited areas of the SLM process currently used for porosity prediction is insufficient considering the complexity of the process. This statement is also applicable to WAAM.

Thus, the 30HGSA steel microstructure has zones whose structural composition does not depend on the surfacing mode, but the surfacing mode affects the structure dispersion and defectiveness. Different results were obtained for 09G2S and 06H19N9T steels [25]. Obtaining results different from those described above may be caused by different weldability of the steel grades under consideration. 30HGSA steel, unlike 09G2S and 06H19N9T steels, is partially weldable. The presence of zoning along the height of the deposited metal was also observed in titanium alloys [26].

Microstructural analysis of samples produced under different surfacing modes identified that the most favorable metal structure is the structure of sample No. 5 ($I=160$ A, $U=24$ V, $Q=921.6$ J/mm), which gives grounds to use it as a working material for further research.

It is necessary as well to carry out additional work to demonstrate the corrosion resistance of samples produced by the WAAM method. In paper [27], using the example of corrosion-resistant SS 316 steel, it is shown that samples produced by the WAAM method have higher corrosion resistance than samples produced by sand casting. At the same time, the lower deposited layers of the WAAM samples had lower corrosion resistance than the upper ones, which is associated with the difference in heat input. Taking into account the non-homogeneity of the 30HGSA steel microstructure along the height of the deposited wall, one should also expect a scatter in the corrosion properties in this section.

However, in [28], the opposite is shown using the example of magnesium alloys. The authors tried to obtain a magnesium alloy using WAAM technology with the prospect of using it in biomedicine. However, at this stage of technology development, this is impossible due to the reduced corrosion resistance, and biocompatibility of magne-

sium alloys produced by the WAAM method. Similar problems are observed for steels.

The work [29] raises the problems of certification of WAAM products, and non-destructive testing. This is a labor-intensive task, since initially it is necessary to remove the WAAM surfacing method from the category of research ones, and used mainly for single production. Only after this, it will be possible to talk about the development of standards that will allow evaluating correctly, the properties of manufactured products.

CONCLUSIONS

1. When surfacing products using various surfacing modes, a change in the material chemical composition is observed, associated with the loss of chemical elements. The degree of loss of C, Cr and Si increases with increasing heat input of the layer surfacing (Q) and changes almost linearly. Mn loss depends on the 3D printing voltage.

2. The metal microstructure does not undergo significant changes when the surfacing mode changes. The main tendencies in the change in the structure along the sample height are preserved: a gradual transition from a bainite structure near the substrate to a troostosorbite structure corresponding to the last surfacing beads, is observed.

3. For all samples, a large number of systemically formed structural defects characteristic of cast and welded products (pores, shrinkage cavities, etc.) was not identified. One should note that a highly dispersed structure was obtained in all samples, regardless of the 3D printing parameters. The exception is the sample deposited using mode No. 9 ($I=200$ A, $U=27$ V, $Q=1296$ J/mm): in this case, the resulting structure was characterized by a larger grain size than the structure of the other samples.

4. The structure of sample No. 5 ($I=160$ A, $U=24$ V, $Q=921.6$ J/mm) was recognized as the most favorable metal structure suitable for subsequent use in the production of goods using 3D printing.

REFERENCES

- Li Johnnie Liew Zhong, Alkahari M.R., Rosli N.A.B., Hasan R., Sudin M.N., Ramli F.R. Review of Wire Arc Additive Manufacturing for 3D Metal Printing. *International Journal of Automation Technology*, 2019, vol. 13, no. 3, pp. 346–353. DOI: [10.20965/ijat.2019.p0346](https://doi.org/10.20965/ijat.2019.p0346).
- Ding Donghong, Pan Zengxi, Cuiuri D., Li Huijun. Wire-feed additive manufacturing of metal components: technologies, developments and future interests. *The International Journal of Advanced Manufacturing Technology*, 2015, vol. 81, pp. 465–481. DOI: [10.1007/s00170-015-7077-3](https://doi.org/10.1007/s00170-015-7077-3).
- Wu Bintaο, Pan Zengxi, Ding Donghong, Cuiuri D., Li Huijun, Xu Jing, Norrish J. A review of the wire arc additive manufacturing of metals: Properties, defects and quality improvement. *Journal of Manufacturing Processes*, 2018, vol. 35, pp. 127–139. DOI: [10.1016/j.jmapro.2018.08.001](https://doi.org/10.1016/j.jmapro.2018.08.001).
- Oskolkov A.A., Matveev E.V., Bezukladnikov I.I., Trushnikov D.N., Krotova E.L. Advanced technologies for additive manufacturing of metal product. *Bulletin of*

- Perm national research polytechnic university. *Mechanical engineering, materials science*, 2018, vol. 20, no. 3, pp. 90–105. DOI: [10.15593/2224-9877/2018.3.11](https://doi.org/10.15593/2224-9877/2018.3.11).
5. Cunningham C.R., Wikshåland S., Xu F., Kemakolam N., Shokrani A., Dhokia V., Newman S.T. Cost modelling and sensitivity analysis of wire and arc additive manufacturing. *Procedia Manufacturing*, 2017, vol. 11, pp. 650–657. DOI: [10.1016/j.promfg.2017.07.163](https://doi.org/10.1016/j.promfg.2017.07.163).
 6. Pant H., Arora A., Gopakumar G.S., Chadha U., Saeidi A., Patterson A.E. Applications of wire arc additive manufacturing (WAAM) for aerospace component manufacturing. *The International Journal of Advanced Manufacturing Technology*, 2023, vol. 127, pp. 4995–5011. DOI: [10.1007/s00170-023-11623-7](https://doi.org/10.1007/s00170-023-11623-7).
 7. Wang Fude, Williams S., Rush M. Morphology investigation on direct current pulsed gas tungsten arc welded additive layer manufactured Ti6Al4V alloy. *The International Journal of Advanced Manufacturing Technology*, 2011, vol. 57, pp. 597–603. DOI: [10.1007/s00170-011-3299-1](https://doi.org/10.1007/s00170-011-3299-1).
 8. Ahmadkhaniha D., Möller H., Zanella C. Studying the Microstructural Effect of Selective Laser Melting and Electropolishing on the Performance of Maraging Steel. *Journal of Materials Engineering and Performance*, 2021, vol. 30, pp. 6588–6605. DOI: [10.1007/s11665-021-05927-6](https://doi.org/10.1007/s11665-021-05927-6).
 9. Beese A.M., Carroll B.E. Review of mechanical properties of Ti–6Al–4V made by laser-based additive manufacturing using powder feedstock. *JOM*, 2016, vol. 68, pp. 724–734. DOI: [10.1007/s11837-015-1759-z](https://doi.org/10.1007/s11837-015-1759-z).
 10. Kirka M.M., Lee Y., Greeley D.A., Okello A., Goin M.J., Pearce M.T., Dehoff R.R. Strategy for texture management in metals additive manufacturing. *JOM*, 2017, vol. 69, pp. 523–531. DOI: [10.1007/s11837-017-2264-3](https://doi.org/10.1007/s11837-017-2264-3).
 11. Williams S.W., Martina F., Addison A.C., Ding J., Pardal G., Colegrove P. Wire + arc additive manufacturing. *Materials Science and Technology*, 2016, vol. 32, no. 7, pp. 641–647. DOI: [10.1179/1743284715Y.0000000073](https://doi.org/10.1179/1743284715Y.0000000073).
 12. Gu Jianglong, Ding Jialuo, Williams S.W., Gu Huimin, Bai Jing, Zhai Yuchun, Ma Peihua. The strengthening effect of inter-layer cold working and post-deposition heat treatment on the additively manufactured Al–6.3Cu alloy. *Materials Science and Engineering: A*, 2016, vol. 651, pp. 18–26. DOI: [10.1016/j.msea.2015.10.101](https://doi.org/10.1016/j.msea.2015.10.101).
 13. Guo Nannan, Leu Ming. Additive manufacturing: Technology, applications and research needs. *Frontiers of Mechanical Engineering*, 2013, vol. 8, pp. 215–243. DOI: [10.1007/s11465-013-0248-8](https://doi.org/10.1007/s11465-013-0248-8).
 14. Xu Fujia, Lv Yaohui, Liu Yuxin, Shu Fengyuan, He Peng, Xu Binshi. Microstructural Evolution and Mechanical Properties of Inconel 625 Alloy during Pulsed Plasma Arc Deposition Process. *Journal of Material Science and Technology*, 2013, vol. 29, no. 5, pp. 480–488. DOI: [10.1016/j.jmst.2013.02.010](https://doi.org/10.1016/j.jmst.2013.02.010).
 15. Kudryashov V.A., Lapyshov A.A. The creation of additive technologies taking into account the fatigue behaviour of a material in aviation engineering. *Izvestiya of Samara Scientific Center of the Russian Academy of Sciences*, 2018, vol. 20, no. 4-3, pp. 406–413. EDN: [YVOALR](https://www.edn.ru/yvoalr).
 16. Kubanova A.N., Sergeev A.N., Dobrovolskiy N.M., Gvozdev A.E., Medvedev P.N., Maliy D.V. Materials and technologies for production products by additive manufacturing. *Chebyshevskii sbornik*, 2019, vol. 20, no. 3, pp. 453–477. DOI: [10.22405/2226-8383-2019-20-3-453-477](https://doi.org/10.22405/2226-8383-2019-20-3-453-477).
 17. Terentev V.F., Korableva S.A. *Ustalost metallov* [Fatigue of metals]. Moscow, Nauka Publ., 2015. 484 p.
 18. Kabaldin Yu.G., Shatagin D.A., Anosov M.S., Kolchin P.V., Kiselev A.V. Diagnostics of 3D printing on a CNC machine by machine learning. *Russian engineering research*, 2021, vol. 41, no. 4, pp. 320–324. DOI: [10.3103/S1068798X21040109](https://doi.org/10.3103/S1068798X21040109).
 19. Atroshchenko V.V., Tefanov V.N., Kraev K.A. Revisited the control of metal transfer during welding by consumable electrode with a short circuit of arc interval. *Vestnik USATU*, 2008, vol. 11, no. 2, pp. 146–154. EDN: [JXECO](https://www.edn.ru/jxecoh).
 20. Anosov M.C., Shatagin D.A., Chernigin M.A., Mordovina Yu.S., Anosova E.S. Structure formation of Np-30KHGSA alloy in wire and arc additive manufacturing. *Izvestiya. Ferrous Metallurgy (Izvestiya vuzov. Chernaya Metallurgiya)*, 2023, vol. 66, no. 3, pp. 294–301. DOI: [10.17073/0368-0797-2023-3-294-301](https://doi.org/10.17073/0368-0797-2023-3-294-301).
 21. Jovičević-Klug P., Lipovšek N., Jovičević-Klug M., Podgornik B. Optimized Preparation of Deep Cryogenic Treated Steel and Al-alloy Samples for Optimal Microstructure Imaging Results. *Materials Today Communications*, 2021, vol. 27, article number 102211. DOI: [10.1016/j.mtcomm.2021.102211](https://doi.org/10.1016/j.mtcomm.2021.102211).
 22. Rybakov A.A., Filipchuk T.N., Demchenko Yu.V. Optimization of the chemical composition and structure of the metal of repair welds when fixing defects in welded pipe joints using multilayer welding. *The Paton Welding Journal*, 2013, no. 12, pp. 24–30. EDN: [SYLXOT](https://www.edn.ru/sylxot).
 23. Chinakhov D.A., Skakov M.K., Gradoboev A.V., Uvaliev B.K., Sharov V.V. Change of microstructure and mechanical properties of multilayered connections from steel 30XGSA at fusion welding using different methods. *Bulletin of the Tomsk Polytechnic University. Geo Assets Engineering*, 2008, vol. 313, no. 2, pp. 119–122. EDN: [JVJFVT](https://www.edn.ru/jvjfvt).
 24. Balyakin A.V., Zhuchenko E.I., Smirnov G.V., Pronichev N.D. The investigation of negative technological heredity appearance during GTE parts manufacturing by SLM method. *Izvestiya of Samara Scientific Center of the Russian Academy of Sciences*, 2019, vol. 21, no. 1, pp. 61–70. EDN: [XHSWIU](https://www.edn.ru/xhswiu).
 25. Zhatkin S.S., Nikitin K.V., Deev V.B., Pankratov S.S., Dunaev D.A. Application of electric arc surfacing in the manufacturing of three-dimensional steel products. *Izvestiya. Ferrous Metallurgy (Izvestiya vuzov. Chernaya Metallurgiya)*, 2020, vol. 63, no. 6, pp. 443–450. DOI: [10.17073/0368-0797-2020-6-443-450](https://doi.org/10.17073/0368-0797-2020-6-443-450).
 26. Wang Fude, Williams S., Colegrove P., Antonysamy A.A. Microstructure and Mechanical Properties of Wire and Arc Additive Manufactured Ti–6Al–4V. *Metallurgical and Materials Transactions A*, 2013, vol. 44, pp. 968–977. DOI: [10.1007/s11661-012-1444-6](https://doi.org/10.1007/s11661-012-1444-6).
 27. Gürol U., Kocaman E., Dilibal S., Koçak M. A comparative study on the microstructure, mechanical properties, wear and corrosion behaviors of SS 316 austenitic stainless steels manufactured by casting and WAAM

- technologies. *CIRP Journal of Manufacturing Science and Technology*, 2023, vol. 47, pp. 215–227. DOI: [10.1016/j.cirpj.2023.10.005](https://doi.org/10.1016/j.cirpj.2023.10.005).
28. Takagi H., Sasahara H., Abe T., Sannomiya H., Nishiyama Sh., Ohta Sh., Nakamura K. Material-property evaluation of magnesium alloys fabricated using wire-and-arc-based additive manufacturing. *Additive Manufacturing*, 2018, vol. 24, pp. 498–507. DOI: [10.1016/j.ADDMA.2018.10.026](https://doi.org/10.1016/j.ADDMA.2018.10.026).
 29. Rodrigues T.A., Duarte V., Miranda R.M., Santos T.G., Oliveira J.P. Current Status and Perspectives on Wire and Arc Additive Manufacturing (WAAM). *Materials*, 2019, vol. 12, no. 7, article number 1121. DOI: [10.3390/ma12071121](https://doi.org/10.3390/ma12071121).
- ### СПИСОК ЛИТЕРАТУРЫ
1. Li Johnnie Liew Zhong, Alkahari M.R., Rosli N.A.B., Hasan R., Sudin M.N., Ramli F.R. Review of Wire Arc Additive Manufacturing for 3D Metal Printing // *International Journal of Automation Technology*. 2019. Vol. 13. № 3. P. 346–353. DOI: [10.20965/ijat.2019.p0346](https://doi.org/10.20965/ijat.2019.p0346).
 2. Ding Donghong, Pan Zengxi, Cuiuri D., Li Huijun. Wire-feed additive manufacturing of metal components: technologies, developments and future interests // *The International Journal of Advanced Manufacturing Technology*. 2015. Vol. 81. P. 465–481. DOI: [10.1007/s00170-015-7077-3](https://doi.org/10.1007/s00170-015-7077-3).
 3. Wu Binta, Pan Zengxi, Ding Donghong, Cuiuri D., Li Huijun, Xu Jing, Norrish J. A review of the wire arc additive manufacturing of metals: Properties, defects and quality improvement // *Journal of Manufacturing Processes*. 2018. Vol. 35. P. 127–139. DOI: [10.1016/j.jmapro.2018.08.001](https://doi.org/10.1016/j.jmapro.2018.08.001).
 4. Осколков А.А., Матвеев Е.В., Безукладников И.И., Трушников Д.Н., Кротова Е.Л. Передовые технологии аддитивного производства металлических изделий // *Вестник Пермского национального исследовательского политехнического университета. Машиностроение, материаловедение*. 2018. Т. 20. № 3. С. 90–105. DOI: [10.15593/2224-9877/2018.3.11](https://doi.org/10.15593/2224-9877/2018.3.11).
 5. Cunningham C.R., Wikshåland S., Xu F., Kernakolam N., Shokrani A., Dhokia V., Newman S.T. Cost modelling and sensitivity analysis of wire and arc additive manufacturing // *Procedia Manufacturing*. 2017. Vol. 11. P. 650–657. DOI: [10.1016/j.promfg.2017.07.163](https://doi.org/10.1016/j.promfg.2017.07.163).
 6. Pant H., Arora A., Gopakumar G.S., Chadha U., Saeidi A., Patterson A.E. Applications of wire arc additive manufacturing (WAAM) for aerospace component manufacturing // *The International Journal of Advanced Manufacturing Technology*. 2023. Vol. 127. P. 4995–5011. DOI: [10.1007/s00170-023-11623-7](https://doi.org/10.1007/s00170-023-11623-7).
 7. Wang Fude, Williams S., Rush M. Morphology investigation on direct current pulsed gas tungsten arc welded additive layer manufactured Ti6Al4V alloy // *The International Journal of Advanced Manufacturing Technology*. 2011. Vol. 57. P. 597–603. DOI: [10.1007/s00170-011-3299-1](https://doi.org/10.1007/s00170-011-3299-1).
 8. Ahmadkhanhiha D., Möller H., Zanella C. Studying the Microstructural Effect of Selective Laser Melting and Electropolishing on the Performance of Maraging Steel // *Journal of Materials Engineering and Performance*. 2021. Vol. 30. P. 6588–6605. DOI: [10.1007/s11665-021-05927-6](https://doi.org/10.1007/s11665-021-05927-6).
 9. Beese A.M., Carroll B.E. Review of mechanical properties of Ti–6Al–4V made by laser-based additive manufacturing using powder feedstock // *JOM*. 2016. Vol. 68. P. 724–734. DOI: [10.1007/s11837-015-1759-z](https://doi.org/10.1007/s11837-015-1759-z).
 10. Kirka M.M., Lee Y., Greeley D.A., Okello A., Goin M.J., Pearce M.T., Dehoff R.R. Strategy for texture management in metals additive manufacturing // *JOM*. 2017. Vol. 69. P. 523–531. DOI: [10.1007/s11837-017-2264-3](https://doi.org/10.1007/s11837-017-2264-3).
 11. Williams S.W., Martina F., Addison A.C., Ding J., Pardal G., Colegrove P. Wire + arc additive manufacturing // *Materials Science and Technology*. 2016. Vol. 32. № 7. P. 641–647. DOI: [10.1179/1743284715Y.0000000073](https://doi.org/10.1179/1743284715Y.0000000073).
 12. Gu Jianglong, Ding Jialuo, Williams S.W., Gu Huimin, Bai Jing, Zhai Yuchun, Ma Peihua. The strengthening effect of inter-layer cold working and post-deposition heat treatment on the additively manufactured Al–6.3Cu alloy // *Materials Science and Engineering: A*. 2016. Vol. 651. P. 18–26. DOI: [10.1016/j.msea.2015.10.101](https://doi.org/10.1016/j.msea.2015.10.101).
 13. Guo Nannan, Leu Ming. Additive manufacturing: Technology, applications and research needs // *Frontiers of Mechanical Engineering*. 2013. Vol. 8. P. 215–243. DOI: [10.1007/s11465-013-0248-8](https://doi.org/10.1007/s11465-013-0248-8).
 14. Xu Fujia, Lv Yaohui, Liu Yuxin, Shu Fengyuan, He Peng, Xu Binshi. Microstructural Evolution and Mechanical Properties of Inconel 625 Alloy during Pulsed Plasma Arc Deposition Process // *Journal of Material Science and Technology*. 2013. Vol. 29. № 5. P. 480–488. DOI: [10.1016/j.jmst.2013.02.010](https://doi.org/10.1016/j.jmst.2013.02.010).
 15. Кудряшов В.А., Лапышев А.А. Создание аддитивных технологий с учетом усталостного поведения материала в авиационном инжиниринге // *Известия Самарского научного центра Российской академии наук*. 2018. Т. 20. № 4-3. С. 406–413. EDN: [YVOALR](https://www.edn.ru/yvoalr/).
 16. Кубанова А.Н., Сергеев А.Н., Добровольский Н.М., Гвоздев А.Е., Медведев П.Н., Малий Д.В. Особенности материалов и технологий аддитивного производства изделий // *Чебышевский сборник*. 2019. Т. 20. № 3. С. 453–477. DOI: [10.22405/2226-8383-2019-20-3-453-477](https://doi.org/10.22405/2226-8383-2019-20-3-453-477).
 17. Терентьев В.Ф., Кораблева С.А. Усталость металлов. М.: Наука, 2015. 484 с.
 18. Кабалдин Ю.Г., Шатагин Д.А., Аносов М.С., Колчин П.В., Киселев А.В. Диагностика процесса 3D-печати на станке с ЧПУ с использованием подходов машинного обучения // *Вестник машиностроения*. 2021. № 1. С. 55–59. DOI: [10.36652/0042-4633-2021-1-55-59](https://doi.org/10.36652/0042-4633-2021-1-55-59).
 19. Атрощенко В.В., Тёфанов В.Н., Краев К.А. К вопросу об управлении переносом электродного металла при дуговой сварке плавящимся электродом с короткими замыканиями дугового промежутка // *Вестник Уфимского государственного авиационного технического университета*. 2008. Т. 11. № 2. С. 146–154. EDN: [JXECOH](https://www.edn.ru/jxecoh/).
 20. Аносов М.С., Шатагин Д.А., Чернигин М.А., Мордовина Ю.С., Аносова Е.С. Структурообразование сплава Нп-30ХГСА при аддитивном электродуговом

- выращивании // Известия высших учебных заведений. Черная металлургия. 2023. Т. 66. № 3. С. 294–301. DOI: [10.17073/0368-0797-2023-3-294-301](https://doi.org/10.17073/0368-0797-2023-3-294-301).
21. Jovičević-Klug P., Lipovšek N., Jovičević-Klug M., Podgornik B. Optimized Preparation of Deep Cryogenic Treated Steel and Al-alloy Samples for Optimal Microstructure Imaging Results // Materials Today Communications. 2021. Vol. 27. Article number 102211. DOI: [10.1016/j.mtcomm.2021.102211](https://doi.org/10.1016/j.mtcomm.2021.102211).
 22. Рыбаков А.А., Филипчук Т.Н., Демченко Ю.В. Оптимизация химического состава и структуры металла ремонтных швов при исправлении дефектов в сварных соединениях труб с применением многослойной сварки // Автоматическая сварка. 2013. № 12. С. 24–30. EDN: [SYLXOT](https://www.edn.net/SYLXOT).
 23. Чинахов Д.А., Скаков М.К., Градобоев А.В., Увалиев Б.К., Шаров В.В. Изменение микроструктуры и механических свойств многослойных соединений из стали 30ХГСА при сварке плавлением разными способами // Известия Томского политехнического университета. Инжиниринг георесурсов. 2008. Т. 313. № 2. С. 119–122. EDN: [JVJFVT](https://www.edn.net/JVJFVT).
 24. Балякин А.В., Жученко Е.И., Смирнов Г.В., Проничев Н.Д. Исследование проблем появления негативной технологической наследственности при изготовлении деталей ГТД методом селективного лазерного сплавления // Известия Самарского научного центра Российской академии наук. 2019. Т. 21. № 1. С. 61–70. EDN: [XHSWIU](https://www.edn.net/XHSWIU).
 25. Жаткин С.С., Никитин К.В., Деев В.Б., Панкратов С.С., Дунаев Д.А. Применение электродуговой наплавки для создания трехмерных объектов из стали // Известия высших учебных заведений. Черная металлургия. 2020. Т. 63. № 6. С. 443–450. DOI: [10.17073/0368-0797-2020-6-443-450](https://doi.org/10.17073/0368-0797-2020-6-443-450).
 26. Wang Fude, Williams S., Colegrove P., Antony-samy A.A. Microstructure and Mechanical Properties of Wire and Arc Additive Manufactured Ti–6Al–4V // Metallurgical and Materials Transactions A. 2013. Vol. 44. P. 968–977. DOI: [10.1007/s11661-012-1444-6](https://doi.org/10.1007/s11661-012-1444-6).
 27. Gürol U., Kocaman E., Dilibal S., Koçak M. A comparative study on the microstructure, mechanical properties, wear and corrosion behaviors of SS 316 austenitic stainless steels manufactured by casting and WAAM technologies // CIRP Journal of Manufacturing Science and Technology. 2023. Vol. 47. P. 215–227. DOI: [10.1016/j.cirpj.2023.10.005](https://doi.org/10.1016/j.cirpj.2023.10.005).
 28. Takagi H., Sasahara H., Abe T., Sannomiya H., Nishiyama Sh., Ohta Sh., Nakamura K. Material-property evaluation of magnesium alloys fabricated using wire-and-arc-based additive manufacturing // Additive Manufacturing. 2018. Vol. 24. P. 498–507. DOI: [10.1016/j.addma.2018.10.026](https://doi.org/10.1016/j.addma.2018.10.026).
 29. Rodrigues T.A., Duarte V., Miranda R.M., Santos T.G., Oliveira J.P. Current Status and Perspectives on Wire and Arc Additive Manufacturing (WAAM) // Materials. 2019. Vol. 12. № 7. Article number 1121. DOI: [10.3390/ma12071121](https://doi.org/10.3390/ma12071121).

Влияние режима 3D-печати на химический состав и структуру стали 30ХГСА

© 2024

Кабалдин Юрий Георгиевич, доктор технических наук, профессор, профессор кафедры «Технология и оборудование машиностроения»

*Аносов Максим Сергеевич**, кандидат технических наук, доцент, доцент кафедры «Технология и оборудование машиностроения»

Мордовина Юлия Сергеевна, аспирант,

инженер по учебному процессу института переподготовки специалистов

Чернигин Михаил Алексеевич, аспирант,

инженер кафедры «Технология и оборудование машиностроения»

Нижегородский государственный технический университет им. П.Е. Алексеева, Нижний Новгород (Россия)

*E-mail: anosov.ms@nntu.ru,
anosov-maksim@list.ru

Поступила в редакцию 31.07.2023

Принята к публикации 18.12.2023

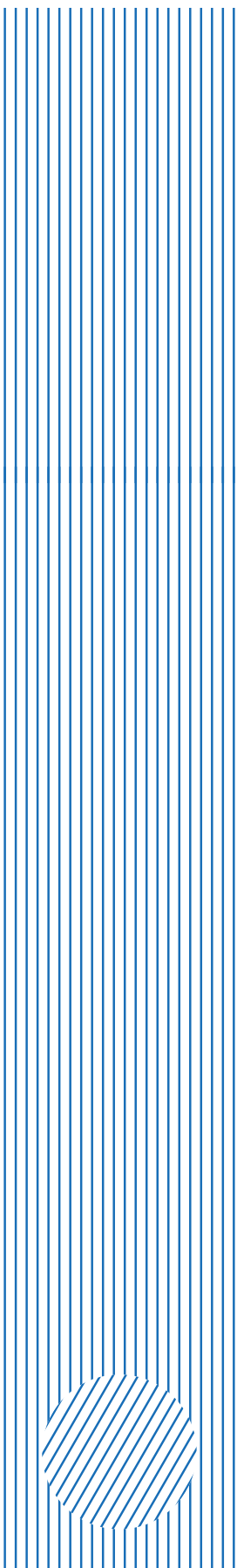
Аннотация: Проведено исследование влияния режимов 3D-печати на структуру и химический состав образцов из стали 30ХГСА (хромансиль, англ. *chromansil*), полученных методом аддитивной электродуговой наплавки. Для исследования влияния режима электродуговой наплавки на химический состав исследуемой стали проведен оптико-эмиссионный анализ образцов. Оценка влияния режима наплавки на получаемую структуру проводилась по всей высоте наплавленных стенок при увеличениях $\times 50$, $\times 100$, $\times 200$ и $\times 500$. В ходе оптико-эмиссионного анализа выявлено изменение химического состава материала, связанное с угаром химических элементов. Установлено, что степень угара C, Cr и Si растет практически линейно и прямо пропорциональна погонной энергии наплавки (Q , Дж/мм). Точного влияния роста величины погонной энергии наплавки на содержание Mn не установлено, но выявлена взаимосвязь между степенью его угара и напряжением (U , В) при наплавке образцов. В ходе микроструктурных исследований всех образцов не выявлено большого количества системно образовавшихся структурных дефектов, характерных для литых и сварных изделий (поры, усадочные раковины и т. д.), что подтверждает

высокое качество металла в изделиях, полученных методом электродуговой наплавки. Анализ микроснимков, сделанных на различных участках образцов, позволил определить, что микроструктура металла не претерпевает сильных изменений при разных режимах наплавки, сохраняются основные тенденции изменения структуры по высоте образца. На всех образцах отмечено получение высокодисперсной структуры вне зависимости от параметров 3D-печати. Наиболее благоприятной структурой металла, подходящей для последующего использования при производстве изделий методом 3D-печати, признана структура образца, наплавленного по режиму № 5 ($I=160$ А, $U=24$ В, $Q=921,6$ Дж/мм). Данный режим может быть использован для дальнейшего изучения проблем аддитивной электродуговой наплавки стали 30ХГСА.

Ключевые слова: сталь 30ХГСА; аддитивная электродуговая наплавка; оптический эмиссионный анализ; металлографические исследования; 3D-печать.

Благодарности: Исследование выполнено при поддержке гранта Российского научного фонда № 22-79-00095 «Разработка научно-технологических основ структурообразования конструкционных материалов полученных путем аддитивного электродугового выращивания для формирования механических свойств при усталости с использованием подходов искусственного интеллекта», <https://www.rscf.ru/project/22-79-00095/>.

Для цитирования: Кабалдин Ю.Г., Аносов М.С., Мордовина Ю.С., Чернигин М.А. Влияние режима 3D-печати на химический состав и структуру стали 30ХГСА // Frontier Materials & Technologies. 2024. № 3. С. 63–73. DOI: 10.18323/2782-4039-2024-3-69-6.



The Publishing Center (until November 1, 2011 – the Editorial and Publishing Center) is a structural subdivision of Togliatti State University, which takes an important place in providing the educational process with high-quality instructional, educational, methodological, and scientific literature.

TSU Publishing Center today

– Publishing center includes an editorial office and a printing shop. In recent years, the base of computer equipment, printing and post-printing equipment has been almost completely updated.

– It publishes books and electronic textbooks for students, graduate students, lecturers, and specialists in almost all branches of modern scientific knowledge, as well as popular science and reference literature, fiction, books of reports (papers) of conferences. Published literature corresponds to all areas of the educational cycles of the university disciplines.

– A considerable volume of printing job is the prompt execution of promotional and information products.

– The publishing center team is a collaboration of highly skilled professionals with wide work experience and young motivated employees.

– Publishing center employees participate in practical seminars to become acquainted with new opportunities in the field of printing technologies and equipment, as well as with advanced materials for digital printing.

Main areas of activity

– Publication of paper-based educational and scientific literature, production of electronic educational and scientific aids.

– Implementation of editorial and publishing cycle stages: editing, production of original layouts, replication, pre-printing and post-printing treatment.

– Methodological and advisory work with the university departments on the issue of educational and scientific publications.

– Interaction with the Russian Book Chamber on the assignment of ISBNs to publications issued by Togliatti State University.

– Preparation of publications issued by Togliatti State University for state registration and sending of statutory copies.

– Markup of papers published in the TSU journals in the Articulus program to place on the eLibrary platform.

Main achievements

– The results of the work were awarded with diplomas of the winners of the annual interregional and all-Russian University Book competitions.

– Publishing center regularly participates in the academic book exhibition of publishing activities “University – Science – City”.

Microstructure, crystallographic texture and mechanical properties of the Zn–1%Mg–1%Fe alloy subjected to severe plastic deformation

© 2024

Vil D. Sitdikov^{*1,2,4}, Doctor of Sciences (Physics and Mathematics),
senior expert, senior researcher

Elvira D. Khafizova^{2,3,5}, PhD (Engineering),

assistant professor of Chair of Materials Science and Metal Physics,

senior researcher at the Research Laboratory “Metals and Alloys under Extreme Exposures”

Milena V. Polenok^{2,3,6}, graduate student of Chair of Materials Science and Physics of Metals,
research assistant at the Research Laboratory “Metals and Alloys under Extreme Exposures”

¹OOO RN-BashNIPIneft, Ufa (Russia)

²Institute of Physics of Molecules and Crystals of Ufa Federal Research Center of RAS, Ufa (Russia)

³Ufa University of Science and Technology, Ufa (Russia)

*E-mail: SitdikovVD@bnipi.rosneft.ru

⁴ORCID: <https://orcid.org/0000-0002-9948-1099>

⁵ORCID: <https://orcid.org/0000-0002-4618-412X>

⁶ORCID: <https://orcid.org/0000-0001-9774-1689>

Received 09.02.2024

Accepted 19.07.2024

Abstract: The paper covers the production, analysis of the microstructure, crystallographic texture and deformation mechanisms of the ultrafine-grained (UFG) Zn–1%Mg–1%Fe zinc alloy demonstrating unique physical and mechanical properties compared to its coarse-crystalline analogs. The zinc alloy with improved mechanical properties was developed in two stages. At the first stage, based on the analysis of literature data, an alloy with the following chemical composition was cast: Zn–1%Mg–1%Fe. Then, the alloy was subjected to high-pressure torsion (HPT) to improve mechanical properties due to grain structure refinement and implementation of dynamic strain aging. The conducted mechanical tensile tests of the samples and assessment of the alloy hardness showed that HPT treatment leads to an increase in its tensile strength to 415 MPa, an increase in hardness to 144 HV, and an increase in ductility to 82 %. The obtained mechanical characteristics demonstrate the suitability of using the developed alloy in medicine as some implants (stents) requiring high applied loads. To explain the reasons for the improvement of the mechanical properties of this alloy, the authors carried out comprehensive tests using microscopy and X-ray diffraction analysis. The microstructure analysis showed that during the formation of the ultrafine-grained structure, a phase transition is implemented according to the following scheme: $Zn_{\text{eutectic}} + Mg_2Zn_{11\text{eutectic}} + FeZn_{13} \rightarrow Zn_{\text{phase}} + Mg_2Zn_{11\text{phase}} + MgZn_{2\text{particles}} + Zn_{\text{particles}}$. It was found that as a result of high pressure torsion in the main phases (Zn, Mg_2Zn_{11}), the grain structure is refined, the density of introduced defects increases, and a developed crystallographic texture consisting of basic, pyramidal, prismatic, and twin texture components is formed. The study showed that the resistance of pyramidal, prismatic and twin texture components at the initial stages of high-pressure torsion determines the level and anisotropy of the strength properties of this alloy. The relationship between the discovered structural features of the produced alloy and its unique mechanical properties is discussed.

Keywords: Zn–1%Mg–1%Fe alloy; phase transformations in zinc alloy; severe plastic deformation; X-ray scattering methods; mechanical properties; strength; ductility; crystallographic texture.

Acknowledgements: The study was funded by the grant of the Russian Science Foundation No. 23-29-00667, <https://rscf.ru/project/23-29-00667>.

For citation: Sitdikov V.D., Khafizova E.D., Polenok M.V. Microstructure, crystallographic texture and mechanical properties of the Zn–1%Mg–1%Fe alloy subjected to severe plastic deformation. *Frontier Materials & Technologies*, 2024, no. 3, pp. 75–88. DOI: 10.18323/2782-4039-2024-3-69-7.

INTRODUCTION

Zinc alloys belong to a new class of biodegradable materials, that demonstrate excellent biocompatibility and biodegradability along with relatively high mechanical strength and sufficient ductility [1–4]. According to the literature, the initial pure zinc is a very brittle material, and its low mechanical properties (yield strength ~10 MPa, tensile strength ~18 MPa, ductility 0.3 %) limit its scope of industrial application [5; 6]. To increase the potential for industrial application of zinc, for example, as implants in medicine, it is

necessary to optimise its physical and mechanical properties [1–4]. Traditionally, this goal is achieved by alloying pure zinc with certain atoms (Mg, Li, Ca, Fe, Mn, Ag, Cu, etc.), and performing thermomechanical treatment [1–4]. However, most zinc alloys produced in this way, suitable for implants, may contain elements toxic to the human body. In this regard, the scientific community is still searching for new materials that, on the one hand, should meet the desired mechanical characteristics for implants, and on the other hand, be biocompatible.

As is known, when developing biodegradable implants from various alloys, it is necessary to control the corrosion rate, since at high rates, the mechanical integrity of the implants is disrupted before the bone heals, and at too slow corrosion rate, inflammatory processes can be activated [7–9]. Clinical studies have shown that in Zn–xAl system implants, the risk of an inflammatory reaction increases [10], and alloying zinc with Fe atoms significantly reduces it [11]. As is known, Fe is one of the most important elements in the human body, but excessive addition of Fe to Zn leads to the formation of a brittle FeZn₁₃ phase, which worsens the mechanical characteristics of Zn–Fe alloys [12]. On the other hand, adding a certain amount of Mg atoms can also strengthen the Zn phase, but the strength and ductility of the resulting Zn–Mg alloys still remain relatively low [13]. In particular, the authors of [13] showed that the ultimate tensile strength of the Zn–Mg alloy can increase to 125 MPa with an increase in the Mg content from 0.1 to 0.8 %, however, the ductility of the resulting alloy remains low (less than 1 %). With a further increase in the Mg content in the alloy to 3.0 %, it is possible to achieve an increase in the ultimate tensile strength to ~150 MPa, and the elongation before failure increases to only 2 % [14; 15]. Moreover, studies have shown that an increase in the Mg content in Zn also leads to an increase in the hardness of the obtained alloy [11; 16]. In particular, it was demonstrated that adding 1 wt. % of Mg to pure Zn, leads to an increase in its hardness from 40 to 78 HV according to the Vickers scale [16], and in [11], the authors have shown that the hardness of the Zn–1.3%Fe alloy can reach 56 HV.

The conducted literature analysis revealed that the Zn–Mg–Fe system alloys can be used to produce zinc alloys with increased strength and biocompatibility in medicine. In this regard, Mg and Fe were also chosen as alloying elements in this work to create a zinc alloy with an improved structure. The choice of these elements was also influenced by the fact, that the solubility rate of Zn in the body is between the solubility rates of Mg and Fe, and the degradation products are biocompatible [2; 7–9]. Moreover, the authors of [17], as a result of varying the degree of alloying of zinc with Mg and Fe atoms, found that the Zn–1%Mg–1%Fe alloy, compared to other Mg and Fe contents in zinc, shows the highest strength properties (ultimate tensile strength σ_{UTS} is 157 MPa, yield strength σ_y is 148 MPa), and an acceptable corrosion rate (0.027 mm/year). However, the ductility δ of the produced alloy was low (no more than 2.3 %) [17]. Nevertheless, the improved mechanical properties, satisfactory corrosion rate and biocompatibility of the coarse-grained Zn–1%Mg–1%Fe alloy became the basis for the authors of this work to choose this alloy for further optimisation of its strength characteristics and ductility, so that it meets the required criteria for implants (σ_{UTS} >300 MPa, σ_y >200 MPa, δ >15 %) [2]. In this case, the authors of this work optimised the mechanical properties of Zn–1%Mg–1%Fe using the method of severe plastic deformation (SPD) [18].

Recently, a number of studies [19; 20] have shown that SPD methods can more effectively increase the strength characteristics of zinc alloys by forming an ultrafine-grained (UFG) structure, increasing the defectiveness of

the structure, and implementing the process of dynamic deformation ageing, during which the strengthening phases of the particle precipitate. At the same time, improving the above-mentioned microstructure parameters, leading to an increase in the mechanical properties of zinc alloys, is possible, due to variations in the applied pressure, temperature, and degree of SPD. In this regard, in this work, improving the mechanical properties of the cast Zn–Mg–Fe alloy was also achieved by optimising the modes (pressure, temperature, deformation degree), of high-pressure torsion (HPT) [18; 19].

The aim of this work is, using high-pressure torsion processing, to produce an ultrafine-grained Zn–1%Mg–1%Fe zinc alloy, demonstrating the required mechanical properties for application as implants (stents) in medicine.

METHODS

Cylindrical specimens of Zn–1%Mg–1%Fe alloy (mass percent), with a diameter of 20 mm and a length of 120 mm were cast from high-purity Zn (>99.9 wt. %), Mg (>99.9 wt. %) and Fe (>99.9 wt. %) at a temperature of 600 °C in a chamber furnace using a graphite crucible. To form a UFG structure in order to improve the strength characteristics, tablets (radius R is 10 mm, thickness is 1.7 mm) of the alloy, cut from cylindrical specimens, were subjected to HPT at room temperature (27 °C), and at a temperature of 150 °C, varying the number of revolutions from 0.5 to 10. After each stage of HPT, corresponding to 0.5; 1; 2; 3; 6; 8 and 10 revolutions of the lower striker (the deformation degree γ corresponds to 28.5; 57.1; 114.2; 171.3; 342.6; 456.8 and 571.0 for the $R/2$ region, according to [18]), the authors analysed the mechanical properties and microstructure of the alloy. The applied hydrostatic pressure during HPT was 6 GPa, the striker rotation rate was set at 1 rpm. Mechanical tensile tests of the alloy were performed, using a specialised testing machine, for small samples (length of the working part is 4 mm, thickness is 1 mm, width is 1 mm). The working part of the tensile samples was located in the area, which was at half the radius of the disk-shaped HPT sample. The frequency of digitising of the deformation values when recording the tensile curves, during continuous testing of the samples was set to 4 Hz. The traverse speed was $4 \cdot 10^{-4}$ mm/s. The microhardness of the alloy, in each structural state, was measured by the Vickers method on a universal Shimadzu HMV-G hardness tester (Japan), with an indenter load of 100 g. The measurements were performed in the area located at half the radius of the disk-shaped HPT sample.

The fine structure parameters of the alloy, were determined by X-ray diffraction analysis (XRD). The XRD diffraction patterns were measured on a Bruker D8 Advance diffractometer (Germany) (Bragg–Brentano scheme). The shooting was carried out in the continuous shooting mode, at a rate of 1.5 °/min within the scattering angle 2θ from 20 to 150°, on copper radiation generated at a voltage of 40 kV and a current of 40 mA. Pulse counting was performed using a LinxEye multichannel detector (Germany). A Ni filter was installed in front of the detector to cut off

unnecessary radiation. The lattice constant was estimated, the average size of the coherent scattering domains (CSD) was determined, and the dislocation density was calculated using the PM2K program [21].

Qualitative X-ray phase analysis was performed, using the PDF-2 diffraction database using the EVAplus program (www.bruker.com). Quantitative X-ray phase analysis, with identifying the ratio of the detected phases, was performed applying the Rietveld method [22] using the TOPAS program, ver. 4.2 (www.bruker.com). In this algorithm, the atomic-structural parameters of all detected phases are input into the model, and the theoretical diffraction pattern is reproduced. For the best approximation of the theoretical $I_{measured}$ curve to the experimental $I_{calculated}$, the fine structure parameters (lattice constant, microstrain, crystallite size, and crystallographic texture) are optimised, taking into account possible errors made during shooting. The microstructure of the alloy under study was analysed by scanning electron microscopy (SEM), using an FEI Thermo Scientific Q250 scanning electron microscope (USA). The main shooting characteristics were: electron accelerating voltage – 25 kV, beam diameter – 2 μm , focal length – 10.0 mm, chamber pressure – $5 \cdot 10^{-4}$ Pa. Microstructure studies using X-ray diffraction and SEM were conducted in the areas where mechanical tests were performed.

RESULTS

The results of mechanical tests of the Zn–1%Mg–1%Fe alloy in different structural states, showed that HPT treatment (except for microhardness at HPT 27 °C) leads to an increase in its strength characteristics (Table 1). In particular, in the initial state, the Vickers microhardness of

the alloy did not exceed 118 HV. At the same time, the application of 1 revolution of HPT treatment to the alloy at room temperature, led to a decrease in the microhardness to 114 HV. With a subsequent increase in the degree of HPT treatment to 6 revolutions, the microhardness of the alloy naturally drops to 109 HV. At high degrees of deformation (10 revolutions), the microhardness of the studied alloy remains virtually unchanged. However, with an increase in the temperature of the HPT treatment (1 revolution, 150 °C), on the contrary, even at the initial stages, a regular increase in microhardness to 131 HV is observed (Table 1). With a further increase in the number of revolutions of the HPT treatment, the alloy demonstrates a slight decrease in its microhardness (Table 1).

The results of mechanical tensile tests of the alloy are also summarised in Table 1. In general, the analysis of Table 1 indicates that the implementation of HPT treatment even at the initial stages of processing (27 °C) leads to an increase in the alloy strength and ductility. In particular, after 1 HPT revolution, an increase in the ultimate tensile strength to 289 MPa is observed, and the ductility reaches 95 %. As the number of HPT revolutions increases to 6, the yield strength and ultimate tensile strength of the alloy slightly decrease, and the level of ductility is maintained. With high degrees of HPT treatment, implemented at room temperature, the strength characteristics increase again, but the ductility of the alloy decreases noticeably. On the other hand, increasing the HPT temperature (150 °C) leads to an increase in both the hardness value, and the values of the ultimate tensile strength and ductility of the alloy. Thus, after 1 HPT revolution, the ultimate tensile strength increases to 399 MPa, which is 110 MPa more than that obtained after 1 HPT (27 °C) revolution. After 3 HPT (150 °C) revolutions, a further increase in the ultimate

Table 1. The values of microhardness and mechanical properties of the Zn–1%Mg–1%Fe alloy
Таблица 1. Значения микротвердости и механических свойств сплава Zn–1%Mg–1%Fe

State		HV	σ_y , MPa	σ_{UTS} , MPa	δ , %
Initial		118 ± 3	28 ± 2	33 ± 3	6 ± 1
HPT 27 °C	1 rev.	114 ± 4	213 ± 12	289 ± 11	95 ± 5
	3 rev.	112 ± 4	189 ± 10	271 ± 9	96 ± 4
	6 rev.	109 ± 3	177 ± 9	255 ± 12	97 ± 6
	10 rev.	110 ± 4	191 ± 8	264 ± 11	61 ± 5
HPT 150 °C	1 rev.	131 ± 4	313 ± 13	399 ± 15	85 ± 6
	3 rev.	129 ± 3	312 ± 14	415 ± 10	82 ± 4
	6 rev.	126 ± 5	307 ± 9	394 ± 13	86 ± 5
	10 rev.	128 ± 4	304 ± 10	387 ± 14	89 ± 6

Note. HV is Vickers microhardness; σ_y is yield stress; σ_{UTS} is ultimate tensile strength; δ is percent elongation to fracture.

Примечание. HV – величина микротвердости по Виккерсу; σ_y – предел текучести; σ_{UTS} – предел прочности;

δ – относительное удлинение до разрушения.

tensile strength value is observed (up to 415 MPa), with maintaining the ductility level. With a subsequent increase in the HPT degree, the alloy strength characteristics decrease slightly, and its ductility increases slightly (Table 1). In general, the mechanical tests showed that at the initial stages of HPT treatment (1–3 revolutions), at a temperature of 150 °C, the zinc alloy demonstrates high strength characteristics with sufficient ductility (Table 1).

Fig. 1 shows the SEM images of the initial zinc alloy microstructure, as well as the results of the surface distribution of Zn, Mg and Fe atoms over a random area of the polished section. According to the phase diagram of Zn–Mg [23] and Zn–Fe [24], the phases of Zn, Mg_2Zn_{11} and $FeZn_{13}$ should be present in the cast Zn–1%Mg–1%Fe alloy. In fact, the data obtained by SEM and X-ray phase analysis (data are given below) showed that the microstructure of the studied alloy contains the Zn, Mg_2Zn_{11} and $FeZn_{13}$ phases (Fig. 1 a). In this case, according to the SEM data, the Mg_2Zn_{11} phase is concentrated at the boundaries of the zinc phase (Fig. 1 a).

Since the atomic mass of Zn is greater than the atomic mass of Mg, the relatively light oval-shaped areas belong to the zinc phase, and the dark areas correspond to the Mg_2Zn_{11} phase (Fig. 1 a). The analysis of the microstructure by the elemental mapping method factually confirms the above-detected shape, and nature of occurrence of the phases identified in the alloy (Fig. 1 b). Calculations showed that the average grain diameter of the Zn phase is 88 μm , and the size of the $FeZn_{13}$ phase varies from 1.5 to 280 μm (Fig. 1 a, 1 b).

Fig. 2 shows SEM images of the microstructure of the studied alloy after heat treatment (150 °C), and HPT processing carried out at different temperatures (27 and 150 °C). After heat treatment, the alloy microstructure contains Zn, Mg_2Zn_{11} and $FeZn_{13}$ phases. These phases are marked with arrows in Fig. 2 a. It is also evident that cylindrical $MgZn_2$ particles precipitate in the Mg_2Zn_{11} phase (dark area) as a result of heat treatment (Fig. 1 a, inset).

We should note that in the cast state, $MgZn_2$ particles in the Mg_2Zn_{11} phase were not detected.

In the case of HPT treatment, even with a small rotation of the anvils (0.5 revolution), noticeable changes in the microstructure of the analysed alloy can be observed (Fig. 2 b). These changes are mainly related to the fact that a band structure of alternating Mg_2Zn_{11} , Zn and $FeZn_{13}$ phases is formed in the alloy (Fig. 2 b). Moreover, HPT treatment led to the fragmentation of $FeZn_{13}$ phase grains, as well as a change in the shape and size of particles that precipitated during annealing, ($MgZn_2$ particles in the Mg_2Zn_{11} phase) (Fig. 2 b, in the inset). With an increase in the number of HPT revolutions, i.e. the degree of deformation, both a decrease in the width of the bands of the observed phases, and a further refinement of the grains of each phase are observed. In particular, a typical microstructure of the alloy after 6 revolutions of HPT treatment is shown in Fig. 2 c. For clarity, this microstructure is presented as a distribution map of the Zn, Mg and Fe elements (Fig. 2 c). It is evident that in this state of the alloy, the band structure consisting of Zn (green areas), Mg_2Zn_{11} (blue areas) and $FeZn_{13}$ (red areas) phases is maintained. In contrast to the early HPT stages, after 6 revolutions, a significant refinement of the grain structure is observed in the Mg_2Zn_{11} phase (Fig. 2 c, in the inset). According to microscopy data, the average grain size of the Mg_2Zn_{11} phase was 320 nm.

At high degrees of HPT treatment (10 revolutions), the alloy is characterised by a decrease in the thickness of the bands corresponding to the Zn and Mg_2Zn_{11} phases (Fig. 2 d). Further refinement of the structure components is observed in these bands (Fig. 2 d). In particular, in this state, the grains of the Mg_2Zn_{11} phase are also characterised by an equiaxial structure, but the average grain size decreases to 230 nm. The analysis showed that at high HPT revolutions, precipitated Zn and $MgZn_2$ particles of spherical morphology could be randomly observed in the Mg_2Zn_{11} phase (Fig. 2 d, inset).

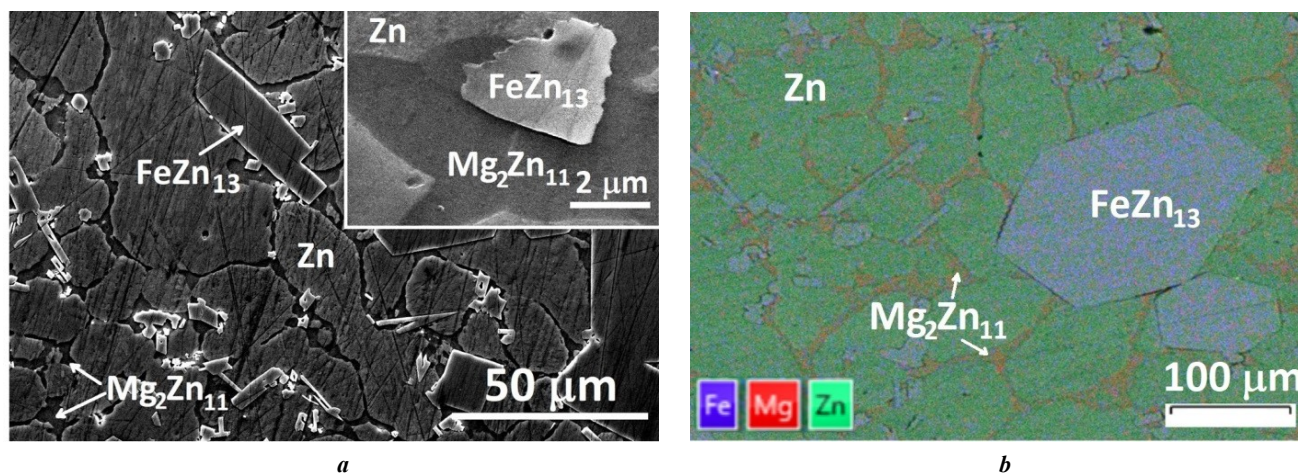


Fig. 1. Microstructure of the Zn–1%Mg–1%Fe alloy (in a random area of the section) in initial (as-cast) state: **a** – image at $\times 2400$ magnification; **b** – image of the distribution of Zn, Mg and Fe atoms at $\times 500$ magnification
Рис. 1. Микроструктура Zn–1%Mg–1%Fe сплава (в произвольном участке шлифа) в исходном (литом) состоянии: **a** – изображение при увеличении $\times 2400$; **b** – изображение распределения атомов Zn, Mg и Fe при увеличении $\times 500$

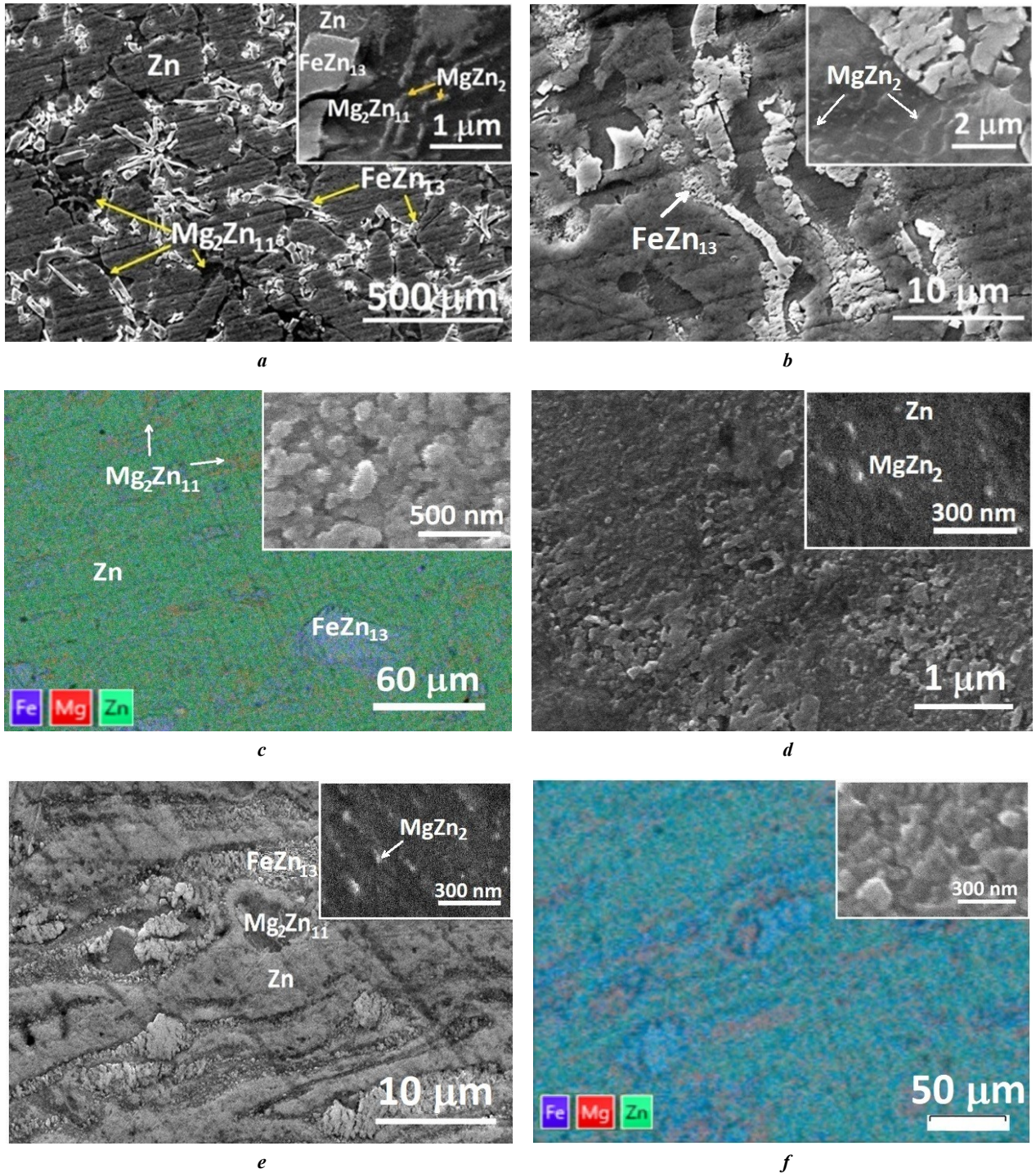


Fig. 2. Microstructure of the Zn–1%Mg–1%Fe alloy in different structural states:
a – after heat treatment; *b* – after 0.5 rev. of HPT 27 °C; *c* – after 6 rev. of HPT 27 °C;
d – after 10 rev. of HPT 27 °C; *e* – after 1 rev. of HPT 150 °C; *f* – after 3 rev. of HPT 150 °C
Рис. 2. Микроструктура Zn–1%Mg–1%Fe сплава в различных структурных состояниях:
a – после термической обработки; *b* – после 0,5 об. ИПДК 27 °C; *c* – после 6 об. ИПДК 27 °C;
d – после 10 об. ИПДК 27 °C; *e* – после 1 об. ИПДК 150 °C; *f* – после 3 об. ИПДК 150 °C

When conducting HPT treatment of the alloy at an elevated temperature (150 °C), a banded structure is formed even after 1 revolution (Fig. 2 e). The average thickness of the Mg_2Zn_{11} phase plates in this state is 2.9 μm , and inside the plates, the average size of equiaxial grains is 362 nm. A similar structure is observed when implementing high degrees of HPT in the alloy at room temperature. With an increase in the HPT degree, the thickness of the Zn and $MgZn_2$ phase plates continues to decrease, and the grain size in these phases becomes less than 300 nm (Fig. 2 f, inset).

Fig. 3 shows the diffraction patterns of the studied alloy in various structural states, as well as the general appearance of the diffraction pattern analysed by the Rietveld method (1 revolution, HPT, 27 °C). The results of qualitative XRD showed that after heat treatment, the Zn, Mg_2Zn_{11} , $FeZn_{13}$ and $MgZn_2$ phases can be identified in the alloy. At the same time, when the alloy is exposed to the HPT method, the general appearance of the diffraction patterns changes significantly (Fig. 3 a). Thus, even after 0.5 revolution of HPT treatment (27 °C), suppression of reflexes corresponding to the $FeZn_{13}$, Mg_2Zn_{11} phases and an increase in reflexes of the Zn phase are observed (Fig. 3 a). In this case, the width of each reflex, especially the Mg_2Zn_{11} phase, increases significantly compared to that characteristic of the initial state (Fig. 3 a). With a further increase in the degree of HPT treatment, the general appearance of the diffraction patterns remains virtually unchanged (Fig. 3 a). However, it should be noted that at high degrees of HPT treatment, a further increase in the width of the reflexes and suppression of the intensity of the reflexes corresponding to the Mg_2Zn_{11} phase are observed.

In the case of HPT treatment at a temperature of 150 °C, an increase in the intensity of the $MgZn_2$ phase reflexes is

observed already at the early stages (Fig. 3 a). In this case, the reflexes corresponding to the Zn and Mg_2Zn_{11} phases become wider, as compared to those obtained after HPT at 27 °C. With a further increase in the degree of HPT treatment, an increase in the intensity of the reflexes corresponding to the Zn and $MgZn_2$ phases, and an increase in the width of their peaks are observed.

An example of the diffraction pattern analysis for the alloy state after 1 HPT revolution is shown in Fig. 3 b. It shows the theoretical and experimental diffraction patterns, the difference line and the background line, the difference electron density for the main phase (Zn), and the positions of the reflexes in the form of peak diagrams (Fig. 3 b). It is evident that the change in the difference value ($\rho_{measured} - \rho_{calculated}$) of the electron density of the experiment, and theory for the main phase is extremely insignificant and is contained in a small range of deviations (from -1.35 to +1.35 units) (Fig. 3 b). At the same time, the difference line also has small deviations (Fig. 3 b). These facts indicate a high degree of convergence of the experimental and calculated curves, and this increases the reliability of the data obtained.

Fig. 4 shows the results of the quantitative ratio of the analysed phases depending on the degree of HPT treatment, as well as other characteristics of the microstructure of the main phases. The quantitative XRD data showed that the use of HPT treatment leads, on the one hand, to an increase in the mass fraction of the Zn phase in the alloy, and on the other hand, to the suppression of the content of the Mg_2Zn_{11} and $FeZn_{13}$ phases (Fig. 4 a). Based on the analysis of the width and positions of reflexes in the diffraction pattern, the average size of the CSD, the average dislocation density, and the values of the lattice constant of the main phases were determined.

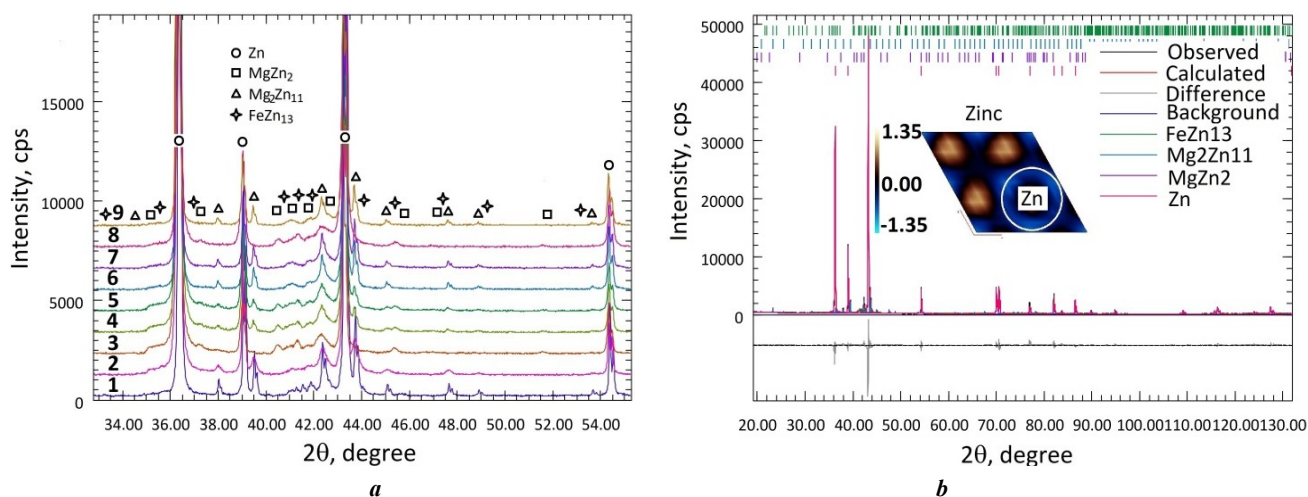


Fig. 3. X-Ray diffraction patterns of the Zn-1%Mg-1%Fe alloy: **a** – general view of diffraction patterns: 1 – heat treatment; 2 – HPT, 1 rev., 27 °C; 3 – HPT, 1 rev., 150 °C; 4 – HPT, 3 rev., 27 °C; 5 – HPT, 3 rev., 150 °C; 6 – HPT, 6 rev., 27 °C; 7 – HPT, 6 rev., 150 °C; 8 – HPT, 10 rev., 27 °C; 9 – HPT, 10 rev., 150 °C;

b – an example of the diffraction pattern processed by the Rietveld method: HPT, 1 rev., 27 °C

Рис. 3. Дифрактограммы сплава Zn-1%Mg-1%Fe: **a** – общий вид дифрактограмм:

1 – термическая обработка; 2 – ИПДК, 1 об., 27 °C; 3 – ИПДК, 1 об., 150 °C; 4 – ИПДК, 3 об., 27 °C; 5 – ИПДК, 3 об., 150 °C; 6 – ИПДК, 6 об., 27 °C; 7 – ИПДК, 6 об., 150 °C; 8 – ИПДК, 10 об., 27 °C; 9 – ИПДК, 10 об., 150 °C; **b** – пример обработанной методом Ритвелда дифрактограммы: ИПДК, 1 об., 27 °C

These microstructure characteristics depending on the degree and temperature of HPT treatment are shown in Fig. 4 b–d.

Fig. 5 shows the changes in the crystallographic orientations of grains in the Zn phase depending on the degree and temperature of HPT treatment. For a convenient and visual understanding of the evolution of texture formation processes, the preferred grain orientations in Fig. 5 are shown in the form of an inverse pole figure (IPF) (0001), which is parallel to the plane of the disk (sample). In the initial state of the alloy, the Zn phase grains are characterised by the presence of basic $\{0001\}\langle 1000 \rangle$, pyramidal $\{10\text{--}11\}\langle 0\text{--}110 \rangle$ and $\{21\text{--}36\}\langle 1\text{--}210 \rangle$, as well as prismatic $\{21\text{--}30\}\langle 1\text{--}210 \rangle$ and $\{31\text{--}40\}\langle 1\text{--}320 \rangle$ texture components (Fig. 5). Moreover, compression twin components $\{11\text{--}22\}\langle uvtv \rangle$ are revealed in some grains (Fig. 5). Analysis of the evolution of the crystallographic texture of Zn

phase during HPT showed that the texture formation processes, depending on the degree and temperature of its treatment, have similarities and differences. In particular, even after 1 revolution of HPT at 27 °C, the character of the distribution of texture maxima on the (0001) IPF changes sharply (Fig. 5). In this case, the basic $\{0001\}\langle 1000 \rangle$ texture components are enhanced, while the prismatic $\{21\text{--}30\}\langle 1\text{--}210 \rangle / \{31\text{--}40\}\langle 1\text{--}320 \rangle$ and pyramidal $\{21\text{--}36\}\langle 1\text{--}210 \rangle$ orientations, on the contrary, are suppressed. At the same time, new components $\{11\text{--}21\}\langle 1\text{--}100 \rangle$, $\{20\text{--}21\}\langle 0\text{--}110 \rangle$ and $\{11\text{--}24\}\langle 1\text{--}100 \rangle$ of pyramidal grain orientations, as well as components $\{10\text{--}12\}\langle uvtv \rangle$ of tension twinning are formed (Fig. 5).

With an increase in the number of revolutions to 3, the pyramidal, prismatic and twin texture components revealed after 1 HPT revolution are suppressed, and the pole density of the basic component is enhanced (Fig. 5). At high revo-

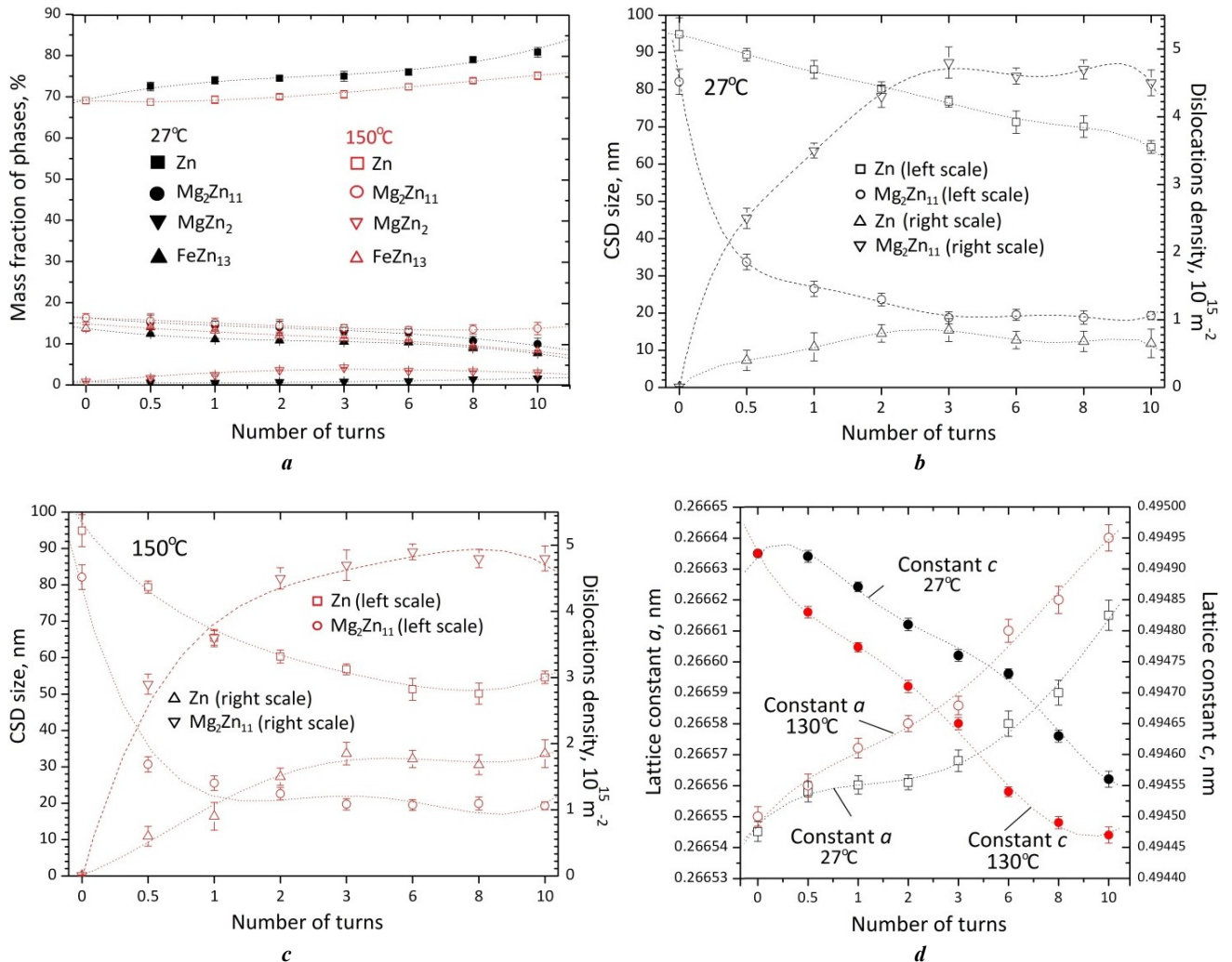


Fig. 4. Patterns of change in fine structure parameters depending on the number of revolutions of the HPT treatment: **a** – mass fraction of detected phases; **b** – average size of coherent scattering domains and average dislocation density at 27 °C; **c** – average size of coherent scattering domains and average dislocation density at 150 °C; **d** – lattice constant of Zn

Рис. 4. Закономерности изменения параметров тонкой структуры в зависимости от числа оборотов ИПДК-обработки: **a** – массовой доли обнаруженных фаз; **b** – усредненного размера областей когерентного рассеяния (ОКР) и средней плотности дислокаций при 27 °C; **c** – усредненного размера ОКР и средней плотности дислокаций при 150 °C; **d** – периода решетки Zn

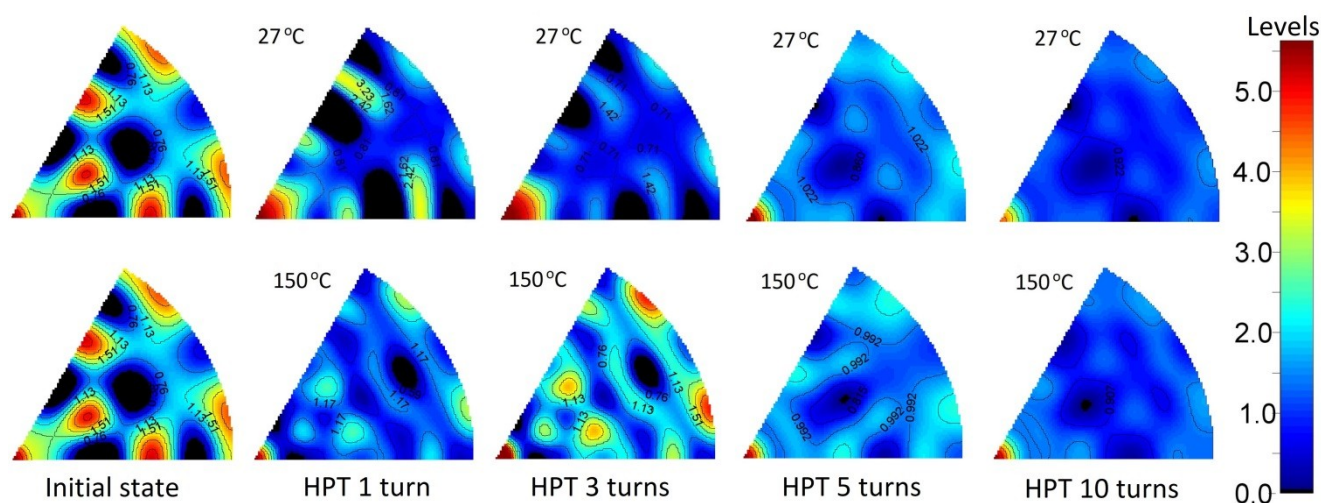


Fig. 5. Inverse pole figures (0001) for the Zn phase in the initial state and after HPT treatment
Рис. 5. Обратные полюсные фигуры (0001) для фазы Zn в исходном состоянии и в состояниях после ИПДК-обработки

lutions of the HPT treatment, further suppression of all texture components in favor of the basic one is observed, which becomes the main texture component (Fig. 5).

During the HPT treatment of the alloy at a temperature of 150 °C, the evolution of texture formation processes in the Zn phase has its own characteristics. Thus, at the initial stage (1 revolution) of the HPT treatment, compared to that implemented during the HPT at 27 °C, additional texture components are formed (Fig. 5). In particular, new components related to the pyramidal $\{21-34\}\langle 1-210\rangle$, $\{21-36\}\langle 1-210\rangle$ and $\{31-44\}\langle 1-320\rangle$ types are visible on the IPF (Fig. 5). The pole densities of additional texture components increase with an increase in the number of HPT revolutions to 3 (Fig. 5). In this state, an increase in the basic $\{0001\}\langle 1000\rangle$ and prismatic $\{21-30\}\langle 1-210\rangle$ / $\{31-40\}\langle 1-320\rangle$ texture components is also observed (Fig. 5). At high degrees of HPT treatment, the basic $\{0001\}\langle 1000\rangle$ texture component predominates over all other components of the crystallographic texture (Fig. 5).

DISCUSSION

The conducted studies have shown that the Zn–1%Mg–1%Fe alloy subjected to HPT treatment demonstrates increased strength characteristics along with sufficient ductility during its extension (Table 1). To determine the reasons for the increase in strength and ductility of this alloy, comprehensive studies of its microstructure were conducted. According to the conducted studies, the initial Zn–Mg–Fe alloy subjected to heat treatment consists of the Zn, Mg_2Zn_{11} and $FeZn_{13}$ phases. In this case, cylindrical $MgZn_2$ particles precipitated in the Mg_2Zn_{11} phase (Fig. 2 a). Earlier, some works [25; 26] also noted that $MgZn_2$ particles strengthening the alloy can precipitate in the Mg_2Zn_{11} phase.

The conducted analysis of the microstructure showed that even at the early stages of HPT treatment (0.5 revolution), the alloy does not exhibit eutectic structures

characteristic of the cast state. In this case, a band structure consisting of a mixture of the Zn, $FeZn_{13}$ and Mg_2Zn_{11} phases is formed, in which $MgZn_2$ particles precipitate (Fig. 2 b). $MgZn_2$ particles inside the Mg_2Zn_{11} bands (darker areas) are revealed as numerous light areas of different morphology (Fig. 2 b, inset). According to microscopy data, with an increase in the degree and temperature of HPT treatment, the width of the bands corresponding to the Zn, Mg_2Zn_{11} and $FeZn_{13}$ phases decreases. Moreover, a refinement of the structural components is observed inside the bands of each phase. In particular, the formation of equiaxial grains with a diameter of 230 nm in the Mg_2Zn_{11} bands is demonstrated in the inset to Fig. 2 c. In addition to the structure refinement, at high speeds of HPT treatment, Zn and $MgZn_2$ particles of spherical morphology strengthening the alloy precipitate in the Mg_2Zn_{11} phase (Fig. 2 d, inset). With an increase in the HPT temperature (150 °C), the dynamic strain ageing process is implemented more completely. This fact is explained by an increase in the proportion of $MgZn_2$ particles in the Mg_2Zn_{11} phase (Fig. 4 a). In this regard, one can argue that the role of dispersion, strengthening of the alloy increases significantly with an increase in the HPT temperature.

The obtained microscopy results are in good agreement with the X-ray diffraction analysis data. In particular, the quantitative X-ray diffraction method found that in the initial (as-cast) state of the alloy, the content of the Zn, Mg_2Zn_{11} , $FeZn_{13}$ and $MgZn_2$ phases is 69.0, 17.3, 13.5, and 0.2 %, respectively (Fig. 4 a). According to the literature data [23; 24], the mixture of Zn and Mg_2Zn_{11} phases is in the eutectic state, and this fact is consistent with the SEM study data. At the same time, the presence of the $FeZn_{13}$ phase in the microstructure was also identified as a result of the SEM analysis, and traces of intense precipitation of $MgZn_2$ particles in the Mg_2Zn_{11} phase were observed after heat treatment of the alloy (Fig. 2 a, 3 a).

In the case of HPT treatment, even a small deformation (0.5 revolutions) leads to changes in the ratio of the identified phases. In particular, it is clear that after 0.5 HPT revolution, a regular decrease in the Mg_2Zn_{11} and $FeZn_{13}$ mass fractions is observed (Fig. 4 a). At the same time, the Zn mass fraction increases monotonically (Fig. 4 a). An increase in the degree of deformation leads to a further regular decrease in the content of the Mg_2Zn_{11} and $FeZn_{13}$ phases (Fig. 4 a). At high degrees and an increase in the HPT temperature, the Zn phase content, as well as the $MgZn_2$ (precipitates) mass fraction increase significantly (Fig. 4 a).

As is known [18; 19; 27; 28], metallic materials subjected to HPT are characterised by a grain refinement, an increased density of induced defects, a developed crystallographic texture and an extremely nonequilibrium state of grain boundaries. The XRD analysis of the zinc alloy data shows that the microstructure changes differently in each of the main phases during HPT deformation. In particular, the Mg_2Zn_{11} phase is characterised by a sharp decrease in the CSD size (Fig. 4 b), which can be associated with grain refinement during HPT. It is evident that even at the initial stages of HPT treatment (up to 1 revolution), the average CSD size of the Mg_2Zn_{11} phase decreases to ~ 30 nm (Fig. 4 b). With an increase in the number of HPT revolutions to 3, a further decrease in the average CSR size down to ~ 20 nm is observed. At high HPT degrees, the average CSD size in the Mg_2Zn_{11} phase remains virtually unchanged, and remains in the range of 18...22 nm (Fig. 4 b). The same pattern of decrease in the CSD size in the Mg_2Zn_{11} phase is observed, with an increase in the HPT temperature (Fig. 4 c). On the other hand, the process of refinement of the structural elements in the Zn phase during HPT treatment is not as effective as expected (Fig. 4 b). In particular, it is obvious that at the early HPT stages (up to 1 revolution), the average CSD size remains virtually unchanged (Fig. 4 b). Only after reaching high degrees of HPT treatment (after 10 revolutions), the average CSD size in the Zn phase decreases to ~ 65 nm (Fig. 4 b). On the contrary, with an increase in the HPT temperature to 150 °C, the CSD size of the Zn phase decreases significantly even at the initial stages of deformation (Fig. 4 c). At high degrees of HPT, the CSD size of the Zn phase reaches saturation and is ~ 50 nm.

Comparative analysis showed, that the average densities of the induced defects in the analysed phases also change non-monotonically (Fig. 4 b). In particular, in the Mg_2Zn_{11} phase, after 3 HPT revolutions, the dislocation density reaches its maximum value ($\sim 4.5 \cdot 10^{15} \text{ m}^{-2}$), and then decreases slightly with an increase in the number of revolutions (Fig. 4 b). According to the X-ray diffraction data, a similar trend is observed in the Zn phase. However, compared to the Mg_2Zn_{11} phase, it has a relatively low dislocation density, not exceeding $0.8 \cdot 10^{15} \text{ m}^{-2}$ (Fig. 4 b). At high degrees of HPT treatment, a decrease in the dislocation density is observed in the Zn phase (Fig. 4 b). With an increase in the HPT temperature to 150 °C, the dislocation density in the Zn phase increases significantly (Fig. 4 c). In this case, in the Mg_2Zn_{11} phase, the dislocation density values found, are comparable with those obtained after HPT at 27 °C (Fig. 4 c).

The changes in the lattice constant values in the Zn phase depending on the degree of HPT treatment shown in Fig. 4 d are interesting. In particular, in the as-cast state, the lattice constant of Zn along the edge a of the hexagonal close-packed (hcp) lattice is 0.266549 nm, and along the basic edge c , it is 0.494952 nm (Fig. 4 d). The values found differ from the tabular data ($a=0.26648$ nm, $c=0.49467$ nm [29]), especially in the direction of the basis c of the hcp lattice. After 0.5 revolution of HPT treatment, a gradual increase in the lattice constant along the edge a , and a decrease in the value along the c direction of the hcp lattice are observed (Fig. 4 d). With a further increase in the number of revolutions and the temperature of HPT, the lattice constant of Zn along the edge a continues to increase, and along the face c it normally decreases. This change in the Zn lattice constant is most likely associated with the presence of Fe and Mg impurity atoms in this phase, which is supported by the SEM analysis data (Fig. 1 d).

As studies have shown, alloying Zn with Mg and Fe atoms and conducting HPT treatment, made it possible to increase significantly the alloy strength characteristics and simultaneously increase its ductility (Table 1), which meet the requirements for fixing bones and stents. Despite the low tensile strength (33 MPa) of the initial alloy, its microhardness (118 HV) is much higher than that of pure zinc (41 HV according to [1]). As SEM studies have shown, the initial alloy contains coarse Mg_2Zn_{11} and $FeZn_{13}$ phases (Fig. 1). Moreover, according to work [30], the hardness of the Mg_2Zn_{11} phase is ~ 300 HV and that of the $FeZn_{13}$ phase is 290 HV [31]. In this regard, the high microhardness of the initial alloy can be explained by the presence of coarse Mg_2Zn_{11} and $FeZn_{13}$ phases in its structure. As a result of HPT treatment (e.g. after 1 revolution, 27 °C), the alloy strength increases to 289 MPa, however, the microhardness of the alloy in this state is no more than 114 HV (Table 1). Studies have shown that HPT treatment of the alloy causes both the fragmentation of the Mg_2Zn_{11} and $FeZn_{13}$ phases (Fig. 2), and a decrease in the content of these phases (Fig. 4). At the same time, the proportion of the Zn phase increases (Fig. 4). These facts apparently limit the growth of the alloy microhardness, and explain the observed decrease in its microhardness during HPT. In general, the formation of a band structure consisting of the Zn, $FeZn_{13}$ and Mg_2Zn_{11} phases, grain refinement in the main phases, and the precipitation of particles in them, turned out to be the main factors in the zinc alloy increasing its mechanical properties. An equally important factor determining the level and anisotropy of the strength properties of the alloy under study is its developed crystallographic texture.

Analysis of the crystallographic textures showed that the Zn phase grain orientations in the initial alloy belong to the basic $\{0001\}\langle 1000 \rangle$, pyramidal $\{10\text{--}11\}\langle 0\text{--}110 \rangle$ and $\{21\text{--}36\}\langle 1\text{--}210 \rangle$, as well as prismatic $\{21\text{--}30\}\langle 1\text{--}210 \rangle$ and $\{31\text{--}40\}\langle 1\text{--}320 \rangle$ texture components. At the same time, there are compression twin components $\{11\text{--}22\}\langle u\text{wvtv} \rangle$ (Fig. 5). However, when the alloy is subjected to HPT treatment, the spatial orientation of the Zn phase grains in the sample changes significantly, as indicated by the texture maxima redistribution on the (0001) IPF (Fig. 5). In particular, already at the early stages of HPT treatment

(after 1 revolution, 27 °C), suppression of prismatic and pyramidal texture components, and strengthening of the basic orientation of grains are observed. In this case, other orientations of the pyramidal $\{11\text{-}21\}\langle 1\text{-}100\rangle$, $\{20\text{-}21\}\langle 0\text{-}110\rangle$ and $\{11\text{-}24\}\langle 1\text{-}100\rangle$ types, as well as $\{10\text{-}12\}\langle \text{uwtv}\rangle$ tension twin components are formed (Fig. 5). With an increase in the number of HPT revolutions to 3, the proportion of the basic $\{0001\}\langle 1000\rangle$ component increases, and all other identified grain orientations are slightly suppressed. At high HPT degrees, further suppression of all texture components is observed in favour of the basic one, which becomes the main one.

With increasing the HPT temperature (150 °C), the texture formation processes proceed identically with the predominance of the basic $\{0001\}\langle 1000\rangle$ texture component (Fig. 5). However, at the early stages of HPT at 150 °C, except for the components characteristic of HPT at 27 °C, new grain orientations are formed in the sample. In this case, the pole densities of the new texture components increase with an increase in the number of HPT revolutions to 3 (Fig. 5). In this state, the basic $\{0001\}\langle 1000\rangle$ and prismatic $\{21\text{-}30\}\langle 1\text{-}210\rangle$ / $\{31\text{-}40\}\langle 1\text{-}320\rangle$ texture components also increase (Fig. 5).

As shown by tensile tests, in the state after 3 revolutions of HPT at 150 °C, the alloy demonstrates the highest mechanical properties (Table 1). In this state, the Zn phase grains have pyramidal, prismatic and twin components of the volume fraction texture, in addition to the basic one. As is known [32; 33], the value of the critical shear stress, which determines the onset of operation of certain slip systems, is minimal for basic systems, and has the highest values for pyramidal, prismatic and twin systems. In this regard, one can argue that the formation of pyramidal, prismatic and twin texture components at the initial stages of HPT treatment of the alloy, contributes to an increase in its strength properties, since their operation requires high loads. At high degrees of HPT, the main orientation is the basic component, and for the operation of the alloy, i. e. for the implementation of its plastic deformation, less impact is required. The formation of a predominantly basic texture component, can explain the decrease in the strength properties of this alloy at high degrees of HPT.

The studies conducted using XRD and microscopy methods showed that as a result of HPT, a unique UFG structure consisting of the Zn, $\text{Mg}_2\text{Zn}_{11}$ and FeZn_{13} phases, in which particles of spherical morphology precipitate, is formed in the Zn–1%Mg–1%Fe alloy. During HPT, the density of introduced structural defects also increases and a developed crystallographic texture is formed. The discovered facts indicate that dispersion, grain-boundary (according to the Hall–Petch relationship), and dislocation strengthening mechanisms are implemented in the alloy. At the same time, the stability of the pyramidal, prismatic and twin texture components during HPT treatment determine the level and anisotropy of the strength properties of this alloy. In general, compared to pure Zn, the Zn–1%Mg–1%Fe alloy, optimised by the HPT method, exhibits higher strength properties (tensile strength, hardness) with sufficient ductility, and with such characteristics it can be used as implants for some applications [34].

CONCLUSIONS

A new Zn–1%Mg–1%Fe alloy with improved mechanical properties (ultimate tensile strength is 415 MPa, ductility is 82 %) to be used in medicine, as implants, has been produced by alloying and forming a UFG structure in it as a result of HPT (3 revolutions, 150 °C). It has been found that HPT in the main phases (Zn and $\text{Mg}_2\text{Zn}_{11}$) results in effective refinement of the grain structure, and an increase in the density of introduced defects. At the initial stages of HPT, a developed crystallographic texture consisting of basic, pyramidal, prismatic and twin texture components is formed in the Zn phase. The stability of the pyramidal, prismatic and twin texture components during HPT, determines the level and anisotropy of the strength properties of this alloy. Effective refinement of grains in the main phases and the formation of the UFG structure, as well as the precipitation of spherical particles with a high content, are the main factors increasing the mechanical properties of this alloy.

REFERENCES

- García-Mintegui C., Córdoba L.C., Buxadera-Palomero J., Marquina A., Jiménez-Piqué E., Ginebra M.-P., Cortina J.L., Pegueroles M. Zn-Mg and Zn-Cu alloys for stenting applications: From nanoscale mechanical characterization to in vitro degradation and biocompatibility. *Bioactive Materials*, 2021, vol. 6, no. 12, pp. 4430–4446. DOI: [10.1016/j.bioactmat.2021.04.015](https://doi.org/10.1016/j.bioactmat.2021.04.015).
- Wei Yuan, Dandan Xia, Shuilin Wu, Yufeng Zheng, Zhenpeng Guan, Rau J.V. A review on current research status of the surface modification of Zn-based biodegradable metals. *Bioactive Materials*, 2022, vol. 7, pp. 192–216. DOI: [10.1016/j.bioactmat.2021.05.018](https://doi.org/10.1016/j.bioactmat.2021.05.018).
- Wątroba M., Mech K., Bednarczyk W., Kawałko J., Marciszko-Wiąckowska M., Marzec M., Shepherd D.E.T., Bała P. Long-term in vitro corrosion behavior of Zn-3Ag and Zn-3Ag-0.5Mg alloys considered for biodegradable implant applications. *Materials & Design*, 2022, vol. 213, article number 110289. DOI: [10.1016/j.matdes.2021.110289](https://doi.org/10.1016/j.matdes.2021.110289).
- Huang Tian, Liu Zhilin, Wu Dachao, Yu Hailiang. Microstructure, mechanical properties, and biodegradation response of the grain-refined Zn alloys for potential medical materials. *Journal of materials research and technology*, 2021, vol. 15, pp. 226–240. DOI: [10.1016/j.jmrt.2021.08.024](https://doi.org/10.1016/j.jmrt.2021.08.024).
- Young J., Reddy R.G. Synthesis, mechanical properties, and in vitro corrosion behavior of biodegradable Zn–Li–Cu alloys. *Journal of Alloys and Compounds*, 2020, vol. 844, article number 156257. DOI: [10.1016/j.jallcom.2020.156257](https://doi.org/10.1016/j.jallcom.2020.156257).
- Zhuo Xiaoru, Wu Yuna, Ju Jia, Liu Huan, Jiang Jinghua, Hu Zhichao, Bai Jing, Xue Feng. Recent progress of novel biodegradable zinc alloys: from the perspective of strengthening and toughening. *Journal of Materials Research and Technology*, 2022, vol. 17, pp. 244–269. DOI: [10.1016/j.jmrt.2022.01.004](https://doi.org/10.1016/j.jmrt.2022.01.004).
- Shao Xiaoxi, Wang Xiang, Xu Fangfang et al. In vivo biocompatibility and degradability of a Zn-Mg-Fe alloy osteosynthesis system. *Bioactive Materials*, 2021, vol. 7, pp. 154–166. DOI: [10.1016/j.bioactmat.2021.05.012](https://doi.org/10.1016/j.bioactmat.2021.05.012).

8. Su Yingchao, Fu Jiayin, Lee Wonsae, Du Shaokang, Qin Yi-Xian, Zheng Yufeng, Wang Yadong, Zhu Donghui. Improved mechanical, degradation, and biological performances of Zn-Fe alloys as bioresorbable implants. *Bioactive Materials*, 2022, vol. 17, pp. 334–343. DOI: [10.1016/j.bioactmat.2021.12.030](https://doi.org/10.1016/j.bioactmat.2021.12.030).
9. He Jin, Li Da-Wei, He Feng-Li et al. A study of degradation behaviour and biocompatibility of Zn-Fe alloy prepared by electrodeposition. *Materials Science and Engineering: C*, 2020, vol. 117, article number 111295. DOI: [10.1016/j.msec.2020.111295](https://doi.org/10.1016/j.msec.2020.111295).
10. Oliver A.A., Guillory R.J., Flom K.L., Morath L.M., Kolesar T.M., Mostaed E., Sikora-Jasinska M., Drellich J.W., Goldman J. Analysis of vascular inflammation against bioresorbable Zn-Ag based alloys. *ACS Applied Bio Materials*, 2020, vol. 3, no. 10, pp. 6779–6789. DOI: [10.1021/acsabm.0c00740](https://doi.org/10.1021/acsabm.0c00740).
11. Kafri A., Ovadia S., Goldman J., Drellich J., Aghion E. The Suitability of Zn–1.3%Fe Alloy as a Biodegradable Implant Material. *Metals*, 2018, vol. 8, no. 3, article number 153. DOI: [10.3390/met8030153](https://doi.org/10.3390/met8030153).
12. Shi Zhang-Zhi, Gao Xi-Xian, Chen Hong-Ting, Liu Xue-Feng, Li Ang, Zhang Hai-Jun, Wang Lu-Ning. Enhancement in mechanical and corrosion resistance properties of a biodegradable Zn-Fe alloy through second phase refinement. *Materials Science and Engineering: C*, 2020, vol. 116, article number 111197. DOI: [10.1016/j.msec.2020.111197](https://doi.org/10.1016/j.msec.2020.111197).
13. Shiyang Liu, Kent D., Doan Nghiem, Dargusch M., Gui Wang. Effects of deformation twinning on the mechanical properties of biodegradable Zn-Mg alloys. *Bioactive Materials*, 2019, vol. 4, pp. 8–16. DOI: [10.1016/j.bioactmat.2018.11.001](https://doi.org/10.1016/j.bioactmat.2018.11.001).
14. Galib R.H., Sharif A. Development of Zn-Mg alloys as a degradable biomaterial. *Advances in Alloys and Compounds*, 2015, vol. 1, no. 1, pp. 1–7.
15. Vojtech D., Kubasek J., Serak J., Novak P. Mechanical and corrosion properties of newly developed biodegradable Zn based alloys for bone fixation. *Acta Biomaterialia*, 2011, vol. 7, no. 9, pp. 3515–3522. DOI: [10.1016/j.actbio.2011.05.008](https://doi.org/10.1016/j.actbio.2011.05.008).
16. Li Huafang, Xie Xin-Hui, Zheng Yufeng et al. Development of biodegradable Zn-1X binary alloys with nutrient alloying elements Mg, Ca and Sr. *Scientific Reports*, 2015, vol. 5, article number 10719. DOI: [10.1038/srep10719](https://doi.org/10.1038/srep10719).
17. Xue Penghao, Ma Minglong, Li Yongjun, Li Xinggang, Yuan Jiawei, Shi Guoliang, Wang Kaikun, Zhang Kui. Microstructure, Mechanical Properties, and in Vitro Corrosion Behavior of Biodegradable Zn-1Fe-xMg Alloy. *Materials*, 2020, vol. 13, no. 21, article number 4835. DOI: [10.3390/ma13214835](https://doi.org/10.3390/ma13214835).
18. Valiev R.Z., Islamgaliev R.K., Alexandrov I.V. Bulk nanostructured materials from severe plastic deformation. *Progress in Materials Science*, 2000, vol. 45, no. 2, pp. 103–189. DOI: [10.1016/S0079-6425\(99\)00007-9](https://doi.org/10.1016/S0079-6425(99)00007-9).
19. Sitdikov V.D., Khafizova E.D., Polenok M.V. Microstructure and properties of the Zn–1%Li–2%Mg alloy subjected to severe plastic deformation. *Frontier Materials & Technologies*, 2023, no. 2, pp. 117–130. DOI: [10.18323/2782-4039-2023-2-64-7](https://doi.org/10.18323/2782-4039-2023-2-64-7).
20. Luqman M., Ali Y., Zaghloul M.M.Y., Sheikh F.A., Chan V., Abdal-hay A. Grain Refinement Mechanism and its effect on Mechanical Properties and Biodegradation Behaviors of Zn Alloys – A Review. *Journal of Materials Research and Technology*, 2023, vol. 24, pp. 7338–7365. DOI: [10.1016/j.jmrt.2023.04.219](https://doi.org/10.1016/j.jmrt.2023.04.219).
21. Leoni M., Confente T., Scardi P. PM2K: A flexible program implementing Whole Powder Pattern Modelling. *Zeitschrift für Kristallographie, Supplement*, 2006, vol. 1, no. 23, pp. 249–254.
22. Rietveld H.M. A profile refinement method for nuclear and magnetic structures. *Journal of Applied Crystallography*, 1969, vol. 2, no. 2, pp. 65–71. DOI: [10.1107/S0021889869006558](https://doi.org/10.1107/S0021889869006558).
23. Pingli Jiang, Blawert C., Zheludkevich M.L. The Corrosion Performance and Mechanical Properties of Mg-Zn Based Alloys – A Review. *Corrosion and Materials Degradation*, 2020, vol. 1, no. 1, pp. 92–158. DOI: [10.3390/cmd1010007](https://doi.org/10.3390/cmd1010007).
24. Shi Zhang-Zhi, Gao Xi-Xian, Zhang Hai-Jun, Liu Xue-Feng, Li Hui-Yan, Zhou Chao, Yin Xu-Xia, Wang Lu-Ning. Design biodegradable Zn alloys: Second phases and their significant influences on alloy properties. *Bioactive Materials*, 2020, vol. 5, no. 2, pp. 210–218. DOI: [10.1016/j.bioactmat.2020.02.010](https://doi.org/10.1016/j.bioactmat.2020.02.010).
25. Ye Lifeng, Huang He, Sun Chao et al. Effect of grain size and volume fraction of eutectic structure on mechanical properties and corrosion behavior of as-cast Zn-Mg binary alloys. *Journal of Materials Research and Technology*, 2021, vol. 16, pp. 1673–1685. DOI: [10.1016/j.jmrt.2021.12.101](https://doi.org/10.1016/j.jmrt.2021.12.101).
26. Huang He, Liu Huan, Wang Lisha, Yan Kai, Li Yuhua, Jiang Jinghua, Ma Aibin, Xue Feng, Bai Jing. Revealing the effect of minor Ca and Sr additions on microstructure evolution and mechanical properties of Zn-0.6 Mg alloy during multi-pass equal channel angular pressing. *Journal of Alloys and Compounds*, 2020, vol. 844, article number 155923. DOI: [10.1016/j.jallcom.2020.155923](https://doi.org/10.1016/j.jallcom.2020.155923).
27. Sitdikov V.D., Kulyasova O.B., Sitdikova G.F., Islamgaliev R.K., Yufeng Zheng. Structural-phase transformations in the Zn-Li-Mg alloy exposed to the severe plastic torsion deformation. *Frontier Materials & Technologies*, 2022, no. 3-2, pp. 44–55. DOI: [10.18323/2782-4039-2022-3-2-44-55](https://doi.org/10.18323/2782-4039-2022-3-2-44-55).
28. Nazarov A.A. Nonequilibrium grain boundaries in bulk nanostructured metals and their recovery under the influences of heating and cyclic deformation. Review. *Letters on materials*, 2018, vol. 8, no. 3, pp. 372–381. DOI: [10.22226/2410-3535-2018-3-372-381](https://doi.org/10.22226/2410-3535-2018-3-372-381).
29. Wyckoff R.W.G. Hexagonal closest packed, hcp, structure. *Crystal Structures*. New York, Interscience Publishers Publ., 1963. Vol. 1, pp. 7–83.
30. Necas D., Marek I., Pinc J., Vojtech D., Kubásek J. Advanced Zinc–Magnesium Alloys Prepared by Mechanical Alloying and Spark Plasma Sintering. *Materials*, 2022, vol. 15, no. 15, article number 5272. DOI: [10.3390/ma15155272](https://doi.org/10.3390/ma15155272).
31. Han Kwangsik, Lee Inho, Ohnuma I., Okuda K., Kainuma R. Micro-Vickers Hardness of Intermetallic Compounds in the Zn-rich Portion of Zn–Fe Binary System. *ISIJ International*, 2018, vol. 58, no. 9, pp. 1578–1583. DOI: [10.2355/isijinternational.ISIJINT-2018-111](https://doi.org/10.2355/isijinternational.ISIJINT-2018-111).
32. Liu Shiyang, Kent D., Zhan Hongyi, Doan Nghiem, Dargusch M., Wang Gui. Dynamic recrystallization of

- pure zinc during high strain-rate compression at ambient temperature. *Materials Science and Engineering: A*, 2020, vol. 784, article number 139325. DOI: [10.1016/j.msea.2020.139325](https://doi.org/10.1016/j.msea.2020.139325).
33. Pham Nguyen, Abbès F., Lecomte J.S., Schuman C., Abbès B. Inverse Identification of Single-Crystal Plasticity Parameters of HCP Zinc from Nanoindentation Curves and Residual Topographies. *Nanomaterials (Basel)*, 2022, vol. 12, no. 3, article number 300. DOI: [10.3390/nano12030300](https://doi.org/10.3390/nano12030300).
 34. Yang Hongtao, Qu Xinhua, Lin Wenjiao, Chen Dafu, Zhu Donghui, Dai Kerong, Zheng Yufeng. Enhanced osseointegration of Zn-Mg composites by tuning the release of Zn ions with sacrificial Mg rich anode design. *ACS Biomaterials Science & Engineering*, 2018, vol. 5, no. 2, pp. 453–467. DOI: [10.1021/acsbomaterials.8b01137](https://doi.org/10.1021/acsbomaterials.8b01137).
- ### СПИСОК ЛИТЕРАТУРЫ
1. García-Mintegui C., Córdoba L.C., Buxadera-Palomero J., Marquina A., Jiménez-Piqué E., Ginebra M.-P., Cortina J.L., Pegueroles M. Zn-Mg and Zn-Cu alloys for stenting applications: From nanoscale mechanical characterization to in vitro degradation and biocompatibility // *Bioactive Materials*. 2021. Vol. 6. № 12. P. 4430–4446. DOI: [10.1016/j.bioactmat.2021.04.015](https://doi.org/10.1016/j.bioactmat.2021.04.015).
 2. Yuan Wei, Xia Dandan, Wu Shuilin, Zheng Yufeng, Guan Zhenpeng, Rau J.V. A review on current research status of the surface modification of Zn-based biodegradable metals // *Bioactive Materials*. 2022. Vol. 7. P. 192–216. DOI: [10.1016/j.bioactmat.2021.05.018](https://doi.org/10.1016/j.bioactmat.2021.05.018).
 3. Wątroba M., Mech K., Bednarczyk W., Kawalko J., Marciszko-Wiąckowska K., Marzec M., Shepherd D.E.T., Bała P. Long-term in vitro corrosion behavior of Zn-3Ag and Zn-3Ag-0.5Mg alloys considered for biodegradable implant applications // *Materials & Design*. 2022. Vol. 213. Article number 110289. DOI: [10.1016/j.matdes.2021.110289](https://doi.org/10.1016/j.matdes.2021.110289).
 4. Huang Tian, Liu Zhilin, Wu Dachao, Yu Hailiang. Microstructure, mechanical properties, and biodegradation response of the grain-refined Zn alloys for potential medical materials // *Journal of materials research and technology*. 2021. Vol. 15. P. 226–240. DOI: [10.1016/j.jmrt.2021.08.024](https://doi.org/10.1016/j.jmrt.2021.08.024).
 5. Young J., Reddy R.G. Synthesis, mechanical properties, and in vitro corrosion behavior of biodegradable Zn–Li–Cu alloys // *Journal of Alloys and Compounds*. 2020. Vol. 844. Article number 156257. DOI: [10.1016/j.jallcom.2020.156257](https://doi.org/10.1016/j.jallcom.2020.156257).
 6. Zhuo Xiaoru, Wu Yuna, Ju Jia, Liu Huan, Jiang Jinghua, Hu Zhichao, Bai Jing, Xue Feng. Recent progress of novel biodegradable zinc alloys: from the perspective of strengthening and toughening // *Journal of Materials Research and Technology*. 2022. Vol. 17. P. 244–269. DOI: [10.1016/j.jmrt.2022.01.004](https://doi.org/10.1016/j.jmrt.2022.01.004).
 7. Shao Xiaoxi, Wang Xiang, Xu Fangfang et al. In vivo biocompatibility and degradability of a Zn-Mg-Fe alloy osteosynthesis system // *Bioactive Materials*. 2021. Vol. 7. P. 154–166. DOI: [10.1016/j.bioactmat.2021.05.012](https://doi.org/10.1016/j.bioactmat.2021.05.012).
 8. Su Yingchao, Fu Jiayin, Lee Wonsae, Du Shaokang, Qin Yi-Xian, Zheng Yufeng, Wang Yadong, Zhu Donghui. Improved mechanical, degradation, and biological performances of Zn-Fe alloys as bioresorbable implants // *Bioactive Materials*. 2022. Vol. 17. P. 334–343. DOI: [10.1016/j.bioactmat.2021.12.030](https://doi.org/10.1016/j.bioactmat.2021.12.030).
 9. He Jin, Li Da-Wei, He Feng-Li et al. A study of degradation behaviour and biocompatibility of Zn-Fe alloy prepared by electrodeposition // *Materials Science and Engineering: C*. 2020. Vol. 117. Article number 111295. DOI: [10.1016/j.msec.2020.111295](https://doi.org/10.1016/j.msec.2020.111295).
 10. Oliver A.A., Guillory R.J., Flom K.L., Morath L.M., Kolesar T.M., Mostaed E., Sikora-Jasinska M., Drelich J.W., Goldman J. Analysis of vascular inflammation against bioresorbable Zn-Ag based alloys // *ACS Applied Bio Materials*. 2020. Vol. 3. № 10. P. 6779–6789. DOI: [10.1021/acsubm.0c00740](https://doi.org/10.1021/acsubm.0c00740).
 11. Kafri A., Ovadia S., Goldman J., Drelich J., Aghion E. The Suitability of Zn–1.3%Fe Alloy as a Biodegradable Implant Material // *Metals*. 2018. Vol. 8. № 3. Article number 153. DOI: [10.3390/met8030153](https://doi.org/10.3390/met8030153).
 12. Shi Zhang-Zhi, Gao Xi-Xian, Chen Hong-Ting, Liu Xue-Feng, Li Ang, Zhang Hai-Jun, Wang Lu-Ning. Enhancement in mechanical and corrosion resistance properties of a biodegradable Zn-Fe alloy through second phase refinement // *Materials Science and Engineering: C*. 2020. Vol. 116. Article number 111197. DOI: [10.1016/j.msec.2020.111197](https://doi.org/10.1016/j.msec.2020.111197).
 13. Liu Shiyang, Kent D., Doan Nghiem, Dargusch M., Wang Gui. Effects of deformation twinning on the mechanical properties of biodegradable Zn-Mg alloys // *Bioactive Materials*. 2019. Vol. 4. P. 8–16. DOI: [10.1016/j.bioactmat.2018.11.001](https://doi.org/10.1016/j.bioactmat.2018.11.001).
 14. Galib R.H., Sharif A. Development of Zn-Mg alloys as a degradable biomaterial // *Advances in Alloys and Compounds*. 2015. Vol. 1. № 1. P. 1–7.
 15. Vojtech D., Kubasek J., Serak J., Novak P. Mechanical and corrosion properties of newly developed biodegradable Zn based alloys for bone fixation // *Acta Biomaterialia*. 2011. Vol. 7. № 9. P. 3515–3522. DOI: [10.1016/j.actbio.2011.05.008](https://doi.org/10.1016/j.actbio.2011.05.008).
 16. Li Huafang, Xie Xin-Hui, Zheng Yufeng et al. Development of biodegradable Zn-IX binary alloys with nutrient alloying elements Mg, Ca and Sr // *Scientific Reports*. 2015. Vol. 5. Article number 10719. DOI: [10.1038/srep10719](https://doi.org/10.1038/srep10719).
 17. Xue Penghao, Ma Minglong, Li Yongjun, Li Xinggang, Yuan Jiawei, Shi Guoliang, Wang Kaikun, Zhang Kui. Microstructure, Mechanical Properties, and in Vitro Corrosion Behavior of Biodegradable Zn-1Fe-xMg Alloy // *Materials*. 2020. Vol. 13. № 21. Article number 4835. DOI: [10.3390/ma13214835](https://doi.org/10.3390/ma13214835).
 18. Valiev R.Z., Islamgaliev R.K., Alexandrov I.V. Bulk nanostructured materials from severe plastic deformation // *Progress in Materials Science*. 2000. Vol. 45. № 2. P. 103–189. DOI: [10.1016/S0079-6425\(99\)00007-9](https://doi.org/10.1016/S0079-6425(99)00007-9).
 19. Сıtdиков В.Д., Хафızова Э.Д., Поленок М.В. Микроструктура и свойства сплава Zn–1%Li–2%Mg, подвергнутого интенсивной пластической деформации // *Frontier Materials & Technologies*. 2023. № 2. С. 117–130. DOI: [10.18323/2782-4039-2023-2-64-7](https://doi.org/10.18323/2782-4039-2023-2-64-7).
 20. Luqman M., Ali Y., Zaghoul M.M.Y., Sheikh F.A., Chan V., Abdal-hay A. Grain Refinement Mechanism and its effect on Mechanical Properties and Biodegradation Behaviors of Zn Alloys – A Review // *Journal of*

- Materials Research and Technology. 2023. Vol. 24. P. 7338–7365. DOI: [10.1016/j.jmrt.2023.04.219](https://doi.org/10.1016/j.jmrt.2023.04.219).
21. Leoni M., Confente T., Scardi P. PM2K: A flexible program implementing Whole Powder Pattern Modelling // Zeitschrift für Kristallographie, Supplement. 2006. Vol. 1. № 23. P. 249–254.
 22. Rietveld H.M. A profile refinement method for nuclear and magnetic structures // Journal of Applied Crystallography. 1969. Vol. 2. № 2. P. 65–71. DOI: [10.1107/S0021889869006558](https://doi.org/10.1107/S0021889869006558).
 23. Jiang Pingli, Blawert C., Zheludkevich M.L. The Corrosion Performance and Mechanical Properties of Mg-Zn Based Alloys – A Review // Corrosion and Materials Degradation. 2020. Vol. 1. № 1. P. 92–158. DOI: [10.3390/cmd1010007](https://doi.org/10.3390/cmd1010007).
 24. Shi Zhang-Zhi, Gao Xi-Xian, Zhang Hai-Jun, Liu Xue-Feng, Li Hui-Yan, Zhou Chao, Yin Xu-Xia, Wang Lu-Ning. Design biodegradable Zn alloys: Second phases and their significant influences on alloy properties // Bioactive Materials. 2020. Vol. 5. № 2. P. 210–218. DOI: [10.1016/j.bioactmat.2020.02.010](https://doi.org/10.1016/j.bioactmat.2020.02.010).
 25. Ye Lifeng, Huang He, Sun Chao et al. Effect of grain size and volume fraction of eutectic structure on mechanical properties and corrosion behavior of as-cast Zn-Mg binary alloys // Journal of Materials Research and Technology. 2021. Vol. 16. P. 1673–1685. DOI: [10.1016/j.jmrt.2021.12.101](https://doi.org/10.1016/j.jmrt.2021.12.101).
 26. Huang He, Liu Huan, Wang Lisha, Yan Kai, Li Yuhua, Jiang Jinghua, Ma Aibin, Xue Feng, Bai Jing. Revealing the effect of minor Ca and Sr additions on microstructure evolution and mechanical properties of Zn-0.6 Mg alloy during multi-pass equal channel angular pressing // Journal of Alloys and Compounds. 2020. Vol. 844. Article number 155923. DOI: [10.1016/j.jallcom.2020.155923](https://doi.org/10.1016/j.jallcom.2020.155923).
 27. Ситдиков В.Д., Кулясова О.Б., Ситдикова Г.Ф., Исламгалиев Р.К., Юфенг Ж. Структурно-фазовые превращения в Zn–Li–Mg сплаве, подвергнутом интенсивной пластической деформации кручением // Frontier Materials & Technologies. 2022. № 3-2. С. 44–55. DOI: [10.18323/2782-4039-2022-3-2-44-55](https://doi.org/10.18323/2782-4039-2022-3-2-44-55).
 28. Nazarov A.A. Nonequilibrium grain boundaries in bulk nanostructured metals and their recovery under the influences of heating and cyclic deformation. Review // Letters on materials. 2018. Vol. 8. № 3. P. 372–381. DOI: [10.22226/2410-3535-2018-3-372-381](https://doi.org/10.22226/2410-3535-2018-3-372-381).
 29. Wyckoff R.W.G. Hexagonal closest packed, HCP, structure // Crystal Structures. New York: Interscience Publishers, 1963. Vol. 1. P. 7–83.
 30. Necas D., Marek I., Pinc J., Vojtech D., Kubásek J. Advanced Zinc–Magnesium Alloys Prepared by Mechanical Alloying and Spark Plasma Sintering // Materials. 2022. Vol. 15. № 15. Article number 5272. DOI: [10.3390/ma15155272](https://doi.org/10.3390/ma15155272).
 31. Han Kwangsik, Lee Inho, Ohnuma I., Okuda K., Kainuma R. Micro-Vickers Hardness of Intermetallic Compounds in the Zn-rich Portion of Zn–Fe Binary System // ISIJ International. 2018. Vol. 58. № 9. P. 1578–1583. DOI: [10.2355/isijinternational.ISIJINT-2018-111](https://doi.org/10.2355/isijinternational.ISIJINT-2018-111).
 32. Liu Shiyang, Kent D., Zhan Hongyi, Doan Nghiem, Dargusch M., Wang Gui. Dynamic recrystallization of pure zinc during high strain-rate compression at ambient temperature // Materials Science and Engineering: A. 2020. Vol. 784. Article number 139325. DOI: [10.1016/j.msea.2020.139325](https://doi.org/10.1016/j.msea.2020.139325).
 33. Nguyen Pham, Abbès F., Lecomte J.S., Schuman C., Abbès B. Inverse Identification of Single-Crystal Plasticity Parameters of HCP Zinc from Nanoindentation Curves and Residual Topographies // Nanomaterials (Basel). 2022. Vol. 12. № 3. Article number 300. DOI: [10.3390/nano12030300](https://doi.org/10.3390/nano12030300).
 34. Yang Hongtao, Qu Xinhua, Lin Wenjiao, Chen Dafu, Zhu Donghui, Dai Kerong, Zheng Yufeng. Enhanced osseointegration of Zn-Mg composites by tuning the release of Zn ions with sacrificial Mg rich anode design // ACS Biomaterials Science & Engineering. 2018. Vol. 5. № 2. P. 453–467. DOI: [10.1021/acsbiomaterials.8b01137](https://doi.org/10.1021/acsbiomaterials.8b01137).

Микроструктура, кристаллографическая текстура и механические свойства сплава Zn–1%Mg–1%Fe, подвергнутого интенсивной пластической деформации

© 2024

Ситдиков Виль Даянович^{*1,2,4}, доктор физико-математических наук, старший эксперт, старший научный сотрудник

Хафизова Эльвира Динифовна^{2,3,5}, кандидат технических наук, доцент кафедры материаловедения и физики металлов,

старший научный сотрудник НИЛ «Металлы и сплавы при экстремальных воздействиях»

Поленок Милена Владиславовна^{2,3,6}, магистрант кафедры материаловедения и физики металлов, лаборант НИЛ «Металлы и сплавы при экстремальных воздействиях»

¹ООО «РН-БашНИПИнефть», Уфа (Россия)

²Институт физики молекул и кристаллов Уфимского федерального исследовательского центра РАН, Уфа (Россия)

³Уфимский университет науки и технологий, Уфа (Россия)

*E-mail: SitdikovVD@bniipi.rosneft.ru

⁴ORCID: <https://orcid.org/0000-0002-9948-1099>

⁵ORCID: <https://orcid.org/0000-0002-4618-412X>

⁶ORCID: <https://orcid.org/0000-0001-9774-1689>

Поступила в редакцию 09.02.2024

Принята к публикации 19.07.2024

Аннотация: Статья посвящена получению, анализу микроструктуры, кристаллографической текстуры и механизмов деформации ультрамелкозернистого (УМЗ) цинкового Zn–1%Mg–1%Fe сплава, демонстрирующего уникальные физико-механические свойства по сравнению с его крупнокристаллическими аналогами. Цинковый сплав с улучшенными механическими свойствами разрабатывали в два этапа. На первом этапе на основе анализа литературных данных отливали сплав со следующим химическим составом: Zn–1%Mg–1%Fe. В дальнейшем сплав подвергали интенсивной пластической деформации кручением (ИПДК) с целью повышения механических свойств в результате измельчения зеренной структуры и реализации в нем динамического деформационного старения. Проведенные механические испытания на растяжения образцов и оценка твердости сплава показали, что ИПДК-обработка приводит к росту предела прочности до 415 МПа, увеличению твердости до значения 144 HV и повышению пластичности до 82 %. Полученные механические характеристики демонстрируют пригодность использования разработанного сплава в медицине в качестве некоторых имплантатов (стендов), требующих больших приложенных нагрузок. Для объяснения причин повышения механических свойств данного сплава проведены комплексные испытания методами микроскопии и рентгеноструктурного анализа. Анализ микроструктуры показал, что при формировании УМЗ структуры реализуется фазовый переход по следующей схеме: $Zn_{\text{эвтектика}} + Mg_2Zn_{11\text{эвтектика}} + FeZn_{13} \rightarrow Zn_{\text{фаза}} + Mg_2Zn_{11\text{фаза}} + MgZn_{2\text{частицы}} + Zn_{\text{частицы}}$. Установлено, что в результате ИПДК-обработки в основных фазах (Zn, Mg_2Zn_{11}) происходит измельчение зеренной структуры, повышение плотности внесенных дефектов и формирование развитой кристаллографической текстуры, состоящей из базисных, пирамидальных, призматических и двойниковых компонент текстуры. Показано, что стойкость пирамидальных, призматических и двойниковых компонент текстуры на начальных этапах ИПДК определяет уровень и анизотропию прочностных свойств данного сплава. Обсуждается взаимосвязь обнаруженных структурных особенностей полученного сплава с его уникальными механическими свойствами.

Ключевые слова: сплав Zn–1%Mg–1%Fe; фазовые переходы в цинковом сплаве; интенсивная пластическая деформация; методы рентгеновского рассеяния; механические свойства; прочность; пластичность; кристаллографическая текстура.

Благодарности: Исследование выполнено за счет гранта Российского научного фонда № 23-29-00667, <https://rscf.ru/project/23-29-00667>.

Для цитирования: Ситдиков В.Д., Хафизова Э.Д., Polenok M.V. Микроструктура, кристаллографическая текстура и механические свойства сплава Zn–1%Mg–1%Fe, подвергнутого интенсивной пластической деформации // Frontier Materials & Technologies. 2024. № 3. С. 75–88. DOI: 10.18323/2782-4039-2024-3-69-7.

Pulse diffusion welding of female joints

© 2024

Evgeny L. Strizhakov, Doctor of Sciences (Engineering), Professor,
leading researcher of the Center for Scientific Competencies
Stanislav V. Nescoromniy*¹, PhD (Engineering), Associate Professor,
Head of Chair “Machines and Automation of Welding Engineering”
Yury G. Lyudmirsky, Doctor of Sciences (Engineering), Professor,
leading researcher of the Center for Scientific Competencies
Nikolay A. Mordovtsev, graduate student

Don State Technical University, Rostov-on-Don (Russia)

*E-mail: nescoromniy@mail.ru

¹ORCID: <https://orcid.org/0000-0003-0243-7241>

Received 09.04.2024

Accepted 16.08.2024

Abstract: Special feature of operation of electrovacuum tubes, in particular the cathode assembly, is constant heating due to bombardment of its surface with electrons. Stable characteristics and durability of the cathode assembly depend on high-quality connection (welding) of the core surfaces with the emitter over the entire area of the overlapped conjugation. The use of diffusion welding for joining a cathode assembly made of dissimilar materials is not possible due to the occurrence of poor welding fusion due to the presence of gaps in the ring sectors of the equipment, and, consequently, a decrease in the service life of the cathode assembly. The authors proposed to implement the process by combining magnetic pulse welding with diffusion welding. The originality of the work is the possibility of remote action on the joint through a dielectric quartz cup, which is a part of the technological vacuum chamber. The inductor system is outside the quartz cup, which allows heating the assembled unit without heating the tool – an inductor made of dissimilar materials – to a temperature of 700 °C and higher. The authors determined the main parameters of the process of pulse diffusion welding in vacuum: pressure in the working chamber is $B=0.66 \cdot 10^{-2}$ Pa ($5 \cdot 10^{-5}$ mm Hg); preheating temperature is $T=700$ – 1250 °C; magnetic field pulse energy is $W=5$ – 17 kJ; operating frequency of current pulse discharge is $f_d=5$ – 15 kHz; magnetic pressure is $P_m > 10^7$ N/m². In this way, cathode assemblies of a wide range of metal pair combinations with a base diameter of $d=20$ mm and a sample length of $L=40$ mm were produced. The proposed technology has been successfully implemented and introduced at Tantal (Open Joint Stock company). The economic effect consists in reducing labor intensity and obtaining joints of stable quality.

Keywords: pulse diffusion welding; welding of female joints; magnetic pulse welding; inductor; magnetic pressure; input energy; dissimilar alloys.

Acknowledgements: The authors of the paper express gratitude to the staff of Microengineering Research Institute and Don State Technical University for their assistance in carrying out research and development work.

For citation: Strizhakov E.L., Nescoromniy S.V., Lyudmirsky Yu.G., Mordovtsev N.A. Pulse diffusion welding of female joints. *Frontier Materials & Technologies*, 2024, no. 3, pp. 89–98. DOI: 10.18323/2782-4039-2024-3-69-8.

INTRODUCTION

In the production of electrovacuum tubes (EVT), emitter materials based on platinum-barium, palladium-barium, iridium-lanthanum, etc. alloys are widely used. The connection of the emitter with the cathode core is a typical female design. The emitter should be welded to the core surface in the solid phase without mixing the materials. Fig. 1 shows typical representatives of cathode assemblies. A specific performance feature of the cathode assembly is its constant heating due to the bombardment of its surface with electrons. To ensure stable operational properties and durability of devices, it is necessary to ensure high quality of welding of the core surfaces with the emitter over the entire area of the overlapped conjugation.

Classical diffusion welding in a protective environment with a static load ensures the production of high-quality connections, which guarantees the required service life of the units. Examples and parameters of diffusion welding modes for metals in homogeneous and heterogeneous combinations are shown in more detail in [1]. Moreover, replac-

ing the factory laser welding technology with diffusion welding allows increasing the productivity of the welding technology up to 75 % [1].

Despite the significant advantages of diffusion welding, if its technology is violated or there is no long-term testing of the resulting joints under various loading conditions (thermal, thermomechanical), defects such as poor welding fusion occur during the production process, and cracks occur during operation, which is unacceptable in EVT. The relationship between defects and the causes of their occurrence, which must be taken into account when developing the technology, as applied to the design of the welded parts is described in [2].

To expand the capabilities of diffusion welding and produce defect-free welded joints, it is possible to use intermediate layers that have sufficient affinity for a pair of metals that are difficult to weld together. It has been proven that the use of intermediate layers allows reducing the temperature of the diffusion welding process to 350–750 °C when welding ARMCO iron with a high-purity nickel alloy [3].

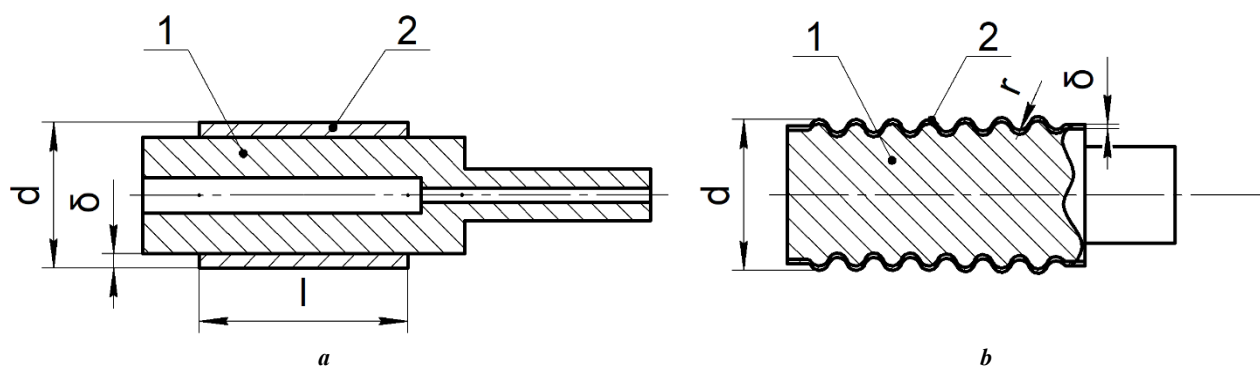


Fig. 1. Design of cathode assemblies:

a – welding on a cylindrical surface; *b* – welding on a developed surface.

1 – core; 2 – emitter; *d* – assembly diameter; δ , *l* – emitter thickness and width; *r* – surface curvature

Рис. 1. Конструкция катодных узлов:

a – сварка по цилиндрической поверхности; *b* – сварка по развитой поверхности.

1 – керн; 2 – эмиттер; *d* – диаметр узла; δ , *l* – толщина и ширина эмиттера; *r* – кривизна поверхности

The authors of [4] used an intermediate Ni layer to reduce the likelihood of intermetallic compound formation and to obtain Mo–Ni and Cu–Ni solid solutions during diffusion welding of Mo–Cu. The paper [5] showed that the use of an intermediate Zn layer facilitates the formation of a strong bond between Al and Cu during a short period of time and at a low temperature of the process between Zn, Cu and Al. When using Ag as an intermediate component [6] and increasing the process temperature to 700 °C, the formation of Ag–Ti intermetallic compounds and an Ag solid solution instead of Cu–Ti intermetallic compounds was identified in the welded joint. The use of CoCrFeMnNi alloy as an intermediate layer during diffusion welding of Cu–Ti or 0Cr18Ni9 allows reducing the brittleness of Cu/Ti joints due to the formation of solid solutions at a process temperature of 800 °C [7; 8]

In the absence of intermediate materials, diffusion welding of Cu and Ti was carried out at temperatures of 800–900 °C. The shear strength of the joints was about 28 MPa. A number of brittle intermetallic compounds, such as β -Cu₄Ti, Cu₂Ti and Cu₃Ti formed at the joint boundary, were found [9].

When implementing the process of diffusion welding at high temperatures, significant thermal stresses were detected in the joint, the grain size of the weld, the near-weld zone and the base metal increased [10]. The authors [10] note that with increasing temperature, the diffusion component of the process increases. Thus, diffusion processes were identified when studying the phase-structural components at a temperature of 830 °C, a pressure of 15 MPa, and even at 550–580 °C and a pressure of 30–40 MPa.

As a result of studies of diffusion welding of dissimilar metals, it was found that it must be carried out at the lowest possible melting temperatures and a short process duration. The intermediate metal must have the lowest melting temperature in relation to the welded parts and have the greatest affinity in crystalline structure [11].

The author of the work [12] presented the results of studies of the possibility of producing bimetallic joints

of the AlMn alloy with kovar (29NK alloy) and nickel (NP2 alloy) by the method of diffusion welding in a vacuum with subsequent fabrication of parts from them. The products were hollow cylindrical blanks of the AlMn alloy, into which the 29NK or NP2 alloy in the form of a cylindrical blank of solid cross-section was pressed with a force of 7000 N at a temperature of 610 °C. Analysis of the resulting joints under these welding conditions showed uniform distribution of elements across the thickness of the transition layer (up to 30 μ m wide) and mutual diffusion achieved at a given temperature and welding force. Intermetallic compounds were not detected.

Analysis of literary sources showed that all welded joints were produced with an initial parallel arrangement of the welded surfaces relative to each other. The arrangement of the welded surfaces at an angle during diffusion welding was not carried out [13]. Despite the wide range of permanent joints obtained by researchers using diffusion welding, the literature does not contain any information on producing joints from copper-nickel alloy with platinum, TP 439 alloy, MPVF molybdenum (pure molybdenum manufactured by vacuum fusion) or nickel-vanadium alloy with PtBa alloy.

At the Don State Technical University, together with the Microengineering Research Institute, a number of magnetic pulse welding (MPW) processes have been developed that make it possible to abandon glancing collision and clean the surfaces to be joined by electrical erosion or vacuum heat treatment. The authors of the paper propose to carry out diffusion welding by means of pulsed magnetic fields, which provide radial pressure on the welded unit according to the “crimping” scheme [13].

As with classical diffusion welding, in this work it is proposed to heat the unit assembled for welding in a vacuum, which leads to a decrease in the resistance of materials, deformation and acceleration of stress relaxation in the joint zone, and helps to clean the surfaces being joined from adsorbed inclusions and other contaminants.

The development of the equipment was based on similar units from dissimilar connections during magnetic-pulse assembly, diffusion welding [14–16]. Fig. 2 shows the equipment for welding facing emission coatings on cylindrical surfaces of cores. The design allows pressing the welded elements during welding due to the difference in the thermal coefficients of linear expansion (TCLE) of its parts. The casing element is usually made of molybdenum, kovar or materials with low TCLE, and the ring sectors of the equipment are made of TP 439 steel with high TCLE.

Due to the presence of gaps in the ring sectors of the equipment, such defects as poor welding fusion occur during diffusion welding of the emitter with the core. With prolonged isothermal action on the processed unit, intermetallic phases often occur in the zone of conjugation of the welded surfaces.

To produce joints of dissimilar materials while maintaining an organized structure, pulse welding methods are widely used. The mechanism for cleaning the welded surfaces is realized due to the glancing collision of the thrown elements, the conjugated surfaces are cleaned with a cumulative jet and the subsequent joint deformation of the materials and, as a result, a connection in the solid phase occurs by analogy with explosion welding. The principle of glancing collision is also used in classical MPW. The energy carrier changes: instead of the action of an explosive substance, the ponderomotive force is used – magnetic pressure, which allows using the MPW technology to weld small-sized units in workshop conditions with increased requirements for process hygiene [17; 18].

For MPW, depending on the design of the assembled parts for welding, various types of inductor systems have been developed and studied, which are characterized by inductive resistance, magnetic induction in the working area, and durability during operation [13–15; 19–21].

The purpose of this work is to study the process of pulse welding in a controlled environment, which allows reducing the duration of producing a joint in the solid phase from dissimilar materials.

METHODS

In electrovacuum tubes, cathode assemblies with a diameter of $d=(5-100)\cdot 10^{-3}$ m are used. To implement pulse diffusion welding (PDW) in a vacuum, the process is carried out using copper shells – satellites [22]. The wall thickness of the copper bushings was selected so that the penetration depth of the magnetic field H through the satellite material – the deformable bushing – did not exceed the thickness of its wall. To produce joints from refractory materials, the satellite material was replaced by nickel or molybdenum with a wall thickness of $t_{sat}=0.2\cdot 10^{-3}$ m. When welding on developed surfaces, the heated satellite behaves like an elastic punch.

Fig. 3 shows the proposed scheme for implementing PDW. The process is carried out as follows. The core (1) with the lining (2), heating element (3) and satellite (4) are installed in the vacuum chamber and placed in the working area of the magnetic-pulse tool – inductor (6). The air in the vacuum chamber is rarefied to a pressure of $0.66\cdot 10^{-2}$ Pa. The heating element increases the temperature of the assembly to 700–1250 °C. The pulse current generator (5) is discharged onto the inductor (6) causing the discharge current I_d (7) to flow through the inductor. In this case, the magnetic flow H (8) induces induced currents in the satellite I_i (9). The magnetic interaction force P_m (10) arises. The satellite (4) is deformed (compressed), and the lining (2) and the core (1) are welded in the solid phase. The duration of the process with isothermal holding does not exceed 100–200 μ s. When calculating the process characteristics, the following parameters were taken as

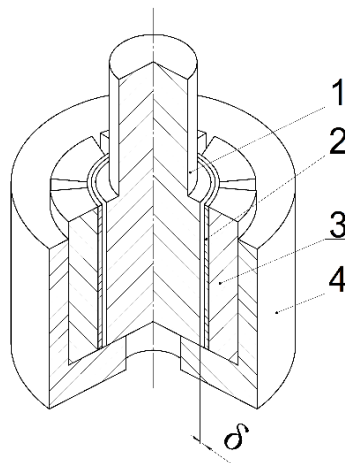


Fig. 2. Equipment for diffusion welding of a cathode assembly:

1 – core; 2 – emitter; 3 – ring sectors of the equipment; 4 – casing element; δ – preliminary gap

Рис. 2. Оснастка для диффузионной сварки катодного узла в сборе:

1 – керн; 2 – эмиттер; 3 – кольцевые секторы оснастки; 4 – корпусной элемент; δ – предварительный зазор

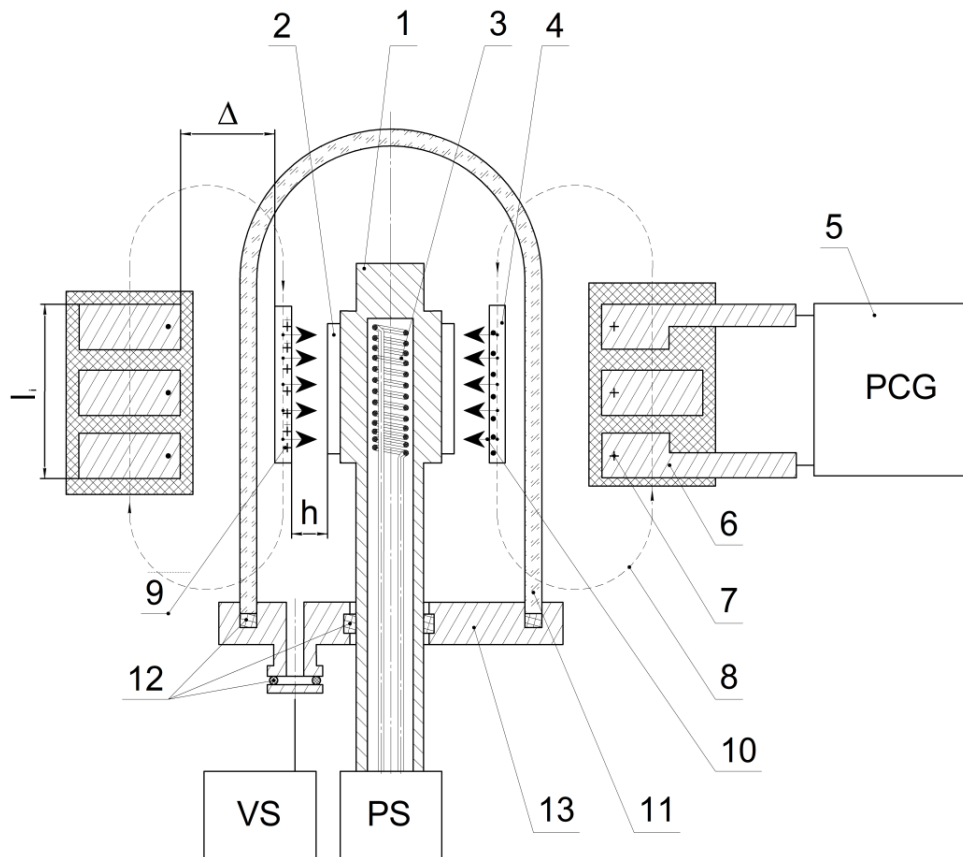


Fig. 3. Structure diagram of a device for pulse diffusion welding in a vacuum:

1 – base (core); 2 – lining (emitter); 3 – heating element;
 4 – satellite; 5 – pulse current generator PCG; 6 – inductor; 7 – discharge current (I_d); 8 – magnetic flow (H);
 9 – induced current (I_i); 10 – magnetic interaction force (P_M); 11 – dielectric cup;
 12 – vacuum seal; 13 – vacuum chamber base;
 PS – power source; VS – vacuum system; h – gap between the emitter and the satellite;
 Δ – gap between the inductor and the satellite; l_i – length of the inductor working zone

Рис. 3. Схема устройства импульсной диффузионной сварки в вакууме:

1 – основание (кern); 2 – облицовка (эмиттер); 3 – нагревательный элемент;
 4 – спутник; 5 – генератор импульсных токов PCG; 6 – индуктор; 7 – ток разряда (I_d); 8 – магнитный поток (H);
 9 – индуцированный ток (I_i); 10 – сила магнитного взаимодействия (P_M); 11 – диэлектрический стакан;
 12 – вакуумный уплотнитель; 13 – основание вакуумной камеры;
 PS – источник питания; VS – вакуумная система; h – зазор между эмиттером и спутником;
 Δ – зазор между индуктором и спутником; l_i – длина рабочей зоны индуктора

constants: the number of inductor turns $n=6$, the inductor diameter $D_i=30 \cdot 10^{-3}$ m, the length of the inductor working zone $l_i=45 \cdot 10^{-3}$ m, the capacity of the installation storage tank $C=1500 \cdot 10^{-6}$ F, and the voltage on the storage tank $U_s=5 \cdot 10^3$ V.

The optimal parameters of the PDW process were determined in accordance with the conditions for producing high-quality welded joints given in the literature [23]. The first and second conditions are the time parameters of the process: the MPW implementation should be completed in $\frac{1}{2}$ of the current discharge period, including the time of contact melting, electroexplosive cleaning, shaping and welding. The third condition states that the values of the induced current density for welding each material must be provided in the range $I_{min}-I_{max}$. The fourth condition describes the time relationships of solid-phase interaction: the duration of contact stresses in the joint zone should be

longer than the time of deformation activation of the contact surface and the relaxation time (relaxation characteristics of the blank and temperature in the interaction zone). The fifth condition consists in determining the specific impulse of the first half-wave of magnetic pressure, taking into account the tool parameters – the inductor, the operating voltage and inductance of the pulse current generator (PCG), the value of which will allow determining the magnitude of the relative deformation ε to level the initial gap between the inductor and the satellite wall. The presented limitations for the operating frequency of the process allow determining the frequency characteristics of the magnetic-pulse equipment, taking into account the low penetration of the magnetic flow into the gap between the inductor and the satellite to ensure cleaning of the welded surfaces – this is the sixth condition of high-quality processing.

Diffusion welding modes were tested in controlled environments on the Impulse-BM magnetic-pulse processing unit manufactured at Microengineering Research Institute (Rostov-on-Don, Russia) [24]. The same equipment is used to implement the technology of pressing, sintering and welding of facing coatings from powder compositions.

The quality of the welded joints produced by pulse diffusion welding was determined based on the test results: leak testing with a TII-50 helium leakage detector (Russia), GOST 3242-79, mechanical shear testing on a UMM-10 machine (Russia), GOST 6996-66, metallographic analysis of the produced joints using a PMT-3 microhardness tester (Russia), GOST 9450-76, multiple cyclic heating in a vacuum by electron bombardment and tenfold heating to a temperature of 1000 °C with holding for 1 h and gradual cooling. The heating and cooling time did not exceed 1 h, which should ensure a vacuum level of at least $0.66 \cdot 10^{-2}$ Pa during testing.

RESULTS

From the dependences of the welded joint shear strength τ on the process temperature T for two values of the input energy of 10 and 12 kJ, it is evident that with an increase in the input energy, the shear strength increases (Fig. 4). At the same time, with an increase in the process temperature, the strength indicators also increase. The highest strength indicators of the samples were found in the temperature range of 500–1000 °C.

Table 1 presents the results of tests for the tightness and mechanical strength of joints of M0b copper with Pt obtained at different degrees of vacuum (pressure). From the obtained data, it follows that with an increase in the degree of vacuum from $1 \cdot 10^{-3}$ to $5 \cdot 10^{-4}$ Pa, the quality of the welded joints improves due to the cleaning of

the joint zone from contaminants, solid-phase interaction occurs over the entire area of impact of the welded surfaces with a clear boundary of the joint zone.

Fig. 5 illustrates the reduced calculated dependences of the inductance L_{i-b} and active resistance R_{i-b} of the inductor-blank system, the operating frequency f_o , the magnetic interaction force P_m , the specific impulse of the first half-wave of the magnetic pressure J_M , the mean time between failures of the inductor N_i on the gap between the inductor and the copper satellite Δ . The gap value Δ depends on the manufacturing accuracy of the satellite itself. The air gap is necessary for feasibility cleaning from contaminants, oxide films under the radial action of ponderomotive forces arising from the interaction of the inductor magnetic flow with induced currents in the satellite wall. The obtained dependences of the quality of the welded joint are conventionally divided into 4 zones: 1) a gap of $(0-2.1) \cdot 10^3$ m – it is impossible in terms of design to assemble the unit in the inductor; 2) a gap of $(2.2-3.5) \cdot 10^3$ m is characterized by low performance characteristics and service life of the cathode assembly; 3) an initial gap of $(3.6-6.1) \cdot 10^3$ m allows producing high-quality welded joints characterized by long service life; 4) a gap of more than $6.1 \cdot 10^3$ m – the efficiency of magnetic pulse action decreases, such defects as poor welding fusion are possible in welded joints.

If the conditions for high-quality material processing are met [23], PDW made it possible to produce permanent joints from the following metals and alloys used when manufacturing electronic products. Base material: M0b alloy, Ni, TP 439 steel, copper-nickel alloy, 29NK alloy, MPVF molybdenum (pure molybdenum manufactured by vacuum fusion), nickel-vanadium alloy. Lining material: Al-Ba, Ni, Pt, Pt-Ba, Ir-La.

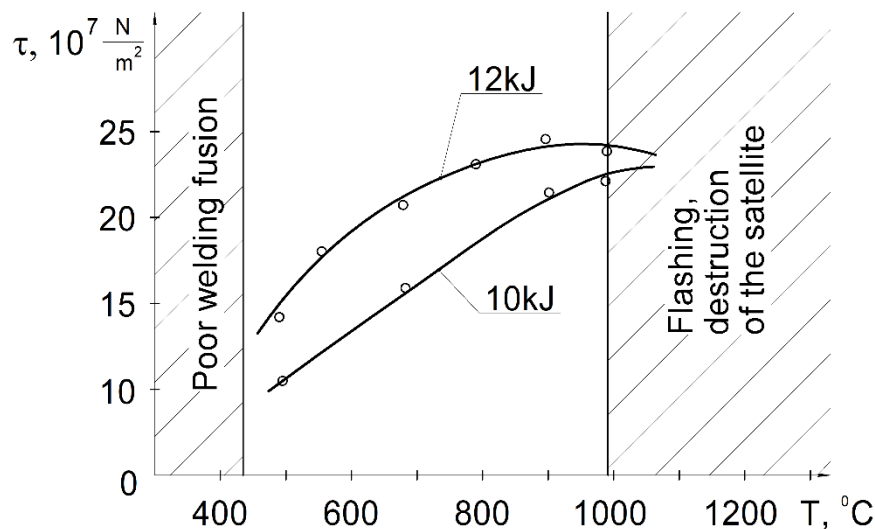


Fig. 4. Dependence of shear strength τ of the Pt + MPVF joint on the preheating temperature T and pulse energy W

Рис. 4. Зависимость прочности соединения на срез τ соединения Pt + МЧВП (молибден) от температуры предварительного разогрева T и энергии импульса W

Table 1. Results of tests for tightness, mechanical strength of joints of M0b copper with Pt obtained at different degrees of vacuum (pressure) in the process chamber
Таблица 1. Результаты испытаний на герметичность, механическую прочность соединений меди M0b с Pt, полученных при различной степени разрежения (давлении) в технологической камере

No.	Pressure, Pa	Results of metallographic analysis after thermal testing	Shear strength, τ N/m ² ·10 ⁷	Leakage, m ³ ·Pa/s
1	1·10	Buckle	5.0	1·10 ⁻⁴
2	5·10 ⁻¹	Buckle	7.5	1·10 ⁻⁴
3	5·10 ⁻²	Pockets and laminations	11.5	4·10 ⁻⁶
4	1·10 ⁻²	Discontinuous poor welding fusion	13.5	1·10 ⁻⁷
5	5·10 ⁻³	No pockets and laminations	14.5	5·10 ⁻¹³
6	1·10 ⁻³	No pockets and laminations, clear joint boundary	15.0	5·10 ⁻¹⁴
7	5·10 ⁻⁴	No pockets and laminations, clear joint boundary	15.0	1·10 ⁻¹⁵

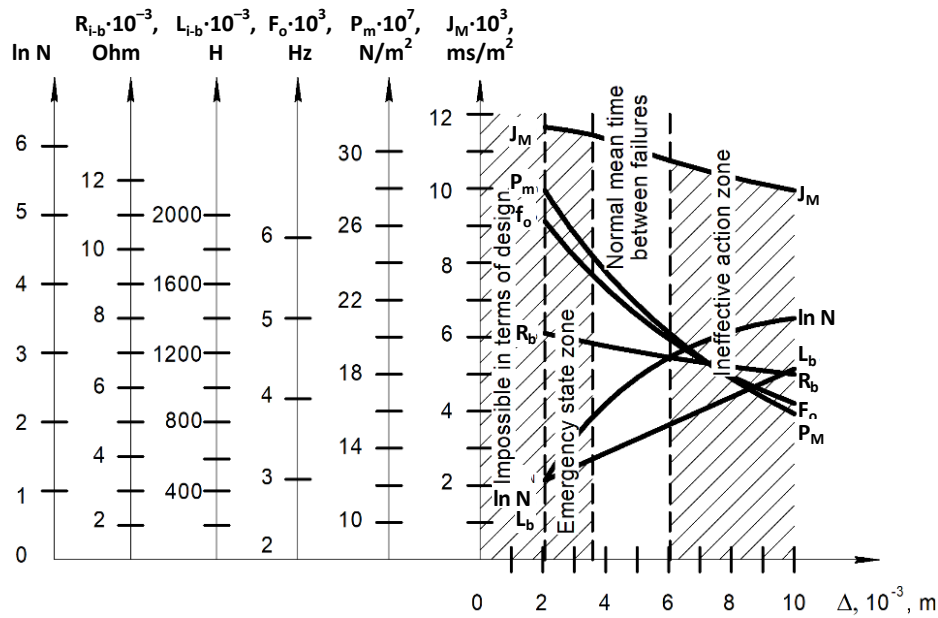


Fig. 5. Calculated dependencies: Δ of the inductance L_{i-b} and active resistance R_{i-b} of the inductor-blank system, the operating frequency f_o , the magnetic interaction force P_m , the specific impulse of the first half-wave of magnetic pressure J_M and the mean time between failures of the inductor N_i on the gap between the inductor and the satellite Δ
Рис. 5. Расчетные зависимости: Δ индуктивности L_{i-b} и активного сопротивления R_{i-b} системы «индуктор – заготовка», рабочей частоты f_o , силы магнитного взаимодействия P_m , удельного импульса первой полуволны магнитного давления J_M и наработки на отказ индуктора N_i от зазора между индуктором и спутником Δ

Geometric dimensions of the joints: base diameter $d=20$ mm, sample length $L=40$ mm. Fig. 6 shows the obtained PDW units consisting of a molybdenum core (pos. 1) with Pt–Ba emitters (pos. 2).

The optimal parameters of the PDW processes for the following cathodes of ultra-high-frequency electrovacuum tubes were determined and experimentally confirmed by calculation [23].

1. Base: core – copper-nickel alloy, diameter is 12 mm; lining: emitter – Pt, thickness is 0.1 mm, length is 20 mm.

PDW mode: operating temperature is $T=700$ °C, input energy is $W=6$ kJ, magnetic pressure is $P_m=10.2 \cdot 10^7$ N/m².

2. Base: core – TP 439 high-alloyed steel, diameter is 12 mm; lining: emitter – PtBa alloy, wall thickness is 0.2 mm, length is 20 mm. PDW mode: operating temperature is $T=700$ °C, input energy is $W=8.67$ kJ, magnetic pressure is $P_m=12.0 \cdot 10^7$ N/m².

3. Base: core – MPVF molybdenum (pure molybdenum manufactured by vacuum fusion), diameter is 17 mm; lining: emitter – PtBa alloy, thickness is $0.1 \cdot 10^{-3}$ mm,

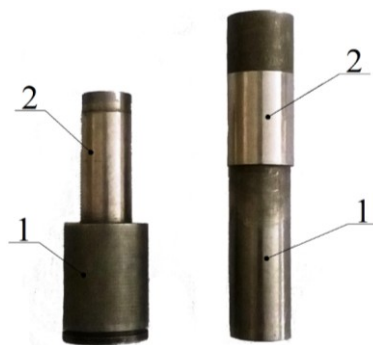


Fig. 6. Cathode assemblies produced by pulse diffusion welding: molybdenum core (1) with Pt–Ba emitter (2)
Рис. 6. Катодные узлы, полученные ИДС: молибденовый kern (1) с эмиттером Pt–Ba (2)

length is 30 mm. PDW mode: operating temperature is $T=900\text{ }^{\circ}\text{C}$, input energy is $W=10.26\text{ kJ}$, magnetic pressure is $P_m=14.22\cdot 10^7\text{ N/m}^2$.

4. Base: core – nickel-vanadium alloy, diameter is 18 mm; lining: emitter – PtBa alloy, thickness is 0.15 mm, length is 40 mm. PDW mode: operating temperature is $T=1000\text{ }^{\circ}\text{C}$, input energy is $W=13.23\text{ kJ}$, magnetic pressure is $P_m=18.33\cdot 10^7\text{ N/m}^2$.

DISCUSSION

The analyzed results of using diffusion welding to join dissimilar metal pairs showed that their diversity is small: Al–Cu, Cu–Ti, AlMn–29NK. As a rule, to reduce the likelihood of intermetallic compounds, an intermediate metal is used that has good adhesion to the welded metals and a low melting point. The results of studies of joints made by diffusion welding of metal pairs – copper-nickel alloy + Pt, TP 439 steel + PtBa, MPVF molybdenum + PtBa, nickel-vanadium alloy + PtBa – were not found in the literature.

Researchers have shown that at temperatures above $700\text{ }^{\circ}\text{C}$, intermetallic compounds are formed during diffusion welding. At temperatures of $350\text{--}700\text{ }^{\circ}\text{C}$, solid solutions of the welded metals with an intermediate one often appear [17–21]. The process scheme proposed by the authors is implemented in the temperature range of $700\text{--}1250\text{ }^{\circ}\text{C}$, which should initiate the formation of intermetallic phases, but due to the short duration of the magnetic-pulse action process of $100\text{--}200\text{ }\mu\text{s}$, their presence in the structure was not detected.

Magnetic pulse welding is mainly used to produce dissimilar joints with high electrical and thermal conductivity, usually Al+Cu. Cleaning during MPW is implemented due to the cumulative jet, which occurs during glancing collision of metals. During magnetic pulse welding of female structures, the cumulative jet is obtained due to the conical shape of one of the welded parts. The developed designs of inductor systems allow concentrating ponderomotive forces in the magnetic-pulse action zone with a magnetic induction value of up to 100 T [13–15; 17–21]. However, the use of composite inductors has a significant drawback – the presence of an uneven magnetic field at the junction of the component elements of the inductor sector, which re-

duces the quality of the welded joint. The twisted inductors used by the authors of the paper have a shorter service life under normal atmospheric pressure compared to sectional inductors; however, this is justified by the fact that they have a uniform distribution of the magnetic field. Moreover, the durability of twisted inductors is compensated by heating the welded products before welding in a vacuum to temperatures of $700\text{--}1250\text{ }^{\circ}\text{C}$, which reduces the amount of input energy, as well as their location outside the heating zone (separated by a heat-resistant, vacuum-tight dielectric (quartz or ceramic) glass), which has not been used by researchers before. This design scheme allows welding of facing joints in a high vacuum with heating of the assembly to a temperature above $700\text{ }^{\circ}\text{C}$ without destruction of the insulation of the tool – the inductor to produce permanent joints from dissimilar pairs of metals of a wider range.

At the same time, as the authors of works on PDW note, the presence of a gap between the inductor and the welded parts reduces the efficiency of magnetic-pulse action [19–21]. Thus, with magnetic-pulse action through a quartz glass on a unit placed in a vacuum (Fig. 5), the greatest efficiency of the Pt + MPVF joint is achieved at temperatures of $500\text{--}1000\text{ }^{\circ}\text{C}$, for other pairs of metals, the temperature can reach $1200\text{ }^{\circ}\text{C}$. At lower temperatures in the joint zone, poor welding fusion is observed, at a temperature above $1000\text{ }^{\circ}\text{C}$, melting and destruction of the copper satellite occurs.

The analysis of the calculated data allowed determining the non-conductive gap zone Δ equal to $(4\div 6)\cdot 10^{-3}\text{ m}$, which is feasible in terms of design and ensures reliable operation of the tool located in the atmosphere, and the corresponding parameters of the process, equipment and inductor tool: L_{i-b} , R_{i-b} , f_{os} , P_m , J_M , and N_i .

The analysis of welded joints produced in optimal modes showed the presence of a clear boundary of the materials being joined, the absence of common grains, increased microhardness in the joint zone, which is typical for various types of solid-phase welding [13] using the example of cathode pairs of pure molybdenum manufactured by vacuum fusion and nickel-vanadium alloy with PtBa alloy.

Visual inspection did not reveal any buckles of the emitter, i.e. no poor welding fusion was detected. In the absence of a high-quality solid-phase connection between the emitter and the core, the latter melts during

operation at the site of poor welding fusion. The analysis of welded joints showed that the formation of the joint occurs in the solid phase, which reduces the probability of the presence of intermetallic inclusions in the joint zone, thereby increasing the service life of the products.

The technology of pulse diffusion welding of cathodes of electrovacuum tube devices was developed at the Micro-engineering Research Institute together with Don State Technical University and implemented at Tantal (Open Joint Stock company). As a result of developing the new process, it was possible to reduce the labor intensity of welding cathode assemblies by 10 times.

CONCLUSIONS

Analysis of the produced welded joints showed that the joint is formed in the solid phase, which reduces the probability of the presence of intermetallic phases in the joint zone, thereby increasing the service life of electronic equipment.

A design scheme of special technological equipment for pulse diffusion welding with an inductor in the atmosphere and a heated welded unit in a vacuum was developed and implemented, which made it possible to ensure the necessary operability of the equipment and reduce the labor intensity of producing secondary-emission cathode assemblies of ultra-high-frequency electrovacuum tubes.

REFERENCES

- Kushpelev Yu.V. Diffusion welding in instrumentation. *Vektor razvitiya*, 2022, no. 11, pp. 72–83. EDN: [JRIGAD](#).
- Barabanova O.A., Polunin V.A., Salmin P.A. Diffusion welding: possible defects of welded joints, reasons for their occurrence, and methods of control. *Svarochnoe proizvodstvo*, 2017, no. 10, pp. 34–43. EDN: [YLYALK](#).
- Lyushinskiy A.V. Comparison of some methods of intensification of the diffusion welding process. *Svarochnoe proizvodstvo*, 2021, no. 12, pp. 22–29. EDN: [JZWQSH](#).
- Zhang Jian Yang, Xu Bin, Naemul Haq Tariq, Sun MingYue, Li DianZhong, Li Yi Yi. Microstructure evolutions and interfacial bonding behavior of Ni-based superalloys during solid state plastic deformation bonding. *Journal of Materials Science & Technology*, 2020, vol. 46, pp. 1–11. DOI: [10.1016/j.jmst.2019.11.015](#).
- Chen Chang, Qian Sanfeng, Liu Rui, Wang Shan, Liao Bin, Zhong Zhihong, Cao Lingfei, Coenen Jan W., Wu Yucheng. The microstructure and tensile properties of W/Ti multilayer composites prepared by spark plasma sintering. *Journal of Alloys and Compounds*, 2019, vol. 780, pp. 116–130. DOI: [10.1016/j.jallcom.2018.11.346](#).
- Shen Qiang, Xiang Huiying, Luo Guoqiang, Wang Chuanbin, Li Meijuan, Zhang Lianmeng. Microstructure and mechanical properties of TC4/oxygen-free copper joint with silver interlayer prepared by diffusion bonding. *Materials Science and Engineering: A*, 2014, vol. 596, pp. 45–51. DOI: [10.1016/j.msea.2013.12.017](#).
- Ding Wen, Liu Ning, Fan Jiacheng, Cao Jing, Wang Xiaojing. Diffusion bonding of copper to titanium using CoCrFeMnNi high-entropy alloy interlayer. *Intermetallics*, 2021, vol. 129, article number 107027. DOI: [10.1016/j.intermet.2020.107027](#).
- Shen Qiang, Xiang Huiying, Luo Quoqiang, Su Xiaopeng, Zhang Lianmeng. Interfacial microstructure and mechanical properties of diffusion bonded TC4/0Cr18Ni9/Oxygen Free Copper joints. *Materials & Design*, 2013, vol. 50, pp. 230–234. DOI: [10.1016/j.matdes.2013.01.042](#).
- Aydin K., Kaya Y., Kahraman N. Experimental study of diffusion welding/bonding of titanium to copper. *Materials & Design*, 2012, vol. 37, pp. 356–368. DOI: [10.1016/j.matdes.2012.01.026](#).
- Wei Yanni, Li Yaru, Zhu Linghao, Chen Yu, Guo Bingbing. Study on inhibition of interfacial compounds and improvement of joint properties by low temperature and high-pressure process in diffusion bonding of Ti/Cu. *Vacuum*, 2023, vol. 218, article number 112636. DOI: [10.1016/j.vacuum.2023.112636](#).
- Feng Wei, Zhang Jian, Guo Hucheng, Xiao Yong, Luo Guoqiang, Shen Qiang. Dissimilar low-temperature diffusion bonding of copper and titanium using a Zn interlayer: Interfacial microstructure and mechanical properties. *Intermetallics*, 2024, vol. 173, article number 108437. DOI: [10.1016/j.intermet.2024.108437](#).
- Klokoval M.S., Ivanov I.A. Research on the production of bimetallic compounds by diffusion welding in a vacuum. *Vakuumnaya tekhnika i tekhnologiya*, 2017, vol. 27, no. 2, pp. 3.1–3.3. EDN: [YVANOD](#).
- Strizhakov E.L., Nescoromniy S.V., Lyudmirskiy Yu.G., Mordovtsev N.A. Methods of magnetic pulse welding. *Izvestiya Volgogradskogo gosudarstvennogo tekhnicheskogo universiteta*, 2024, no. 2, pp. 70–77. DOI: [10.35211/1990-5297-2024-2-285-70-77](#).
- Chernikov D.G., Yusupov R.Yu., Pesotskiy V.I., Alekhina V.K. Designs of assembly joints and magnetic-pulse technology for their implementation. *Aerokosmicheskaya tekhnika i tekhnologii*, 2023, vol. 1, no. 3, pp. 173–182. EDN: [FFZSNM](#).
- Glushchenkov V.A. Magnetic pulse assembly technology in the production of bimetallic earthing. *Kuznechno-shtampovochnoe proizvodstvo. Obrabotka materialov davleniem*, 2019, no. 8, pp. 16–25. EDN: [XOTGOY](#).
- Cherepnin Yu.S., Semenov A.N., Uvarov A.A. Development of the design and technology of diffusion welding of bimetallic cylindrical joints "austenitic steel – zirconium alloy". *Svarochnoe proizvodstvo*, 2018, no. 9, pp. 16–19. EDN: [YLVDFB](#).
- Sapanathan T., Raelison R.N., Buiron N., Rachik M. Magnetic Pulse Welding: An Innovative Joining Technology for Similar and Dissimilar Metal Pairs. *Industrial Engineering and Management. Joining Technologies*, 2016, pp. 243–273. DOI: [10.5772/63525](#).
- Angshuman Kapil, Abhay Sharma. Magnetic pulse welding: an efficient and environmentally friendly multi-material joining technique. *Journal of Cleaner Production*, 2015, vol. 100, pp. 35–58. DOI: [10.1016/j.jclepro.2015.03.042](#).
- Chen Yingzi, Yang Zhiyuan, Peng Wenxiong, Zhang Huaqing. Experimental investigation and optimization on field shaper structure parameters in magnetic pulse welding. *Proceedings of the Institution of Mechanical Engineers, Part B: Journal of Engineering Manufacture*, 2021, vol. 235, no. 13, pp. 2108–2117. DOI: [10.1177/09544054211014846](#).

20. Zaytsev E., Krutikov V., Spirin A., Pararin S. Development of Multi-Part Field-Shapers for Magnetic Pulse Welding Using Nanostructured Cu-Nb Composite. *Journal of Manufacturing and Materials Processing*, 2024, vol. 8, no. 3, article number 97. DOI: [10.3390/jmmp8030097](https://doi.org/10.3390/jmmp8030097).
21. Ashish K. Rajak, Ramesh Kumar, Kore S.D. Designing of field shaper for the electro-magnetic crimping process. *Journal of Mechanical Science and Technology*, 2019, vol. 33, pp. 5407–5413. DOI: [10.1007/s12206-019-1035-1](https://doi.org/10.1007/s12206-019-1035-1).
22. Yakovlev S.P., Yakovlev S.S., Chudin V.N., Sobolev Ya.A. Shape formation and diffusion welding of structural elements. *Izvestiya Tluskogo gosudarstvennogo universiteta. Tekhnicheskie nauki*, 2009, no. 1-1, pp. 76–85. EDN: [KGLJNZ](https://www.edn.ru/kgljnz/).
23. Strizhakov E.L., Batsemakin M.Yu., Nescoromnyy S.V. Conditions for quality processing and algorithm of estimation and selection of parameters of magnetic-pulse welding of lapped joints. *Fizika i khimiya obrabotki materialov*, 2007, no. 1, pp. 64–67. EDN: [KVNXST](https://www.edn.ru/kvnxst/).
24. Strizhakov E.L., Nescoromnyy S.V., Ageev S.O., Lemeshev S.V. Development of discharge-pulsed equipment for applied studies of magnetic-pulsed welding processes. *Welding International*, 2016, vol. 30, no. 10, pp. 813–816. DOI: [10.1080/09507116.2016.1148409](https://doi.org/10.1080/09507116.2016.1148409).
- СПИСОК ЛИТЕРАТУРЫ**
1. Кушпелев Ю.В. Диффузионная сварка в приборостроении // Вектор развития. 2022. № 11. С. 72–83. EDN: [JRIGAD](https://www.edn.ru/jrigad/).
2. Барабанова О.А., Полуниин В.А., Салмин П.А. Диффузионная сварка: возможные дефекты сварных соединений, причины их возникновения и методы контроля // Сварочное производство. 2017. № 10. С. 34–43. EDN: [YLXALK](https://www.edn.ru/ylxalk/).
3. Люшинский А.В. Сравнение некоторых методов интенсификации процесса диффузионной сварки // Сварочное производство. 2021. № 12. С. 22–29. EDN: [JZWQSH](https://www.edn.ru/jzwqsh/).
4. Zhang Jian Yang, Xu Bin, Naemul Haq Tariq, Sun Mingyue, Li Dianzhong, Li Yi Yi. Microstructure evolutions and interfacial bonding behavior of Ni-based superalloys during solid state plastic deformation bonding // *Journal of Materials Science & Technology*. 2020. Vol. 46. P. 1–11. DOI: [10.1016/j.jmst.2019.11.015](https://doi.org/10.1016/j.jmst.2019.11.015).
5. Chen Chang, Qian Sanfeng, Liu Rui, Wang Shan, Liao Bin, Zhong Zhihong, Cao Lingfei, Coenen Jan W., Wu Yucheng. The microstructure and tensile properties of W/Ti multilayer composites prepared by spark plasma sintering // *Journal of Alloys and Compounds*. 2019. Vol. 780. P. 116–130. DOI: [10.1016/j.jallcom.2018.11.346](https://doi.org/10.1016/j.jallcom.2018.11.346).
6. Shen Qiang, Xiang Huiying, Luo Guoqiang, Wang Chuanbin, Li Meijuan, Zhang Lianmeng. Microstructure and mechanical properties of TC4/oxygen-free copper joint with silver interlayer prepared by diffusion bonding // *Materials Science and Engineering: A*. 2014. Vol. 596. P. 45–51. DOI: [10.1016/j.msea.2013.12.017](https://doi.org/10.1016/j.msea.2013.12.017).
7. Ding Wen, Liu Ning, Fan Jiacheng, Cao Jing, Wang Xiaojing. Diffusion bonding of copper to titanium using CoCrFeMnNi high-entropy alloy interlayer // *Intermetallics*. 2021. Vol. 129. Article number 107027. DOI: [10.1016/j.intermet.2020.107027](https://doi.org/10.1016/j.intermet.2020.107027).
8. Shen Qiang, Xiang Huiying, Luo Guoqiang, Su Xiaopeng, Zhang Lianmeng. Interfacial microstructure and mechanical properties of diffusion bonded TC4/0Cr18Ni9/Oxygen Free Copper joints // *Materials & Design*. 2013. Vol. 50. P. 230–234. DOI: [10.1016/j.matdes.2013.01.042](https://doi.org/10.1016/j.matdes.2013.01.042).
9. Aydın K., Kaya Y., Kahraman N. Experimental study of diffusion welding/bonding of titanium to copper // *Materials & Design*. 2012. Vol. 37. P. 356–368. DOI: [10.1016/j.matdes.2012.01.026](https://doi.org/10.1016/j.matdes.2012.01.026).
10. Wei Yanni, Li Yaru, Zhu Linghao, Chen Yu, Guo Bingbing. Study on inhibition of interfacial compounds and improvement of joint properties by low temperature and high-pressure process in diffusion bonding of Ti/Cu // *Vacuum*. 2023. Vol. 218. Article number 112636. DOI: [10.1016/j.vacuum.2023.112636](https://doi.org/10.1016/j.vacuum.2023.112636).
11. Feng Wei, Zhang Jian, Guo Hucheng, Xiao Yong, Luo Guoqiang, Shen Qiang. Dissimilar low-temperature diffusion bonding of copper and titanium using a Zn interlayer: Interfacial microstructure and mechanical properties // *Intermetallics*. 2024. Vol. 173. Article number 108437. DOI: [10.1016/j.intermet.2024.108437](https://doi.org/10.1016/j.intermet.2024.108437).
12. Клокова М.С., Иванов И.А. Исследования по получению биметаллических соединений методом диффузионной сварки в вакууме // Вакуумная техника и технология. 2017. Т. 27. № 2. С. 3.1–3.3. EDN: [YVANOD](https://www.edn.ru/yvanod/).
13. Стрижаков Е.Л., Нескоромный С.В., Людмирский Ю.Г., Мордовцев Н.А. Методы магнитно-импульсной сварки (обзор) // Известия Волгоградского государственного технического университета. 2024. № 2. С. 70–77. DOI: [10.35211/1990-5297-2024-2-285-70-77](https://doi.org/10.35211/1990-5297-2024-2-285-70-77).
14. Черников Д.Г., Юсупов Р.Ю., Песочкий В.И., АLEXИНА В.К. Конструкции сборочных соединений и магнитно-импульсная технология для их реализации // Аэрокосмическая техника и технологии. 2023. Т. 1. № 3. С. 173–182. EDN: [FFZSNM](https://www.edn.ru/ffzsnm/).
15. Глушечков В.А. Магнитно-импульсная технология сборки при производстве биметаллического заземлителя // Кузнечно-штамповочное производство. Обработка материалов давлением. 2019. № 8. С. 16–25. EDN: [XQTGQY](https://www.edn.ru/xqtgqy/).
16. Черепнин Ю.С., Семенов А.Н., Уваров А.А. Разработка конструкции и технологии диффузионной сварки биметаллических цилиндрических соединений «аустенитная сталь – сплав циркония» // Сварочное производство. 2018. № 9. С. 16–19. EDN: [YLVDFB](https://www.edn.ru/ylvdfb/).
17. Sapanathan T., Raoulison R.N., Buiro N., Rachik M. Magnetic Pulse Welding: An Innovative Joining Technology for Similar and Dissimilar Metal Pairs // *Industrial Engineering and Management. Joining Technologies*. 2016. P. 243–273. DOI: [10.5772/63525](https://doi.org/10.5772/63525).
18. Angshuman Kapil, Abhay Sharma. Magnetic pulse welding: an efficient and environmentally friendly multi-material joining technique // *Journal of Cleaner Production*. 2015. Vol. 100. P. 35–58. DOI: [10.1016/j.jclepro.2015.03.042](https://doi.org/10.1016/j.jclepro.2015.03.042).
19. Chen Yingzi, Yang Zhiyuan, Peng Wenxiong, Zhang Huaiqing. Experimental investigation and optimization on field shaper structure parameters in magnetic pulse welding // *Proceedings of the Institution of Mechanical Engineers, Part B: Journal of Engineering*

- Manufacture. 2021. Vol. 235. № 13. P. 2108–2117. DOI: [10.1177/09544054211014846](https://doi.org/10.1177/09544054211014846).
20. Zaytsev E., Krutikov V., Spirin A., Pararin S. Development of Multi-Part Field-Shapers for Magnetic Pulse Welding Using Nanostructured Cu-Nb Composite // Journal of Manufacturing and Materials Processing. 2024. Vol. 8. № 3. Article number 97. DOI: [10.3390/jmmp8030097](https://doi.org/10.3390/jmmp8030097).
21. Ashish K. Rajak, Ramesh Kumar, Kore S.D. Designing of field shaper for the electro-magnetic crimping process // Journal of Mechanical Science and Technology. 2019. Vol. 33. P. 5407–5413. DOI: [10.1007/s12206-019-1035-1](https://doi.org/10.1007/s12206-019-1035-1).
22. Яковлев С.П., Яковлев С.С., Чудин В.Н., Соболев Я.А. Формообразование и диффузионная сварка элементов конструкций // Известия Тульского государственного университета. Технические науки. 2009. № 1-1. С. 76–85. EDN: [KGLNJZ](https://www.edn.net/KGLNJZ).
23. Стрижаков Е.Л., Бацемакин М.Ю., Нескоромный С.В. Условия качественной обработки и алгоритм расчета и выбора параметров магнитно-импульсной сварки нахлесточных соединений // Физика и химия обработки материалов. 2007. № 1. С. 64–67. EDN: [KVNXST](https://www.edn.net/KVNXST).
24. Strizhakov E.L., Nescoromniy S.V., Ageev S.O., Lemeshev S.V. Development of discharge-pulsed equipment for applied studies of magnetic-pulsed welding processes // Welding International. 2016. Vol. 30. № 10. P. 813–816. DOI: [10.1080/09507116.2016.1148409](https://doi.org/10.1080/09507116.2016.1148409).

Импульсная диффузионная сварка охватывающих соединений

© 2024

Стрижаков Евгений Львович, доктор технических наук, профессор, ведущий научный сотрудник Центра научных компетенций
Нескоромный Станислав Валерьевич*¹, кандидат технических наук, доцент, заведующий кафедрой «Машины и автоматизация сварочного производства»
Людмирский Юрий Георгиевич, доктор технических наук, профессор, ведущий научный сотрудник Центра научных компетенций
Мордовцев Николай Алексеевич, магистрант

Донской государственный технический университет, Ростов-на-Дону (Россия)

*E-mail: nescoromniy@mail.ru

¹ORCID: <https://orcid.org/0000-0003-0243-7241>

Поступила в редакцию 09.04.2024

Принята к публикации 16.08.2024

Аннотация: Особенностью эксплуатации электровакуумных приборов, в частности катодного узла, является постоянный нагрев за счет бомбардировки его поверхности электронами. Стабильные характеристики и стойкость катодного узла зависят от качественного соединения (сварки) поверхностей керна с эмиттером по всей площади нахлесточного сопряжения. Использование диффузионной сварки для соединения катодного узла из разнородных материалов не представляется возможным по причине возникновения непроваров из-за наличия зазоров в кольцевых секторах оснастки, а следовательно, снижения срока службы катодного узла. Авторами предложено реализовать процесс путем совмещения магнитно-импульсной сварки с диффузионной. Оригинальность работы заключается в возможности дистанционного воздействия на соединение через диэлектрический кварцевый стакан, который входит в состав технологической вакуумной камеры. Индукторная система находится снаружи кварцевого стакана, что позволяет осуществлять нагрев собранного узла без нагрева инструмента – индуктора из разнородных материалов – до температуры 700 °C и выше. Определены основные параметры процесса импульсной диффузионной сварки в вакууме: давление в рабочей камере $P=0,66 \cdot 10^{-2}$ Па ($5 \cdot 10^{-5}$ мм рт. ст.); температура предварительного разогрева $T=700-1250$ °C; энергия импульса магнитного поля $W=5 \div 17$ кДж; рабочая частота разряда импульсов тока $f_b=5-15$ кГц; магнитное давление $P_m > 10^7$ Н/м². Таким образом были получены катодные узлы широкой номенклатуры сочетаний пар металлов с диаметром основания $d=20$ мм и длиной образца $L=40$ мм. Предложенная технология успешно реализована и внедрена на ОАО «Тантал». Экономический эффект заключается в снижении трудоемкости и получении соединений стабильного качества.

Ключевые слова: импульсная диффузионная сварка; сварка охватывающих соединений; магнитно-импульсная сварка; индуктор; магнитное давление; вводимая энергия; разнородные сплавы.

Благодарности: Авторы статьи выражают благодарность сотрудникам НИИ «Микротехника» и Донскому государственному техническому университету за содействие в выполнении научно-исследовательской и опытно-конструкторской работы.

Для цитирования: Стрижаков Е.Л., Нескоромный С.В., Людмирский Ю.Г., Мордовцев Н.А. Импульсная диффузионная сварка охватывающих соединений // Frontier Materials & Technologies. 2024. № 3. С. 89–98. DOI: [10.18323/2782-4039-2024-3-69-8](https://doi.org/10.18323/2782-4039-2024-3-69-8).

The influence of cutting mode elements on the technological parameters of the process of milling blanks of titanium alloy thin-walled parts

© 2024

*Aleksandr N. Unyanin*¹, Doctor of Sciences (Engineering), Associate Professor

Aleksandr V. Chudnov^{*}, postgraduate student

Ulyanovsk State Technical University, Ulyanovsk (Russia)

*E-mail: chudnov73ru@gmail.com

¹ORCID: <https://orcid.org/0000-0002-5557-4197>

Received 03.08.2023

Accepted 06.06.2024

Abstract: The purpose of a rational mechanical processing mode remains an urgent task of pre-production engineering. Known recommendations and methods for selecting this mode are focused on the processing of solid blanks and do not take into account the fact that when processing thin-walled blanks, the temperatures in the processing zone and the surface layer of the blank differ. The study is aimed at identifying patterns in changing the parameters of the milling process of thin-walled blanks depending on the mode elements, as well as developing recommendations for selecting this mode. The authors performed numerical simulation of technological parameters of the milling process of solid and thin-walled blanks made of titanium alloy under various modes. The cutting speed, cutting depth and feed per cutter tooth were varied. The cutting force, power and densities of heat sources and the temperature in the surface layer of the blank, in the contact zones of the cutter tooth with the blank and the chips with the front surface of the tooth were calculated. It has been found that when milling thin-walled blanks, the temperature field differs significantly from that formed when processing solid blanks due to low heat removal from the unprocessed surface. Increasing the feed per tooth by 45 % leads to an insignificant decrease in temperatures in the cutting zone (by 5...12 %). Increasing the cutting speed by 25 %, on the contrary, leads to an increase in temperatures by 5...10 %. Increasing the cutting depth leads to an increase in the temperature in the chip-tooth contact zone by 1.5 times and to an increase in the temperature in the tooth-blank contact zone.

Keywords: cutting mode; technological parameters of milling process; temperature field; yield strength; thin-walled blank; cutting force; cutting zone temperature.

Acknowledgements: The study was carried out with a grant of the Russian Science Foundation No. 24-29-00206, <https://rscf.ru/project/24-29-00206/>.

For citation: Unyanin A.N., Chudnov A.V. The influence of cutting mode elements on the technological parameters of the process of milling blanks of titanium alloy thin-walled parts. *Frontier Materials & Technologies*, 2024, no. 3, pp. 99–107. DOI: 10.18323/2782-4039-2024-3-69-9.

INTRODUCTION

The temperature field formed during mechanical processing of thin-walled blanks differs from the field during processing of blanks of parts of considerable thickness [1; 2]. The reason is that during processing of a thin-walled blank, its surface opposite to the processed one has a significant effect on the temperature field. However, known recommendations and methods for selecting the mode are focused on the processing of solid blanks, and do not take into account the fact that when processing thin-walled blanks, the temperatures in the processing zone and the surface layer of the blank differ. This is caused by the low level of heat removal from the unprocessed surface – heat removal to the environment is significantly less than that occurred during heat removal to the underlying layers of a solid blank [2; 3].

Knowledge of the patterns of thermal processes of mechanical treatment, and the ability to control these processes, are necessary to increase processing productivity and ensure the quality of processed parts. The temperature of the surface layers of the blank affects their structural and phase composition, microhardness and stress state of the material [4]. The temperatures of the tool surfaces

contacting with the blank and chip determine the wear resistance and service life of the tool, i.e. its operability [5; 6]. However, the influence of thermal processes on the cutting process is often not considered as a significant factor [7; 8].

The arguments of the dependencies for calculating the powers of heat sources are the cutting forces, which, in turn, depend on the mechanical characteristics of the material of the processed blank (yield strength and tensile strength). To determine the mechanical characteristics, it is necessary to know the temperature in the plastic deformation zone. To determine this temperature, a dependence is proposed, the argument of which is the average tangential stresses in the conventional shear surface depending on the temperature in this zone. This circumstance complicates the possibility of determining the yield strength of the blank material in the plastic deformation zone.

It is possible to ensure the operability of the tool, and the quality parameters of thin-walled parts by selecting a rational processing mode, but there are no corresponding recommendations in the literature. Studies related to the determination of a rational mode for processing

thin-walled blanks, take into account the elastic deformation of the technological system elements, including the blank itself [9; 10]. Vibrations and pulsations of cutting forces are taken into account, which is also relevant for thin-walled blanks [11–13]. Temperature fields and the effect of temperatures on the mechanical properties of the blank material, during processing were studied for solid blanks [14]. However, it was not taken into account that the temperature field formed, when processing thin-walled blanks, is different from that when processing solid blanks, and the effect of the blank temperature on the yield strength of its material was not considered [15; 16]. In [17; 18], the processes of machining thin-walled blanks, as well as blanks with a complex profile, were studied, but recommendations for choosing cutting modes were not provided.

The patterns of changing the parameters of the milling process of thin-walled blanks made of titanium alloys depending on the mode elements, have not been studied.

The aim of this study is to investigate the influence of the elements of the milling mode of thin-walled titanium alloy blanks on the technological parameters of the process, including the forces and temperatures arising during the processing.

METHODS

The friction forces of the chip on the tooth front surface, the tooth back surface on the blank, and the main component of the cutting force, were calculated using the dependencies obtained by transforming the corresponding dependencies proposed in [19; 20]. These forces were obtained under the condition that the assessment of the blank material destruction is carried out, based on the flow plasticity theory ("flow plasticity method") used in [12; 18]. One of the main factors determining this process is the yield strength of the blank material, which depends on the deformed layer temperature:

$$\sigma_{st} = f(T_d),$$

where T_d is the temperature of the deformed layer of the blank material, K.

The calculation of the σ_{st} parameter was performed using the formula [7; 17]:

$$\sigma_{st} = \sigma_s \cdot \left(1 - \frac{T_d}{T_p}\right),$$

where σ_s is the yield stress of the blank material at a temperature of 293 K, Pa;

T_p is the melting temperature of the material, K.

The powers and densities of heat sources in the zone of deformation and in the contact zones of the tooth with the chip and the blank were calculated using the dependencies [20; 21].

The authors assumed that the blank material (VT6 titanium alloy, the closest analogue according to DIN is 3.7164) is isotropic, and the phase transformations during

its heating were not taken into account in the calculation. This assumption is valid, since numerical simulation and experiments have found that the temperature in the surface layer of the blank does not reach the values at which the transformations occur.

To calculate the milling process parameters, we used our own software, implementing the temperature field calculation using the finite element method. It allowed calculating the temperature of the deformed layer of the blank material T_d and the yield strength of the blank material σ_{st} at this temperature.

The time during which heat exchange occurs is divided into finite small intervals. The deformable layer temperature calculated for a certain moment in time is used to calculate the yield strength of the blank material at the next moment in time.

The σ_{st} parameter is the argument of the dependencies for calculating the friction forces, and the main component of the cutting force P_z . The forces per 1 mm of the cutter tooth height were calculated.

The adequacy of the physical and mathematical models adopted for calculating the temperatures to real conditions, was checked by comparing the average temperature in the surface layer of the machined blank made of VT6 titanium alloy, obtained by calculation, with the results of measurement by a semi-artificial thermocouple. By averaging the temperature of the surface layers of a solid blank, at different moments in time, and at different points at a distance from the blank surface equal to the diameter of the thermocouple wire (0.05 mm), the average calculated temperature was obtained. Milling mode: feed per cutter tooth is $S_z=0.16$ mm/tooth; cutting speed is $V=120$ and 150 m/min; cutting depth is $t=0.3$ mm; feed rate is $V_s=1.91$ m/min. The other experimental conditions corresponded to those used in the subsequent numerical simulation. At speeds $V=120$ and 150 m/min, the calculated temperatures were 686 and 701 K, and the experimental values were 618 and 623 K.

The discrepancies between the calculated and experimental temperature values recorded at different cutting speeds do not exceed 12 %, which indicates the possibility of using the proposed methods for the thermophysical analysis of the milling process.

The parameters of the milling process of blanks made of VT6 titanium alloy, were numerically simulated using the cylindrical surface of an end mill made of T5K10 hard alloy with a diameter of 20 mm. The thermophysical characteristics of the blank and cutter material (density, thermal conductivity and heat capacity coefficients) depending on the temperature and the yield stress of the blank material at a temperature of 293 K were determined from reference data. The process parameters were recorded during cutting of the blank by the twenty-fifth tooth of the successive series of working teeth of the cutter. The process of cooling the cutting zone with a lubricating fluid was simulated, taking the coefficient of heat transfer from the surfaces contacting with the coolant to be 5000 W/(m²·K); the heat transfer coefficient of the surfaces contacting with air was taken to be 40 W/(m²·K).

The authors simulated the process of milling a solid blank with a thickness of 10 mm, as well as blanks with

a thickness of 0.7 and 0.5 mm after processing. The following mode elements were varied: feed per cutter tooth $S_z - 0.11$ and 0.16 mm/tooth; cutting speed $V - 120$ and 150 m/min; milling depth $t - 0.3$ and 0.5 mm. The process parameters were recorded at the last moment of contact between the cutter tooth and the blank (this time depends on the milling mode elements) and at a time that was $8 \cdot 10^{-5}$ s less than the last.

Table 1 shows a plan for numerical simulation of the parameters for processing thin-walled blanks with varying mode elements.

RESULTS

The studies carried out during the machining of blanks made of VT6 titanium alloy, showed that blanks with a thickness of 10 mm and more are classified as solid blanks; during their machining, the surface opposite to the blank does not affect the temperature field in the blank.

Tables 2 and 3 present the results of calculating the milling process parameters for a solid blank with a thickness of 10 mm and thin-walled blanks, the thickness of which after the allowance removal is 0.7 and 0.5 mm. Under these conditions and cutting mode, visible changes in the temperature field were recorded when milling blanks with a thickness of 1 mm after machining. When machining a thin-walled blank, the temperatures in the zones of contact of the chip with the tooth front surface, the tooth rear surface with the blank and in the deformation zone are higher than when machining a solid blank. An increase in the temperature of the deformed layer of the blank material T_d leads to a decrease in the yield strength of the material of the thin-walled blank σ_{st} .

Tables 4 and 5 present the results of calculating the parameters of the milling process for a 0.7 mm thick workpiece, after removing the allowance for different mode

elements. Table 6 presents the results of calculating the temperatures. With an increase in the feed S_z from 0.11 to 0.16 mm/tooth (by 45 %), the maximum depth of tooth penetration into the workpiece a_{max} (on average by 45 %), and the maximum length of contact of the chip with the front surface of the tooth l increase. The parameter l increases to a greater extent at a cutting depth of $t=0.3$ mm – by 64 %. An increase in the parameters a_{max} and l is the reason for an increase in the friction forces and the main component P_z of the cutting force. The effect of the feed on the friction force of the tooth on the workpiece F_2 is insignificant; the friction force of the chip on the front surface of the tooth F_1 and the force P_z increase by 15...42 % and 14...21 %, respectively. This leads to an increase in the power of heat sources in the chip-tooth contact zones W_1 and in the deformation zone W_g ; the power of the heat source in the tooth-to-workpiece contact zone W_2 increases insignificantly.

With an increase in the cutting speed V from 120 to 150 m/min, i.e. by 25 %, the power of all heat sources increases by 17...27 %. This leads to an increase in the average and maximum temperatures T_1 and T_2 by 5...10 %. Consequently, with an increase in the cutting speed V , the temperature of the surface layer of the workpiece increases.

The kinematic parameters of the milling process – the length of the tooth-to-workpiece contact trajectory l_K , the maximum tooth penetration depth into the workpiece a_{max} and the maximum length of chip contact with the front surface of the tooth l – are not affected by the cutting speed.

An increase in the cutting depth leads to an increase in the kinematic parameters. With increasing parameter a_{max} , the friction force F_1 and the force P_z , as well as the powers of the heat sources W_1 and W_g , increase. The friction force F_2 and the power of the source W_2 are not affected by the change in the cutting depth.

*Table 1. Numerical simulation plan
Таблица 1. План численного моделирования*

Experiment number	Varying parameters			
	Feed per cutter tooth S_z , mm/tooth	Cutting speed V , m/min	Milling depth t , mm	Feed speed V_s , m/min
1	0.11	120	0.3	1.05
2	0.16	120	0.3	1.52
3	0.11	150	0.3	1.31
4	0.16	150	0.3	1.91
5	0.11	120	0.5	1.05
6	0.16	120	0.5	1.52
7	0.11	150	0.5	1.31
8	0.16	150	0.5	1.91

Table 2. Milling process parameters at various sizes (thicknesses) of a processed blank:
 $S_z=0.16$ mm/tooth; $V=150$ m/min; $t=0.5$ mm; feed speed $V_s=1.91$ m/min

Таблица 2. Параметры процесса фрезерования при различных размерах (толщинах) обработанной заготовки:
 $S_z=0,16$ мм/зуб; $V=150$ м/мин; $t=0,5$ мм; скорость подачи $V_s=1,91$ м/мин

Blank size (thickness) after processing, mm	Force of friction of a chip on a tooth front surface F_1 , N	Force of friction of a tooth on a blank F_2 , N	Cutting force major component P_z , N	Heat source power, W, in the zone of		
				deformation W_g	chip-tooth contact W_1	tooth-blank contact W_2
10	54.8/62.7	54.3/55.1	118.1/128.1	109.0/124.9	82.2/94.1	163.0/165.4
0.7	54.7/62.6	54.2/55.0	117.7/127.8	108.7/124.6	82.0/93.9	162.5/165.0
0.5	53.4/61.3	54.0/49.8	117.0/127.2	108.2/124.1	81.6/93.5	162.0/164.5

Note. F_1 , F_2 , P_z are forces per 1 mm of the cutter tooth height.

The denominators represent the process parameters recorded at the last moment of contact between the cutter tooth and the blank, and the numerators represent the same parameters at the previous moment.

Примечание. F_1 , F_2 , P_z – силы, приходящиеся на 1 мм высоты зуба фрезы.

В знаменателях представлены параметры процесса, зафиксированные в последний момент времени контакта зуба фрезы с заготовкой, в числителях – в предыдущий момент.

Table 3. Temperatures at various sizes (thicknesses) of a processed blank:
 $S_z=0.16$ mm/tooth; $V=150$ m/min; $t=0.5$ mm; $V_s=1.91$ m/min

Таблица 3. Температуры при различных размерах (толщинах) обработанной заготовки:
 $S_z=0,16$ мм/зуб; $V=150$ м/мин; $t=0,5$ мм; $V_s=1,91$ м/мин

Blank size (thickness) after processing, mm	Average temperature in the contact zone of		Temperature of the deformed layer of the blank material T_d , K	Yield strength of the blank material σ_{st} , MPa	Temperature of a blank T_3 , K at a distance from the processed surface	
	a tooth with a blank T_2 , K	a chip with a tooth T_1 , K			30 μ m	180 μ m
	10	1,000/1,018			1,004/1,012	365/337
0.7	1,006/1,023	1,008/1,013	371/341	782/794	497/ 491	406/406
0.5	1,014/1,031	1,014/1,015	379/347	778/791	514/506	425/425

Note. The denominators represent the process parameters recorded at the last moment of contact between the cutter tooth and the blank, and the numerators represent the same parameters at the previous moment.

Примечание. В знаменателях представлены параметры процесса, зафиксированные в последний момент времени контакта зуба фрезы с заготовкой, в числителях – в предыдущий момент.

With increasing cutting depth, the average value of temperature T_2 decreases at $S_z=0.11$ mm/tooth, and increases at $S_z=0.16$ mm/tooth. The maximum value of temperature T_2 increases for all combinations of parameters S_z and V , except for $S_z=0.11$ mm/tooth and $V=150$ m/min. The workpiece temperature T_3 at a depth of 30 μ m increases with increasing cutting depth for all combinations of parameters S_z and V , except for $S_z=0.16$ mm/tooth and $V=150$ m/min. The temperature at the tooth tip T_E slightly decreases with increasing parameter t , except for the calculation for the mode $S_z=0.11$ mm/tooth and $V=120$ m/min.

DISCUSSION

When milling thin-walled blanks, the cutting force P_z and the power of the heat sources are somewhat lower due to the lower value of the σ_{st} parameter. However, due to less intense heat removal from the zone of processing thin-walled blanks, the contact temperatures are somewhat higher [3] than when machining solid ones (Tables 2 and 3). The temperatures in the surface layer of the blanks increase to a greater extent, and the greater the distance from the machined surface, the greater the difference in temperatures between the solid and thin-walled blanks.

Table 4. Process technological parameters at various milling mode elements
Таблица 4. Технологические параметры процесса при различных элементах режима фрезерования

Experiment number according to Table 3	Path length of the tooth-blank contact l_K , mm	Maximum depth of tooth penetration in a blank a_{max} , μm	Maximum length of a contact of a chip with the tooth front surface l , μm	Temperature of the deformed layer of the blank material T_d , K	Yield strength of the blank material σ_{sp} , MPa
1	2.46	26.8	76.5	385/366	776/784
2	2.46	39.0	125.8	376/354	779/789
3	2.46	26.8	85.2	388/365	774/784
4	2.46	39.0	125.8	376/351	779/790
5	3.18	34.4	111.0	394/365	772/784
6	3.18	50.1	161.5	371/345	781/792
7	3.18	34.4	111.5	396/363	781/792
8	3.18	50.1	161.5	371/341	782/794

Note. The denominators represent the process parameters recorded at the last moment of contact between the cutter tooth and the blank, and the numerators represent the same parameters at the previous moment.

Примечание. В знаменателях представлены параметры процесса, зафиксированные в последний момент времени контакта зуба фрезы с заготовкой, в числителях – в предыдущий момент.

Table 5. Process parameters at various milling mode elements
Таблица 5. Параметры процесса при различных элементах режима фрезерования

Experiment number	Force of friction of a chip on a tooth front surface F_1 , N	Force of friction of a tooth on a blank F_2 , N	Cutting force major component P_z , N	Heat source power, W, in the zone of		
				deformation W_g	chip-tooth contact W_1	tooth-blank contact W_2
1	28.0/31.5	53.8/54.4	86.2/90.8	46.0/51.8	35.0/39.4	134.4/135.8
2	38.4/45.0	54.0/54.7	98.8/106.9	63.7/74.3	48.3/56.2	135.0/136.6
3	28.0/31.5	53.7/54.3	86.0/90.8	55.1/62.2	41.9/47.2	161.0/163.0
4	38.8/45.2	54.0/54.7	99.0/107.2	76.7/89.6	58.2/67.8	162.0/164.1
5	39.8/44.1	53.5/54.3	99.6/105.5	65.6/72.8	49.7/55.1	133.7/135.8
6	54.0/61.7	54.2/54.9	116.9/126.7	89.4/102.4	67.5/77.1	135.4/137.3
7	39.7/44.1	53.4/54.4	99.5/105.6	78.6/87.4	59.6/66.2	160.3/163.2
8	54.7/62.6	54.2/55.0	117.7/127.8	108.7/124.6	82.0/93.9	162.5/165.0

Note. F_1 , F_2 , P_z are forces per 1 mm of the cutter tooth height.

The denominators represent the process parameters recorded at the last moment of contact between the cutter tooth and the blank, and the numerators represent the same parameters at the previous moment.

Примечание. F_1 , F_2 , P_z – силы, приходящиеся на 1 мм высоты зуба фрезы.

В знаменателях представлены параметры процесса, зафиксированные в последний момент времени контакта зуба фрезы с заготовкой, в числителях – в предыдущий момент.

Table 6. Temperatures at various milling mode elements
Таблица 6. Температуры при различных элементах режима фрезерования

Experiment number	Temperature in the tooth-blank contact zone T_2 , K		Temperature in the chip-tooth contact zone T_1 , K		Temperature at the tip of the cutter tooth T_E , K	Blank temperature T_3 , K
	average	maximum	average	maximum		
1	967/972	1,282/1,288	874/871	961/961	1,025/1,017	532/525
2	922/936	1,301/1,317	959/934	1,277/1,290	1,019/1,010	506/496
3	1,042/1,052	1,462/1,475	946/958	1,305/1,312	1,036/1,025	539/531
4	966/987	1,441/1,467	963/970	1,384/1,403	1,013/1,001	502/491
5	957/960	1,285/1,294	948/946	1,273/1,277	1,034/1,024	542/537
6	956/969	1,330/1,348	967/970	1,380/1,393	1,014/1,001	507/500
7	1,011/1,017	1,424/1,437	986/985	1,380/1,388	1,027/1,016	539/535
8	1,006/1,023	1,477/1,504	1,008/1,013	1,506/1,528	1,008/991	497/491

Note. Blank temperature T_3 was determined at a distance of 30 μm from the processed surface.

The denominators represent the process parameters recorded at the last moment of contact between the cutter tooth and the blank, and the numerators represent the same parameters at the previous moment.

Примечание. Температура заготовки T_3 определена на расстоянии 30 мкм от обрабатываемой поверхности.

В знаменателях представлены параметры процесса, зафиксированные в последний момент времени контакта зуба фрезы с заготовкой, в числителях – в предыдущий момент.

The densities of all heat sources increase insignificantly, since with an increase in the feed, both the power of the heat sources and their areas increase. The average temperatures in the contact zone of the tooth with the blank T_2 , the temperature at the tip of the cutter tooth T_E and the temperature of the blank T_3 in almost all cases decrease insignificantly, with an increase in the feed (by 5...12 %). This can be explained by a decrease in the time the blank is opposite the heat source with an insignificant increase in the densities of the heat sources. The average and maximum temperatures in the chip-tooth contact zone T_1 increase with increasing feed.

The blank temperature at a distance of 30 μm from the machined surface does not change, or decreases slightly, with increasing speed V , which is explained by a decrease in the time of action of the heat source on the blank.

At the last moment of contact of the tooth with the blank, the temperature of the deformed layer is slightly lower than at the previous one. This is a consequence of the fact that the tooth comes into contact with the blank material heated to a lesser extent as a result of the operation of the previous teeth. Therefore, at the last moment of time, the yield strength σ_{st} is higher, as, consequently, are the cutting and friction forces, and the power and density of heat sources. For all milling modes, the values of the average and maximum temperature T_2 are higher at this moment of time than at the previous one. The blank temperature T_3 , the temperature at the tooth tip T_E and the temperature of the deformed layer, are slightly lower at the last moment of time than at the previous one. The maximum value of temperature T_1 is higher at the last

moment of time, and the average value of this temperature changes insignificantly. Therefore, the following dependencies for evaluating the process parameters were obtained for: the average value of temperature T_2 and force P_z recorded at the last moment of contact time; temperatures T_E and T_3 – at the previous moment; when calculating the average temperature T_1 , the temperature averaged for two moments of time was used.

When machining thin-walled blanks, a mode should be used that ensures forces and temperatures that do not exceed those that occur when machining solid [14] blanks at maximum productivity.

The studies performed allow selecting the required mode. For example, if mode No. 6 according to Table 3 is used ($t=0.5$ mm; $S_z=0.16$ mm/tooth and $V=120$ m/min), then the force P_z , as well as the average and maximum values of temperatures T_1 and T_2 are expected to be lower than when machining a solid blank (Tables 2 and 3). In this case, the feed rate will decrease from 1.91 to 1.52 m/s, i.e. the productivity during processing of thin-walled blanks will slightly decrease. There are also other modes of processing thin-walled blanks providing lower forces P_z and temperatures in comparison with processing of a solid blank, however, under these modes, productivity decreases significantly.

It is difficult to provide recommendations concerning processing of thin-walled blanks due to the ambiguous influence of any mode element on the process parameters with various combinations of others. Therefore, to determine the rational mode, one can use the following dependencies obtained as a result of processing the results of numerical simulation:

$$T_1 = 223.9 + 1141.3 \cdot S_z + 31.095 \cdot V + 272 \cdot t - 141.3 \cdot S_z \cdot V - 2400 \cdot S_z \cdot t - 30.68 \cdot V \cdot t + 355.56 \cdot S_z \cdot V ;$$

$$T_2 = 1320 + 13110 \cdot S_z + 905.4 \cdot V + 4184 \cdot t - 5340 \cdot S_z \cdot V - 25900 \cdot S_z \cdot t - 16900 \cdot V \cdot t + 11000 \cdot S_z \cdot V ;$$

$$T_E = 439.3 + 3820 \cdot S_z + 296.6 \cdot V + 1351 \cdot t - 1760 \cdot S_z \cdot V - 8600 \cdot S_z \cdot t - 576 \cdot V \cdot t + 3000 \cdot S_z \cdot V ;$$

$$T_3 = 306.9 + 1110 \cdot S_z + 118.8 \cdot V + 525 \cdot t - 680 \cdot S_z \cdot V - 2500 \cdot S_z \cdot t - 188 \cdot V \cdot t + 800 \cdot S_z \cdot V \cdot t ;$$

$$P_z = 37.12 + 1141.3 \cdot S_z + 6.52 \cdot V + 63.8 \cdot t - 62 \cdot S_z \cdot V - 70 \cdot S_z \cdot t - 23.2 \cdot V \cdot t + 220 \cdot S_z \cdot V \cdot t .$$

Using these dependencies, one can calculate the mode, at which the technological parameters, when processing a thin-walled blank, will not exceed the permissible values.

CONCLUSIONS

1. It has been found that during milling of thin-walled blanks, the temperature field differs significantly from that formed during processing of solid blanks.

2. Regularities in changing the parameters of the milling process of thin-walled blanks depending on the mode elements have been identified.

3. Mathematical dependencies describing the relationship between temperatures and cutting forces with the milling mode elements have been obtained.

4. The results of the research, and the obtained dependencies allow determining the processing mode for a thin-walled blank, at which the technological parameters, including temperatures, will not exceed the permissible values.

REFERENCES

- Khudobin L.V., Khusainov A.Sh. *Shlifovanie zagotovok klinovidnykh izdeliy* [Grinding of blanks of wedge products]. Ulyanovsk, UIGTU Publ., 2007. 249 p.
- Hishihara T., Okuyama S., Kawamura S., Hanasaki S. Study on the geometrical accuracy in surface grinding. Thermal deformation of workpiece in traverse grinding. *International journal Japanese society precision engineering*, 1993, vol. 59, no. 7, pp. 1145–1150. DOI: [10.2493/jjspe.59.1145](https://doi.org/10.2493/jjspe.59.1145).
- Kuts V.V., Gridin D.S. Comprehensive study of the process of cutting screw grooves on the inner surface of a cylindrical thin-walled bronze bushing. *Izvestiya Tul'skogo gosudarstvennogo universiteta. Tekhnicheskie nauki*, 2020, no. 10, pp. 72–79. EDN: [PXWMTS](https://www.edn.ru/pxwmts).
- Ladyagin R.V., Yakimov M.V. Study of the effect of force and temperature in the process of high-speed cutting on the accuracy of treatment of the cylinder blade case. *Izvestia of Samara Scientific Center of the Russian Academy of Sciences*, 2020, vol. 22, no. 3, pp. 111–115. DOI: [10.37313/1990-5378-2020-22-3-111-115](https://doi.org/10.37313/1990-5378-2020-22-3-111-115).
- Lapshin V.P., Khristoforova V.V., Nosachev S.V. Relationship of temperature and cutting force with tool wear and vibration in metal turning. *Obrabotka metallov / Metal working and material science*, 2020, vol. 22, no. 3, pp. 44–58. DOI: [10.17212/1994-6309-2020-22-3-44-58](https://doi.org/10.17212/1994-6309-2020-22-3-44-58).
- Duan Zhenjing, Li Changhe, Ding Wenfeng et al. Milling Force Model for Aviation Aluminum Alloy: Academic Insight and Perspective Analysis. *Chinese Journal of Mechanical Engineering*, 2021, vol. 34, article number 18. DOI: [10.1186/s10033-021-00536-9](https://doi.org/10.1186/s10033-021-00536-9).
- Radu P., Schnakovszky C. A Review of Proposed Models for Cutting Force Prediction in Milling Parts with Low Rigidity. *Machines*, 2024, vol. 12, no. 2, article number 140. DOI: [10.3390/machines12020140](https://doi.org/10.3390/machines12020140).
- Zawada-Michałowska M., Kuczmaszewski J., Legutko S., Pieško P. Techniques for Thin-Walled Element Milling with Respect to Minimising Post-Machining Deformations. *Materials*, 2020, vol. 13, no. 21, article number 4723. DOI: [10.3390/ma13214723](https://doi.org/10.3390/ma13214723).
- Eremeykin P.A., Zhargalova A.D., Gavryushin S.S. Problem of technological deformations of thin-walled workpieces during milling. *Obrabotka metallov / Metal working and material science*, 2019, vol. 21, no. 3, pp. 17–27. DOI: [10.17212/1994-6309-2019-21-3-17-27](https://doi.org/10.17212/1994-6309-2019-21-3-17-27).
- Kiselev E.S., Imandinov Sh.A., Nazarov M.V. Quality assurance features non-rigid aluminum blanks when milling with ultrasonic vibrations. *Izvestiya Volgogradskogo gosudarstvennogo tekhnicheskogo universiteta*, 2017, no. 12, pp. 14–17. EDN: [ZVLFAR](https://www.edn.ru/zvlfar).
- Vasilkov D.V., Aleksandrov A.S., Golikova V.V. Self-oscillations during cutting processing. *Sistemnyy analiz i analitika*, 2018, no. 3, pp. 25–35. EDN: [YNNEGL](https://www.edn.ru/ynnegl).
- Vorontsov A.L., Sultan-Zade N.M., Albagachiev A.Yu. Development of a new theory of cutting 7. Mathematical description of the formation of different chips, pulsation of the cutting force, and contact parameters of the machined billet surface and the rear cutter surface. *Russian Engineering Research*, 2008, vol. 28, no. 7, pp. 674–680. DOI: [10.3103/S1068798X08070101](https://doi.org/10.3103/S1068798X08070101).
- Chen Tao, Liu Jiaqiang, Liu Gang, Xiao Hui, Li Chunhui, Liu Xianli. Experimental Study on Titanium Alloy Cutting Property and Wear Mechanism with Circular-arc Milling Cutters. *Chinese Journal of Mechanical Engineering*, 2023, vol. 36, article number 57. DOI: [10.1186/s10033-023-00887-5](https://doi.org/10.1186/s10033-023-00887-5).
- Balyakin A.V., Khaymovich A.I., Chempinskiy L.A. Modeling of the high-speed milling of titanium alloy VT-9. *Izvestia of Samara Scientific Center of the Russian Academy of Sciences*, 2013, vol. 15, no. 6-3, pp. 572–583. EDN: [SHQPHB](https://www.edn.ru/shqphb).
- Evdokimov D.V., Skuratov D.L., Bukatyy A.S. Technological residual deformations prediction of GTE blades by numerical method after end milling. *Izvestia of Samara Scientific Center of the Russian Academy of Sciences*, 2022, vol. 24, no. 1, pp. 11–19. DOI: [10.37313/1990-5378-2022-24-1-11-19](https://doi.org/10.37313/1990-5378-2022-24-1-11-19).
- Vasilkov D.V., Aleksandrov A.S., Golikova V.V. Rheology of contact interactions during cutting processing. *Sistemnyy analiz i analitika*, 2018, no. 2, pp. 13–20. EDN: [YVMXEW](https://www.edn.ru/yvmxew).

17. Unyanin A.N., Semdyankin I.V. Modeling of parameters and temperature field of the process of milling blanks of thin-walled parts with different feed speeds. *Vestnik Ulyanovskogo gosudarstvennogo tekhnicheskogo universiteta*, 2021, no. 1, pp. 40–43. EDN: [TCGJNX](#).
18. Zhilyaev A.S., Kugultinov S.D. Mathematical simulation of thermal processes when milling aluminum alloy formed parts. *Vestnik Koncerna VKO "Almaz – Antey"*, 2019, no. 2, pp. 65–70. EDN: [FKRVYF](#).
19. Vorontsov A.L., Sultan-Zade N.M., Albagachiev A.Yu. Development of a new theory of cutting 9. Practical calculations of cutting parameters in turning. *Russian Engineering Research*, 2008, vol. 28, no. 9, pp. 878–888. DOI: [10.3103/S1068798X08090116](#).
20. Reznikov A.N., Reznikov L.A. *Teplovye protsessy v tekhnicheskikh sistemakh* [Thermal processes in manufacturing systems]. Moscow, Mashinostroenie Publ., 1990. 288 p.
21. Unyanin A.N. Analytical research on the temperature field at milling with ultrasonic oscillations superposition. *Vestnik RGATU im. P.A. Soloveva*, 2017, no. 2, pp. 229–235. EDN: [YPZFHX](#).
22. Zawada-Michałowska M., Kuczmaszewski J., Legutko S., Pieško P. Techniques for Thin-Walled Element Milling with Respect to Minimising Post-Machining Deformations // *Materials*. 2020. Vol. 13. № 21. Article number 4723. DOI: [10.3390/ma13214723](#).
23. Еремейкин П.А., Жаргалова А.Д., Гаврюшин С.С. Проблема технологических деформаций при фрезерной обработке тонкостенных заготовок // *Обработка металлов (технология, оборудование, инструменты)*. 2019. Т. 21. № 3. С. 17–27. DOI: [10.17212/1994-6309-2019-21.3-17-27](#).
24. Киселёв Е.С., Имандинов Ш.А., Назаров М.В. Особенности обеспечения качества нежестких алюминиевых заготовок при фрезеровании с наложением ультразвуковых колебаний // *Известия Волгоградского государственного технического университета*. 2017. № 12. С. 14–17. EDN: [ZVLFAR](#).
25. Васильков Д.В., Александров А.С., Голикова В.В. Автоколебания при обработке резанием // *Системный анализ и аналитика*. 2018. № 3. С. 25–35. EDN: [YNN EGL](#).
26. Воронцов А.Л., Султан-Заде Н.М., Албагачиев А.Ю. Разработка новой теории резания. 7. Математическое описание образования стружки разных видов, пульсации сил резания и параметров контакта обработанной поверхности заготовки с задней поверхностью реза // *Вестник машиностроения*. 2008. № 7. С. 56–60. EDN: [JVNRFL](#).
27. Chen Tao, Liu Jiaqiang, Liu Gang, Xiao Hui, Li Chunhui, Liu Xianli. Experimental Study on Titanium Alloy Cutting Property and Wear Mechanism with Circular-arc Milling Cutters // *Chinese Journal of Mechanical Engineering*. 2023. Vol. 36. Article number 57. DOI: [10.1186/s10033-023-00887-5](#).
28. Балякин А.В., Хаймович А.И., Чемпинский Л.А. Моделирование режима высокоскоростного фрезерования титанового сплава ВТ-9 // *Известия Самарского научного центра Российской академии наук*. 2013. Т. 15. № 6-3. С. 572–583. EDN: [SHQPHB](#).
29. Евдокимов Д.В., Скуратов Д.Л., Букатый А.С. Расчетное прогнозирование технологических остаточных деформаций лопаток ГТД на этапе конечного фрезерования // *Известия Самарского научного центра Российской академии наук*. 2022. Т. 24. № 1. С. 11–19. DOI: [10.37313/1990-5378-2022-24-1-11-19](#).
30. Васильков Д.В., Александров А.С., Голикова В.В. Реология контактных взаимодействий при обработке резанием // *Системный анализ и аналитика*. 2018. № 2. С. 13–20. EDN: [YVMXEW](#).
31. Унянин А.Н., Семдянкин И.В. Моделирование параметров и температурного поля процесса фрезерования заготовок тонкостенных деталей с различными скоростями подачи // *Вестник Ульяновского государственного технического университета*. 2021. № 1. С. 40–43. EDN: [TCGJNX](#).
32. Жиляев А.С., Кугультинов С.Д. Математическое моделирование тепловых процессов при фрезеровании сложнопрофильных деталей из алюминиевых сплавов // *Вестник Концерна ВКО «Алмаз – Антей»*. 2019. № 2. С. 65–70. EDN: [FKRVYF](#).

СПИСОК ЛИТЕРАТУРЫ

1. Худобин Л.В., Хусаинов А.Ш. Шлифование заготовок клиновидных изделий. Ульяновск: УлГТУ, 2007. 249 с.
2. Hishihara T., Okuyama S., Kawamura S., Hanasaki S. Study on the geometrical accuracy in surface grinding. Thermal deformation of workpiece in traverse grinding // *International journal Japanese society precision engineering*. 1993. Vol. 59. № 7. P. 1145–1150. DOI: [10.2493/jjspe.59.1145](#).
3. Куц В.В., Гридин Д.С. Комплексное исследование процесса нарезания винтовых канавок на внутренней поверхности цилиндрической тонкостенной бронзовой втулки // *Известия Тульского государственного университета. Технические науки*. 2020. № 10. С. 72–79. EDN: [PXWMTS](#).
4. Ладягин Р.В., Якимов М.В. Исследование влияния силы и температуры в процессе высокоскоростного резания на точность обработки гильзы блока цилиндров // *Известия Самарского научного центра Российской академии наук*. 2020. Т. 22. № 3. С. 111–115. DOI: [10.37313/1990-5378-2020-22-3-111-115](#).
5. Лапшин В.П., Христофорова В.В., Носачев С.В. Взаимосвязь температуры и силы резания с износом и вибрациями инструмента при токарной обработке металлов // *Обработка металлов (технология, оборудование, инструменты)*. 2020. Т. 22. № 3. С. 44–58. DOI: [10.17212/1994-6309-2020-22.3-44-58](#).
6. Duan Zhenjing, Li Changhe, Ding Wenfeng et al. Milling Force Model for Aviation Aluminum Alloy: Academic Insight and Perspective Analysis // *Chinese Journal of Mechanical Engineering*. 2021. Vol. 34. Article number 18. DOI: [10.1186/s10033-021-00536-9](#).
7. Radu P., Schnakovszky C. A Review of Proposed Models for Cutting Force Prediction in Milling Parts with Low Rigidity // *Machines*. 2024. Vol. 12. № 2. Article number 140. DOI: [10.3390/machines12020140](#).

19. Воронцов А.Л., Султан-Заде Н.М., Албагачиев А.Ю. Разработка новой теории резания. 9. Практические расчеты параметров резания при точении // Вестник машиностроения. 2008. № 9. С. 67–76. EDN: [JVNSAD](#).
20. Резников А.Н., Резников Л.А. Тепловые процессы в технологических системах. М.: Машиностроение, 1990. 288 с.
21. Унянин А.Н. Аналитическое исследование температурного поля при фрезеровании с наложением ультразвуковых колебаний // Вестник РГАТУ им. П.А. Соловьева. 2017. № 2. С. 229–235. EDN: [YPZFHX](#).

Влияние элементов режима резания на технологические параметры процесса фрезерования заготовок тонкостенных деталей из титанового сплава

© 2024

Унянин Александр Николаевич¹, доктор технических наук, доцент
Чуднов Александр Владимирович*, аспирант

Ульяновский государственный технический университет, Ульяновск (Россия)

*E-mail: chudnov73ru@gmail.com

¹ORCID: <https://orcid.org/0000-0002-5557-4197>

Поступила в редакцию 03.08.2023

Принята к публикации 06.06.2024

Аннотация: Назначение рационального режима процесса механической обработки остается актуальной задачей технологической подготовки производства. Известные рекомендации и методики назначения этого режима ориентированы на обработку массивных заготовок и не учитывают того обстоятельства, что при обработке тонкостенных заготовок температуры в зоне обработки и поверхностном слое заготовки отличаются. Исследование направлено на выявление закономерностей в изменениях параметров процесса фрезерования заготовок тонкостенных деталей в зависимости от элементов режима, а также разработку рекомендаций по назначению этого режима. Выполнено численное моделирование технологических параметров процесса фрезерования заготовок массивных и тонкостенных деталей из титанового сплава при различных режимах. Варьировали скорость резания, глубину резания и подачу на зуб фрезы. Рассчитывали силу резания, мощности и плотности источников тепловыделения и температуру в поверхностном слое заготовки, в зонах контакта зуба фрезы с заготовкой и стружки с передней поверхностью зуба. Установлено, что при фрезеровании заготовок тонкостенных деталей температурное поле значительно отличается от формирующегося при обработке массивных заготовок из-за низкого теплоотвода от необрабатываемой поверхности. Увеличение подачи на зуб на 45 % приводит к незначительному снижению температур в зоне резания (на 5...12 %). Увеличение скорости резания на 25 %, напротив, приводит к росту температур на 5...10 %. Увеличение глубины резания приводит к увеличению температуры в зоне контакта стружки с зубом в 1,5 раза, а также к увеличению температуры в зоне контакта зуба с заготовкой.

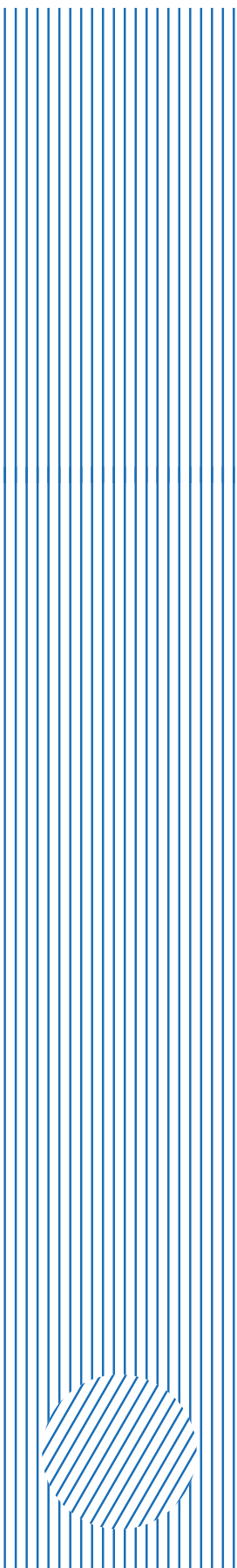
Ключевые слова: режим резания; технологические параметры процесса фрезерования; температурное поле; предел текучести; тонкостенная заготовка; сила резания; температура в зоне резания.

Благодарности: Исследование выполнено за счет гранта Российского научного фонда № 24-29-00206, <https://rscf.ru/project/24-29-00206/>.

Для цитирования: Унянин А.Н., Чуднов А.В. Влияние элементов режима резания на технологические параметры процесса фрезерования заготовок тонкостенных деталей из титанового сплава // Frontier Materials & Technologies. 2024. № 3. С. 99–107. DOI: 10.18323/2782-4039-2024-3-69-9.



GENERAL PUBLICATION REQUIREMENTS FOR AUTHORS



The journal publishes two versions of papers: in Russian and in English. The data of manuscript has to be original and never submitted or published before in other journals. All submitted papers are checked in the Anti-Plagiarism system (“Antiplagiat” system).

For publication, authors need to submit an application to the editorial office by sending the materials to the e-mail of the journal vektornaukitgu@yandex.ru or by uploading them to their personal account on the website <https://www.vektornaukitech.ru>.

Required structural elements of the manuscript

- *UDC identifier*;
- *the title* of the scientific manuscript;
- *copyright sign and year*;
- *information about the authors*: surname and initials of the author, academic degree, academic status, occupation; company, city, country; ORCID. The author corresponding to the editorial staff should provide his/her E-mail;
 - *abstract* (200–250 words) should contain a brief summary of the paper’s concept in order to interest a potential reader;
 - *keywords* (the main criterion of choosing keywords is their potential value to summarize the content of the document or to help the readers to find the document);
 - *acknowledgements* to individuals, granting organizations;
 - *the text of the manuscript* structured in accordance with the rules;
 - *references* (at least 20 sources).

Article structure

The structure of the article should conform to the IMRAD (Introduction, Methods, Results, and Discussion) standard, applied by Science World Community:

- INTRODUCTION
- METHODS
- RESULTS
- DISCUSSION
- CONCLUSIONS

Tables and figures formatting

Tables and figures should not fall outside the page layout. The use of landscape pages is not allowed. The titles of the tables and figures captures are required. If the text contains figures, diagrams, and tables from other literary sources, it is necessary to indicate where they were taken from..

Formulas typing

Formulas are edited in Microsoft Equation 3 formula editor. Formulas should not be longer than 80 mm. The size of the formula is 100 %. Converting formulas to figures is not allowed.

References and citations formatting

References are listed in the order of citation in the article. Reference list should not include the sources not cited in the article. In the journal it is not common to cite textbooks and study guides, except the flagship in their respective field, thesis papers and synopsis of a thesis. Not less than a quarter of the sources listed in the reference list should be published in the last 3–5 years. References to print publications only are acceptable (excluding e-journals). References to internet sites are not accepted. Not more than 20 % of the sources can be references on the own author’s publications. If a cited source has a DOI, the DOI should be indicated at the end of bibliographic description of this source. All DOIs should be valid links

Microstructure and strength of a 3D-printed Ti–6Al–4V alloy subjected to high-pressure torsion

© 2024

*Emil I. Usmanov*¹, engineer of the Research Institute of Physics of Advanced Materials

*Yana N. Savina*², research engineer of the Research Institute of Physics of Advanced Materials

*Roman R. Valiev*³, PhD (Engineering), senior researcher of the Research Institute of Physics of Advanced Materials
Ufa University of Science and Technology, Ufa (Russia)

*E-mail: usmanovei@uust.ru

¹ORCID: <https://orcid.org/0000-0002-1725-4651>

²ORCID: <https://orcid.org/0000-0003-1387-8819>

³ORCID: <https://orcid.org/0000-0003-1584-2385>

Received 27.06.2023

Accepted 12.02.2024

Abstract: Currently, one of the effective 3D printing methods is wire-feed electron-beam additive manufacturing (EBAM), which allows producing large-sized commercial billets from Ti–6Al–4V titanium alloy. However, Ti–6Al–4V alloy produced by this method demonstrates reduced strength properties. It is known that it is possible to increase the strength properties of metallic materials by refining their grain structure by high-pressure torsion (HPT). This work is aimed at studying the influence of high-pressure torsion on the microstructure, and mechanical strength of a structural Ti–6Al–4V titanium alloy produced by the wire-feed electron-beam additive manufacturing method. The microstructure of a 3D-printed Ti–6Al–4V alloy in the initial state, and after high-pressure torsion, was studied using optical, scanning and transmission electron microscopy. An EBSD analysis of the material in its original state was carried out. The microhardness of the material in the initial and deformed states was measured. Using the dependence of the yield strength on microhardness, the estimated mechanical strength of the material after processing by the high-pressure torsion method was determined. The microstructural features of the 3D-printed Ti–6Al–4V alloy after high-pressure torsion, which provide increased strength of this material, are discussed. The research results demonstrate that 3D printing, using the electron-beam additive manufacturing method, allows producing a Ti–6Al–4V titanium alloy with a microstructure unusual for this material, which consists of columnar primary β -grains with a transverse size of 1–2 mm, inside of which martensitic α' -Ti needles are located. Thin β -Ti layers with a thickness of about 200 nm are observed between the α' -Ti needles. Further deformation treatment of the alloy, using the high-pressure torsion method, allowed forming an ultrafine-grained structure in its volume, presumably consisting of α -grains with an average size of (25 ± 10) nm. High-pressure torsion of the 3D-printed alloy allowed achieving rather high microhardness values of (448 ± 5) HV_{0.1}, which, according to the HV=2.8–3 σ_y ratio, corresponds to the estimated yield strength of approximately 1460 MPa.

Keywords: 3D-printed Ti–6Al–4V titanium alloy; Ti–6Al–4V titanium alloy; wire-feed electron-beam additive manufacturing; high-pressure torsion; microstructure; mechanical properties.

Acknowledgements: The study was supported by the Russian Science Foundation grant No. 22-19-00445, <https://rscf.ru/en/project/22-19-00445/>.

The research was carried out using the equipment of the Core Facility Centre “Nanotech” of Ufa University of Science and Technology.

The paper was written on the reports of the participants of the XI International School of Physical Materials Science (SPM-2023), Togliatti, September 11–15, 2023.

For citation: Usmanov E.I., Savina Ya.N., Valiev R.R. Microstructure and strength of a 3D-printed Ti–6Al–4V alloy subjected to high-pressure torsion. *Frontier Materials & Technologies*, 2024, no. 3, pp. 109–116. DOI: 10.18323/2782-4039-2024-3-69-10.

INTRODUCTION

High-pressure torsion (HPT) is one of the most well-known methods of severe plastic deformation, which allows refining effectively, the microstructure in metal materials and providing an ultrafine-grained (UFG) structure, with dimensions less than 100 nm, and accordingly, an increase in their strength properties [1–3]. There are a number of works on the use of high-pressure torsion for processing the Ti–6Al–4V titanium alloy (Russian name – VT6), which is popular in industry. In this work [4], the authors applied HPT treatment on Ti–6Al–4V titanium alloy produced by hot rolling. As a result, a significant grain structure refinement to 100–200 nm, and as a consequence, a strong increase in strength up to $\sigma_u=1740$ MPa were ob-

served. In the work [5], the authors subjected Ti–6Al–4V titanium alloy with a plate structure to high-pressure torsion treatment. The research results showed, that 10 revolutions of high-pressure torsion at a pressure of 7.5 GPa allows forming a nanostructured state in the Ti–6Al–4V alloy with an average grain size of 52.7 nm and a microhardness of 432 HV. At the same time, a significant increase in tribological properties, such as friction and wear resistance, was observed. Works [6–8] show that the formation of a UFG structure in the Ti–6Al–4V alloy ensures the manifestation of superplasticity under relatively low temperatures (550–650 °C).

In recent years, it has been demonstrated that the Ti–6Al–4V alloy, and products made from it, can be success-

fully manufactured by 3D additive technologies [9–11]. Moreover, works [12–14] show that the method of wire-feed electron-beam additive manufacturing (EBAM) is one of the most promising and opens broad prospects for the production of large-sized complex-shaped parts from titanium alloys. The main advantages of this technology are high productivity (up to 2500 cm³/h), and almost 100 % efficiency of raw material consumption. Moreover, wire is much cheaper than powder raw materials, and its products are available for sale in a much wider range.

3D-printed Ti-6Al-4V titanium alloy has a specific initial microstructure, which significantly differs from the same alloy obtained by traditional production methods (casting, stamping, etc.). In particular, the microstructure after EBAM treatment consists of large columnar grains of the initial β -phase containing a lamellar martensitic α' -phase, which is formed due to the rapid solidification of the melt pool, and multiple phase transformations caused by repeated thermal cycles [10; 12]. However, such a structure is characterised by lower strength properties, and is noticeably inferior to those in comparison with the hot-rolled state [15; 16]. In this regard, an urgent task is to study the transformation of the microstructure obtained by additive technologies to increase the strength properties of the alloy. Of great interest is the study of the ultrafine-grained structure formation when exposed to severe plastic deformation (SPD) methods. Recently, such work was carried out on a Ti-6Al-4V alloy produced by the directed energy deposition (DED) technology, where the effect of equal channel angular pressing (ECAP) on the microstructure and mechanical properties was studied [17]. It was found that the alloy subjected to equal channel angular pressing exhibited a noticeable increase in mechanical properties in terms of strength and ductility.

High-pressure torsion treatment leads to a more significant refinement of the structure, and the possible unique properties that a 3D-printed Ti-6Al-4V alloy can acquire, after this treatment, are of scientific interest. This work is fundamental in nature. In the future, its results can become the basis for research aimed at improving the mechanical properties of 3D-printed parts of different geometries, using the SPD friction stir method, which, as is known, can be applied to treat the surface of various materials, including titanium alloys [18].

The purpose of this research is to study the effect of high-pressure torsion processing, on the microstructure and mechanical strength, of 3D-printed Ti-6Al-4V titanium alloy using wire-feed electron-beam additive manufacturing.

METHODS

As a material for research, the Ti-6Al-4V titanium alloy was used produced at the Institute of Strength Physics and Materials Science of the Siberian Branch of the Russian Academy of Sciences, Tomsk, Russia, using a unique scientific installation for wire-feed electron-beam additive manufacturing [12; 13]. As the raw material, a wire with a diameter of 1.6 mm made of Ti-6Al-4V titanium alloy was used, which was melted by an electron gun with a plasma cathode in a vacuum of 1.3×10^{-3} Pa. The wire was fed at

a speed of 2 m/min at an angle of 35° to the base plate surface. The base plate moved at a speed of 2.2 mm/s relative to the electron beam along a meander path with layers deposited in an inversed manner. A rod of $\varnothing 20$ mm was turned from the resulting blank. Then samples, with a diameter of 20 mm and a height of 2 mm, were cut out of it using an ARTA-120 electrical erosive machine for deformation processing and further research.

Samples of titanium alloy produced by electron beam melting of a wire, were subjected to high-pressure torsion on a SKRUDZH-200 unique scientific device at the Research Institute of Ufa University of Science and Technology, Ufa, Russia, at a specific compressive pressure of 6 GPa according to the mode: number of revolutions – 10, striker rotation speed – 0.2 rpm. After deformation, samples with a diameter of 20 mm and a height of 0.9–1.0 mm were obtained. These processing modes are described in detail in [2; 4].

The microstructure of the original and deformed samples was studied, using an Olympus GX51 optical microscope, a TESCAN MIRA LM scanning electron microscope, and a JEM-2100 transmission electron microscope (JEOL, Japan) with an accelerating voltage of 200 kV. Samples for TEM after high-pressure torsion were produced from an area 5 mm from the centre of the sample.

Microhardness was assessed using the Vickers method with a diamond pyramid at a load of 100 g for 15 s on a DuraScan 50 (EMCO-Test, Austria) device. To obtain an average value for each structural state, measurements were carried out at least 40 times.

RESULTS

Fig. 1 shows the microstructure of the Ti-6Al-4V alloy produced by the wire-feed electron-beam additive manufacturing method in the initial state. In the image obtained in an optical microscope (Fig. 1 a), columnar primary β -grains with a transverse size of 1–2 mm are observed in the volume, of which α -morphology grains were formed during the surfacing process. Such grains consist of a combination of lamellar and acicular martensitic α' -phase (dark contrast in the image). Large β -phase plates, the dimensions of which reach approximately (10 ± 2) μm (light contrast in the image), are also observed. Detailed studies of the microstructure of the samples in SEM and TEM allowed determining the thickness of the α' -phase plates, which is approximately (1.5 ± 0.5) μm , as well as thin interlayers, with a thickness of about 200 nm (Fig. 1 b–d), which are represented by β -phase. In the wide α' -phase plates, individual dislocations are visible.

Fig. 2 presents the results of EBSD analysis of a Ti-6Al-4V alloy sample in the initial state. In EBSD images in this state, a lamellar microstructure, united in large clusters with predominantly low-angle misorientation of grain boundaries, is observed. The length of the high-angle boundaries was 17.6 μm , and the low-angle boundaries were 1.16 μm .

Due to deformation treatment using the high-pressure torsion method, it was possible to refine significantly the structure in the Ti-6Al-4V alloy (Fig. 3). Inhomogeneous contrast is observed, because of the high level of internal

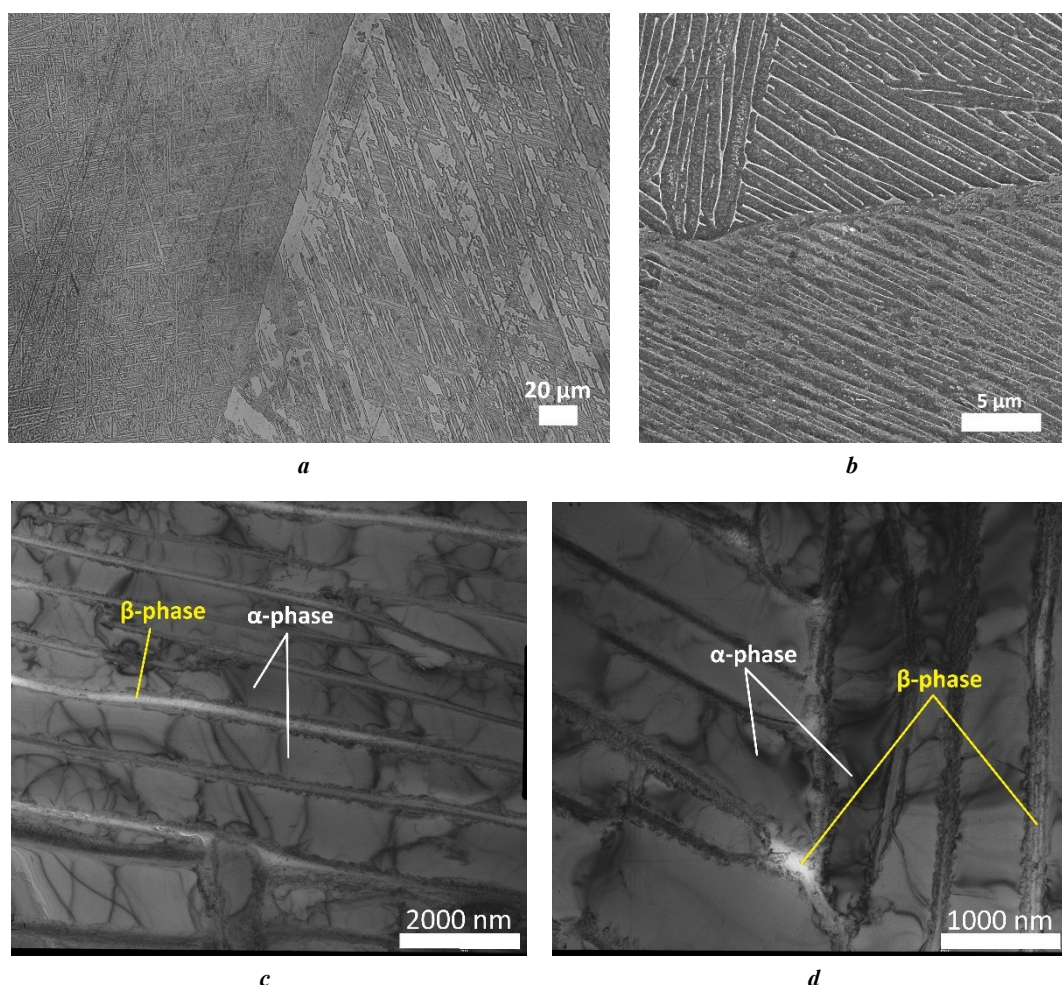


Fig. 1. Microstructure of a 3D-printed Ti-6Al-4V alloy:
a – in an optical microscope (OM); *b* – in a scanning electron microscope (SEM);
c, d – in a transmission electron microscope (TEM)

Рис. 1. Микроструктура 3D-напечатанного сплава Ti-6Al-4V:
a – в оптическом микроскопе (ОМ); *b* – в растровом электронном микроскопе (РЭМ);
c, d – в просвечивающем электронном микроскопе (ПЭМ)

stresses caused by the increased density of crystal lattice defects. According to dark-field images, the structure consists of equiaxial grains with an average size of (25 ± 10) nm. Electron diffraction patterns show numerous reflections located around a circle, which indicates the presence of grains with predominantly high-angle boundaries. The blurring of diffraction reflections also indicates high internal stresses and elastic distortions of the crystal lattice.

Unfortunately, due to the small grain size and high internal stresses, it was not possible to obtain EBSD microstructure maps of Ti-6Al-4V alloy produced using EBAM and subjected to HPT.

In the initial state, the average microhardness of the EBAM-produced Ti-6Al-4V sample is (308 ± 4) HV_{0.1} (Fig. 4 and Table 1). Subsequent HPT processing of the 3D-printed Ti-6Al-4V alloy made it possible to increase significantly the microhardness of the material. In this case, a slight heterogeneity along the diameter of the sample is observed, which is typical for torsional deformation. The best development in the HPT process is

observed in the region of the middle of the radius, where the average microhardness is approximately (448 ± 5) HV_{0.1}.

DISCUSSION

In current work, the authors studied Ti-6Al-4V titanium alloy produced by wire-feed electron-beam additive manufacturing, and subjected to high-pressure torsion. The microstructure of the initial state consists of columnar primary β -grains, inside of which martensitic α' -Ti plates with transverse dimensions of about (1.5 ± 0.5) μm are located. Between the martensitic plates, thin β -phase interlayers about 200 nm thick are also visible. A similar structure is often observed in Ti-6Al-4V titanium alloy, produced by additive technologies [12–14]. This structure is caused by the fact that in the process of wire-feed electron-beam additive manufacturing, the action of an electron beam leads to the formation of a melt pool in the near-surface volume of the substrate. Subsequently, as a result of solidification of the pools and upper layers of the grown metal, a columnar structure of β -grains is

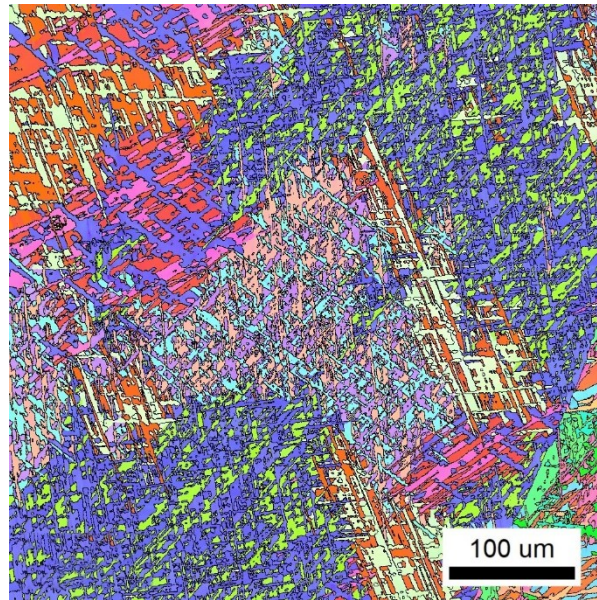


Fig. 2. EBSD image of a 3D-printed Ti–6Al–4V alloy sample
Рис. 2. EBSD-картина 3D-напечатанного образца сплава Ti–6Al–4V

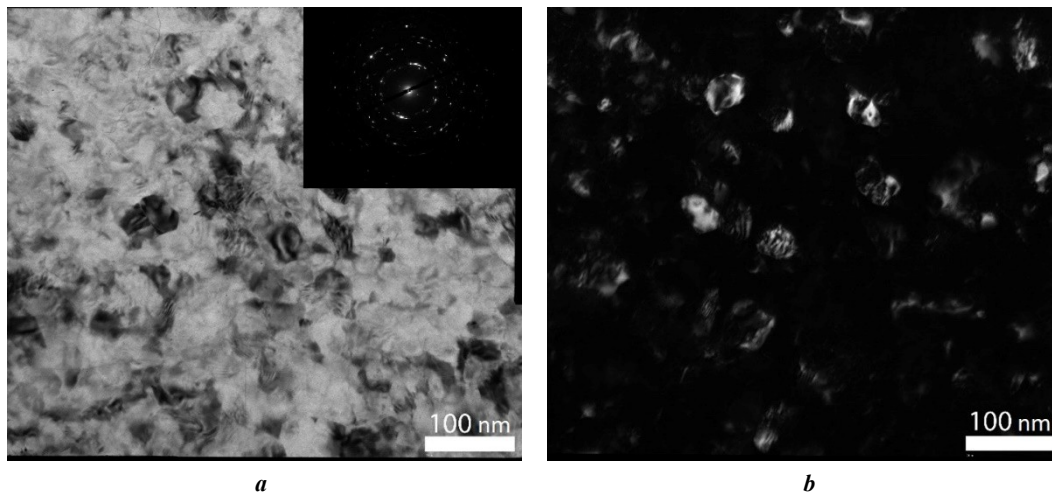


Fig. 3. TEM images of the structure of a 3D-printed Ti–6Al–4V alloy after high-pressure torsion (HPT):
a – bright-field image; *b* – dark-field image
Рис. 3. ПЭМ-изображения структуры 3D-напечатанного сплава Ti–6Al–4V после КВД:
a – светлопольное изображение; *b* – темнопольное изображение

formed. During crystallisation of the deposited layer, epitaxial growth of columnar primary β -grains takes place, the sizes of which are determined by the cooling rate of the melt pool. After passing through the electron beam, the material solidifies into β -grains, and then undergoes rapid cooling, transforming into the martensitic α' -phase, which occupies almost the entire volume of the β -grain. The high cooling rate of the melt pool during 3D printing leads to a low content of the β stabilising element (vanadium) in the β -phase, and its presence in the α -phase [19].

Subsequently, the sample with the initial structure was subjected to high-pressure torsion in a mode of 10 revolutions, the rotation speed of the striker was 0.2 rpm, at a spe-

cific compressive pressure of 6 GPa, which allowed refining significantly the grain structure to (25 ± 10) nm and increasing considerably the level of internal stresses. The resulting structure presumably consists entirely of the α -phase, since it is known that during high-pressure torsion of the Ti–6Al–4V alloy the β -phase dissolves [5–7]. The resulting microstructure differs from that observed after high-pressure torsion in the Ti–6Al–4V titanium alloy, with an $(\alpha+\beta)$ structure characteristic of the hot-rolled state. The difference in structures manifests itself primarily in the sizes of deformed grains. Thus, in the hot-rolled Ti–6Al–4V alloy after high-pressure torsion under various modes, the average grain size ranges from 40 to 100 nm [4–6],

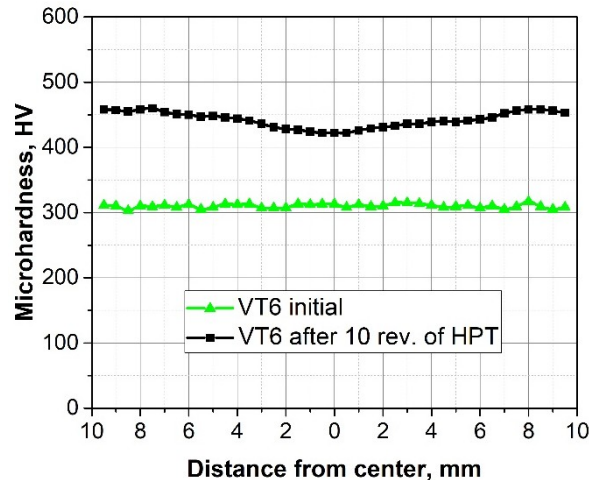


Fig. 4. Microhardness distribution along the diameter of a 3D-printed Ti-6Al-4V alloy in the initial state and after high-pressure torsion (HPT)
Рис. 4. Распределение микротвердости по диаметру 3D-напечатанного сплава Ti-6Al-4V в исходном состоянии и после кручения под высоким давлением (КВД)

Table 1. Average values of grain size and microstructure of a 3D-printed sample of the Ti-6Al-4V titanium alloy
Таблица 1. Средние значения размера зерен и микротвердости 3D-напечатанного образца титанового сплава Ti-6Al-4V

State	Average grain size	Microhardness, HV _{0.1}
Initial state	(1.5±0.5) μm	308±4
High-pressure torsion	(25±10) nm	448±5

while in the Ti-6Al-4V titanium alloy produced by electron-beam additive manufacturing, grain refinement to (25±10) nm is observed. This difference in the structures of the Ti-6Al-4V titanium alloy after high-pressure torsion is determined by different initial states. In 3D-printed Ti-6Al-4V, rapid cooling of the material during wire-feed electron-beam additive manufacturing leads to the formation of a predominantly martensitic α'-phase. Research [6; 7] shows that such an initial Ti-6Al-4V microstructure influences significantly the structure and properties of the alloy after high-pressure torsion. The martensitic structure contains a high level of residual stresses, dislocations and stacking faults, as well as twins due to shear transformation [6; 7]. Moreover, the initial microstructure has a high volume fraction of martensitic α'-phase boundaries, which likely act as nucleation sites for rapid grain fragmentation, and subgrain formation during the initial stages of HPT treatment.

The average value of microhardness of the 3D-printed Ti-6Al-4V alloy in the initial state is (308±4) HV_{0.1}, which is typical for the coarse-grained hot-rolled Ti-6Al-4V titanium alloy [5-7]. High-pressure torsion treatment allowed increasing significantly the values of the 3D-printed Ti-6Al-4V alloy microhardness to a level of the order of

(448±5) HV_{0.1}. The obtained microhardness values are quite high for the Ti-6Al-4V alloy subjected to high-pressure torsion [5-7]. Using the known ratio of microhardness and yield strength (HV=2.8-3σ_y), it is possible to determine the expected mechanical strength of the Ti-6Al-4V alloy [20; 21]. Thus, one can assume that after high-pressure torsion, the yield strength of the Ti-6Al-4V titanium alloy 3D-printed, using the electron-beam additive manufacturing method, reaches 1460 MPa, which is a rather high value for this material.

As is known, the high strength of metal materials with a UFG structure, obtained by the methods of severe plastic deformation can be caused by a number of factors [3; 22; 23] – grain structure refinement, the presence of a high density of dislocations, impurity atoms, dispersed particles of second phases, twins, etc. Moreover, an important factor is the structure and state of grain boundaries, which usually have a nonequilibrium structure and contain a significant amount of grain boundary segregations and insertions [22]. It is obvious that the nature of the high strength of the 3D-printed Ti-6Al-4V titanium alloy, after high-pressure torsion obtained in this work, is determined by a number of structural features, including a highly refined grain structure and a high density of crystal lattice defects.

CONCLUSIONS

1. High-pressure torsion processing of a 3D-printed Ti-6Al-4V alloy allows refining significantly the grain structure to dimensions of (25 ± 10) nm. Such strong refinement is not observed in the initial hot-rolled state of the alloy and is associated with the initial martensitic structure of Ti-6Al-4V.

2. High-pressure torsion of the 3D-printed Ti-6Al-4V alloy allowed increasing significantly the microhardness of the material to a level of approximately (448 ± 5) HV_{0.1}, which, according to the HV=2.8–3 σ_y ratio, corresponds to $\sigma_y\approx 1460$ MPa. Such a high strength is associated with the strong refinement of the structure and the significant density of crystal lattice defects.

3. The results of the study demonstrate, that the initial state of the Ti-6Al-4V alloy significantly affects the grain refinement, and phase transformations caused by high-pressure torsion, which consequently affects the strength characteristics achieved during this treatment.

REFERENCES

- Valiev R.Z., Zhilyaev A.P., Langdon T.G. *Bulk Nanostructured Materials: Fundamentals and Applications*. New Jersey, John Wiley & Sons Publ., 2013. 468 p.
- Horita Z., Edalati K. Severe Plastic Deformation for Nanostructure Controls. *Materials Transactions*, 2020, vol. 61, no. 11, pp. 2241–2247. DOI: [10.2320/matertrans.MT-M2020134](https://doi.org/10.2320/matertrans.MT-M2020134).
- Valiev R.Z., Straumal B., Langdon T.G. Using Severe Plastic Deformation to Produce Nanostructured Materials with Superior Properties. *Annual Review of Materials Research*, 2022, vol. 52, pp. 357–382. DOI: [10.1146/annurev-matsci-081720-123248](https://doi.org/10.1146/annurev-matsci-081720-123248).
- Valiev R.R., Lomakin I.V., Stotskiy A.G., Modina Yu.M., Shafranov P.G., Gadzhiev F.A. Enhanced strength and ductility of an ultrafine-grained Ti alloy processed by HPT. *Defect and Diffusion Forum*, 2018, vol. 385, pp. 331–336. DOI: [10.4028/www.scientific.net/DDF.385.331](https://doi.org/10.4028/www.scientific.net/DDF.385.331).
- Deng Guanyu, Zhao Xing, Su Lihong, Wei Peitang, Zhang Liang, Zhan Lihua, Chong Yan, Zhu Hongtao, Tsuji Nobuhiro. Effect of high pressure torsion process on the microhardness, microstructure and tribological property of Ti6Al4V alloy. *Journal of Materials Science & Technology*, 2021, vol. 94, pp. 183–195. DOI: [10.1016/j.jmst.2021.03.044](https://doi.org/10.1016/j.jmst.2021.03.044).
- Shahmir H., Naghdi F., Pereira P.H.R., Yi Huang, Langdon T.G. Factors influencing superplasticity in the Ti-6Al-4V alloy processed by high-pressure torsion. *Materials Science and Engineering: A*, 2018, vol. 718, pp. 198–206. DOI: [10.1016/j.msea.2018.01.091](https://doi.org/10.1016/j.msea.2018.01.091).
- Shahmir H., Langdon T.G. Using heat treatments, high-pressure torsion and post-deformation annealing to optimize the properties of Ti-6Al-4V alloys. *Acta Materialia*, 2017, vol. 141, pp. 419–426. DOI: [10.1016/j.actamat.2017.09.018](https://doi.org/10.1016/j.actamat.2017.09.018).
- Sergueeva A.V., Stolyarov V.V., Valiev R.Z., Mukherjee A.K. Superplastic behaviour of ultrafine-grained Ti-6Al-4V alloys. *Materials Science and Engineering: A*, 2002, vol. 323, no. 1-2, pp. 318–325. DOI: [10.1016/S0921-5093\(01\)01384-3](https://doi.org/10.1016/S0921-5093(01)01384-3).
- Pan Wang, Xipeng Tan, Mui Ling Sharon Nai, Shu Beng Tor, Jun Wei. Spatial and geometrical-based characterization of microstructure and microhardness for an electron beam melted Ti-6Al-4V component. *Materials & Design*, 2016, vol. 95, pp. 287–295. DOI: [10.1016/j.matdes.2016.01.093](https://doi.org/10.1016/j.matdes.2016.01.093).
- Shunyu Liu, Yung C. Shin. Additive manufacturing of Ti6Al4V alloy: a review. *Materials & Design*, 2019, vol. 164, article number 107552. DOI: [10.1016/j.matdes.2018.107552](https://doi.org/10.1016/j.matdes.2018.107552).
- Džugan J., Novy Z. Powder Application in Additive Manufacturing of Metallic Parts. *Powder Metallurgy – Fundamentals and Case Studies*, 2017, article number 8. DOI: [10.5772/66874](https://doi.org/10.5772/66874).
- Panin A., Kazachenok M., Perevalova O., Martynov S., Panina A., Sklyarova E. Continuous electron beam post-treatment of EBF3-fabricated Ti-6Al-4V parts. *Metals*, 2019, vol. 9, no. 6, article number 699. DOI: [10.3390/met9060699](https://doi.org/10.3390/met9060699).
- Panin A.V., Kazachenok M.S., Dmitriev A.I., Nikonov A.Y., Perevalova O.B., Kazantseva L.A., Sinyakova E.A., Martynov S.A. The effect of ultrasonic impact treatment on deformation and fracture of electron beam additive manufactured Ti-6Al-4V under uniaxial tension. *Materials Science and Engineering: A*, 2022, vol. 832, article number 142458. DOI: [10.1016/j.msea.2021.142458](https://doi.org/10.1016/j.msea.2021.142458).
- Fuchs J., Schneider C., Enzinger N. Wire-based additive manufacturing using an electron beam as heat source. *Welding in the World*, 2018, vol. 62, pp. 267–275. DOI: [10.1007/s40194-017-0537-7](https://doi.org/10.1007/s40194-017-0537-7).
- Hayes B.J., Martin B.W., Welk B. et al. Predicting tensile properties of Ti-6Al-4V produced via directed energy deposition. *Acta Materialia*, 2017, vol. 133, pp. 120–133. DOI: [10.1016/j.actamat.2017.05.025](https://doi.org/10.1016/j.actamat.2017.05.025).
- Panin A.V., Kazachenok M.S., Panin S.V., Berto F. Scale Levels of Quasi-Static and Dynamic Fracture Behavior of Ti-6Al-4V Parts Built by Various Additive Manufacturing Methods. *Theoretical and Applied Fracture Mechanics*, 2020, vol. 110, article number 102781. DOI: [10.1016/j.tafmec.2020.102781](https://doi.org/10.1016/j.tafmec.2020.102781).
- Trojanová Z., Halmešová K., Drozd Z., Džugan J., Valiev R.Z., Podaný P. The influence of severe plastic deformation on the thermal expansion of additively manufactured Ti6Al4V alloy. *Journal of Materials Research and Technology*, 2022, vol. 19, pp. 3498–3506. DOI: [10.1016/j.jmrt.2022.06.097](https://doi.org/10.1016/j.jmrt.2022.06.097).
- Mironov S., Sato Y.S., Kokawa H. Friction-stir welding and processing of Ti-6Al-4V titanium alloy: A review. *Journal of Materials Science & Technology*, 2018, vol. 34, no. 1, pp. 58–72. DOI: [10.1016/j.jmst.2017.10.018](https://doi.org/10.1016/j.jmst.2017.10.018).
- Vlasov I.V., Egorushkin V.E., Panin V.E., Panin A.V., Perevalova O.B. Fractography, Fracture Toughness and Structural Turbulence Under Low-Temperature Shock Loading of a Nonequilibrium Titanium Alloy Ti-6Al-4V. *Mechanics of Solids*, 2020, vol. 55, no. 5, pp. 633–642. DOI: [10.3103/S0025654420050155](https://doi.org/10.3103/S0025654420050155).
- Syed A.K., Zhang Xiang, Caballero A., Shamir M., Williams S. Influence of deposition strategies on tensile and fatigue properties in a wire + arc additive manufactured Ti-6Al-4V. *International Journal of Fatigue*, 2021, vol. 149, article number 106268. DOI: [10.1016/j.ijfatigue.2021.106268](https://doi.org/10.1016/j.ijfatigue.2021.106268).

21. Semenova I.P., Shchitsyn Y.D., Trushnikov D.N., Gareev A.I., Polyakov A.V., Pesin M.V. Microstructural Features and Microhardness of the Ti-6Al-4V Alloy Synthesized by Additive Plasma Wire Deposition Welding. *Materials*, 2023, vol. 16, no. 3, article number 941. DOI: [10.3390/ma16030941](https://doi.org/10.3390/ma16030941).
22. Valiev R.Z., Usmanov E.I., Rezyapova L.R. The Super-strength of Nanostructured Metallic Materials: Their Physical Nature and Hardening Mechanisms. *Physics of Metals and Metallography*, 2022, vol. 123, pp. 1272–1278. DOI: [10.1134/S0031918X22601627](https://doi.org/10.1134/S0031918X22601627).
23. Morris D.G. Strengthening mechanisms in nanocrystalline metals. *Nanostructured Metals and Alloys*, 2011, pp. 299–328. DOI: [10.1533/9780857091123.3.299](https://doi.org/10.1533/9780857091123.3.299).
10. Shunyu Liu, Yung C. Shin. Additive manufacturing of Ti6Al4V alloy: a review // *Materials & Design*. 2019. Vol. 164. Article number 107552. DOI: [10.1016/j.matdes.2018.107552](https://doi.org/10.1016/j.matdes.2018.107552).
11. Džugan J., Novy Z. Powder Application in Additive Manufacturing of Metallic Parts // *Powder Metallurgy – Fundamentals and Case Studies*. 2017. Article number 8. DOI: [10.5772/66874](https://doi.org/10.5772/66874).
12. Panin A., Kazachenok M., Perevalova O., Martynov S., Panina A., Sklyarova E. Continuous electron beam post-treatment of EBF3-fabricated Ti-6Al-4V parts // *Metals*. 2019. Vol. 9. № 6. Article number 699. DOI: [10.3390/met9060699](https://doi.org/10.3390/met9060699).
13. Panin A.V., Kazachenok M.S., Dmitriev A.I., Nikonov A.Y., Perevalova O.B., Kazantseva L.A., Sinyakova E.A., Martynov S.A. The effect of ultrasonic impact treatment on deformation and fracture of electron beam additive manufactured Ti-6Al-4V under uniaxial tension // *Materials Science and Engineering: A*. 2022. Vol. 832. Article number 142458. DOI: [10.1016/j.msea.2021.142458](https://doi.org/10.1016/j.msea.2021.142458).
14. Fuchs J., Schneider C., Enzinger N. Wire-based additive manufacturing using an electron beam as heat source // *Welding in the World*. 2018. Vol. 62. P. 267–275. DOI: [10.1007/s40194-017-0537-7](https://doi.org/10.1007/s40194-017-0537-7).
15. Hayes B.J., Martin B.W., Welk B. et al. Predicting tensile properties of Ti-6Al-4V produced via directed energy deposition // *Acta Materialia*. 2017. Vol. 133. P. 120–133. DOI: [10.1016/j.actamat.2017.05.025](https://doi.org/10.1016/j.actamat.2017.05.025).
16. Panin A.V., Kazachenok M.S., Panin S.V., Berto F. Scale Levels of Quasi-Static and Dynamic Fracture Behavior of Ti-6Al-4V Parts Built by Various Additive Manufacturing Methods // *Theoretical and Applied Fracture Mechanics*. 2020. Vol. 110. Article number 102781. DOI: [10.1016/j.tafmec.2020.102781](https://doi.org/10.1016/j.tafmec.2020.102781).
17. Trojanová Z., Halmešová K., Drozd Z., Džugan J., Valiev R.Z., Podaný P. The influence of severe plastic deformation on the thermal expansion of additively manufactured Ti6Al4V alloy // *Journal of Materials Research and Technology*. 2022. Vol. 19. P. 3498–3506. DOI: [10.1016/j.jmrt.2022.06.097](https://doi.org/10.1016/j.jmrt.2022.06.097).
18. Mironov S., Sato Y.S., Kokawa H. Friction-stir welding and processing of Ti-6Al-4V titanium alloy: A review // *Journal of Materials Science & Technology*. 2018. Vol. 34. № 1. P. 58–72. DOI: [10.1016/j.jmst.2017.10.018](https://doi.org/10.1016/j.jmst.2017.10.018).
19. Vlasov I.V., Egorushkin V.E., Panin V.E., Panin A.V., Perevalova O.B. Fractography, Fracture Toughness and Structural Turbulence Under Low-Temperature Shock Loading of a Nonequilibrium Titanium Alloy Ti-6Al-4V // *Mechanics of Solids*. 2020. Vol. 55. № 5. P. 633–642. DOI: [10.3103/S0025654420050155](https://doi.org/10.3103/S0025654420050155).
20. Syed A.K., Zhang Xiang, Caballero A., Shamir M., Williams S. Influence of deposition strategies on tensile and fatigue properties in a wire + arc additive manufactured Ti-6Al-4V // *International Journal of Fatigue*. 2021. Vol. 149. Article number 106268. DOI: [10.1016/j.ijfatigue.2021.106268](https://doi.org/10.1016/j.ijfatigue.2021.106268).
9. Pan Wang, Xipeng Tan, Mui Ling Sharon Nai, Shu Beng Tor, Jun Wei. Spatial and geometrical-based characterization of microstructure and microhardness for an electron beam melted Ti-6Al-4V component // *Materials & Design*. 2016. Vol. 95. P. 287–295. DOI: [10.1016/j.matdes.2016.01.093](https://doi.org/10.1016/j.matdes.2016.01.093).

СПИСОК ЛИТЕРАТУРЫ

1. Valiev R.Z., Zhilyaev A.P., Langdon T.G. Bulk Nanostructured Materials: Fundamentals and Applications. New Jersey: John Wiley & Sons, 2013. 468 p.
2. Horita Z., Edalati K. Severe Plastic Deformation for Nanostructure Controls // *Materials Transactions*. 2020. Vol. 61. № 11. P. 2241–2247. DOI: [10.2320/matertrans.MT-M2020134](https://doi.org/10.2320/matertrans.MT-M2020134).
3. Valiev R.Z., Straumal B., Langdon T.G. Using Severe Plastic Deformation to Produce Nanostructured Materials with Superior Properties // *Annual Review of Materials Research*. 2022. Vol. 52. P. 357–382. DOI: [10.1146/annurev-matsci-081720-123248](https://doi.org/10.1146/annurev-matsci-081720-123248).
4. Valiev R.R., Lomakin I.V., Stotskiy A.G., Modina Yu.M., Shafranov P.G., Gadzhiev F.A. Enhanced strength and ductility of an ultrafine-grained Ti alloy processed by HPT // *Defect and Diffusion Forum*. 2018. Vol. 385. P. 331–336. DOI: [10.4028/www.scientific.net/DDF.385.331](https://doi.org/10.4028/www.scientific.net/DDF.385.331).
5. Deng Guanyu, Zhao Xing, Su Lihong, Wei Peitang, Zhang Liang, Zhan Lihua, Chong Yan, Zhu Hongtao, Tsuji Nobuhiro. Effect of high pressure torsion process on the microhardness, microstructure and tribological property of Ti6Al4V alloy // *Journal of Materials Science & Technology*. 2021. Vol. 94. P. 183–195. DOI: [10.1016/j.jmst.2021.03.044](https://doi.org/10.1016/j.jmst.2021.03.044).
6. Shahmir H., Naghdi F., Pereira P.H.R., Yi Huang, Langdon T.G. Factors influencing superplasticity in the Ti-6Al-4V alloy processed by high-pressure torsion // *Materials Science and Engineering: A*. 2018. Vol. 718. P. 198–206. DOI: [10.1016/j.msea.2018.01.091](https://doi.org/10.1016/j.msea.2018.01.091).
7. Shahmir H., Langdon T.G. Using heat treatments, high-pressure torsion and post-deformation annealing to optimize the properties of Ti-6Al-4V alloys // *Acta Materialia*. 2017. Vol. 141. P. 419–426. DOI: [10.1016/j.actamat.2017.09.018](https://doi.org/10.1016/j.actamat.2017.09.018).
8. Sergueeva A.V., Stolyarov V.V., Valiev R.Z., Mukherjee A.K. Superplastic behaviour of ultrafine-grained Ti-6Al-4V alloys // *Materials Science and Engineering: A*. 2002. Vol. 323. № 1-2. P. 318–325. DOI: [10.1016/S0921-5093\(01\)01384-3](https://doi.org/10.1016/S0921-5093(01)01384-3).

22. Valiev R.Z., Usmanov E.I., Rezyapova L.R. The Super-strength of Nanostructured Metallic Materials: Their Physical Nature and Hardening Mechanisms // *Physics of Metals and Metallography*. 2022. Vol. 123. P. 1272–1278. DOI: [10.1134/S0031918X22601627](https://doi.org/10.1134/S0031918X22601627).
23. Morris D.G. Strengthening mechanisms in nanocrystalline metals // *Nanostructured Metals and Alloys*. 2011. P. 299–328. DOI: [10.1533/9780857091123.3.299](https://doi.org/10.1533/9780857091123.3.299).

Микроструктура и прочность 3D-напечатанного сплава Ti-6Al-4V, подвергнутого кручению под высоким давлением

© 2024

Усманов Эмиль Ильдарович^{*1}, инженер НИИ физики перспективных материалов
Савина Яна Николаевна², инженер-исследователь НИИ физики перспективных материалов
Валиев Роман Русланович³, кандидат технических наук,
старший научный сотрудник НИИ физики перспективных материалов
Уфимский университет науки и технологий, Уфа (Россия)

*E-mail: usmanovei@uust.ru

¹ORCID: <https://orcid.org/0000-0002-1725-4651>²ORCID: <https://orcid.org/0000-0003-1387-8819>³ORCID: <https://orcid.org/0000-0003-1584-2385>

Поступила в редакцию 27.06.2023

Принята к публикации 12.02.2024

Аннотация: В настоящее время одним из эффективных методов 3D-печати является проволочная электронно-лучевая аддитивная технология (ЭЛАТ), которая позволяет изготавливать крупногабаритные промышленные заготовки из титанового сплава Ti-6Al-4V. Однако Ti-6Al-4V, полученный данным методом, демонстрирует пониженные прочностные свойства. Известно, что повысить прочностные свойства металлических материалов можно посредством измельчения их зеренной структуры кручением под высоким давлением (КВД). Настоящая работа направлена на исследование влияния КВД на микроструктуру и механическую прочность конструкционного титанового сплава Ti-6Al-4V, полученного методом ЭЛАТ. Посредством оптической, растровой и просвечивающей электронной микроскопии изучена микроструктура 3D-напечатанного сплава Ti-6Al-4V в исходном состоянии и после КВД. Проведен EBSD-анализ материала в исходном состоянии. Измерена микротвердость материала в исходном и деформированном состояниях. С использованием зависимости предела текучести от микротвердости определена предположительная механическая прочность материала после обработки методом КВД. Обсуждаются микроструктурные особенности 3D-напечатанного сплава Ti-6Al-4V после КВД, за счет которых обеспечивается повышенная прочность данного материала. Результаты исследований демонстрируют, что 3D-печать методом ЭЛАТ позволяет получить титановый сплав Ti-6Al-4V с необычной для данного материала микроструктурой, которая состоит из столбчатых первичных β-зерен с поперечным размером 1–2 мм, внутри которых располагаются мартенситные иглы α'-Ti. Между иглами α'-Ti наблюдаются тонкие прослойки β-Ti толщиной около 200 нм. Дальнейшая деформационная обработка сплава методом КВД позволила сформировать в его объеме ультрамелкозернистую структуру, состоящую предположительно из α-зерен со средним размером (25±10) нм. КВД-обработка 3D-напечатанного сплава позволила достичь довольно высоких значений микротвердости (448±5) HV_{0,1}, что по соотношению HV=2,8–3σ_T соответствует предположительному пределу текучести, равному примерно 1460 МПа.

Ключевые слова: 3D-напечатанный титановый сплав Ti-6Al-4V; титановый сплав Ti-6Al-4V; электронно-лучевая проволочная аддитивная технология; 3D-печать; кручение под высоким давлением; микроструктура; механические свойства.

Благодарности: Исследование выполнено за счет гранта Российского научного фонда № 22-19-00445, <https://rscf.ru/project/22-19-00445/>.

Исследования выполнены с использованием оборудования ЦКП «Нанотех» ФГБОУ ВО «УУНИТ».

Статья подготовлена по материалам докладов участников XI Международной школы «Физическое материаловедение» (ШФМ-2023), Тольятти, 11–15 сентября 2023 года.

Для цитирования: Усманов Э.И., Савина Я.Н., Валиев Р.Р. Микроструктура и прочность 3D-напечатанного сплава Ti-6Al-4V, подвергнутого кручению под высоким давлением // *Frontier Materials & Technologies*. 2024. № 3. С. 109–116. DOI: 10.18323/2782-4039-2024-3-69-10.

OUR AUTHORS

Anosov Maksim Sergeevich, PhD (Engineering), Associate Professor, assistant professor of Chair “Technology and Equipment of Mechanical Engineering”.
Address: R.E. Alekseev Nizhny Novgorod State Technical University, 603155, Russia, Nizhny Novgorod, Minin Street, 24.
E-mail: anosov.ms@nntu.ru

Antipova Evgeniya Dmitrievna, postgraduate student of Chair “Mechanical Engineering Technology, Machines and Tools”.
Address: Samara State Technical University, 443100, Russia, Samara, Molodogvardeyskaya Street, 244.
E-mail: antipova.ev.smr@yandex.ru

Astafurova Elena Gennadyevna, Doctor of Sciences (Physics and Mathematics), Head of Laboratory of Physics of Hierarchic Structures in Metals and Alloys.
Address: Institute of Strength Physics and Materials Science of Siberian Branch of RAS, 634055, Russia, Tomsk, Akademichesky Prospekt, 2/4.
E-mail: elena.g.astafurova@gmail.com

Astapov Denis Olegovich, student.
Address: Tomsk State University, 634050, Russia, Tomsk, Lenin Prospekt, 36.
E-mail: denis.0612@mail.ru

Belova Galina Sergeevna, PhD (Engineering), junior researcher of the Laboratory “Digital Twins of Materials and Technological Procedures of their Processing”.
Address: Samara State Technical University, 443100, Russia, Samara, Molodogvardeyskaya Street, 244.
E-mail: galya.belova.94@mail.ru

Chernigin Mikhail Alekseevich, postgraduate student, engineer of Chair “Technology and Equipment of Mechanical Engineering”.
Address: R.E. Alekseev Nizhny Novgorod State Technical University, 603155, Russia, Nizhny Novgorod, Minin Street, 24.
E-mail: honeybadger52@yandex.ru

Chudnov Aleksandr Vladimirovich, postgraduate student.
Address: Ulyanovsk State Technical University, 432027, Russia, Ulyanovsk, Severny Venets Street, 32.
E-mail: chudnov73ru@gmail.com

Denisenko Aleksandr Fedorovich, Doctor of Sciences (Engineering), Professor, professor of Chair “Mechanical Engineering Technology, Machines and Tools”.
Address: Samara State Technical University, 443100, Russia, Samara, Molodogvardeyskaya Street, 244.
E-mail: tmsi@samgtu.ru

Gnusina Anastasiya Mikhailovna, postgraduate student of Chair “Nanotechnologies, Materials Science and Mechanics”.
Address: Togliatti State University, 445020, Russia, Togliatti, Belorusskaya Street, 14.
E-mail: anastasiya.gnusina@vaz.ru

Grishin Roman Georgievich, PhD (Engineering), Associate Professor, assistant professor of Chair “Mechanical Engineering Technology, Machines and Tools”.
Address: Samara State Technical University, 443100, Russia, Samara, Molodogvardeyskaya Street, 244.
E-mail: grg-s1@mail.ru

Gruzkov Igor Viktorovich, postgraduate student,
Head of the Laboratory of Optical and Electron Microscopy.
Address 1: Togliatti State University,
445020, Russia, Togliatti, Belorusskaya Street, 14.
Address 2: IT-Service Limited Liability Company,
443001, Russia, Samara, Ulyanovskaya/Yarmarochnaya Street, 52/55.
E-mail: gruzkov@its-samara.com

Gurtova Darya Yuryevna, student.
Address: Tomsk State University,
634050, Russia, Tomsk, Lenin Prospekt, 36.
E-mail: dasha_gurtova@mail.ru

Kabaldin Yuri Georgievich, Doctor of Sciences (Engineering), Professor,
professor of Chair “Technology and Equipment of Mechanical Engineering”.
Address: R.E. Alekseev Nizhny Novgorod State Technical University,
603155, Russia, Nizhny Novgorod, Minin Street, 24.
E-mail: uru.40@mail.ru

Khafizova Elvira Dinifovna, PhD (Engineering),
assistant professor of Chair of Materials Science and Metal Physics,
senior researcher at the Research Laboratory “Metals and Alloys under Extreme Exposures”.
Address 1: Institute of Physics of Molecules and Crystals
of Ufa Federal Research Center of RAS,
450054, Russia, Ufa, Prospekt Oktyabrya, 71.
Address 2: Ufa University of Science and Technology,
450076, Russia, Ufa, Zaki Validi Street, 32.
E-mail: ela.90@mail.ru

Lyudmirsky Yuri Georgievich, Doctor of Sciences (Engineering), Professor,
leading researcher of the Center for Scientific Competencies.
Address: Don State Technical University,
344010, Russia, Rostov-on-Don, Gagarin Square, 1.
E-mail: lyudmirskiy40@mail.ru

Maidan Dmitry Aleksandrovich, PhD (Engineering), Associate Professor,
assistant professor of Chair “Materials Science, Powder Metallurgy, Nanomaterials”.
Address: Samara State Technical University,
443100, Russia, Samara, Molodogvardeyskaya Street, 244.
E-mail: mtm.samgtu@mail.ru

Melnikov Evgeny Vasilyevich, junior researcher
of Laboratory of Physics of Hierarchic Structures in Metals and Alloys.
Address: Institute of Strength Physics and Materials Science of Siberian Branch of RAS,
634055, Russia, Tomsk, Akademichesky Prospekt, 2/4.
E-mail: melnickow.jenya@yandex.ru

Mordovina Yuliya Sergeevna, postgraduate student,
educational process engineer of the Institute of Retraining of Specialists.
Address: R.E. Alekseev Nizhny Novgorod State Technical University,
603155, Russia, Nizhny Novgorod, Minin Street, 24.
E-mail: ips4@nntu.ru

Mordovtsev Nikolay Alekseevich, graduate student.
Address: Don State Technical University,
344010, Russia, Rostov-on-Don, Gagarin Square, 1.
E-mail: map642@mail.ru

Nescoromniy Stanislav Valeryevich, PhD (Engineering), Associate Professor,
Head of Chair “Machines and Automation of Welding Engineering”.
Address: Don State Technical University,
344010, Russia, Rostov-on-Don, Gagarin Square, 1.
E-mail: nescoromniy@mail.ru

Panchenko Marina Yuryevna, junior researcher
of Laboratory of Physics of Hierarchic Structures in Metals and Alloys.
Address: Institute of Strength Physics and Materials Science of Siberian Branch of RAS,
634055, Russia, Tomsk, Akademichesky Prospekt, 2/4.
E-mail: panchenko.marina4@gmail.com

Polenok Milena Vladislavovna, graduate student
of Chair of Materials Science and Physics of Metals,
research assistant at the Research Laboratory “Metals and Alloys under Extreme Exposures”.
Address 1: Institute of Physics of Molecules and Crystals
of Ufa Federal Research Center of RAS,
450054, Russia, Ufa, Prospekt Oktyabrya, 71.
Address 2: Ufa University of Science and Technology,
450076, Russia, Ufa, Zaki Validi Street, 32.
E-mail: renaweiwei.179@mail.ru

Savina Yana Nikolaevna, research engineer
of the Research Institute of Physics of Advanced Materials.
Address: Ufa University of Science and Technology,
450076, Russia, Ufa, Zaki Validi Street, 32.
E-mail: savina.yana18@yandex.ru

Sitdikov Vil Dayanovich, Doctor of Sciences (Physics and Mathematics),
senior expert, senior researcher.
Address 1: OOO RN-BashNIPIneft,
450006, Russia, Ufa, Lenin Street, 86/1.
Address 2: Institute of Physics of Molecules and Crystals
of Ufa Federal Research Center of RAS,
450054, Russia, Ufa, Prospekt Oktyabrya, 71.
E-mail: SitdikovVD@bnipi.rosneft.ru

Strizhakov Evgeny Lvovich, Doctor of Sciences (Engineering), Professor,
leading researcher of the Center for Scientific Competencies.
Address: Don State Technical University,
344010, Russia, Rostov-on-Don, Gagarin Square, 1.
E-mail: strizhakov@inbox.ru

Svyatkin Aleksey Vladimirovich, PhD (Engineering),
assistant professor of Chair “Nanotechnologies, Materials Science and Mechanics”.
Address: Togliatti State University,
445020, Russia, Togliatti, Belorusskaya Street, 14.
E-mail: astgl@mail.ru

Titova Yulia Vladimirovna, PhD (Engineering), Associate Professor,
assistant professor of Chair “Materials Science, Powder Metallurgy, Nanomaterials”.
Address: Samara State Technical University,
443100, Russia, Samara, Molodogvardeyskaya Street, 244.
E-mail: titova600@mail.ru

Unyanin Aleksandr Nikolaevich, Doctor of Sciences (Engineering), Associate Professor.
Address: Ulyanovsk State Technical University,
432027, Russia, Ulyanovsk, Severny Venets Street, 32.
E-mail: a_un@mail.ru

Usmanov Emil Ildarovich, engineer
of the Research Institute of Physics of Advanced Materials.
Address: Ufa University of Science and Technology,
450076, Russia, Ufa, Zaki Validi Street, 32.
E-mail: usmanovei@uust.ru

Valiev Roman Ruslanovich, PhD (Engineering),
senior researcher of the Research Institute of Physics of Advanced Materials.
Address: Ufa University of Science and Technology,
450076, Russia, Ufa, Zaki Validi Street, 32.
E-mail: rovaliev@gmail.com

Vyboishchik Mikhail Aleksandrovich, Doctor of Sciences (Physics and Mathematics), Professor, professor of Chair “Welding, Pressure Treatment of Materials and Allied Processes”.

Address: Togliatti State University,
445020, Russia, Togliatti, Belorusskaya Street, 14.
E-mail: vma63vma@yandex.ru

Yakubova Alsu Faridovna, postgraduate student.

Address: Samara State Technical University,
443100, Russia, Samara, Molodogvardeyskaya Street, 244.
E-mail: minekhanovaaf@mail.ru

НАШИ АВТОРЫ

Аносов Максим Сергеевич, кандидат технических наук, доцент,
доцент кафедры «Технология и оборудование машиностроения».
Адрес: Нижегородский государственный технический университет им. Р.Е. Алексеева,
603155, Россия, г. Нижний Новгород, ул. Минина, 24.
E-mail: anosov.ms@nntu.ru

Антипова Евгения Дмитриевна, аспирант
кафедры «Технология машиностроения, станки и инструменты».
Адрес: Самарский государственный технический университет,
443100, Россия, г. Самара, ул. Молодогвардейская, 244.
E-mail: antipova.ev.smr@yandex.ru

Астапов Денис Олегович, студент.
Адрес: Томский государственный университет,
634050, Россия, г. Томск, пр-т Ленина, 36.
E-mail: denis.0612@mail.ru

Астафурова Елена Геннадьевна, доктор физико-математических наук,
заведующий лабораторией физики иерархических структур в металлах и сплавах.
Адрес: Институт физики прочности и материаловедения Сибирского отделения РАН,
634055, Россия, г. Томск, Академический пр-т, 2/4.
E-mail: elena.g.astafurova@gmail.com

Белова Галина Сергеевна, кандидат технических наук, младший научный сотрудник
лаборатории «Цифровые двойники материалов и технологических процессов их обработки».
Адрес: Самарский государственный технический университет,
443100, Россия, г. Самара, ул. Молодогвардейская, 244.
E-mail: galya.belova.94@mail.ru

Валиев Роман Русланович, кандидат технических наук,
старший научный сотрудник НИИ физики перспективных материалов.
Адрес: Уфимский университет науки и технологий,
450076, Россия, г. Уфа, ул. Заки Валиди, 32.
E-mail: rovaliev@gmail.com

Выбойщик Михаил Александрович, доктор физико-математических наук, профессор,
профессор кафедры «Сварка, обработка материалов давлением и родственные процессы».
Адрес: Тольяттинский государственный университет,
445020, Россия, г. Тольятти, ул. Белорусская, 14.
E-mail: vma63vma@yandex.ru

Гнусина Анастасия Михайловна, аспирант
кафедры «Нанотехнологии, материаловедение и механика».
Адрес: Тольяттинский государственный университет,
445020, Россия, г. Тольятти, ул. Белорусская, 14.
E-mail: anastasiya.gnusina@vaz.ru

Гришин Роман Георгиевич, кандидат технических наук, доцент,
доцент кафедры «Технология машиностроения, станки и инструменты».
Адрес: Самарский государственный технический университет,
443100, Россия, г. Самара, ул. Молодогвардейская, 244.
E-mail: grg-s1@mail.ru

Грузков Игорь Викторович, аспирант,
заведующий лабораторией оптической и электронной микроскопии.
Адрес 1: Тольяттинский государственный университет,
445020, Россия, г. Тольятти, ул. Белорусская, 14.
Адрес 2: ООО «ИТ-Сервис»,
443001, Россия, г. Самара, ул. Ульяновская/Ярмарочная, 52/55.
E-mail: gruzkov@its-samara.com

Гуртова Дарья Юрьевна, студент.

Адрес: Томский государственный университет,
634050, Россия, г. Томск, пр-т Ленина, 36.
E-mail: dasha_gurtova@mail.ru

Денисенко Александр Федорович, доктор технических наук, профессор,
профессор кафедры «Технология машиностроения, станки и инструменты».

Адрес: Самарский государственный технический университет,
443100, Россия, г. Самара, ул. Молодогвардейская, 244.
E-mail: tmsi@samgtu.ru

Кабалдин Юрий Георгиевич, доктор технических наук, профессор,
профессор кафедры «Технология и оборудование машиностроения».

Адрес: Нижегородский государственный технический университет им. Р.Е. Алексеева,
603155, Россия, г. Нижний Новгород, ул. Минина, 24.
E-mail: uru.40@mail.ru

Людмирский Юрий Георгиевич, доктор технических наук, профессор,
ведущий научный сотрудник Центра научных компетенций.

Адрес: Донской государственный технический университет,
344010, Россия, г. Ростов-на-Дону, пл. Гагарина, 1.
E-mail: lyudmirskiy40@mail.ru

Майдан Дмитрий Александрович, кандидат технических наук, доцент,
доцент кафедры «Металловедение, порошковая металлургия, наноматериалы».

Адрес: Самарский государственный технический университет,
443100, Россия, г. Самара, ул. Молодогвардейская, 244.
E-mail: mtm.samgtu@mail.ru

Мельников Евгений Васильевич, младший научный сотрудник
лаборатории физики иерархических структур в металлах и сплавах.

Адрес: Институт физики прочности и материаловедения Сибирского отделения РАН,
634055, Россия, г. Томск, Академический пр-т, 2/4.
E-mail: melnickow.jenya@yandex.ru

Мордовина Юлия Сергеевна, аспирант,

инженер по учебному процессу института переподготовки специалистов
Адрес: Нижегородский государственный технический университет им. Р.Е. Алексеева,
603155, Россия, г. Нижний Новгород, ул. Минина, 24.
E-mail: ips4@nntu.ru

Мордовцев Николай Алексеевич, магистрант.

Адрес: Донской государственный технический университет,
344010, Россия, г. Ростов-на-Дону, пл. Гагарина, 1.
E-mail: mar642@mail.ru

Нескоромный Станислав Валерьевич, кандидат технических наук, доцент,
заведующий кафедрой «Машины и автоматизация сварочного производства».

Адрес: Донской государственный технический университет,
344010, Россия, г. Ростов-на-Дону, пл. Гагарина, 1.
E-mail: nescoromniy@mail.ru

Панченко Марина Юрьевна, младший научный сотрудник
лаборатории физики иерархических структур в металлах и сплавах.

Адрес: Институт физики прочности и материаловедения Сибирского отделения РАН,
634055, Россия, г. Томск, Академический пр-т, 2/4.
E-mail: panchenko.marina4@gmail.com

Поленок Милена Владиславовна, магистрант кафедры материаловедения и физики металлов, лаборант НИЛ «Металлы и сплавы при экстремальных воздействиях».
 Адрес 1: Институт физики молекул и кристаллов Уфимского федерального исследовательского центра РАН, 450054, Россия, г. Уфа, пр-т Октября, 71.
 Адрес 2: Уфимский университет науки и технологий, 450076, Россия, г. Уфа, ул. Заки Валиди, 32.
 E-mail: renaweiwei.179@mail.ru

Савина Яна Николаевна, инженер-исследователь НИИ физики перспективных материалов.
 Адрес: Уфимский университет науки и технологий, 450076, Россия, г. Уфа, ул. Заки Валиди, 32.
 E-mail: savina.yana18@yandex.ru

Святкин Алексей Владимирович, кандидат технических наук, доцент кафедры «Нанотехнологии, материаловедение и механика».
 Адрес: Тольяттинский государственный университет, 445020, Россия, г. Тольятти, ул. Белорусская, 14.
 E-mail: astgl@mail.ru

Ситдиков Виль Даянович, доктор физико-математических наук, старший эксперт, старший научный сотрудник.
 Адрес 1: ООО «РН-БашНИПИнефть», 450006, Россия, г. Уфа, ул. Ленина, 86/1.
 Адрес 2: Институт физики молекул и кристаллов Уфимского федерального исследовательского центра РАН, 450054, Россия, г. Уфа, пр-т Октября, 71.
 E-mail: SitdikovVD@bnipi.rosneft.ru

Стрижаков Евгений Львович, доктор технических наук, профессор, ведущий научный сотрудник Центра научных компетенций.
 Адрес: Донской государственный технический университет, 344010, Россия, г. Ростов-на-Дону, пл. Гагарина, 1.
 E-mail: strizhakov@inbox.ru

Титова Юлия Владимировна, кандидат технических наук, доцент, доцент кафедры «Металловедение, порошковая металлургия, наноматериалы».
 Адрес: Самарский государственный технический университет, 443100, Россия, г. Самара, ул. Молодогвардейская, 244.
 E-mail: titova600@mail.ru

Унянин Александр Николаевич, доктор технических наук, доцент.
 Адрес: Ульяновский государственный технический университет, 432027, Россия, г. Ульяновск, ул. Северный Венец, 32.
 E-mail: a_un@mail.ru

Усманов Эмиль Ильдарович, инженер НИИ физики перспективных материалов.
 Адрес: Уфимский университет науки и технологий, 450076, Россия, г. Уфа, ул. Заки Валиди, 32.
 E-mail: usmanovei@uust.ru

Хафизова Эльвира Динифовна, кандидат технических наук, доцент кафедры материаловедения и физики металлов, старший научный сотрудник НИЛ «Металлы и сплавы при экстремальных воздействиях».
 Адрес 1: Институт физики молекул и кристаллов Уфимского федерального исследовательского центра РАН, 450054, Россия, г. Уфа, пр-т Октября, 71.
 Адрес 2: Уфимский университет науки и технологий, 450076, Россия, г. Уфа, ул. Заки Валиди, 32.
 E-mail: ela.90@mail.ru

Чернигин Михаил Алексеевич, аспирант, инженер

кафедры «Технология и оборудование машиностроения».

Адрес: Нижегородский государственный технический университет им. Р.Е. Алексеева,
603155, Россия, г. Нижний Новгород, ул. Минина, 24.

E-mail: honeybadger52@yandex.ru

Чуднов Александр Владимирович, аспирант.

Адрес: Ульяновский государственный технический университет,
432027, Россия, г. Ульяновск, ул. Северный Венец, 32.

E-mail: chudnov73ru@gmail.com

Якубова Алсу Фаридовна, аспирант.

Адрес: Самарский государственный технический университет,
443100, Россия, г. Самара, ул. Молодогвардейская, 244.

E-mail: minekhanovaaf@mail.ru

On the cover: Microstructure of 08KhMFA steel after quenching (SEM). Authors of the photo: M.A. Vyboishchik, professor of Chair “Welding, Pressure Treatment of Materials and Allied Processes” (Togliatti State University, Togliatti, Russia), I.V. Gruzkov, postgraduate student (Togliatti State University, Togliatti, Russia), Head of the Laboratory of Optical and Electron Microscopy (IT-Service Limited Liability Company, Togliatti, Russia).

На обложке: Микроструктура стали 08ХМФА после закалки (СЭМ). Авторы фото: М.А. Выбойщик, профессор кафедры «Сварка, обработка материалов давлением и родственные процессы» (Тольяттинский государственный университет, Тольятти, Россия), И.В. Грузков, аспирант (Тольяттинский государственный университет, Тольятти, Россия), заведующий лабораторией оптической и электронной микроскопии (ООО «ИТ-Сервис», Тольятти, Россия).